The Interaction of Circumbinary Discs and Planets and Binary Stars

Dissertation

der Mathematisch-Naturwissenschaftlichen Fakultät

der Eberhard Karls Universität Tübingen

zur Erlangung des Grades eines

Doktors der Naturwissenschaften

(Dr. rer. nat.)

vorgelegt von

Anna Beate Tabea Penzlin

aus Bad Soden am Taunus

Tübingen

2022

Gedruckt mit Genehmigung der Mathematisch-Naturwissenschaftlichen Fakultät der Eberhard Karls Universität Tübingen.

Tag der mündlichen Qualifikation:	24.05.2022
Dekan:	Prof. Dr. Thilo Stehle
1. Berichterstatter/-in:	Prof. Dr. Klaus Werner
2. Berichterstatter/-in:	Prof. Dr. Cornelis Dullemond

For Willy Kley

Contents

Abstract

Binary configurations are very common in astronomy. $\sim 50\%$ of all stars are in a binary or multiple system. With the Kepler mission, planets orbiting around a binary configuration, circumbinary planets, have been detected. Nowadays, instruments like ALMA and the SPHERE spectrometer on the Very Large Telescope allow very detailed images of circumbinary discs, which are another key to understand not only the formation and evolution of planets, but also the evolution of the binary components themselves in the early phase with a disc present. As observations show only single images, numerical simulations are necessary to model the processes leading to the observed conditions. In this thesis circumbinary discs and embedded planets are investigated using simulations with the finite volume code GPU-PLUTO. The work discusses the structure of circumbinary discs in comparison to observations of the GG Tau A system and the migration of planets in circumbinary discs with varying disc parameters to identify which lead to the observed planet configurations. Furthermore, the theoretical possibility to create a planetary 1:1 resonance by the special conditions inside a circumbinary disc is demonstrated and the change of the binary orbits due to the circumbinary disc is explored for a large parameter space.

Zusammenfassung

Konfigurationen von zwei gravitativ gebundenen Objekten sind keine Seltenheit im astronomischen Kontext. Etwa $\sim 50\%$ aller Sterne befinden sich in einem Doppel- oder Mehrfachsternsystem. Mit Hilfe der Kepler Mission konnten Planeten auf Orbits um solche Doppelsterne detektiert werden. Heutzutage ermöglichen Instrumente wie das "Atacama Large Millimeter/submillimeter Array", ALMA, oder das "Very large Telescope", VLT, mit dem "SPHERE"-Spektrometer detailiert aufgelöste Bilder von Akkretionsscheiben um Doppelsternsysteme, sogenannten circumbinären Scheiben. Diese Beobachtungen sind ein anderer Schlüssel um die Formation und Entwickung von Planeten, ebenfalls des Doppelsternsystems selbst zu verstehen. Da Beobachtungen nur einzelne Bilder ziegen, sind numerische Simulationen nötig um die Prozesse zu modellieren, die zu den beobachteten Zuständen führen. In dieser Arbeit werden circumbinäre Scheiben und in Scheiben eingebettete Planeten untersucht unter zur Hilfenahme der Finite-Volumen Simulationssoftware GPU-PLUTO. Dafür werden die Strukturen von Modellen circumbinärer Scheiben mit den Beobachtung des GG Tau A systems verglichen, außerdem werden Akkretionsscheibenparameter variiert und identifiziert welche zu den detektierten Planetkonfigurationen führen. Darüber hinaus betrachtet die Arbeit die theoretische Möglichkeit eine planetare 1-zu-1 Resonanz zu erreichen unter besonderen Bedingungen in der circumbinären Scheibe und erschließt die Effekte der Scheibe auf den Doppelsternorbit für einen weiten Parameterraum.

1 Introduction

Tatooine is one fictional example of a circumbinary planet, with its two suns rising over the desert. In reality more and more such planets have been discovered in the recent years and more are to come, as stars in binary or multiple systems make up half of all stars, like for example our Sun's closest neighbours α-, β- and Proxima Centauri. The formation of stars does not happen in an empty void, but in large molecular clouds, in cores of gas and dust inside winding filaments and clumps, giving rise to numerous stars often in binaries and multiples. However, to understand planet formation the picture is often simplified to just one central star. While this approach simplifies modelling and allows to understand the basic principles of planet formation, it leaves out many star systems. As the theory for single star planet formation has advanced significantly, in this thesis we will take a look at how binaries change the picture and what we can even derive from the evolution of circumbinary discs and planets for circumstellar discs in general using hydrodynamics simulations and insights gained from observations.

This Chapter 1 introduces the current knowledge about the binary and planet formation environment from an observational perspective. In Chapter 2 the physics needed to understand a protoplanetary disc and the particulars of a circumbinary environment is layed out. How to create a hydrodynamical model of the circumbinary disc including planets using a finite volume grid code is explained in Chapter 3. Thereafter, Chapter 4 summarizes the results of the published articles. More ongoing investigations and open question about physical and numerical additions to the circumbinary model are discussed in Chapter 5 and all will be summarized in Chapter 6. Finally the publications quoted in Chapter 4 are attached in Chapter 7. This work is meant to not only highlight the importance of the circumbinary environment for investigation into the planet formation process but also to teach how to create a circumbinary disc model.

1.1 Binary systems

A binary system describes a configuration of two objects that orbit a common center of gravity. Binary objects in an astrophysical context are common configurations as objects form in clusters and filament structures. From galaxies to black holes, stars, and down to asteroids, binary configurations exist over a wide range of scales in a variety of objects. In this work we will mostly shed light on stellar binaries. However, given the right environment parameters, the mechanics of all those systems is comparable and results can be scaled to other hydrodynamical systems. Besides binary stars, there are also multiple configurations, which consist of more then two hierarchically organized stellar objects that all orbit one common center of gravity. An example of such systems would be the closest star system to the Sun, α Centauri A and B and Proxima Centauri. Here the A and B components are in a close 80 year orbit and the Proxima component orbits both at a far orbit of 550 000 years. Another example would be the Castor system with 6 stars (see Sketch 1.1). Castor consists of two inner pairs of binaries, Castor Aa and Ab and Castor Ba and Bb, that are orbited by a third binary Castor Ca and Cb. The close binaries have orbital periods of less than 10 days while the orbit between A and B has a period of 445 years and the C binary revolves on a 14 000 years orbit. As these multiple systems consist of hierarchical binary structures at multiple relevant length scales it is possible to simplify the system to a binary at the length scale of interest and treat for example inner binaries as single components. Therefore, in this work, when talking about binaries we will include multiple systems as their dynamics at every level is approximated by binary behaviour.

Research in binary stars is highly relevant, as $\sim 50\%$ of all stars are in binary configurations. The rate of how many stars are in a binary depends on the spectral type, i.e. the mass of the stars. Brighter, more massive stars are favourably binary with rates of $> 80\%$ for OB stars with $M_* > 16\,M_\odot$, while for M-type stars with $M_* < 0.5\,M_\odot$ the binary rate smoothly drops to only $\leq 26\%$. The mass ratio between primary and secondary star appears to be evenly distributed between $M_2/M_1 = 0.1 - 1.0$ (Duchêne & Kraus 2013). However, recent work for close binaries show that equal mass configurations are favoured (Kounkel et al. 2021). For solar-like binaries the most probable separation is $a_{\rm bin} \approx 45$ au (Raghavan et al. 2010). Closer and wider binary are increasingly unlikely. Only 4% of solar-like binaries have orbits of $> 10\,000$ au. In observational astronomy such statistics can be biased by the observation method. However, Raghavan et al. (2010) includes the search for binary companions for 56% of primaries up to separations of 10 000 au.

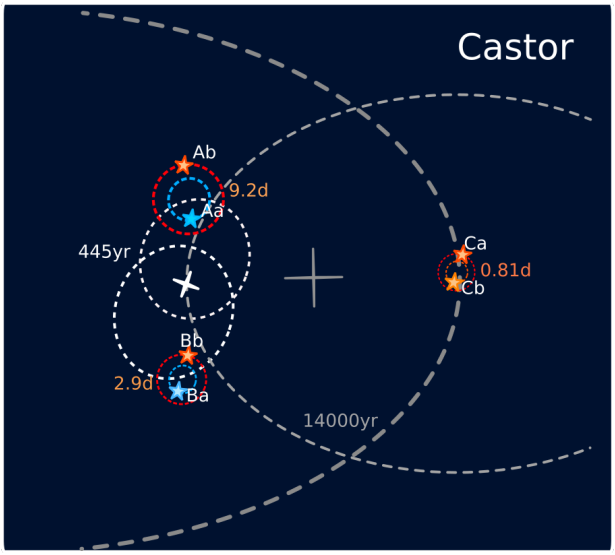

Figure 1.1: Sketch of the Castor sixtuple system

To identify binary stars there are several methods used. In order of separation from close to far the most important methods for identifying binaries are listed here:

- spectroscopic binary; a Doppler shift in the spectral lines is observed caused by the binary motion.
- eclipsing binary; a periodic variation in luminosity is observed, as the secondary moves in the line of sight of the primary.
- photometric binary; the luminosity of the binary object is brighter, than the luminosity assumed by a single object Planck spectrum.
- visual binary; both binary stars are observed in their common orbit.
- astrometric binary; the motion of a light source is wobbling as it orbits around the common center of mass.
- Common proper motion (CPM) binary; two observed stars have a common proper motion.

During formation, stars are likely to form in multiples or binaries as explained for example in the review by Larson (2003). This can either happen already during a rotating collapse or a massive star can form companions by disc fragmentation.

When binaries form together they are surrounded by one common circumbinary disc (CBD). These circumbinary discs have been observed. Two well-known examples of CBDs are HD142527 (e.g. Hunziker et al. 2021) and GG Tau A. Fig. 1.2 shows the polarized scattered light image of GG Tau A using the SPHERE (Beuzit et al. 2019) and IRDIS instrument of the Very Large Telescope (VLT) for the H-band ($1.63\,\mu m$) (Keppler et al. 2020), which traces the surface of the disc. The inner region displays a large gap. This is typical for circumbinary discs as will be discussed in more detail in Chapter 4.

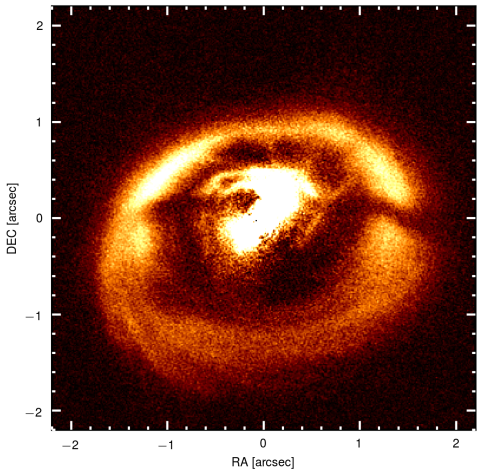

Figure 1.2: Polarized scattered light image of GG Tau A using VLT/SPHERE by Keppler et al. (2020).

1.2 Protoplanetary discs

The circumbinary discs around protostars like GG Tau A are special cases of planet-forming discs known as protoplanetary discs (PPD). When stars form from collapsing clouds of gas and dust, angular momentum conservation can lead not only to the formation of binaries but also to the formation of a thin disc surrounding the star. The initial collapsing molecular cloud cores usually have a size of $\approx 0.1\,\text{parsec}$ with mean gas number densities of $10^4\,\text{cm}^{-3}$ (Bergin & Tafalla 2007), while the protoplanetary disc collapses to a size of $\approx 100\,\text{au}$ with a mean number density of $\sim 10^{12} - 10^{14}\,\text{cm}^{-3}$ (Weidenschilling 1977). The existence of PPDs were postulated long before directly resolved observations were possible, by analysing the spectral energy distribution (SED). The heated gas disc adds an excess signal

at long wavelengths that has been already used to estimate the disc life time by Strom et al. (1989). Figure 1.3 sketches the SED for different stages of the star formation process with the current structure of the protoplanetary system. Initially the envelope blocks most of the starlight and only allows remitted light to pass through. As a disc forms, distinct overlapping emission spectra become observable due to the Planck curve of the star and a distribution from the disc. Eventually, as the inner disc starts to dissipate and a cavity forms in the case of a transition disc, the SED shows a valley between the high-energy star curve and the shrinking long wavelength disc contribution (see also Chiang & Goldreich 1997).

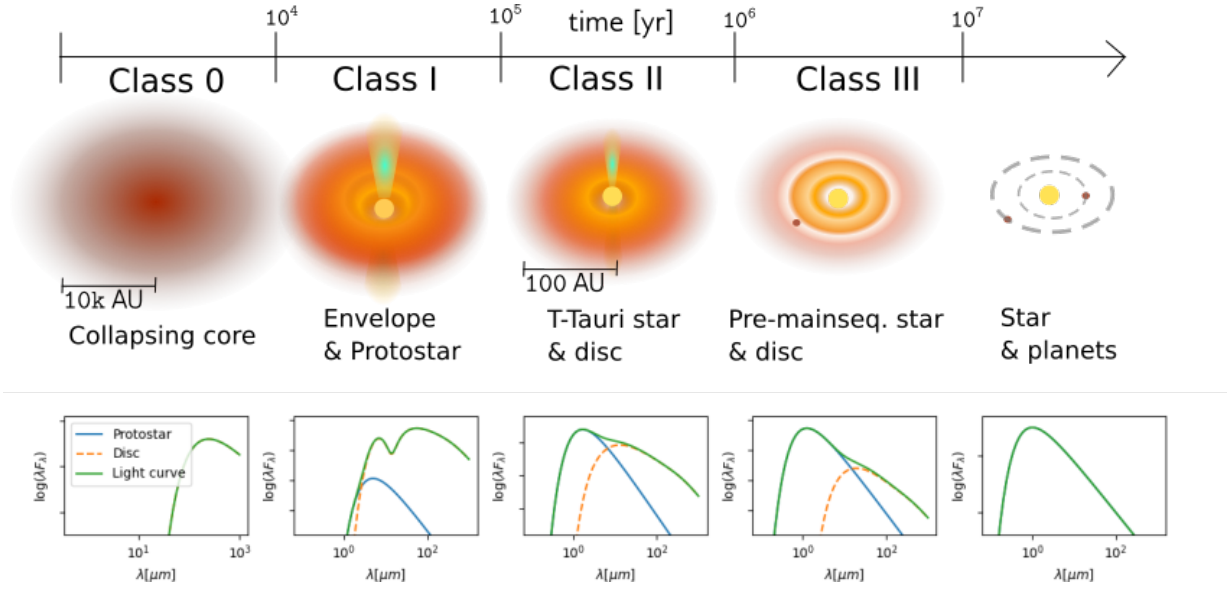

Figure 1.3: Sketch of the stellar energy distribution (SED) for the evolutionary stages of star formation.

Nowadays, the emissions of PPDs can be spacially resolved. However, the quantitatively most important component of the disc, the hydrogen gas, can not be directly observed. The observation of the disc, like any astronomical observation, relies on light signals of either specific frequencies or frequency ranges. A gas or small dust grains alter a light signal via the scattering, absorption and remission. The disc contains small, mainly silicate and ice dust grains with typical sizes of $> 1\,\mu$m to millimetre sizes (even larger bodies are called "pebbles" and contribute little to the observations). Such dust grains can scatter the light at wavelengths roughly similar to their size with Mie scattering. The direction of the light follows a mostly uniform distribution with an excess in forward scattering and depending on the specific wavelength to grain size ratio. However, Mie scattering is only

an approximation as the dust can be porous, asymmetric and build from smaller monomers (attempts to include this can be found in Tazaki 2021). For scattered light images of PPD usually infrared wavelengths $\sim 1\,\mu$m are used. The dust opacity at these wavelengths is so high that the disc appears optically thick, meaning that light can not travel through the disc, but only a surface of the disc is observed. One problem, however, is that central star emits at the same wavelength exceeding the discs contribution, so it has to be removed from the observation.

The scattering causes a change to a main polarization perpendicular to the incident light. By clever deductions of different polarized signals, the light of the star can be filtered out and only extended disc features remain. The details how this is done in the SPHERE/IDRIS mode in the VLT can be found in van Holstein et al. (2020).

While the dust scatters the light, it also absorbs enough to heat up and remit throughout the disc. For this, the dust can be considered to emit blackbody radiation according to the local temperature inside the disc usually between hundreds and tens of Kelvin, which translates into a wavelength in the sub-millimetre to millimetre range. This dust continuum emission usually can trace the dust close to the mid plane of the disc, depending on the dust settling and the opacity.

The disc also contains a variety of gas molecules, many different species of which have been found inside PPDs (see Öberg & Bergin 2021, for details) . However, for observation of the disc the most abundant molecules with a strong spectral line are used. In the context of PPDs, this is mostly CO and CO-isotopologues (Molyarova et al. 2017). As CO is composed of two different atoms, it can emit energy from rotational energy levels that are lower than orbital levels. For CO the rotation-vibrational transition $J2 \rightarrow J1$ for example is at 230.538 GHz or 1.3004 mm. Such a long wavelength requires so little energy to excite that the cold outer disc can be traced using CO. However, the ratio between CO and molecular hydrogen in disc has been debated in the recent years (e.g. Dodson-Robinson et al. 2018). This is a large model uncertainty as the actual amount of gas contained in PPDs is unclear. The most common assumption for the disc mass is $\approx 1\%$ of the stellar mass with a dust to gas ratio of $\approx 1\%$.

With the Atacama Large Millimeter/submillimeter Array (ALMA), an interferometer consisting of 66 radio telescope dishes operating in the infrared wavelength range, structures in PPDs could be resolved for dust emission as well as molecular tracer lines. The DSHARP survey (Disk Substructures at High Angular Resolution Project, Andrews et al. 2018) resolved 20 discs in the dust continuum emission, as shown in Fig. 1.4. The most common theory to explain the rings and gaps in the

discs is the presence of one or multiple planets that accrete the material near their orbit and thereby create a gap in the disc. As the planets are much smaller then the length scale resolved by ALMA, they could not be observed in the DSHARP survey, to prove or disprove the theory.
The Molecules with ALMA at Planet-forming Scales (MAPS) survey (Öberg et al. 2021) recently could observe with multiple gas species the structure of 5 PPDs (shown in Fig. 1.5). The gas structures are correlated with dust rings and gaps in the inner part (< 150 au) of the disc.
With the planets PDS 70b&c, planets that formed a gap inside a disc were directly observed (Keppler et al. 2018, 2019) and confirmed by the accretion onto the planets (Haffert et al. 2019). The new observational capabilities uncover new details of planet formation and the structure of the protoplanetary disc in which planets form.

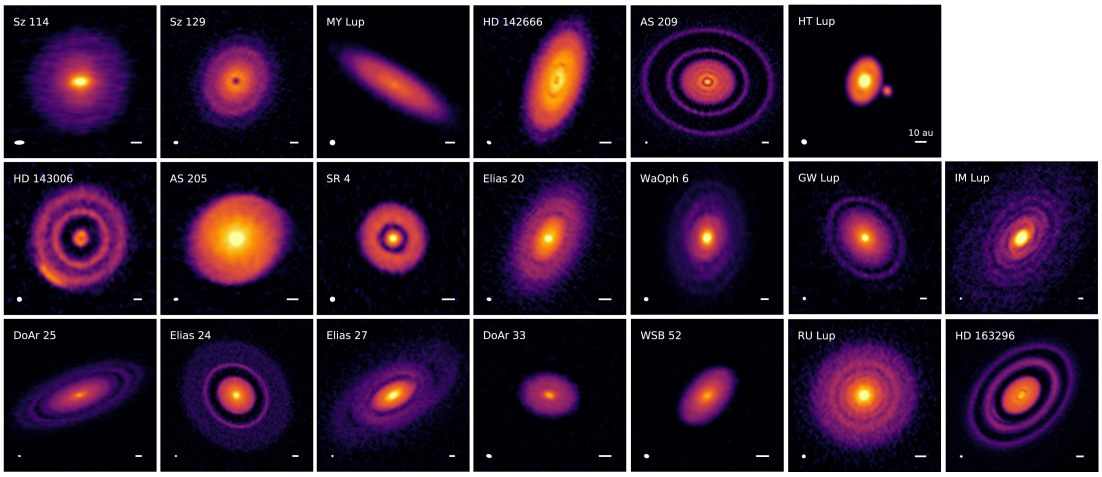

Figure 1.4: The DSHARP dust continuum observations at 1.25 mm of 20 PPDs with ALMA (Credit/Details: Andrews et al. 2018)

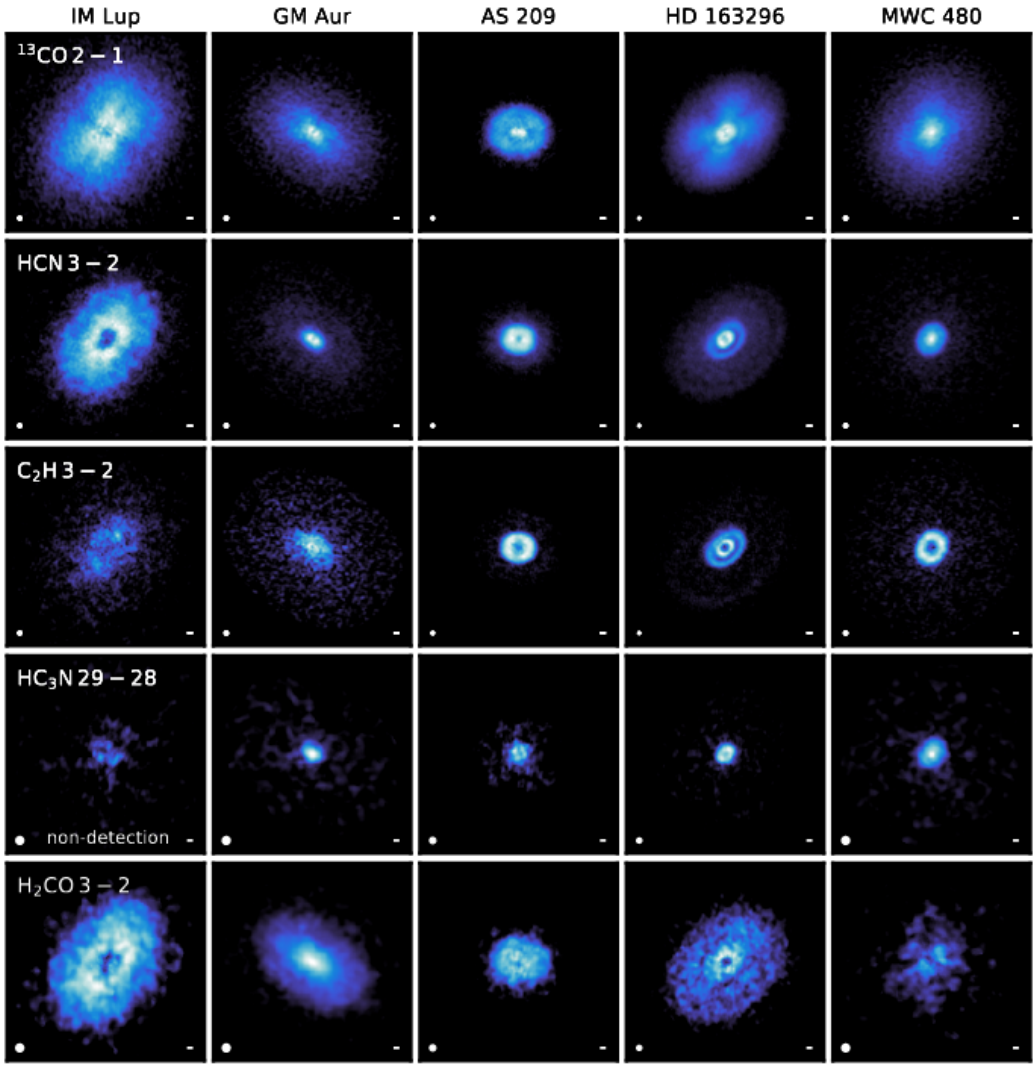

Figure 1.5: Results of the MAPS survey: The molecular line emissions of 5 PPDs with ALMA for five different species noted in the figure. The white dots mark the resolution and the white lines mark 10 au (Credit/Details: Öberg et al. 2021)

1.3 Circumbinary planets

Less than 3 decades ago exoplanets were purely theoretical, until Mayor & Queloz (1995) discovered the first exoplanet orbiting a main-sequence star. By the end of January 2022, more than 3260 exoplanets have been confirmed around ≥ 2466 host stars. It can be estimated that almost every star in the Milky Way, on average, hosts a planet (Cassan et al. 2012). The Kepler mission detected 2398 of these planets and many more planet candidates. In this mission a field of the sky was continuously observed for over 7 years, and the observed light intensity of every object was monitored. When a planet transits in front of the host star the light intensity drops, and by the duration and timing of the periodic drop in intensity the planet size, orbit and eccentricity can be determined. This is known as the transit method of planet detection and it is only sensitive to planets with a specific alignment relative to the observer. As a follow-up mission the Transiting Exoplanet Survey Satellite (TESS) is currently deployed scanning $\sim 85\%$ of the sky for further planet detections (Ricker et al. 2015).

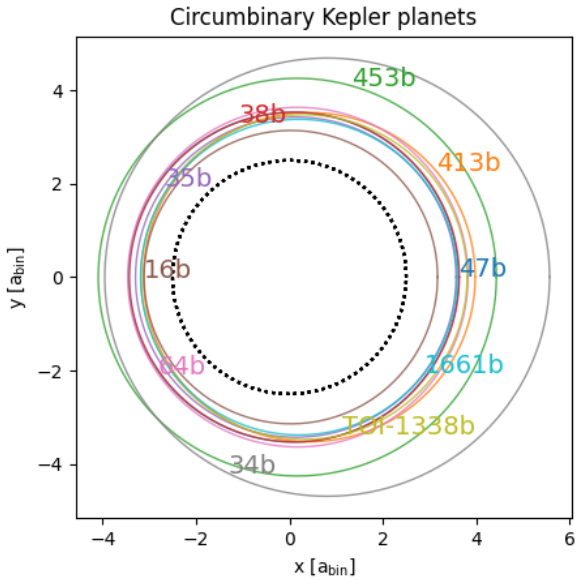

Figure 1.6: Orbits of the circumbinary planets in Tab. 1.1(solid lines) with the stability limit at $\sim 2.5\, a_{\mathrm{bin}}$(dotted line)

Circumbinary planet detections are still few. This is to some extent due to difficulties in detection (more details in Li et al. 2016; Martin 2018). There are two configurations of planets in binary systems: the s-type planet that orbits a

single binary star and the p-type planet that orbits both stars. As the distances between the binary stars can be more than 10 000 au wide, more s-type binary planets (see e.g. Fontanive & Bardalez Gagliuffi 2021) have been detected than p-type planets. In the following we will refer to the p-type configuration when talking about circumbinary planets (CBP). The transit method is biased towards short period planets and therefore CBPs around close spectroscopic binary stars with separations of less than 1 au. Table 1.1 contains most observed CBP systems (see also Kostov et al. 2021). Around binary stars exists a zone of $\approx 2.5\,a_{\rm bin}$, in which orbits are unstable and which is within the cavity of the circumbinary disc. Holman & Wiegert (1999) numerically evaluated this unstable region a_c for binaries with different eccentricities $e_{\rm bin}$ and mass ratio $\mu_{\rm bin} = M_2/M_{\rm bin}$ and found the best–fit expression of:

$$a_c = (1.60 + 5.10e - 2.22e_{\rm bin}^2 + 4.12\mu_{\rm bin} - 4.27e_{\rm bin}\mu_{\rm bin} - 5.09\mu_{\rm bin}^2 + 4.61e_{\rm bin}^2\mu_{\rm bin}^2)a_{\rm bin}.$$

Interestingly the most observed planets orbit just beyond the unstable region at $\approx$3–4 $a_{\rm bin}$, as is shown in Figure 1.6. Also the planets observed close to the binary are mostly Saturn-like or smaller. Pierens et al. (2020) argued that in-situ formation of planets so close to the binary in a disturbed disc is not possible with a pebble accretion scenario and that the planets migrated into these similar orbits. Therefore, the idea of a common circumbinary parking mechanism was already discuss in the summary of Li et al. (2016) for even less observed circumbinary planets than today, and without a explanation of such a mechanism. Today, we are much closer to understanding the underlying dynamics and we will discuss in Section 4.3 how it is possible to park most of the observed planets in the observed orbits. To fully understand how we can arrive at a realistic model that can explain all the observed disc and planets, we will now introduce the relevant physics assumptions in Chapter 2.

Kepler	$M_{\rm bin}$ [$M_\odot$]	$q_{\rm bin}$	$e_{\rm bin}$	$m_{\rm p}$ [$m_{\rm jup}$]	$a_{\rm p}$ [$a_{\rm bin}$]	$e_{\rm p}$	$m_{\rm p}/M_{\rm bin}$ [$\times 10^{-5}$]
38	1.20	0.26	0.10	0.38	3.16	0.03	30
35	1.70	0.91	0.14	0.12	3.43	0.04	7.1
453	1.14	0.21	0.05	0.05	4.26	0.04	4.3
64	1.77	0.28	0.21	0.1	3.64	0.05	5.4
34	2.07	0.97	0.52	0.22	4.76	0.18	10
47	1.32	0.35	0.02	0.05	3.53	0.03	3.7
16	0.89	0.29	0.16	0.33	3.14	0.006	35
413	1.36	0.66	0.04	0.21	3.55	0.12	15
1661	1.10	0.31	0.11	0.05	3.39	0.06	4.6
TOI-1338	1.34	0.28	0.16	0.10	3.49	0.09	6.8

Table 1.1: List of most known circumbinary planets (See Orosz et al. (2012), Welsh et al. (2012), Welsh et al. (2015), Schwamb et al. (2013), Orosz et al. (2019), Doyle et al. (2011), Kostov et al. (2014), Kostov et al. (2020), Socia et al. (2020))

2 Physics

While the observations presented before give us a snapshot of possible planetary and protoplanetary environments, the evolution can only be inferred from models. These models need conditions and underlying physical laws that prescribe the most relevant physical effects for the system.

2.1 Astrophysical discs

An astrophysical disc consists of thin gas on very large length scales. This can be approximated with an fluid that can be described with general hydrodynamics equations, i.e., the Navier–Stokes equations.

$$\frac{\partial \rho}{\partial t} + \nabla \cdot (\rho \vec{v}) = 0 \tag{2.1}$$

$$\frac{\partial \rho \vec{v}}{\partial t} + \nabla \cdot (\rho \vec{v} \times \vec{v}) = -\nabla P + \nabla \cdot \boldsymbol{\tau} - \nabla \Phi \tag{2.2}$$

$$\frac{\partial \rho e}{\partial t} + \nabla \cdot (\rho e \vec{v}) = -P(\nabla \cdot \vec{v}) + (\boldsymbol{\tau} \cdot \nabla) \cdot \vec{v} + S \tag{2.3}$$

The first of these equation is an expression for the mass conservation using the gas density ρ and the velocity vector $\vec{v}$. The second equation describes momentum conservation, that includes additional source terms: the pressure gradient ∇P, a viscous term using the stress tensor $\boldsymbol{\tau}$, and the gradient of the gravitational potential $\nabla\Phi$. The equation of state ((2.3)) can include additional sources and sinks of radiation that are denoted by S that will be discussed later in Sec. 2.1.2. As generally the Navier–Stokes equation has no known analytic solution, we will first add simplifying assumptions relating to the structure of the disc problem that allow some simplified solutions and later introduce numerical methods to evolve disc in Chapter 3. A more detailed description of accretion discs can be found in the books by Frank et al. (2002), Armitage (2020) or by Armitage (2019) & Kley (2019).

A typical PPD is geometrically thin with a pressure scale height H of $\leq 10\%$ the radial distance, a number also called aspect ratio h in the context of discs. The stratified gas profile is vertically pressure supported ($1/\rho \cdot \mathrm{d}P/\mathrm{d}z$) against the gravitational force ($F_{\mathrm{grav}} \approx z/r \cdot GM/r^2$). The pressure P can be rewritten using the isothermal sound speed $c_{\mathrm{s,iso}}$ and the density ρ as $P = c_{\mathrm{s,iso}}^2 \rho$. Hence, the density ρ at radius r can be expressed with the mid-plane density ρ_{mid} as:

$$\rho(r,z) \approx \rho_{\mathrm{mid}}(r) \exp\left(-\frac{\mathrm{G}Mz^2}{2c_{\mathrm{s,iso}}^2 r^3}\right) = \rho_{\mathrm{mid}}(r) \exp\left(-\frac{z^2}{2H^2}\right) \tag{2.4}$$

$$\text{with} \quad H(r) \equiv c_{\mathrm{s,iso}} \sqrt{r^3/GM} = c_{\mathrm{s,iso}}/\Omega_{\mathrm{K}}, \tag{2.5}$$

Ω_{K} is the Keplerian angular velocity a body needs on a stable orbit around the point mass M. Thereby the vertically integrated density or so-called surface density is given by

$$\Sigma(r) = \int_{-\infty}^{\infty} \rho(r,z)\mathrm{d}z \approx \sqrt{2\pi}\rho_{\mathrm{mid}}(r)H(r). \tag{2.6}$$

We have neglected here the azimuthal component of the disc, because undisturbed discs can be approximated as rotationally symmetric, so $\partial_\phi \rho = 0$. Using these conditions, Pringle (1981) approximated the radial velocity and thereby the steady-state mass flow through a disc. This can be derived from the continuum equations of mass and angular momentum $\vec{L}$ that simplify with these conditions to:

$$0 = \partial_t \Sigma + \nabla \cdot \Sigma \vec{v} = \partial_t \Sigma + \frac{1}{r}\partial_r (r v_r \Sigma) \tag{2.7}$$

$$\nabla \Theta = \partial_t \vec{L} + \nabla \cdot \vec{L}\vec{v} \rightarrow \frac{1}{2\pi}\partial_r \Theta = r v_r \Sigma \partial_r (r^2 \Omega) \tag{2.8}$$

Here Ω is the angular velocity of the gas and Θ is the disc torque. The torque arises from friction inside the disc, so given an inviscid disc with viscosity $\nu = 0$ this Θ would be zero. Then Θ relates the radial velocity v_r to the viscosity ν using the continuum equations:

$$\Theta = 2\pi r \cdot \nu\Sigma r\partial_r(r\Omega) \tag{2.9}$$

$$\rightarrow \frac{1}{r}\partial_r(rv_r\Sigma) = \frac{1}{2\pi r}\partial_r\frac{1}{\partial_r r^2\Omega}\partial_r\Theta = -\frac{3}{r}\partial_r\left[\sqrt{r}\partial_r(\sqrt{r}\nu\Sigma)\right] = -\partial_t\Sigma \tag{2.10}$$

$$\rightarrow v_r = -\frac{3}{\sqrt{r}\Sigma}\partial_r(\sqrt{r}\nu\Sigma) \tag{2.11}$$

Assuming a steady-state disc the velocity simplifies to $v_r = -3/2 \cdot \nu/r$ and a constant mass accretion rate through the disc can be expressed as $\dot{M} = -2\pi r\Sigma v_r = 3\pi\nu\Sigma$. As we have seen, the viscosity determines the flow through the disc and, hence, plays a crucial role.

2.1.1 Viscosity

In a fluid with areas of different velocity boundaries, like for example a fluid flowing through a pipe, the velocity gradually changes from 0 at the pipe wall to a steady flow, and this gradient is determined by the viscosity. The dynamic viscosity μ describes how effective the shear stress changes the local velocity of a flowing fluid. If the effect of a boundary reaches far into the fluid, like slowly flowing honey, the material is considered very viscous, whereas a material where the flow beyond the boundary is only weakly affected by the boundary (like water flowing through a pipe) has a comparably lower viscosity. In the astrophysical context with very thin gases a density-normalized viscosity – the kinematic viscosity $\nu = \mu/\rho$ – is used.
Thermodynamically for ideal gases the molecular viscosity can be defined by the mean-free path λ, the molecular weight μ_{gas}, temperature T and the specific ideal gas constant $\mathfrak{R}$:

$$\nu = \frac{2}{3}\lambda\sqrt{\frac{2\mathfrak{R}T}{\pi\mu_{\text{gas}}}} = \sqrt{\frac{8}{9\pi}}\lambda c_{\text{s,iso}} \tag{2.12}$$

For a PPD this results in a very low viscosity. Using this molecular viscosity in the steady-state accretion rate in Section 2.1 would result in a mass accretion that is multiple orders of magnitude smaller than the observed mass accretion rates of $\sim 10^{-8}\,M_\odot/\text{yr}$. So the molecular viscosity alone can not be responsible for the shear leading to accretion inside the disc.
Shakura & Sunyaev (1973) have introduced the idea that macroscopic turbulent eddies in the gas can create an interaction between the gas beyond the molecular viscosity, the turbulent viscosity. The eddies in the disc, however, need to be

fuelled by some unstable hydrodynamical process. Identifying and understanding such hydrodynamical instabilities has occupied the astrophysical community for the last two decades.

Suggested instabilities include the magneto-rotational instability (MRI) (Balbus & Hawley 1991), the vertical shear instability (VSI)(e.g. Nelson et al. 2013), the baroclinic instability (e.g. Klahr & Bodenheimer 2003), the gravitational instability, the streaming instability (Youdin & Goodman 2005; Johansen & Youdin 2007) and the induced Kelvin–Helmholtz instability. Each instability operates on specific distances from the central object(s) and requires specific conditions to work (further details can be found in e.g. Armitage 2019). For example the magneto-rotational instability intertwines charged molecules in the disc's magnetic field, such that the differing orbit velocities of the molecules at different radii lead to a stress that induces a turbulent motion. To operate the MRI therefore requires a magnetic field and charges. However, the number of charges in the gas is reduced by dust inside the optically thick parts of the disc. Therefore the MRI is gravely reduced in the mid plane between $\approx 1 - 10\,\mathrm{au}$ (Gressel et al. 2015).

On the other hand the VSI can only be active in parts of the disc where the gas can radiate away received heat efficiently around $\approx 10\,\mathrm{au}$ (see e.g. Lyra & Umurhan 2019, for comparison to other instabilities). The VSI arises from the difference of the vertical profile of the angular momentum $j = \Omega R^2$ and the kinetic energy $E_{\mathrm{kin}} = \Omega^2 R^2$. As the angular velocity Ω changes vertically, the kinetic energy of a vertically displaced parcel of gas with the same angular momentum becomes higher than the kinetic energy of the surrounding environment. Hence, the parcel can continue to accelerate and vertical sheets of turbulent gas form in the disc, but only if the parcel can cool fast enough to avoid buoyancy due to the temperature from its initial location.

Computing a hydrodynamical model that includes all known instabilities and the imposed physical models like a magnetic field for the MRI, dust-gas interaction for the streaming instability and Kelvin-Helmholtz instability, self-gravitating gas for the gravitational instability, is unfeasible and might still be an incomplete picture of the effects affecting the de-facto viscosity. Therefore the viscosity created by the various instabilities is simply parametrized with the Shakura–Sunyaev parameter α, such that the viscosity in a PPD is simply expressed by:

$$\nu = \alpha H c_{\mathrm{s}} \quad \text{with} \quad \alpha \ll 1\,. \tag{2.13}$$

In this equation the scale height H and the sound speed c_{s} give natural upper limits

to the mean free path and the velocity of the gas. The largest turbulent eddy in the disc can not exceed the height of the disc. In Section 2.1.3 we will further discuss how sensible choices for the viscosity and other parameters are found.

2.1.2 Thermodynamics inside the disc

The dynamics of the disc depends also on the local pressure as described in Section 2.1. The pressure P relates in a ideal gas to the local sound speed c_s and thereby temperature T, in the following way:

$$c_\mathrm{s} = \sqrt{\gamma \frac{P}{\rho}} = \sqrt{\gamma \frac{\Re T}{\mu_\mathrm{gas}}} = c_\mathrm{s,iso}\sqrt{\gamma}\,. \tag{2.14}$$

The index γ is the adiabatic index of a gas with $\gamma = 7/5$ for an ideal equation of state or $\gamma = 1$ for an isothermal solution. So it is evident that the temperature inside the disc is vital to the pressure and the pressure scale height $H(r)$ in Eq. (2.5).
The easiest temperature model assumes that the central object emits radiation and all gas directly follows a resulting, usually outwards decreasing temperature profile. This is called the **locally isothermal model** and introduces the temperature and thereby $c_\mathrm{s,iso}$ as follows:

$$T(r) = T_0 \left(\frac{r}{r_0}\right)^q \rightarrow c_\mathrm{s,iso}(r) = c_\mathrm{s,iso}(T_0) \left(\frac{r}{r_0}\right)^{q/2} \tag{2.15}$$

For a flat disc the exponent is $q = -1$, meaning H/R is constant throughout the disc. The disc is flared for $q > -1$ and shadowed for $q < -1$, as the scale height simplifies to:

$$H = c_\mathrm{s,iso}/\Omega = H(r_0) \left(\frac{r}{r_0}\right)^{(q+3)/2} \tag{2.16}$$

Hence, in the locally isothermal model the pressure scale height H and sound speed $c_\mathrm{s,iso}$ are constant in time and the pressure P then solely depends on the changes in density over time. This is one reason the locally isothermal equation is widely used in models: it eliminates one free variable in the hydrodynamics equations and thereby requires one less equation in Eq. (2.3).
In reality, the temperature profile is not a simple constant function of instantly thermally equilibrated gas. The temperature is determined by different terms of heating and cooling reaching an equilibrium. In a viscous disc the viscous stress

introduces **viscous heating** $Q_{\text{visc+}}$ to the disc that depends on the stress tensor $\boldsymbol{\tau}$. Assuming that the heating is not shock–driven, the term in Eq. (2.3) can be approximated in a symmetric, viscous disc without a vertical component as described in Sec. 2.1 as:

$$Q_{\text{visc+}} = (\boldsymbol{\tau} \cdot \nabla) \cdot \vec{v} \approx \frac{9}{4} \nu \Sigma \Omega_{\text{K}}^2 \tag{2.17}$$
$$\text{with} \quad \tau_{ab} = \eta \left(\frac{\partial u_b}{\partial x_a} + \frac{\partial u_a}{\partial x_b} - \frac{2}{3} (\nabla \cdot \vec{v}) \delta_{ab} \right) + \zeta (\nabla \cdot \vec{v}) \delta_{ab}, \quad a, b \in 1, 2, 3$$

For accretion discs, it is assumed that the bulk viscosity coefficient ζ is zero and the shear viscosity coefficient is given by the kinematic viscosity $\eta = \nu\rho$.

The introduced heating has to be radiated away for the disc to reach an equilibrium state. Thermal emission is part of the radiative transfer emission occurring in the disc. Absorption and emission depend on the material opacity, the wavelength of the radiation and the density of the material.

For now we will assume that the disc absorbs a temporally constant amount of heat Q_{abs} inside the disc as before, but depending on the radial position, density and the materials in the disc the emission changes. This is the same as saying there is a **radiative cooling** of the disc that will emit the heat from the disc. Generally thermal emission can be written with the Stefan–Boltzmann law as $Q_{\text{rad}-} = -2\sigma_{\text{SB}} T_{\text{eff}}^4$, with the effective temperature T_{eff} and the Stefan–Boltzmann constant σ_{SB}. The effective temperature depends on the received heat and the ability of the disc to emit radiation through the disc, such that the local temperature T is corrected by an effective optical depth τ_{eff} to $T^4 = \tau_{\text{eff}} T_{\text{eff}}^4$, as derived in Hubeny (1990). For a 2D simplification the midplane temperature can be inserted as T and the optical depth integrated through the full vertical disc extent. This τ_{eff} is then given by the optical depth τ as

$$\tau_{\text{eff}} = \frac{3}{8}\tau + \frac{\sqrt{3}}{4} + \frac{1}{4\tau} \quad \text{with} \quad \tau = \int \rho \kappa \mathrm{d}z \approx \frac{1}{2\sqrt{2\pi}} \Sigma \kappa \tag{2.18}$$

In this equation κ is the flux-weighted Rosseland mean opacity. The Rosseland mean opacity is an approximation of the opacity that uses a temperature derivation of the Planck distribution and assumes a local thermal equilibrium, such that the radiation field is locally isotropic. A complete opacity spectrum would require full knowledge of the composition of dust and gas as well as the full temperature and density structure. Such detailed observations are not possible inside the optically

thick disc and a chemically complete opacity spectrum is not feasible to include in models. In Lin & Papaloizou (1985) the Rosseland mean opacity was described as a series of power-law functions depending on temperature and density to include the most relevant features of the astrophysical disc. In Lin & Papaloizou (1985); Müller & Kley (2012); Kley et al. (2019) these features include electron scattering, bremsstrahlung, photoionisation, the transitions in atomic and molecular gas, as well as the sublimation and presence of silicate and ice grains.

As the models of radiative cooling have generally large uncertainties, there are also approaches to simplify the cooling term with a single choosable parameter β, the so called **β-cooling model** (Gammie 2001). In this model the cooling time t_{cool} over the whole disc is simply proportional to the local Kepler period as $t_{\mathrm{cool}} = \beta/\Omega_{\mathrm{K}}$. Hence, the derivation of temperature T is given as:

$$\partial_t T = (T_0 - T)\frac{\Omega_{\mathrm{K}}}{\beta} \tag{2.19}$$

Thereby the relaxation heat term Q_{beta} in 2D can be identified as:

$$Q_{\mathrm{beta}} = c_{\mathrm{v}}\Sigma\partial_t T = \frac{\Omega_{\mathrm{K}} c_{\mathrm{v}}\Sigma}{\beta}(T_0 - T) \quad \text{with} \quad c_{\mathrm{v}} = \frac{\Re}{\mu_{\mathrm{gas}}(\gamma - 1)} \tag{2.20}$$

In this equation c_{v} is the specific heat capacity. This prescription allows a very easy estimation of the equilibrium temperature, if the disc is primarily heated by viscous heating from Eq. (2.17) and cooled by β–cooling, such that $Q_{\mathrm{beta}} + Q_{\mathrm{visc+}} = 0$. Assuming an α-viscosity (Eq. 2.13) it follows with Eq. (2.5) & (2.14):

$$\frac{9}{4}\alpha\sqrt{\gamma}c^2_{\mathrm{s,iso}}(T)\Sigma = -\frac{c_{\mathrm{v}}\Sigma}{\beta}(T_0 - T) \rightarrow T = T_0[1 - \frac{9}{4}\sqrt{\gamma}(\gamma - 1)\alpha\beta]^{-1} \tag{2.21}$$

In this way the approximate equilibrium temperature for an initial temperature profile T_0 based on the isothermal scale height H can be given as an initial condition without waiting for the temperature equilibrium to develop throughout the disc. It also becomes evident that a $\beta \rightarrow 0$ leads to a locally isothermal condition, where the current temperature equals the initial equilibrium temperature at all times.

Besides these heat terms the disc temperature can also be influenced e.g. by irradiation from the central star and cosmic radiation, by chemical transitions and reactions, by sublimation of abundant ices like water, carbon dioxide, carbon oxide or methane, by shock waves and by gas compression, etc. So for a quasi-realistic

model, Eq. (2.3) would look like this:

$$\frac{\partial \rho e}{\partial t} + \vec{v} \cdot \nabla(\rho e) = -P(\nabla \cdot \vec{v}) + Q_{\text{visc+}} + Q_{\text{shock+}} + Q_{\text{comp+/-}} + Q_{\text{rad-}} + Q_{\text{irrad+}} + Q_{\text{XUV+}} + Q_{\text{chem+/-}} \cdots$$

Every term introduces its own approximations and uncertainties. Hence for computational models only the most relevant terms or simplifications like the β-cooling are included to reduce the computation time without losing too much model accuracy. In the context of close circumbinary discs the viscous heating is the most relevant heat source as is shown in Kley et al. (2019).

2.1.3 Typical protoplanetary environment

While we have well–resolved images of the dust structure and the profile of specific tracer gases, the relevant parameters for hydrodynamics simulations, such as the viscosity, the hydrogen gas mass and the dust–to–gas ratio, are still difficult to infer from observations. Here, we will discuss the typical planet formation environment and how it is determined.

One attribute of the disc, that can directly be extracted from observations is the gas/dust pressure **scale height** H of the disc, and nowadays even more complex disc structures in gas and dust can be determined. The emission temperature of the disc can be used to calculate the H using Eq. (2.5)&(2.14) (e.g. in Pinte et al. 2016; Dullemond et al. 2018). The height of the optically thick surface can be observed in tracer gas and dust to even create a structured model of the disc temperature in the recent study by Calahan et al. (2021). During the disc's evolution the scale height drops as the disc loses mass and cools. Overall discs are generally thin with a pressure scale height of only few percent of disc radius or $H/R \approx 3 - 10\%$. The outer parts of the disc can be flared as the material is so thin that radiation can penetrate deep into the disc and heat it up (Chiang & Goldreich 1997)

For the absolute **disc mass** an often used estimation is the minimum mass solar nebula (MMSN) (Weidenschilling 1977). In this estimation the mass of gas and solid components of the solar system planets is spread out over the solar system. This simplification of the minimal mass that a PPD in a solar-like system needs results in a surface density of $\Sigma \approx 1700(\frac{r}{1\text{au}})^{-3/2}\text{g/cm}^2$ or a disc mass of $\approx 1\%$ the stellar mass. Another approach is to use CO as a gas tracer to not just get the overall mass of the gas contained but also the gas structure in the disc. However,

the chemical processing of CO inside the disc introduces some uncertainties such that the CO–to–H_2 ratio is between 5×10^{-5} and 10^{-6} depending on the mass of the central star and the characteristic radius as shown in Molyarova et al. (2017). In general the **dust-to-gas ratio** is roughly 1% assuming a ratio from the interstellar medium. From measuring dust continuum emissions and CO as a gas tracer the dust-to-gas ratio can be estimated. It would also depend on the size distribution of particles in the gas, as compact large particles will provide a smaller cross section per mass and contribute thereby less to the absorption and remission surface in the disc.
As already explained in Section 2.1.1, molecular **viscosity** is not sufficient to explain the observed accretion on the central star. Another way of approximating the viscosity is the spreading of dust rings in the DSHARP survey (Dullemond et al. 2018) and HL Tau (Pinte et al. 2016). This method yields a viscosity with an $\alpha \approx 10^{-2}$–10^{-4}.

2.2 Gravitational potential in the two–body system

So far the physical prescriptions of the astrophysical disc assumed a single central object. However, while in most PPDs the gravitational potential is treated well with a simple constant function of radius, the binary consists of two gravitational attractors on time dependent orbits that might even be eccentric. Neglecting the gravitation of the elliptic disc, the binary can be described with the simple analytical 2–body Kepler equations. The two stars orbit the common centre with a synchronous angular velocity $\Omega_{\rm bin} = \sqrt{\mathrm{G}M_{\rm bin}/a_{\rm bin}^3}$. In this equation $a_{\rm bin}$ is the semi-major axis between the binary components. We will use the mass ratio $q = M_2/M_1$. Then the gravitational potential Φ and the orbits of both binary components in binary units are given in time as:

$$\Phi(r) = -\mathrm{G} \cdot \left(\frac{M_1}{|\vec{r_1} - \vec{r}|} + \frac{M_2}{|\vec{r_2} - \vec{r}|} \right) = -\frac{\mathrm{G}M_{\rm bin}}{1+q} \cdot \left(\frac{1}{|\vec{r_1} - \vec{r}|} + \frac{q}{|\vec{r_2} - \vec{r}|} \right)$$
$$r_1 = r_{\rm bin}(\phi_1)\frac{q}{1+q};\ r_2 = r_{\rm bin}(\phi_1)\frac{1}{1+q};\ \phi_2 = \phi_1 + \pi$$
$$\text{with } r_{\rm bin}(\phi_1) = \frac{a_{\rm bin}(1-e_{\rm bin}^2)}{1 + e_{\rm bin}\cos(\phi_1)} = a_{\rm bin}(e_{\rm bin}\cosh E(t) - 1) \tag{2.22}$$

In this equation the angle ϕ_1 and the radius $r_{\rm bin}(\phi_1)$ are time dependent and can be calculated using the eccentric anomaly E. As the fraction of a complete period, the mean anomaly $M = n(t - T_{\rm bin})$ can be expressed with $M = E - e_{\rm bin} \sin E$. The orbital period is given with $T_{\rm bin} = 2\pi/\Omega_{\rm bin}$. Thereby an analytical time-dependent two body potential can be calculated. With our typical disc mass of $\sim 1\%\, M_{\rm bin}$ this potential is a good approximation for the acting gravitational potential. However, if additionally planets are added to disc, the real overall potential becomes more complex and no longer analytically solvable and an n-body integration will be needed. Such a case will be discussed in Sec. 3.4.

2.3 Precession and resonance

As a planet has a small mass compared to stars $M_{\rm p} \approx 10^{-4}\, M_{\rm bin}$ and is far enough from the central binary, the system can be approximated with a restricted three–body problem. To first-order approximation the planets orbit the centre of mass on a Keplerian orbit. However, the rotation of the binary induces a torque on the planet that leads to a precession of the orbit. The precession time $T_{\rm prec}$ can be calculated analytically with:

$$T_{\rm prec} = \frac{4}{3}\frac{(q+1)^2}{q}\left(\frac{a}{a_{\rm bin}}\right)^{3.5}\frac{(1-e_p)^2}{1+1.5e_{\rm bin}^2}T_{\rm bin} \tag{2.23}$$

Usually the precession rate is in the order of $\sim 10^3\, T_{\rm bin}$ at 3–5 $a_{\rm bin}$, which is the range of the observed close planet orbits.

Additionally to the precession, the circumbinary planet dynamics differs from a normal planet by the presence of mean motion resonant orbits that can destabilize the planet orbit. The resonance occurs when the period of the binary $P_{\rm bin}$ and the orbit period of the planet $P_{\rm p}$ are a rational fraction of each other: $P_{\rm p}/P_{\rm bin} = n/m$ with $n, m \in \mathbb{N}$. Such resonances mean that within n to m orbits the three objects will have the same configuration again, that induces the same forces periodically. Therefore n:1 resonances destabilize the orbit as the outer body receives a periodic kick. On the other hand, n:2 resonances alternate between a maximum and minimum distance and are thereby more stable. Due to the gravitational interaction with the binaries the planet can librate on its orbit and get into resonances and be destabilized, especially when the orbit is to close to the binary. The unstable inner region close to the binary was first analysed and given lower limits by Dvorak (1986) and Holman & Wiegert (1999). It depends also on the eccentricity of

the binary and the planet. High eccentricity in any of the components leads to a larger unstable region. The topic of unstable circumbinary orbits is still actively researched including more orbital parameters and investigating specific planetary systems (Popova & Shevchenko 2016; Chen et al. 2019, 2020; Quarles et al. 2018). Orosz et al. (2019) observed multiple planets around a binary in the Kepler-47 system, showing that not only can there be the resonance between binary and planet but also between different planets in the system. However, this is no longer analytically solvable with more than 3 bodies in the system, and needs to be evaluated with numerical n-body simulations. In the context of planet–planet resonances, there is a possibility of a coorbital resonance, the 1:1 resonance. In this case two bodies orbit the centre of mass on the same mean orbit. There are two main configurations in which the orbits of both bodies can be stable: the tadpole orbit, where one planet follows the other on the Lagrange point 4 or 5, comparable to the Trojans or Greeks on orbit with Jupiter; and the horseshoe orbit, where the planets exchange angular momentum periodically such that the inner, faster planet orbits until it catches up to the other and gets gravitationally pulled on an outer orbit while the second planet loses angular momentum and drops to the faster inner orbit. From the perspective of one planet the other planet's orbit appears like a horseshoe, therefore the name. This particular resonance was studied further theoretically by Leleu et al. (2019). Cresswell & Nelson (2009) found that this resonance can be stable for planets around a single star, if an additional large companion is present. How stable 1:1 resonant planets can evolve around binaries will be discussed in Section 4.4 and we will give an outlook on the stability of 1:1 resonant orbits around binaries in Section 5.3.

2.4 Binary-disc interaction

If we now include the circumbinary disc to the binary, its mass can introduce changes in the binary orbit by angular momentum, momentum and mass transport between binary and disc. The overall effect has been studied in recent years in many publications (Miranda et al. 2017; Moody et al. 2019; Muñoz et al. 2019, 2020; Tiede et al. 2020). Our own findings are presented in Section 4.2. In the case of a zero-eccentricity binary, three contributions have to be taken into account for the interaction between disc and binary: the gravitational torque between disc and stars τ_{grav}, the mass accreted on the binary M_{adv} and the angular momentum added by accretion J_{adv}.
In most of our simulations, we include the gravitational torque on the binary in

the model. It can be calculated for a 2D cylindrical model for every mass object M_i in the disc using:

$$\tau_{\rm grav}(M_i) = \mathrm{G}M_i \int \Sigma(r,\phi) \frac{\vec{r_i} \times (\vec{r} - \vec{r_i})}{|\vec{r} - \vec{r_i}|^3} r \mathrm{d}\phi \mathrm{d}r \tag{2.24}$$

So in this equation the sum of the vector product between position and gravitational force between all mass elements is evaluated. The overall torque will be the sum of all torques including also the torques between the objects. As the disc is asymmetric the disc's torque is a noticeable contribution of the order of $10^{-4} - 10^{-6} L_{\rm disc,0}/T_{\rm bin}$ to the transfer of angular momentum. The effect is still small enough to be excluded without changing the dynamics of the disc and the binary significantly except for very long timescales.

Additionally, the binary will receive advected mass and angular momentum. This, however, is difficult to include without knowing the accretion dynamics and ratio onto the binary components at a small scale and therefore is not included in the circumbinary models presented in Section 4.2. In a steady disc we can approximate the mass flowing onto the binary by the mass flow through any radius r_a

$$\dot{M}_{\rm adv}(r_a) = \oint \Sigma r_a |v_r| \mathrm{d}\phi \,. \tag{2.25}$$

The same works for the angular momentum flow through the steady disc,

$$\dot{J}_{\rm adv}(r_a) = \oint \Sigma r_a |v_r| v_\phi r_a \mathrm{d}\phi \,. \tag{2.26}$$

As the main part of the CBD experiences time–variable changes due to the rotating stars and the precessing motion of the disc, r_a should be chosen as close as possible to the binary inside the cavity to best reflect the accretion. To accurately capture advection, fluxes would need to be evaluated at the surface of the stars, which is difficult to include in a large scale model of the surrounding disc and will be subject to resolutions issues. Tiede et al. (2021) found, however, that nearly all material inside $1\,a_{\rm bin}$ will be accreted, and therefore even without the highest resolution fair approximations of the fluxes onto both of the binaries can be achieved. Muñoz et al. (2019) presented mesh-refining models that could thereby include the individual accretion on the component and the momentum transfer, however this is only feasible for models that evolve quickly. The magnitude of this effect is comparable to $\tau_{\rm grav}$ such that excluding the accretion will not significantly alter the dynamics of the disc or binary on a relevant time scale.

2.5 Planet migration

Planets embedded in a protoplanetary disc are not just subject to the gravitational potential of the central object, or even additional companions and planets, but also to torques caused by the gas disc, that alter the orbital motion and lead to planet migration. In general three types of migration are distinguishable, which depend on the level of embedding of the planet in the disc. A more detailed summary can be found in Papaloizou et al. (2007).

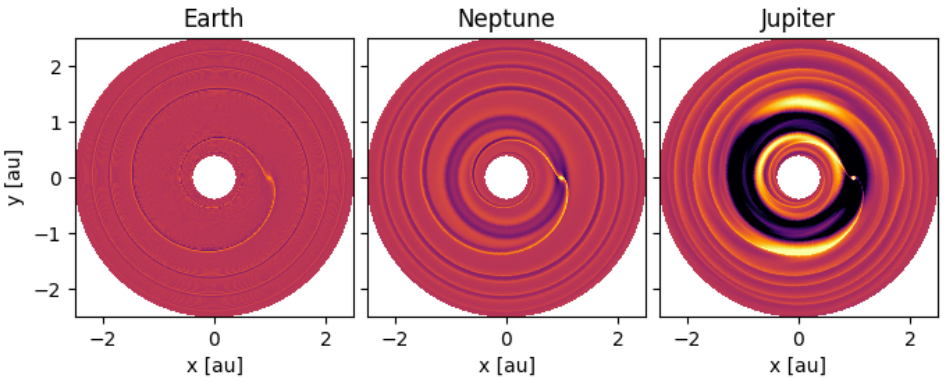

Figure 2.1: The example disc structure caused an Earth-mass object (left), Neptune-mass (middle) and a Jupiter-mass object (right), showing the spiral wake due to an embedded planet and the gap created by a massive planet. The density is normalized to the initial profile.(Test simulation using FARGO3D (Benítez-Llambay & Masset 2016))

In **Type I** migration the planet does not open a gap in the disc. This can be seen in the Earth-mass example in Fig. 2.1. Thereby the planet is directly affected by torques of the gas with two contributions, one from the corotational resonances and one from epicyclic, so-called Lindblad, resonances. In the corotational region, the gas moves on a horseshoe orbit relative to the planet. This implies that the planet causes the inner, fast, trailing gas to switch to further out orbits and the outer, slower, leading gas to faster, inner orbits and this process is asymmetric and therefore the planet receives the corotation torque. Usually this torque is positive, causing outwards migration. However, the effect of the Lindblad torque

supersedes the corotational torque for Type I migrating planets. The motion of the planet creates an epicyclic wave in the disc that propagates outwards and inwards as a spiral wake in density (see Fig. 2.1 left). The gravitational back–reaction of the spiral arms cause a torque on the planet. The leading, inner spirals cause a positive torque contribution and the outer, trailing spirals cause a negative torque on the planet. The negative torque outweighs the other contributions in most cases (Goldreich & Tremaine 1979; Paardekooper et al. 2010).
For **Type II** migration planets need to be massive. If the planet is massive enough it clears its orbit by increasing the gas angular momentum exterior and decreasing the gas angular momentum interior to the planet causing the gas to recede from the planet's orbit. Hence the planet creates a steep density gap in the disc as long as viscosity and pressure do not rise so high that the they exceed the planet's effect and cause the gap to fill up again. The gap appears for the example of Jupiter in Fig. 2.1. To estimate this gap opening ability, Crida et al. (2006) has formulated a gap opening criterion.

$$\frac{3H}{4R_{\mathrm{hill}}}\frac{50\nu}{q_{\mathrm{p}}a_{\mathrm{p}}\Omega_{\mathrm{p}}} \leq 1 \tag{2.27}$$

Here the viscosity ν and the scale height H are balancing the planet's sphere of gravitational influence, the hill radius R_{hill}, and the velocity of the planet $a_{\mathrm{p}}\Omega_{\mathrm{p}}$ weighted with the planet-to-central-body mass ratio q_{p}. If the above condition is met, in the region of the planet the gas density is reduced such that the torques of Type I migration become negligible. However, the planet can still migrate either due to the general disc accretion taking the planet inwards with the disc (Lin & Papaloizou 1986), or due to the local disc mass and gravitational torque on the planet (Dürmann & Kley 2015). In most discs this migration is inwards but slower than Type I migration.
Type III migration (Masset & Papaloizou 2003) acts in a regime when the planet gap is shallow enough to have significant material in the horseshoe orbit of the planet inside the gap, as for example the middle panel in Fig. 2.1. This causes a density asymmetry in the coorbital region that occurs e.g. for a planet already migrating and interacting with the horseshoe flow. The asymmetric coorbital gas will create a increasing torque leading to run-away migration and thereby changing the planet's orbit usually on a fast time scale. However, for this type of migration, the exact form of the asymmetry has a significant impact on the direction of migration.

3 Numerics

As already encountered in the previous chapter, the dynamic of PPDs can analytically only be approximated for specific conditions like axisymmetry. This is instantly invalidated by the presence of a binary. Therefore, to understand the dynamics of a CBD and other perturbed PPDs, numerical methods are necessary to simulate how they will evolve with time. In this chapter we will in short introduce how a numerical simulation can be set up to produce a good approximation of reality.

3.1 Numeric integration

As seen in Section 2.1 the fundamental challenge is to solve or approximate the set of three partial differential equations Eq.(2.1)-(2.3) for the quantities of density, velocity and internal energy or pressure. With numeric discretisation, this can be understood as a Riemann problem, which describes a problem with specific initial conditions for a set of conservation equations. To integrate these equations over time, numerical methods can be employed. Common methods using grid discretisation are the finite element, finite volume and finite difference methods. The general idea of all methods is to discretise the integrated time evolution to finite time steps Δt and evaluate the change of a defined, spacially discretised property within this small time step. Very generally said, in finite difference method the profile of the property is approximated by constructing a curve between the values at the grid points, in the finite volume method the profile is approximated by a series of step–function of the averaged property inside grid cells and in the finite element method the local function slope of the property inside the cell is evaluated. These methods are not mutually exclusive. However, for the problem of disc dynamics mostly finite volume and finite difference schemes are in use (e.g. FARGO3D & PLUTO Benítez-Llambay & Masset 2016; Mignone et al. 2007). The finite volume method has the advantage of conserving mass and is used in the PLUTO code. We will shortly explain how it is applied in the numerical integration.

Finite volume means using property-conserving averages in the whole volume of a cell and update this volume via a related flux from the neighbour cells through the cell surface. Therefore, this approach is conserving the property inside the grid as long as the boundary does not introduce a sink or source. So as a first step to integrate in time the initial function is discretized to the average value centred on the centre of the cell. And at every time step the updated values are stored this way (see first panel in Sketch 3.1).

As the values at the cell centres can deviate from the values at the cell boundaries, the representation of the initial function can be enhanced by reconstruction. This means that a simple slope through the central value point is constructed that captures the approximate direction of flow of each cell and still integrates to the average value over the cell. An example is shown in the second step in Sketch 3.1 There are a number of schemes for this data reconstruction, details can be found in Chap. 13 in the book by Toro (2009).

With the time integration step and using the Equations (2.1)-(2.3) the hydrodynamical problem fulfils the conditions of a problem that can be solve using Riemann solvers. More details on numerical methods and Riemann solvers are explained in the book by Toro (2009). The following will be a short summary of the general idea of the Riemann solver based on the book. Riemann solver generally solve an initial boundary value problem, meaning that there is a partial differential equation (PDE) that has a given initial condition and boundary conditions at the end of the domain of interest. The interface of the grid cells can be understood as a Riemann problem. The partial differential equations (2.1)–(2.3) governing the hydrodynamical problem are already mentioned in Section 2.1, the equations can be combined to one equation utilising a vector $\mathbf{U}$ that incorporates density ρ, velocity v and pressure P or specific energy e. How we create those initial and boundary conditions specifically to describe a PPD will be discussed in Sec. 3.2 & 3.3. However, generally we can just state:

$$\mathbf{U}_t + \mathbf{F}_x(\mathbf{U}) = 0 \quad \text{(PDE)} \tag{3.1}$$

$$\mathbf{U}(0, x) = \mathbf{U}_0(x) \quad \text{(inital condition)} \tag{3.2}$$

$$\mathbf{U}(t, x_{\min}) = \mathbf{U}_{\min}(t); \quad \mathbf{U}(t, x_{\max}) = \mathbf{U}_{\max}(t) \quad \text{(boundary condition)} \tag{3.3}$$

Here $\mathbf{U}_t$ is a partial time derivative of a vector of conserved variables and $\mathbf{F}(\mathbf{U})$ is the corresponding flux vector of $\mathbf{U}$ through x, $\mathbf{U}_0(x)$ is a spacial function at time $t = 0$ and $\mathbf{U}_{\min}$ & $\mathbf{U}_{\max}$ are defined spacial boundaries for a domain $[x_{\min}, x_{\max}]$. According to the finite volume method idea, with all of these conditions known

the problem can be numerically integrated for a time $t(n)$ after n steps $t(n)$ and a position in a gridded domain $x(i)$ $(n, i \in \mathbb{N})$ by:

$$\mathbf{U}_i^{n+1} = \mathbf{U}_i^n - \frac{\Delta t}{\Delta x}\left(\mathbf{F}_{i+1/2}^n - \mathbf{F}_{i-1/2}^n\right) \tag{3.4}$$

Essentially, the current state in the current cell is updated by the fluxes entering and leaving through the surfaces of the cell in the current time step. Now exactly defining these fluxes is the challenge of the different Riemann solvers. Looking at Equation (3.1), the flux vector $\mathbf{F}_x(\mathbf{U}) = \partial\mathbf{F}(\mathbf{U})/\partial x$ can be expressed with the matrix $\mathbf{A}(\mathbf{U}) = \partial\mathbf{F}(\mathbf{U})/\partial\mathbf{U}$ as $\mathbf{F}_x(\mathbf{U}) = \mathbf{A}(\mathbf{U})\partial\mathbf{U}/\partial x$. This conversion to a matrix creates a quasi-linear problem, where the eigenvalues can be used to extract the information propagation speed. Now, each matrix has three eigenvalues. These eigenvalues and corresponding eigenvectors describe the waves propagating to or from the cell through the fluxes on its interfaces, however, the wave speed does not generally correspond to the material speed. As indicated in Sketch 3.1 the two outer waves can be shock (solid line) or rarefaction waves (blurry line) which require different solutions and the middle wave is a contact discontinuity (dashed line). So the system can be understood as two waves between 3 constant states. The Riemann solver by Harten, Lax & van Leer (HLL) takes this approach to directly obtain the intercell fluxes to approximate the solution of the Riemann problem like in Eq. (3.4). HLL, mostly used for the presented models, is explained in detail in Chapter 10 of Toro (2009).
As the fluxes have now been determined the last step not needed is the actual time integration step. For the models we use a 2-order Runge–Kutta method. The size of time step can be adapted to the current model using the Courant–Friedrichs–Lewy condition, which compares the velocities v in the simulation to the time and spacial resolution Δt and Δx with the Courant number as $C = v\Delta t/\Delta x \leq C_{\max}$. As any information should propagate less than one cell of Δx the Courant number needs to be smaller at all times than $1 \geq C$. Hence, the fastest velocity in the system will slow down the computations, therefore it can be costly to extent the domain closer to strong sources of gravity as the velocity will increase. Further details on the used methods can be found in Thun et al. (2017).

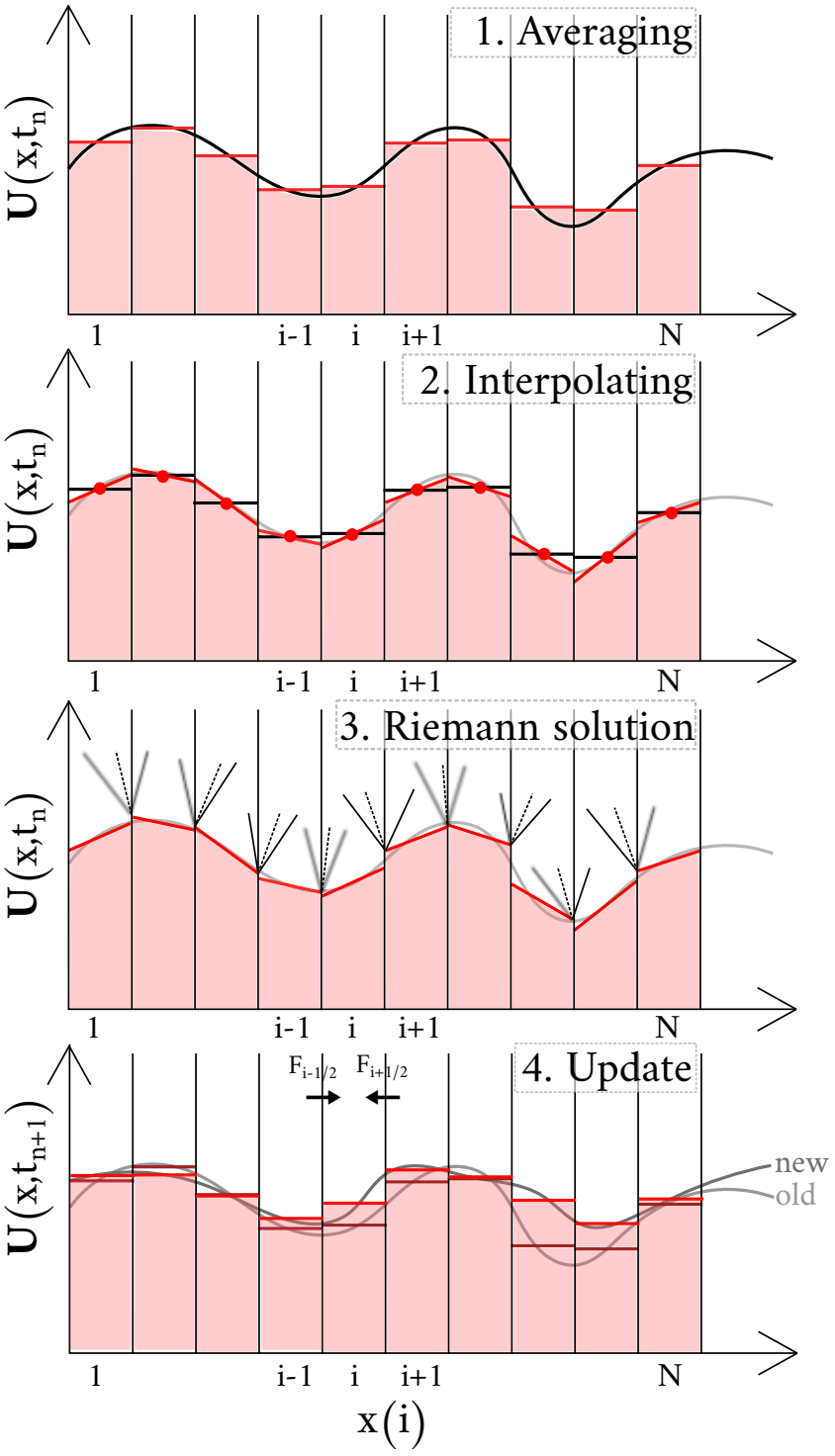

Figure 3.1: Schematic Sketch of the numerical algorithm to evolve the hydrodynamical equations by one step.

3.2 Initial setup

To evolve a hydrodynamical system an initial state and a description of the boundary condition of the problem have to be given. Theoretically, any continuous distribution of density, pressure/internal energy and velocities over the domain could be evolved. However, in many cases the goal of the simulation is to recreate a stable state of the PPD with only small variations like migrating planets or other perturbations introduced, which represents systems in the observed universe. Therefore initial conditions are chosen to best represent a steady state. For a single star this can be achieved by assuming a steady radial mass transported through the disc as already shown in Section 2.1, this can be analytically approximated to $\dot{M} = -2\pi\Sigma r v_r = 3\pi\nu\Sigma$, where we also use the analytical radial velocity profile $v_r = 3/2 \cdot r/\nu$. As even simpler initial radial velocity $v_r = 0$ can also be assumed globally without wasting much computation time, as radial drift usually happens on comparably long time scales in PPDs. The viscosity and specially the α viscosity depends on the local pressure scale height $\nu = \alpha c_\mathrm{s} H = \alpha c_\mathrm{s}^2/\Omega_\mathrm{K}/\sqrt{\gamma}$ (see Sec. 2.1.1). The Keplerian angular velocity scales with radius as $\Omega_\mathrm{K} \propto r^{-3/2}$ and the sound speed depending on the local temperature initially will be given by a radial profile $T \propto r^q$. For a simple approach of irradiation from the center the temperature is often approximated using the Stefan-Boltzmann law with $L = \sigma 4\pi r^2 T^4 \rightarrow T \propto r^{-1/2}$. Assuming that the density follows a radial profile $\Sigma \propto r^p$ it can thereby be inferred for the steady mass flow $\dot{M} = \text{const.}$, that

$$\dot{M} \propto r^{p+q+3/2} \approx r^{p-1/2+3/2} \rightarrow \Sigma \propto r^{-1}. \tag{3.5}$$

For the initial pressure needed in a non-isothermal case, pressure is given using temperature and density $P = \Sigma c_{\mathrm{s,iso}}^2(T) \propto r^{p+q}$.

This radial power-law condition is a simple solution. But other solutions are possible, like for example the self–similar solution by Lynden-Bell & Pringle (1974) that includes an outer density drop and does not assume an infinitely extending disc. Similarly, for circumbinary discs it is known that the inner region is unstable and a cavity forms (Artymowicz & Lubow 1994). Therefore it is useful to already start from initial conditions with a cleared inner cavity. An easy way to do this is to initially assume a circular inner cavity as in e.g. Pierens & Nelson (2013); Thun et al. (2017). Such an initial density profile Σ_ini is then created using an

exponential cut-off function $f_{\rm cav}$ as follows

$$\Sigma_{\rm ini}(r) = \Sigma_{\rm ref} \cdot \left(\frac{r}{a_{\rm bin}}\right)^p f_{\rm cav} \quad \text{with} \quad f_{\rm cav} = \left[1 + \exp\left(-\frac{r - R_{\rm cav}}{0.1 R_{\rm cav}}\right)\right]^{-1} \tag{3.6}$$

In the same way, the outer part of the disc can also be truncated to create a torus-like disc well inside the computational domain as done in Muñoz et al. (2020) by multiplying additionally a function for the outer cut-off

$$f_{\rm out} = [1 + \exp(r - R_{\rm out})]^{-1}$$

.

However, even with the circular inner cavity, the disc profile is far from the convergent circumbinary disc profile that exhibits an eccentric inner cavity and inner disc. Hence, reaching the convergent circumbinary disc profile requires a long time integration of up to $\sim 10^6\, T_{\rm bin}$. Reproducing this profile as an initial condition for varying disc and binary properties, is an ongoing investigation, in parts laid out in this thesis in 5.1 & 5.4.4.

Finally we need to define an initial azimuthal velocity. For a disc on a mostly circular orbit around a central potential, the easiest assumption is Keplerian speed $v_\phi = v_{\rm K} = \sqrt{{\rm G}M/r}$. However, a gas disc is not only influenced by the gravitational potential of the central object, but also by the pressure of the surrounding gas. As the gas density generally increases inward the pressure gradient creates an outwards push on the gas, leading to a slightly sub-Keplerian azimuthal velocity in hydrostatic equilibrium. Assuming power-law profiles for Σ and T and that v_r can be neglected, $v_r \approx 0$, it can be calculated in the following way:

$$\frac{v_\phi^2}{r} = \frac{1}{\Sigma}\frac{\partial P}{\partial r} + \frac{\partial \Phi}{\partial r} \rightarrow v_\phi = v_{\rm K}\sqrt{1 + (p+q)h^2} \tag{3.7}$$

3.3 Boundary conditions and resolution

As described before the finite–volume method requires also a spacial discretization, at which flows are exchanged between cells. This does not have to be uniform and for the problem of discs. A cylindrical or spherical grid has a better suited geometry, but, nevertheless, the grid has an outer boundary at a maximum and minimum radius for example. The outermost cells need to be set by boundary conditions.

Suitable conditions have to be defined that are close enough to the quasi-steady state of the simulation inside the domain to ensure that the boundaries are not unphysical or heavily influencing in the outcome of the simulation.
The easiest to define in a cylindrical or spherical grid is the azimuthal boundary. The disc should continuously orbit the center, therefore the grid needs to be periodic in this direction. For any quantity x, this means that all ghost cells on either side $n = [-2, -1, N, N+1]$ are set to values x of the other side of the domain, $x(-1) = x(N-1); \quad x(-2) = x(N-2); \quad x(N) = x(0); \quad x(N+1) = x(1)$.
Boundaries that, in fact, border the physical domain are usually not periodic for disc simulations, like all boundaries in Cartesian grids or the radial direction in cylindrical and spherical grids and also often the polar angle in spherical coordinates, if the domain does not cover the full polar axis. Instead boundaries either get set to constant analytical approximations as discussed for the initial conditions in the above Section 3.2 or are adjusted to the adjacent cells.
One example usable to conserve the total mass inside the domain is a reflective boundary condition. To achieve this the ghost cells represent the mirrored values of the end of the domain, meaning equal density, pressure and azimuthal velocity and inverted radial velocity. Such a boundary, however, reflects waves back into the domain that can overlay with the general features inside the disc. Boundary–created features can also occur inside the domain for other boundary conditions. To avoid such features inside the relevant domain, damping zones can be introduced that will be discussed later.
For the problem of an accretion disc, it is natural that mass should be able to leave the simulation at the inner radial domain to approximate an accretion flow. The easiest way to achieve that would be to just set the density in the ghost cells to a very low value. This will create strong infall close to the inner boundary and an inner density drop. However, for a steady disc this profile stabilizes. A more steady way to create the infall is a $\partial_r \Sigma = 0$ condition such that $\Sigma(-1) = \Sigma(0)$, with a diode radial velocity that always is negative $v_r(-1) = -|v_r(0)|$. With this condition only infall is possible, but the density profile shows no overly strong inner drop.
At the same time there are options for the azimuthal velocity to conserve azimuthal velocity $\partial_r v_\phi = 0$, angular velocity $\partial_r \Omega = 0$ or angular momentum $\partial_r L = 0$ with $L \approx mrv_\phi$. Azimuthal velocity is simply conserved with $v_\phi(-1) = v_\phi(0)$. The effects between these possible conditions on the main domain are small and they become most relevant for studies of the accretion through the inner domain, if at all.

As mentioned, some boundary conditions can introduce unwanted features or waves reflected back into the domain. Behaviour like this can be suppressed by prescribing a damping zone that adjust density or velocity to the initial profile with a ramping function that increasingly reduces the dynamic behaviour to the set profile and thereby smoothly transitions between simulation and damping condition.

3.4 N-body integration

Since binaries include at least two large gravitationally interacting objects in the system, the positions of all gravity sources in the system need to be updated between every hydro time step. While for two bodies without disc effects an analytical solution can be constructed following Section 2.2, this is no longer possible for a gravitating 3-body configuration. In this case the positions of all bodies need to be numerically evolved in time. The detailed implementation steps and order of execution with reference to the hydrodynamics simulations are described in the Appendix of Thun & Kley (2018). Here we will describe the principle computation implemented in the models.
The motion of a point mass in vacuum can be described by the energy balance between kinetic and potential energy, as energy is conserved.

$$0 = \sum_{i,j} \left(\frac{m_i}{2} \dot{\vec{x}}_i^2 - \mathrm{G} \frac{m_i m_j}{|\vec{x}_i - \vec{x}_j|} \right) \quad \text{with} \quad \ddot{\vec{x}}_i = \sum_j \frac{\mathrm{G} m_j}{(\vec{x}_i - \vec{x}_j)^2} \hat{e}_{x,ij} \tag{3.8}$$

This second–order ordinary differential equation relates the current velocity $\dot{\vec{x}}_i$ and current acceleration $\ddot{\vec{x}}_i$ to the position $\vec{x}_i$ of all bodies, which will change according to velocity and acceleration. This can not be solved analytically for more than 2 point masses. So in order to update position, velocity and acceleration of the N bodies a 4th–order Runge–Kutta (RK4) integration method is implemented, such that property $y(t) = \int \dot{y}(t) \mathrm{d}t$ is numerically integrated with:

$$y(t + \delta t) = y(t) + \frac{\Delta t}{6} (k_1 + 2k_2 + 2k_3 + k_4) \tag{3.9}$$

$$k_1 = \frac{\mathrm{d}y(t)}{\mathrm{d}t}; \quad k_2 = \frac{\mathrm{d}(y(t) + k_1 \Delta t/2)}{\mathrm{d}t}; \quad k_3 = \frac{\mathrm{d}(y(t) + k_2 \Delta t/2)}{\mathrm{d}t}; \quad k_4 = \frac{\mathrm{d}(y(t) + k_3 \Delta t)}{\mathrm{d}t};$$

The time step Δt corresponds to the hydrodynamics simulation time step such that both can be integrated simultaneously. In additional to the N-body interaction,

the N bodies can also feel the gravitational torque from the disc. This can be added as an additional, summed up acceleration, calculated from the gravitational potential by the mass in each cell and the distance to the cell's centre.
For the N-body problem, there also exists the REBOUND software by Rein & Liu (2012) that includes various different integration methods, especially also energy-conserving or symplectic higher-order integrators (Rein et al. 2019). This software is used in Sec. 5.3 to test the stability of planets around binaries, however for the hydrodynamical models the described less elaborate RK4 was used in order to reducing computational overhead.

3.5 GPU-PLUTO

The software used for the simulations of the binaries is the PLUTO 4.2 code by Mignone et al. (2007) in a GPU–supported version developed by Daniel Thun (Thun et al. 2017) for the general hydrodynamics in 2D and 3D.
As the disc is discretized into cells, for every cell the same equations are solved in the time integration. This is an ideal case for GPU calculations that are designed to solve the same equation on large arrays, speeding up calculations by computing for all cells at the same time. To develop algorithms for GPU there is the CUDA platform that allows creating NVIDIA-GPU supported software. To develop functions for the GPU they need to be written in the CUDA–specific CUDA-C language to interface to C or C++ programs, as is the case for the official PLUTO code by Mignone et al. (2007). A more detailed description of this simulation software is given in the thesis by Thun (2019).

4 Results

In this chapter the results of the four attached publications (see Chapter 7) are summarized. They are not ordered chronologically but logically, starting with an observational verification that the numerical models are viable in Section 4.1, then showing how disc and binary interact and what we can learn about the binary evolution from the disc model in Sec. 4.2. Planets are included in the models in Sec. 4.3 and the final orbit of the circumbinary planets due to planet migration is discussed. The special case of multiple planet moving into a stable 1:1 resonance around a binary follows in Sec.4.4. More ongoing work and the preliminary results are included in the next Chapter 5. As the way to construct the models was shown in the last two chapters, it will not be in focus here. The details of the models are given in the attached publications in Chapter 7.

4.1 Result I: GG Tau A— Simulating observation to understand the disc

In this work of (Keppler et al. 2020) we compared the scattered light observations for the GG Tau A circumbinary disc with numerical simulations. In fact, GG Tau is a young, $\sim 1.5\,$Myr-old multiple star system of 5 stars. GG Tau A consists of three stars: The K-Type star Aa and close spectroscopic binary M-dwarf stars Ab1 and Ab2 with an estimated separation of $\sim 5\,$au. GG Tau A is surrounded by a thick circumbinary disc with an inner cavity of $\sim 190\,$au and the disc is truncated by the GG Tau B binary orbiting with $\sim 1400\,$au separation to the A component. Previously the distance and inclination of the central binary objects Aa and Ab was debated, based on claims that the extent of the circumbinary disc could not be explained by hydrodynamical simulations of the best observationally derived distance of $\sim 35\,$au (Köhler 2011; Cazzoletti et al. 2017) but should rather be as large as $60\,$au.
We tested the best fit parameters for a coplanar disc (Köhler 2011) with a long-evolved ($> 10\,000\,T_{\rm bin}$) hydrodynamical simulation with an α-viscosity of 10^{-3}.

M_{Aa}	M_{Ab}	a_{bin}	e_{bin}	h_{mid}	h_{surf}	M_{disc}
$0.75\,M_{\mathrm{sun}}$	$0.65\,M_{\mathrm{sun}}$	35 au	0.28	0.11	0.15	$0.12\,M_{\mathrm{bin}}$

Table 4.1: Best fit parameters used for the hydrodynamical simulation of GG Tau A. M_{Aa} and M_{Ab} are the masses for the two binary components, a_{bin} and e_{bin} are binary semi-major axis and eccentricity (Köhler 2011). The aspect ratio of the disc at the mid plane derived from the continuum emission is h_{mid} (Dutrey et al. 2014) and h_{surf} the aspect ratio at the surface traced by ^{13}CO (Guilloteau et al. 1999). M_{disc} is the mass of the disc (Guilloteau et al. 1999)

.

The best fit parameters used are given in Table 4.1. With the large extent of the disc, we believe a locally isothermal model to be a reasonable prescription. As Thun et al. (2017) already established, the excitation of the disc from the circular initial profile as described in Eq. (3.6) to the physical realistic state is slow and in the order of $> 10\,000\,T_{\mathrm{bin}}$. This can be seen in Fig. 4.1 for the two upper limit and lower limit temperatures at the surface and mid plane of the disc and in Fig. 4.2 for different viscosities for the mid plane temperature (Dutrey et al. 2014). In the early state of the model after $\approx$1000–3000 T_{bin} the inner cavity can be artificially small due to an unconverged meta-stable state for $\approx$100–1000 T_{bin}. This has led to the debate about the true binary separation. However, eventually the cavity profile converged to a cavity size of 3.9–4.6 a_{bin} depending on the assumed temperature and scale height. The disc density then peaks at 215–230 au which agrees very well with the observed extent of the disc. As Fig. 4.2 shows, when lowering the viscosity the cavity becomes less eccentric, yet remaining above a cavity size of $> 4\ a_{\mathrm{bin}}$ such that a less eccentric disc can be explained by a lower viscosity.

Using RADMC-3D (Dullemond et al. 2012) artificial polarized scatter light images of the model could be compared to the real observation. To produce these images a dust fraction of 5×10^{-4} gas density in the relevant grain size was chosen assuming that the dust to be well enough coupled to the gas to follow the gas density. Fig. 4.3 displays the linearly polarized scatter light intensity of SPHERE observations (left panel) and the high-pass filtered image of GG Tau A (middle and right panels) highlighting the spiral and streamer features. The blue indicated shadows might be evidence of the inner circumstellar disc around Aa and will therefore not be recreated by the simulations. The other features in Fig. 4.3 are well comparable with the artificially created image in Fig. 4.4.

The right panel shows the mid plane temperature assumption while the left panel

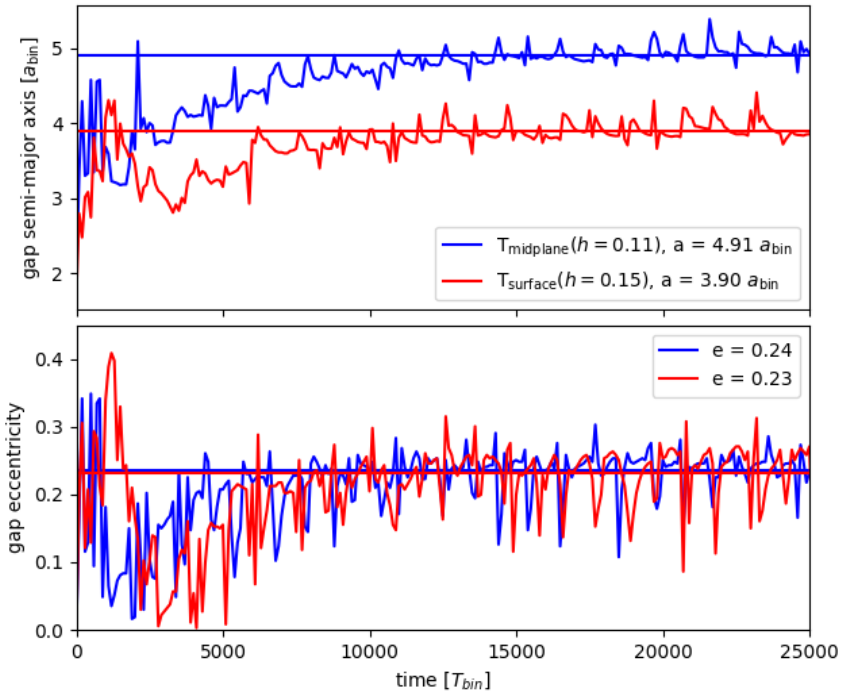

Figure 4.1: The time evolution of semi-major axis (top) and eccentricity (bottom) of the cavity in the models of GG Tau for the surface temperature (red) and the mid plane temperature (blue).

is the surface temperature case, which has a slightly smaller extent. A high-pass filter is applied on both. The simulated and observed discs show spiral patterns inside the disc and streams flowing through the cavity.
In general this work demonstrates that the models of circumbinary discs indeed reproduce realistic disc structures and sizes, when given the correct viscosity and evolved until convergence.

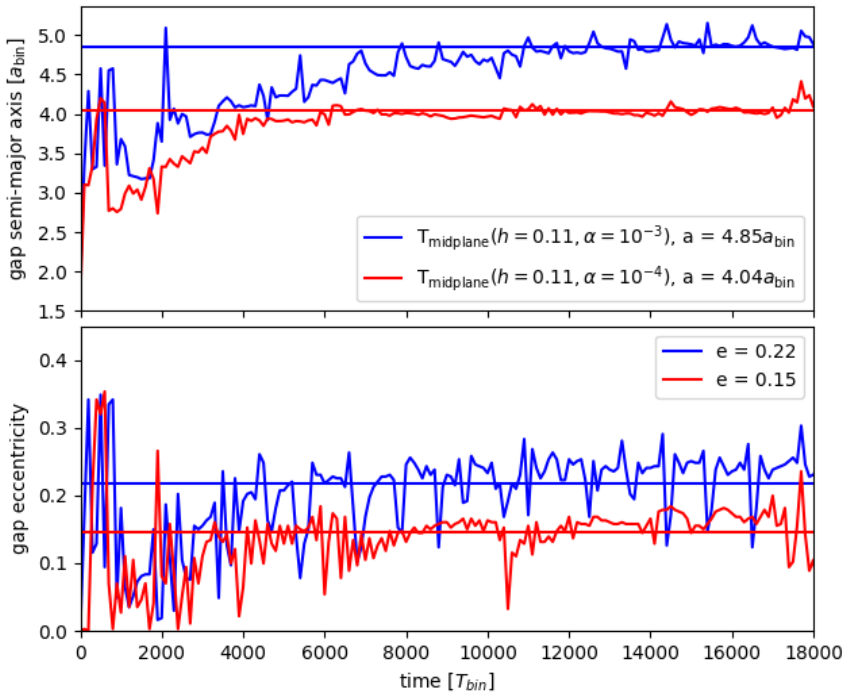

Figure 4.2: The time evolution of semi-major axis (top) and eccentricity (bottom) of the cavity in the models of GG Tau A for different α-viscosities with mid plane temperatures ($H/r = 0.11$). Red refers to $\alpha = 10^{-4}$ and blue to $\alpha = 10^{-3}$

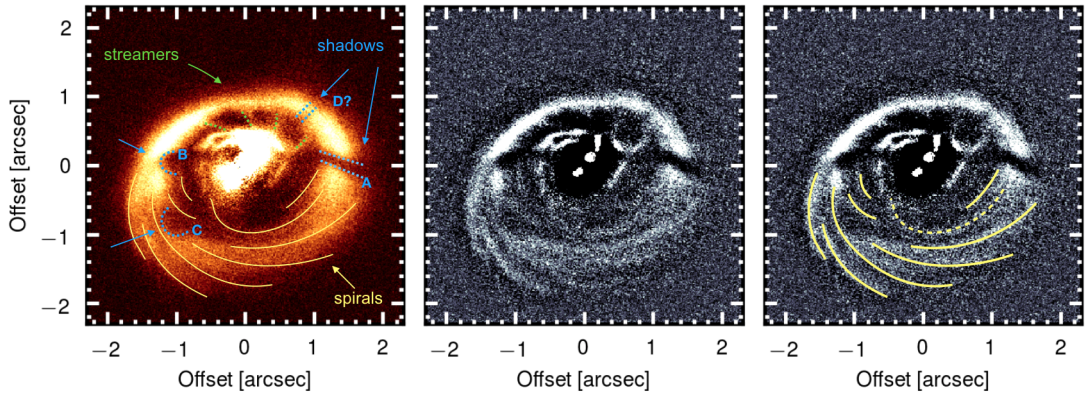

Figure 4.3: The observation of GG Tau A in linear polarized intensity scattered light is displayed in the left panel and the high-pass filtered image of GG Tau A in the middle and right panels, marking spiral structures in yellow, shadows in blue and streamers in green.

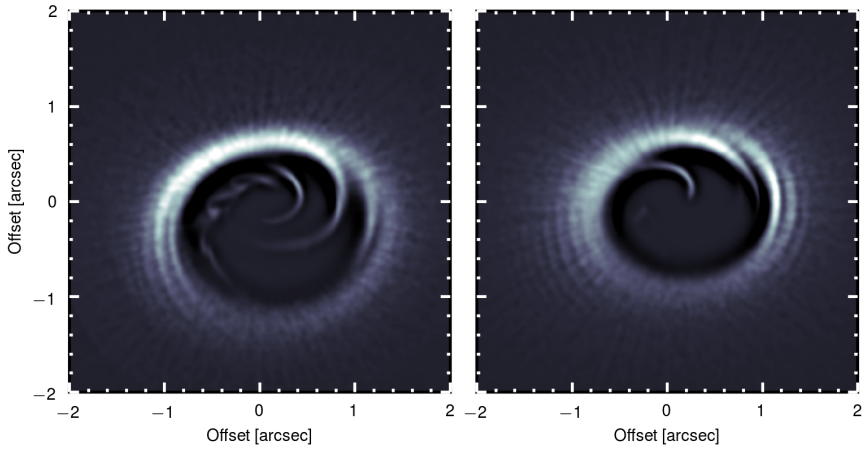

Figure 4.4: Synthetic polarized scattered light observations of the $\alpha = 10^{-3}$ models for mid plane temperature ($h = 0.11$) on the right and surface temperature ($h = 0.15$) on the left. The image contains a high-pass filter to compare to Fig. 4.3

4.2 Result II: Binary disc interaction and orbital evolution of the binary

Miranda et al. (2017) discovered that the momentum transfer from the disc to the binary can lead to expanding binary orbits, whereas it was previously believed that the gravitational torques of the disc would cause the binary orbits to shrink. Thereafter a number of studies were conducted to refine whether and when the binary disc interaction causes shrinking or expansion of the binary orbit. In our study, we compared our results to the already conducted surveys by Muñoz et al. (2020) and Tiede et al. (2020), who studies this effect in the context of black hole binaries with a range of α-viscosity between $10^{-1} - 10^{-2}$ and disc Mach numbers of $r/H = [10-40]$, respectively. Furthermore we expanded the parameter space to include the case of protoplanetary circumbinary discs, running long-term simulations for thin discs with low viscosities.

To analyse the shrinking or expansion of the binary orbits one can use the angular momentum conservation in the binary–disc system. The exchange of angular momentum in the disc can be tracked with $\dot{J}_{\rm bin} = -\dot{J}_{\rm disc} = -(\tau_{\rm grav} + \dot{J}_{\rm adv})$, where $\tau_{\rm grav}$ and $\dot{J}_{\rm adv}$ are given in Eq. (2.24) & (2.26). Using $\dot{M}_{\rm bin} = -\dot{M}_{\rm adv}$ we get the normalized specific angular momentum transfer $j_s = \dot{J}_{\rm disc}/\dot{M}_{\rm adv}({\rm G}M_{\rm bin}a)^{-1/2}$. The example run for $h = \alpha = 0.1$ and $M_2/M_1 = 0.5$ is shown in Fig. 4.5. The top panel shows the advective mass transfer and the mass loss from the disc, the middle panel shows the contributions of $\tau_{\rm grav}$ and $\dot{J}_{\rm adv}$ and the overall resulting angular momentum transfer and the bottom panel shows the specific normalized angular momentum j_s. After a short initial phase, j_s becomes constant in time. A critical threshold value above which the binary expands can be analytically calculated dependent on binary mass ratio $q_{\rm bin}$ and binary accretion ratio f. It converges to 3/8 for $q \to 1$ and is for all parameters in the range of (0,1). For the test simulation with $q = 0.5$ in Fig. 4.5 j_s is well above 3/8 and with $j_s = 0.86$, it is safe to say the binary would therefore expand.

We performed further simulations similar to Muñoz et al. (2019) with a torus-like disc (with the inner and outer cut-off described in Sec. 3.2) with varying viscosity and aspect ratio H/r at the same time. The results for $q = 1$ can be found in Fig. 4.6. We could confirm the findings of Muñoz et al. (2020), that for thick disc with $h = 10\%$ the binary orbit will expand and we expanded the parameter space to viscosities as low as $\alpha = 10^{-3}$ finding the same behaviour for thick discs.

However, for thinner discs the behaviour of the binary orbit can change for low viscosities. We found that, while advection follows the viscosity linearly as explained

in Sec. 2.1 also in the case of binaries, the torque changes from a stream–dominated torque from within the cavity for high viscosities with the same linear trend, to an increasingly eccentric disc–influenced torque for low viscosities. To visualize this Fig. 4.7 shows the 2D structure of the models with $h = 0.05$. The viscosity decreases from left to right and with the reduced viscosity the features inside the cavity subside, reducing the torque from the cavity region, while the change in the disc structure is comparably small. So, while the accretion of angular momentum and mass scales linearly, the torque is a more complex relation between contributions linked to accretion features that scale linearly with viscosity and the general disc that remains roughly constant. This is shown in Fig. 4.8. The mass accretion normalized torque increases for small viscosities. Hence, the torque leading to orbital shrinking overtakes the angular momentum advection for small viscosities. For a $h = 5\%$, $\alpha < 5 \times 10^{-3}$ disc the binary begins to shrinks and for thinner discs($h = 4\%$) the binary orbits shrink even for higher viscosities in agreement with Tiede et al. (2020).
For the protoplanetary, circumbinary disc we could determine that the binary–disc interaction will cause the binary orbit to shrink. However, the time scale of the change in semi-major axis is in the order of $\dot{a}_{\rm bin} \approx 10^{-6} - 10^{-7}\, a_{\rm bin}/T_{\rm bin}$ for the low viscosity case of a protoplanetary disc, such that the effect of the binary orbit evolution has little effect on the dynamics of the disc or embedded planets that will migrate orders of magnitude faster as will be demonstrated in the next Section.

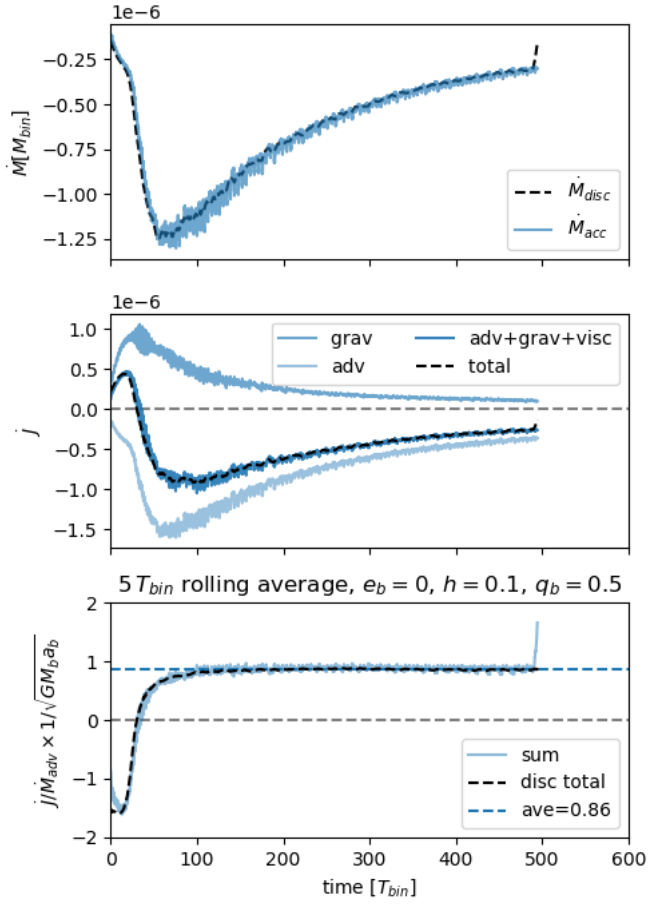

Figure 4.5: Angular momentum transfer between the circumbinary disc and the binary. **Top panel** shows the mass loss of the disc (dashed) compared to the mass accretion through the inner boundary (solid blue). The **mid panel** shows the angular momentum transport by advection (light blue), the torque of the disc on the binary (mid blue) and the combined effect of all angular momentum change terms (blue) compared to the loss of angular momentum from the disc (dashed). The **bottom panel** is the resulting normalized specific angular momentum change j_s.

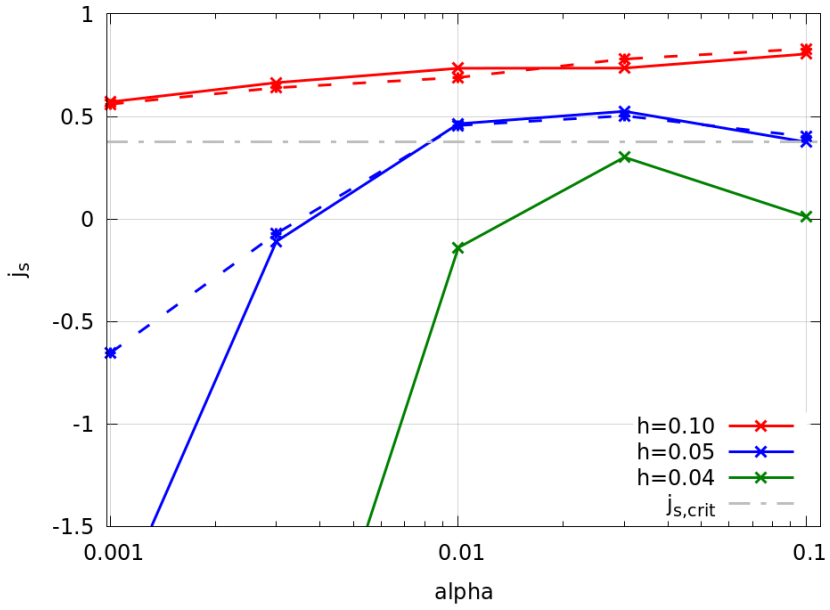

Figure 4.6: The value for j_s for the parameter space of viscous α on the x-axis and aspect ratio h by color. The dashed grey line marks the $j_{\mathrm{s,crit}}$, models above which exhibit expanding binaries.

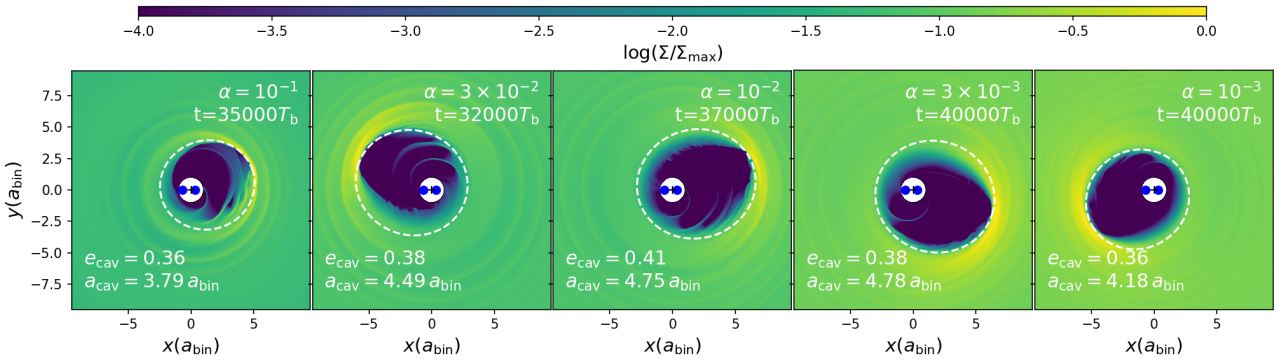

Figure 4.7: The 2D logarithmic density structure of binary models with an $h = 5\%$ and $M_2/M_1 = 0.5$ from highly viscous $\alpha = 0.1$ (left) to low viscosity with $\alpha = 0.001$ (right). The cavities are marked with white, dashed lines and their shape parameters are display in the bottom left corners of each panel.

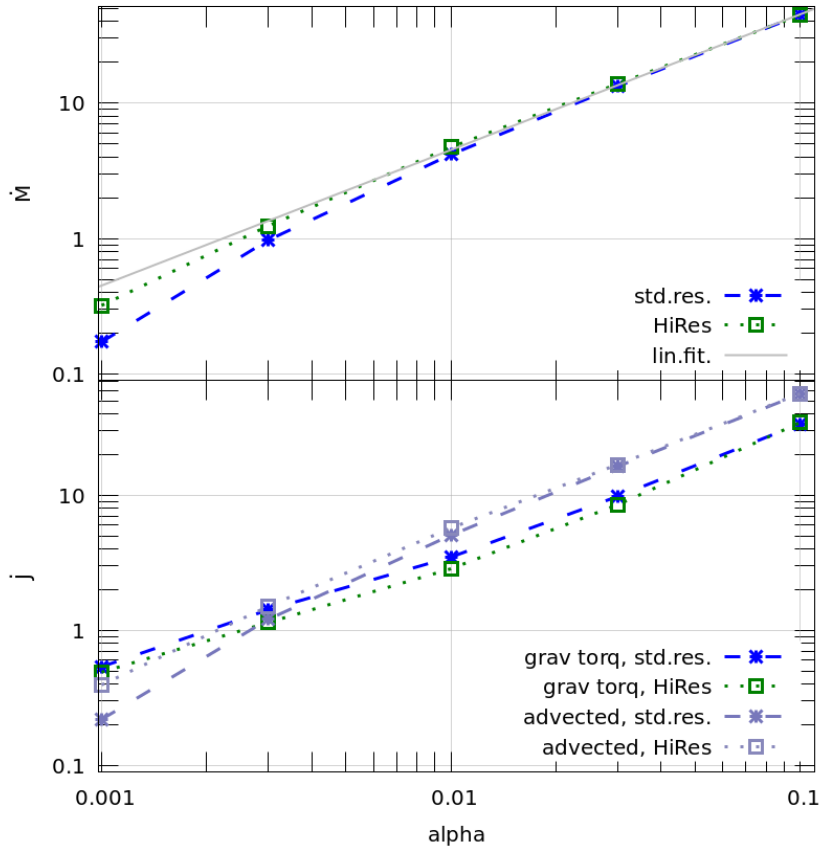

Figure 4.8: Average mass and angular momentum change of the disc. Top: mass accretion for a model with normal (blue) and double (green) resolution. The grey line denotes the theoretical viscous accretion rate for a single star. Bottom: advected angular momentum (light purple lines) compared to the gravitational torque contribution (blue and green lines).

4.3 Result III: Planet orbits

Not just the binary and the disc interact in a protoplanetary, circumbinary disc, but also the forming planets. In recent years about a dozen circumbinary planets have been confirmed by the Kepler mission and TESS. These planets interestingly share many properties, like orbital position close to the instability limit, mass range and low eccentricities (see also Table 1.1). Therefore it is reasonable to believe that they all followed comparable evolutions. So in this work (Penzlin et al. 2021) we set out to find a disc parameter set, that could explain most of the observations. Paardekooper et al. (2012), Meschiari (2012) and Silsbee & Rafikov (2015) all presented arguments for how in-situ formation is inhibited in the inner disc at the observed orbits of the planets, due to inefficient pebble accretion and planetesimal accretion being thwarted by tidal perturbations by the binary motion. Therefore we investigated the migration of the planet inside the circumbinary disc.

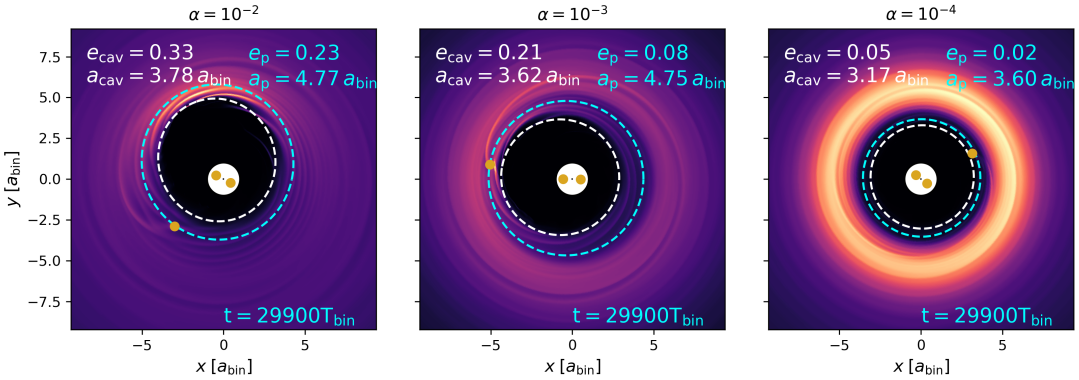

Figure 4.9: The 2D gas density structure and final parking parking orbits (cyan, dashed lines) of a Kepler-35-like system for $\alpha = [10^{-2}, 10^{-3}, 10^{-4}]$ (from left to right). The cavities of the CBDs are denoted by white, dashed lines.

In Kley et al. (2019) a lowered viscosity could successfully reproduce the orbit of Kep-38b, hence viscosity and aspect ratio h in the models were varied in a locally isothermal setting. First, for all systems and parameter sets, we evolved the disc models for $> 25\,000\,T_{\rm bin}$, before the planets were inserted at an outer orbit of the converged disc.

Fig. 4.9 gives an example of the effect of varying viscosity using a Kepler-35-like setup. With decreasing viscosity, the depth of the gap caused by the planet in the disc increases until for $\alpha = 10^{-4}$ the gap is sufficiently deep to allow the planet to

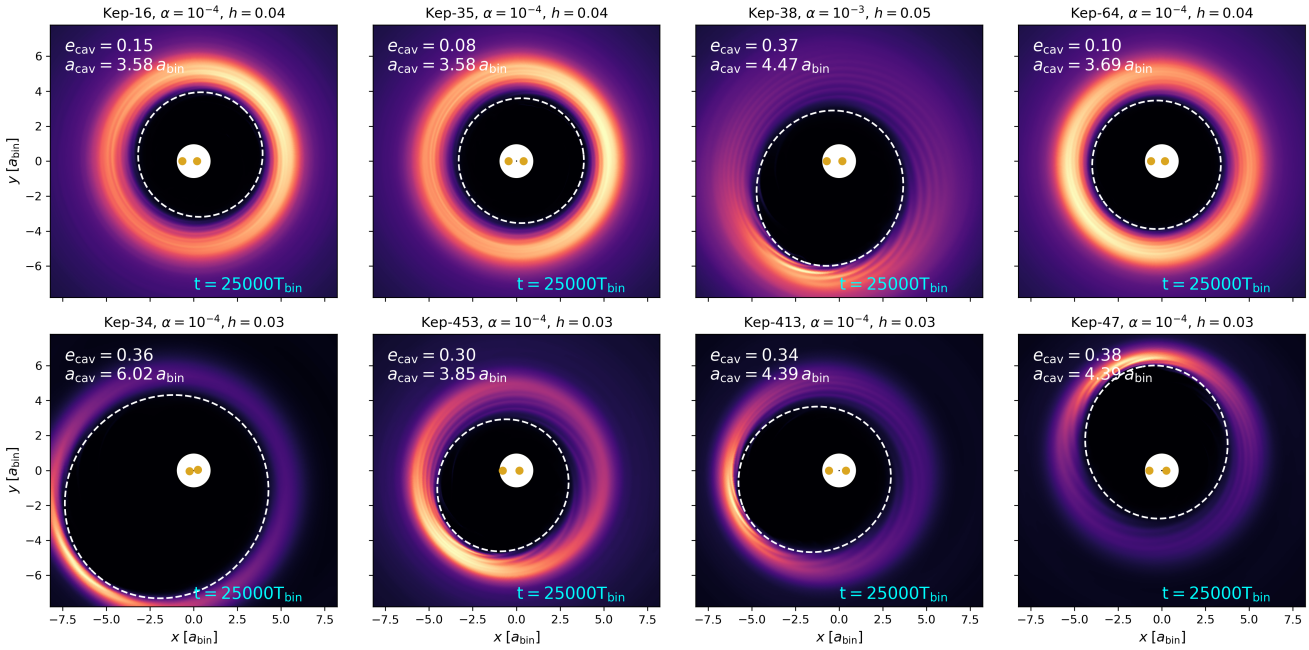

Figure 4.10: The 2D gas density structure of the best-fit model discs before the planets are inserted for the systems and parameters labelled above each panel.

migrate independently of the eccentric gas into the inner cavity and by its later orbit inside the cavity the planet circularizes the disc beyond.

With the disc parameters of $\alpha = 10^{-4}$ and $h = 0.04$, most planets migrated successfully to a final orbit within 10% of the observed value and parked there. The convergent disc profiles of these models are displayed in Fig. 4.10. For low viscosities the eccentricity of the disc is low especially for intermediate binary eccentricities $0.05 < e_{bin} < 0.3$ (Top row). This disc structure already aids the migration of the planet through the disc. In Fig. 4.11 the final orbit of the planet is shown, indicated with the cyan dashed line. The top row shows successful migration, while in the bottom row planets remain in orbits further out, even though Kepler-453b resides within $\sim$ 12% of its observed orbit. Only planets around very eccentric and circular binaries, both resulting in a very eccentric inner cavity and disc, did not overcome the inner disc and migrate to the observed location inside the cavity. The orbits of these planets remain perfectly aligned with the local eccentric disc, matching the precession rate. The planets that could reach an orbit inside the inner cavity further circularized the disc, such that disc

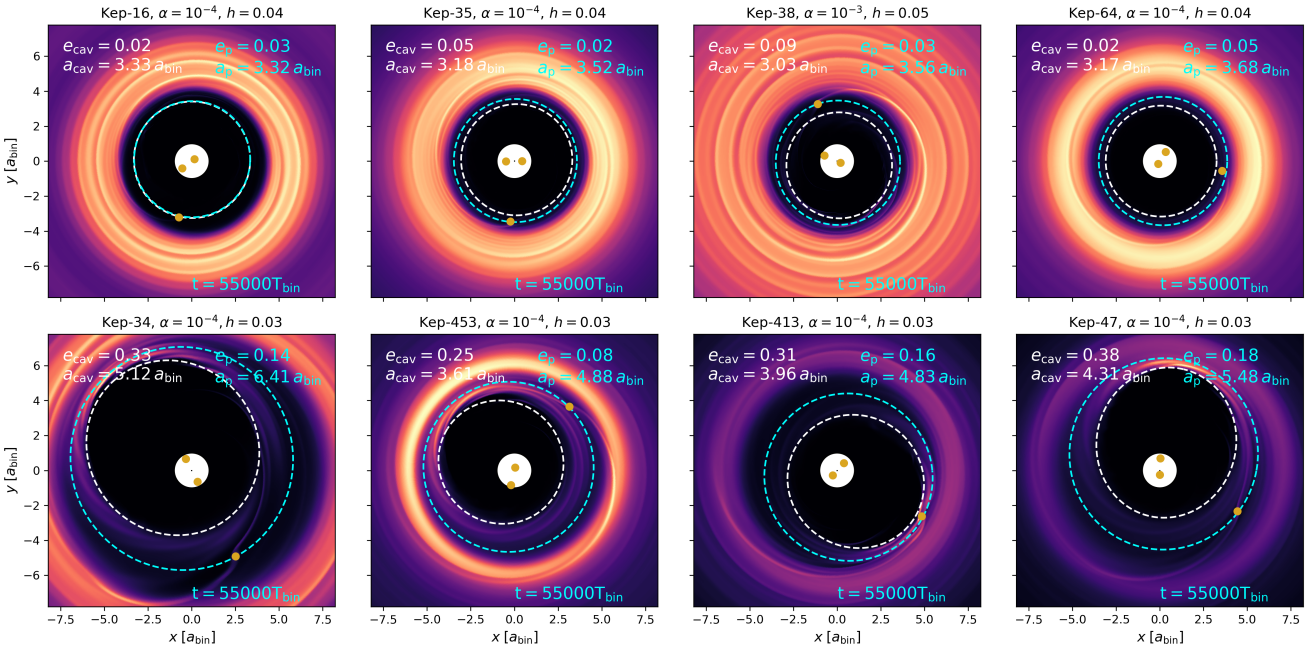

Figure 4.11: The 2D gas density structure of the best-fit model discs with the final planet positions (cyan line) at time $t = 55\,000\,T_{\rm bin}$ for the systems and parameters labelled above each panel.

semi-major axis and eccentricity is lowered. By artificially increasing the planet masses we could reach the observed orbit for even more planets. This result further supports the insight that the gap-opening capability of the planet is crucial to its ability to detach from the disc and reach orbits inside the cavity. With the used low viscosity, most planets are just in the range of the thermal mass, allowing them to open a gap in the gas of >10% the initial gas density (e.g. Crida et al. 2006).

In Fig. 4.12 the migration track of all successfully migrating planets is shown. As soon as they approach the peak density in the eccentric inner disc at $> 6\,a_{\rm bin}$, migration is slowed and even shortly reversed in humps that ultimately continue this inward trend until the inner cavity is reached.

The simple approach of testing disc conditions for multiple observed planets to find a common working model allows to gain an insight into the no-longer observable disc. Thereby, the observed planet orbits can constrain the disc parameters needed to reproduce such systems and further hint that viscosities in protoplanetary discs are in the order of $\alpha \approx 10^{-4}$.

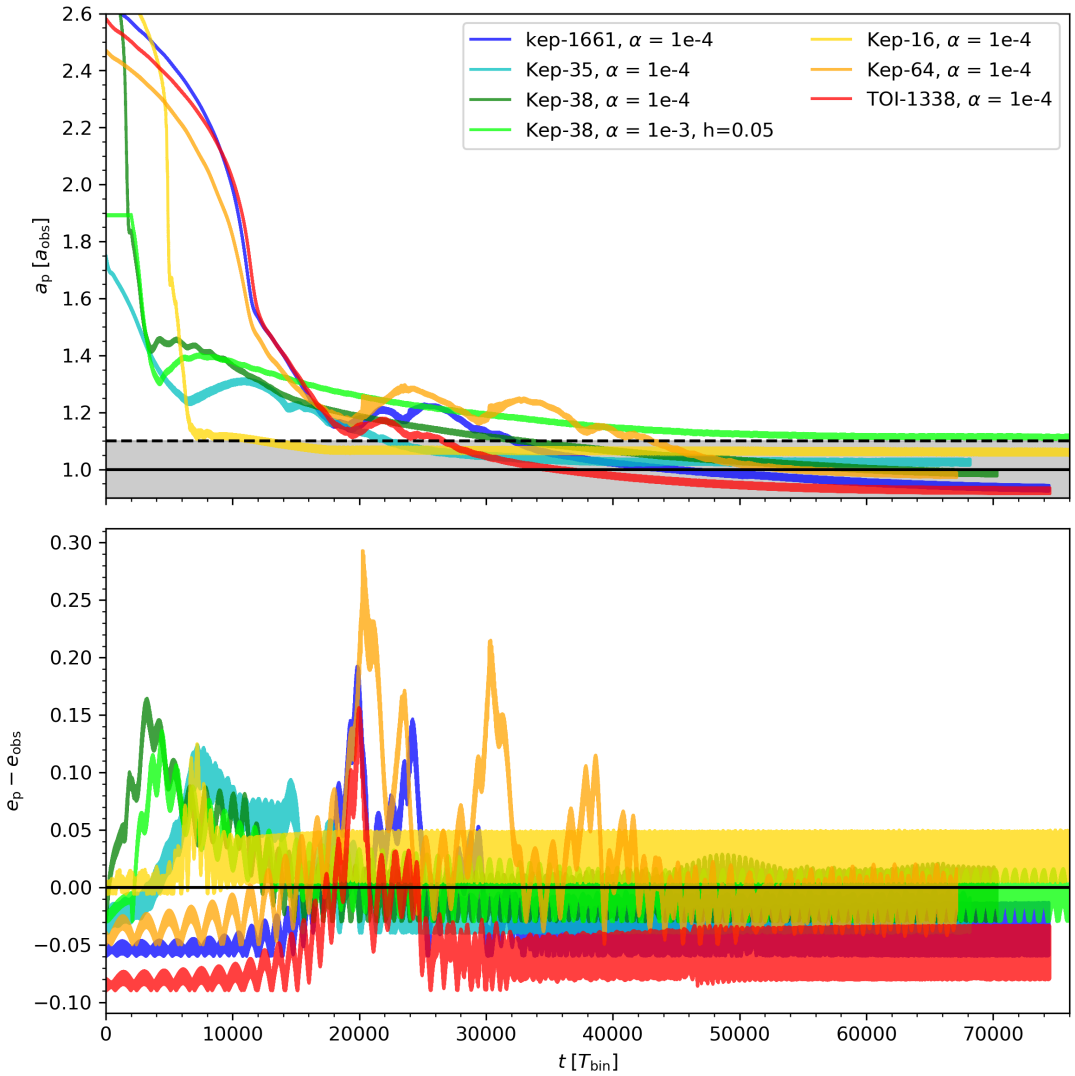

Figure 4.12: The time evolution of the planet orbits inside the circumbinary disc for the labelled Kepler system models. Scales are relative to the observed orbits. Top shows the semi-major axis of the planets, bottom shows the eccentricity.

4.4 Result IV: 1:1 resonances of planets around binary stars

If planets are not gap-opening like in Section 4.3, they are trapped and parked on eccentric orbits inside the disc. The final migration orbit of multiple planets of comparable mass is so similar in this case that they can enter into a 1:1 resonance. This is the subject of Penzlin et al. (2019). Especially for eccentric discs created by uneccentric binaries like Kepler-413 and -47, it is easy to capture similar mass planets in 1:1 resonances. Here, we used the binary parameters of these systems (see Table 1.1).

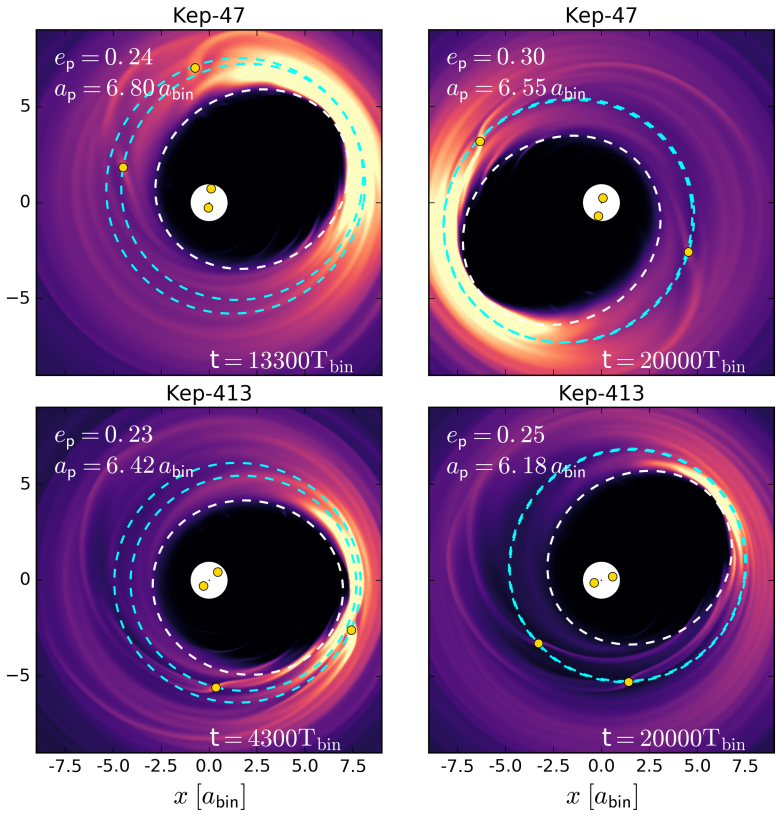

Figure 4.13: The disc density structure and the planet orbits (cyan lines) before (left) and after (right) capture into 1:1 resonance. The top row compares to a Kepler-47-like system, the bottom row to a Kepler-413-like system.

In Fig. 4.13, the planets before and after they enter the 1:1 resonance are shown

within the disc. Even before the planets are in resonance, the disc damps their orbit to align to the argument of periastron of the disc. After they enter 1:1 resonance, they are still well embedded in and aligned with the disc. Fig. 4.14 shows how the mean longitude and the semi-major axis between planets changes over the course of $10\,000\,T_{\mathrm{bin}}$. They are on a horseshoe orbit moving around L4 and L5, however never getting closer than 20°.

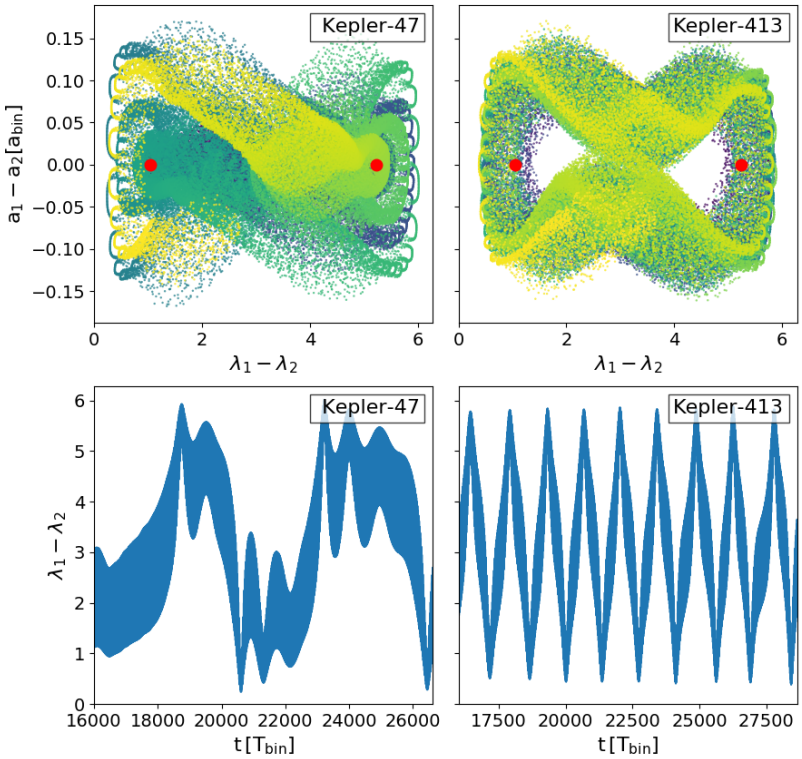

Figure 4.14: Planet dynamics of 1:1-resonant circumbinary planets embedded in the disc for a Kepler 47 like system (left) and a 413 like system (right). **Top**: Relative orbital motion of the two planets. The color advances with the time given in the lower panel from blue to yellow. **Bottom**: Time evolution of the relative mean longitude.

To analyse whether such orbits can remain stable without the damping effect of the disc, the final n-body orbits were continued with a pure n-body simulation. The orbits remained stable and even more regular as Fig. 4.15 shows. The semi-major axis and eccentricity exchange periodically between the two planets. Especially of interest is that the eccentricity of the planet ~ 0.3 does not cause a problem in this configuration and around a binary even an eccentric orbit can be stable for

1:1 resonant planet. We will give a quick outlook into the stability of 1:1 resonant planet orbits in Sec. 5.3.

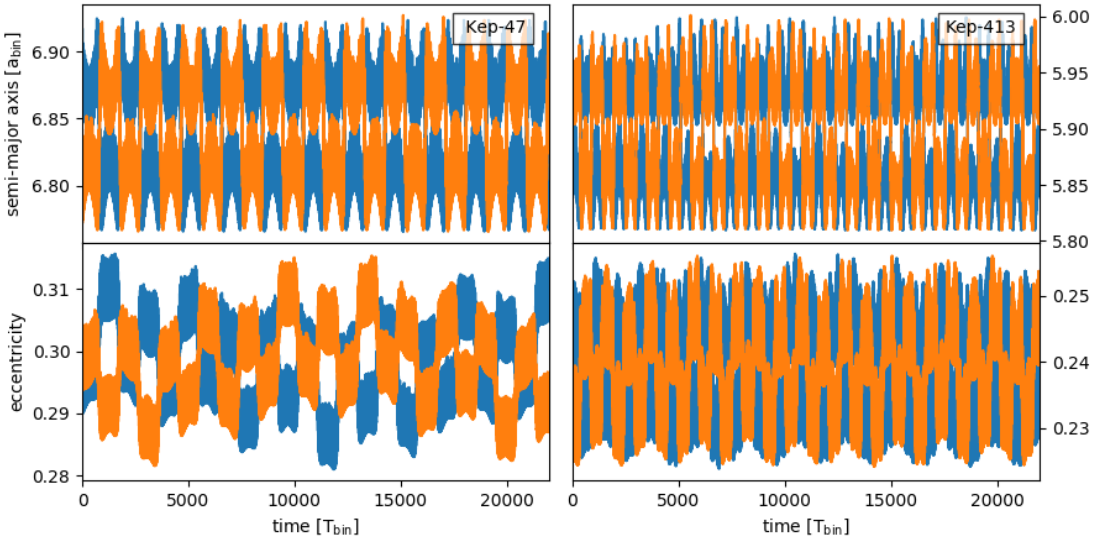

Figure 4.15: Planet dynamics of 1:1 resonant circumbinary planets without the disc for a Kepler-47-like system (left) and a 413-like system (right). **Top**: Time evolution of the orbit semi-major of both planets. **Bottom**: Time evolution of the eccentricity of both planets.

New simulations of other multi-planet configurations show recurring 1:1-resonant phases also for less eccentric disc profiles (see also Section 5.4). For accreting planets in the disc, however, the gap-opening and thereby continued migration might disrupt the 1:1 resonance. To evaluate the effect of accretion and thereby introduced slow gap-opening inside a circumbinary disc would be a question for a future study.

5 Outlook and discussion

While we have just seen how the numerical models match the observations with given simple assumptions creating specific conditions, the models need to be evaluated for various conditions. For example, ranges of disc parameters, cooling prescriptions, additional objects and the planets' orbits can change the dynamics of discs and planets. All of these are part of further studies that are ongoing. The questions, ideas and preliminary results of such investigations are explained in this chapter.

5.1 Viscosity in circumbinary discs

As already mentioned in the previous Chapter 4, the shape and size of the inner cavity depends on the viscosity. However, the evolution time scale for low viscosity environments can become very long, in a locally isothermal setting as $> 30\,000\,T_{\rm bin}$ and in the radiative models in Kley et al. (2019) even up to $\sim 200\,000\,T_{\rm bin}$. This means clearly a very long computation time for many methods and software of hydrodynamical simulations. The GPU capability enables us to run these models for a fairly low computational cost. As a comparison table between observations and simulations, we ran over 100 locally-isothermal 2D simulations with varying viscous alpha or aspect ratios and different binary eccentricity. The changes due to different binary mass ratio $q_{\rm bin}$ plays a minor role as shown in Thun & Kley (2018). Therefore we chose one fixed mass ratio of one of the Kepler binary systems at random. The parameters are displayed in Table 5.1. Initially all simulations ran with a resolution of $N_R\ times N_\phi = 684 \times 584$, but for smaller $H/R \leq 0.05$ it was increased to $N_R\ times N_\phi = 684 \times 1168$ for a radially logarithmic domain between $1 - 40\,a_{\rm bin}$. The disc has an outer damping zone with a width of 10% of the domain size, relaxing to the initial profile. The initial density profile follows Eq. (3.6) with a cutoff of $2.5\,a_{\rm bin}$ and an exponent of -1.5. All simulations where run for at least $> 100/\alpha^{1/2} T_{\rm bin}$ and until they converged.
We interpolated the data between the set of simulations and thereby created a heat map of cavity size and eccentricity for the $\alpha - e_{\rm bin}$ and $H/R - e_{\rm bin}$ parameter space as

	$q = M_2/M_1$	α	H/R	$M_{\rm disc}$	$e_{\rm bin}$
standard	0.26	10^{-3}	0.05	$1\%\, M_{\rm bin}$	
range		$10^{-1} - 10^{-4}$	$0.03 - 0.10$		$0.0 - 0.4$

Table 5.1: The simulation parameters. The "standard" is used while the other is varied and is not stated otherwise. The range is the explored parameter space. The binary eccentricity $e_{\rm bin}$ was varied in combination with viscous α and aspect ratio H/R.

shown in Figs. 5.1 & 5.2. Both show one horizontal and one vertical turning point, with the cavity size and eccentricity being maximal at an $\alpha \approx 10^{-2.5}$ or $H/R \approx 0.06$ and the cavity size and eccentricity being minimal at $e_{\rm bin} \approx 0.15$, which is the same bifurcation point already established in Thun et al. (2017) and Thun & Kley (2018). The cavity becomes the smallest for very high viscosities $\alpha \geq 0.1$, when material drifts into the cavity rapidly giving the excitation through the binary too little time to create the converged eccentric profiles stronger than the incoming streams. In such systems, humps and asymmetric features as described in Calcino et al. (2019) can occur even after longer evolution. However, for protoplanetary, circumbinary discs, the profile will converge without moving features with the highest density always in the apocenter traffic jam. This highest density is time-variable as the disc-binary orbit alignment creates an oscillation in cavity size and eccentricity over every precession period between disc and binary orbit.
The heat maps of cavity shapes are created to allow to quickly infer disc properties from observed circumbinary discs, and thereby better understand the environment of young stars.

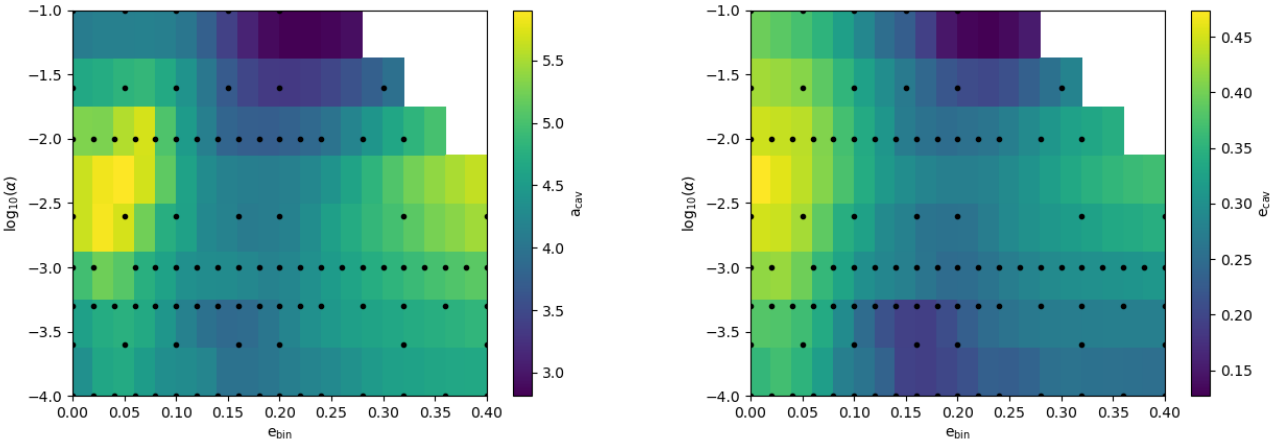

(a) (b)

Figure 5.1: Map of the cavity shape for H/R=0.5 when varying e_{bin} and viscous α (axis). The colors denote semi-major axis (left) and eccentricity (right) of the CBD cavity. The black dots mark simulations and the inbetween values are interpolated.

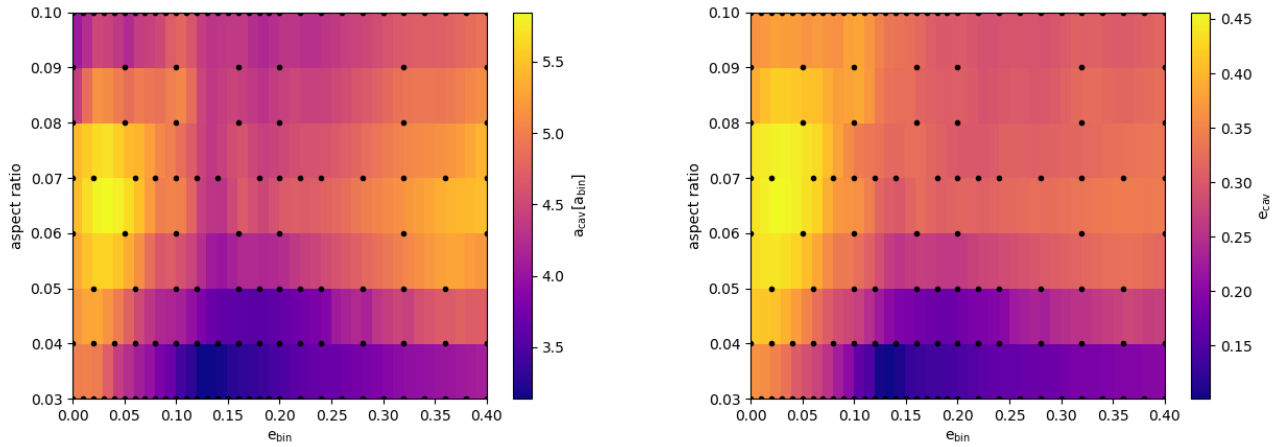

(a) (b)

Figure 5.2: Map of the cavity shape for $\alpha = 10^{-3}$ when varying e_{bin} and H/R (axis). The colors denote semi-major axis (left) and eccentricity (right) of the CBD cavity. The black dots mark simulations and inbetween values are interpolated.

5.2 Influence of the cooling prescription

Kley et al. (2019) used a radiative cooling prescription using the Rosseland mean opacity as also described in Sec. 2.1.2, and the results were comparable to the locally isothermal model in Thun & Kley (2018), even though the cooling times for the chosen close binary Kepler systems differ significantly between an instant locally isothermal cooling and a low $\propto \alpha^{-1}$ radiative cooling. To test the structure of the disc for both cases and also all in-between cooling times we have, in a collaboration with Alexandros Ziampras and Prakruti Sudarshan, set up locally isothermal, radiative and β-cooling models for $\beta = [10^{-2}, 1, 10^2]$. We chose a setup that makes the disc comparable to most of the Kepler systems with close binaries. The setup is given in Table 5.2.

For the simulations we chose a resolution of $N_R \times N_\phi = 684 \times 1168$ with a radially logarithmic domain from $1 - 40\,a_{\rm bin}$ with a 10% domain width outer dampening zone relaxing to the initial profile, as before. The initial gas profile follows a radial power-law with $p = 0.5$ exponent and an inner cut-off at $2.5\,a_{\rm bin}$ (see Sec. 3.2).

As we have seen in the previous Sec. 5.1, the binary eccentricity significantly influences the shape of the inner cavity. Therefore we chose here a set of 3 different binary eccentricities $e_{\rm bin}$, probing both sides and the minimum of the bifurcation curve discussed in Sec. 5.1 or Thun et al. (2017) and Thun & Kley (2018).

The density profile of all simulations is displayed in Fig. 5.3. The cavity is tracked with the green ellipse. For locally isothermal models and radiatively cooled models the cavities are comparable, but the structure of the inner disc and the width of the peak density changes. The cavity becomes small and circular for all models with $\beta = 1$, this hints at an effect similar to the analysis Miranda & Rafikov (2020) did for the structure of planet gaps for differing cooling parameters. Low-β models present an excellent match to the locally isothermal models as expected. The $\beta = 100$ model for $e_{\rm bin} = 0$ deviates from the radiatively cooled model, due to the inaccurate cooling at the inner edge of the disc. Here the aspect ratio overshoots up to $\sim 20\%$ due to the parametrized cooling, that is not able to accurately capture the quick cooling time inside the optically thin cavity. For the radiative model a change of the β-value between disc and low-density region can be understood with

$M_{\rm bin}$	M_2/M_1	$a_{\rm bin}$	$e_{\rm bin}$	$h_{\rm ini}$	α
$1\,M_{\rm sun}$	0.5	0.2 au	[0.0,0.15,0.3]	5%	10^{-3}

Table 5.2: System setup for the different cooling models.

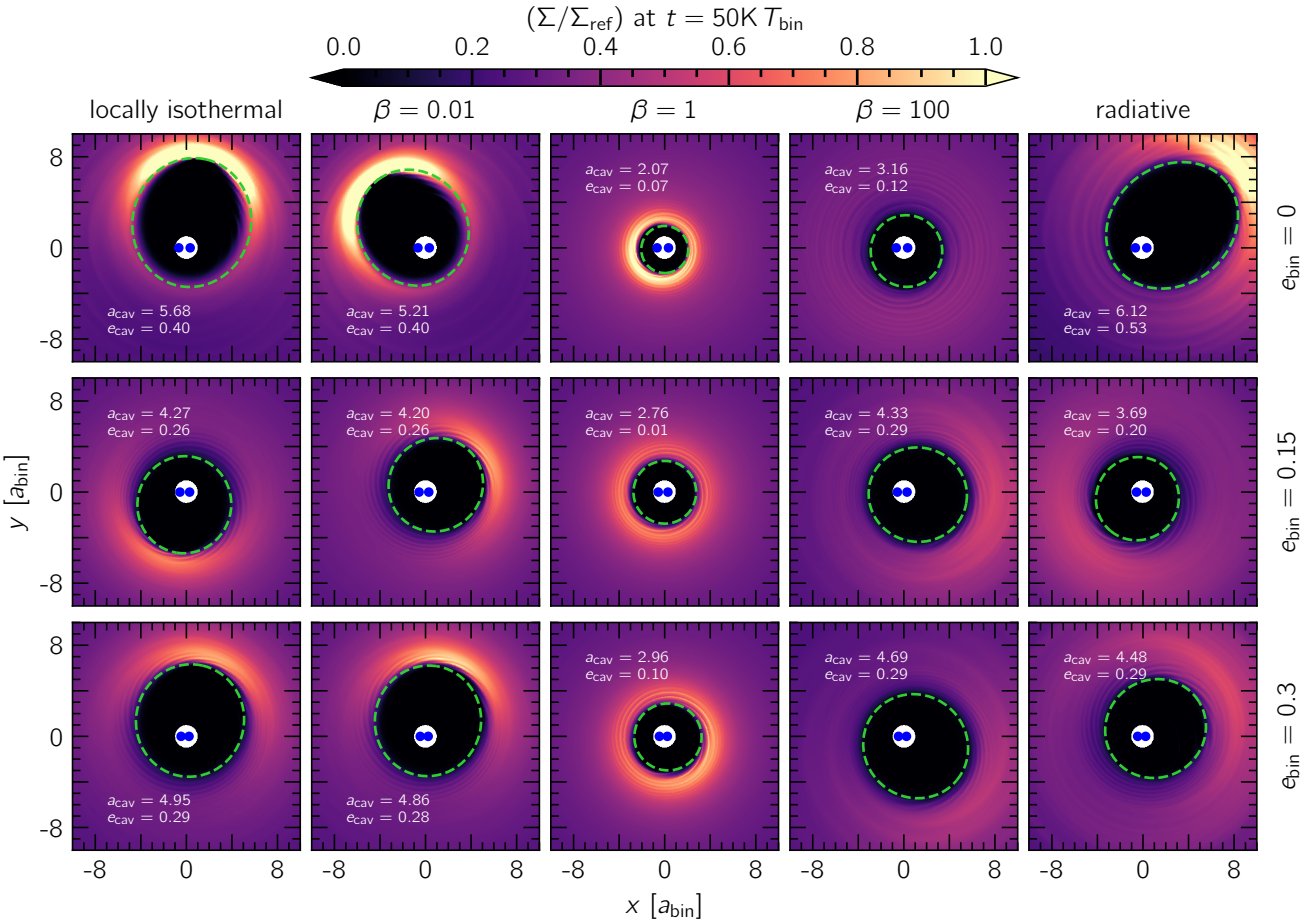

Figure 5.3: Surface density heatmaps of the disc models in Table 5.2 (top to bottom) for different cooling time scales from short to long (left to right) including locally isothermal (left) and radiative (right) models.

Fig. 5.4. Here the effective β calculated from Eq. (2.20) is mapped. While the disc is heated viscously, this is not true for the cavity, and therefore in the radiative model, the effective β significantly differs between disc and cavity.

In Fig. 5.5 the time evolution of the inner cavity is shown. For the $\beta = 1$ case the profile stabilizes extremely quickly, while for the $\beta = 100$ and radiative models the convergence takes longest, and might not even be complete for $e_{\mathrm{bin}} = 0$ after $10^6\,T_{\mathrm{bin}}$. In the radiative case the evolving profile stabilizes to slightly smaller H/R like in Kley et al. (2019), therefore the semi-major axis can decrease and the final shape can also be smaller. This happens as the radiative model is not adjusted to the initially prescribed pressure scale height but dynamically changes

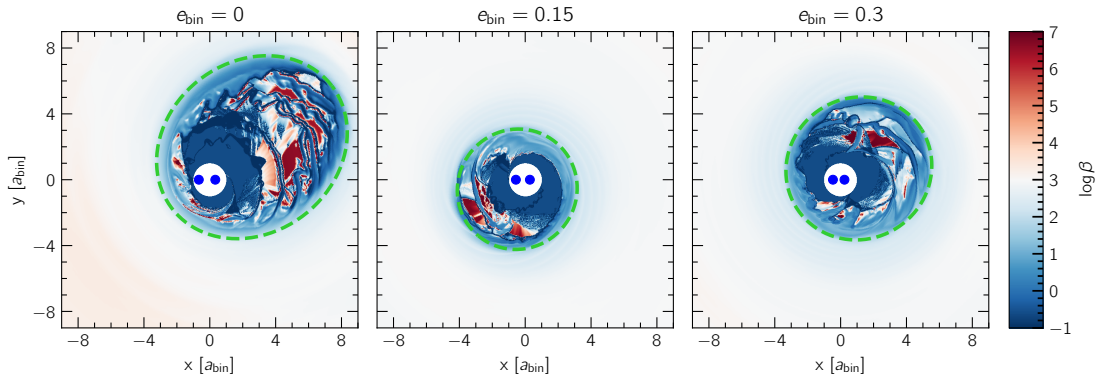

Figure 5.4: The 2D structure of the effective cooling time scale β in the radiatively cooled discs for $e_{\rm bin} = [0, 0.15, 0.3]$ (left to right) at time $50\,000\,T_{\rm bin}$.

also depending on the overall mass in the disc. The oscillations in the curves are a feature of the disc precession, causing varying alignment between binary orbit and disc argument of periastron.

For all different binary eccentricities the special case of small circular cavity appears for a $\beta = 1$. As this is only the result of a few simulations, it is not yet clear that this special behaviour is centred around $\beta = 1$. So for $e_{\rm bin} = 0.15$ we added some additional simulations at $\beta = [0.1, 10]$ and, additionally, we ran a model in which we changed the value of β over $40\,000\,T_{\rm bin}$ smoothly from 100 to 0.01. The change of the cavity for these changing betas is displayed in Fig. 5.6. The Figure shows that indeed $\beta = 1$ is the minimum case. For the higher β-values, the curve lags behind the individual simulations because the disc adjusts too slowly to the long but reduced cooling time. For low values the dynamic model and individual runs match well. This re-enforces the idea that the circumbinary disc might be a special case of the β-influence on the gap structure studied in Miranda & Rafikov (2020).

The main effect of cooling is the width and location of the density peak. The findings suggest caution with the use of parametrized cooling models for circumbinary discs.

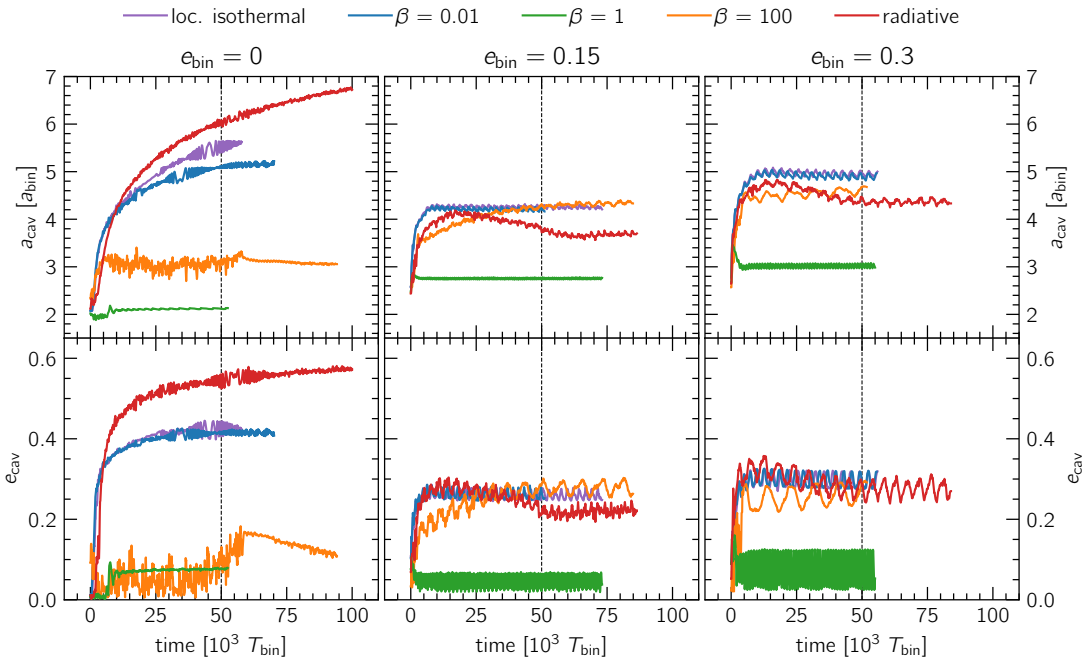

Figure 5.5: The time evolution of the semi-major axis (top) and eccentricity (bottom) of the cavities of the models displayed in Fig. 5.4. The colors denote the cooling model or time scale and $e_{\rm bin}$ is rising from left to right.

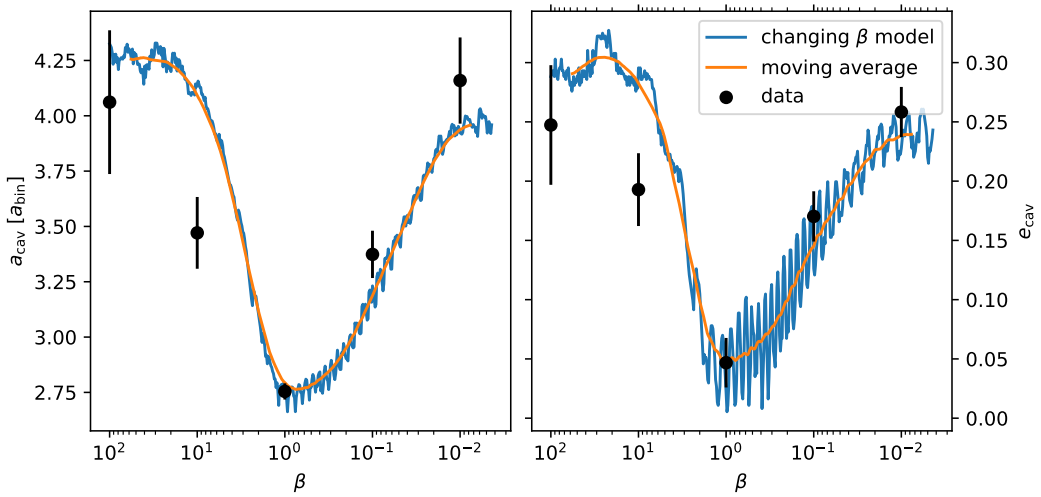

Figure 5.6: The shape of the cavity for different parametrized cooling time scales β for $e_{bin} = 0.15$. The black dots mark the final averaged values of semi-major axis (left) and eccentricity (right), and the blue curve represents a model that changes over $40\,000\,T_{bin}$ with a rolling average over $5000\,T_{bin}$ displayed as the orange curve.

5.3 The stability of 1:1 resonant planets in binaries

In Sec. 4.4 we demonstrated how a 1:1 resonant planet configuration can occur around a binary. This opens the question which orbits allow a stable 1:1 resonance. To answer it, in a collaboration with Stefan Adelbert and Willy Kley, the stability of 1:1 resonant initialized planets was probed using the REBOUND code by Rein & Spiegel (2015) for a time of $10^5\,T_{bin}$. Kepler-413 was used as the example system with the parameters in Table 1.1. This is one of almost circular binary systems with $e_{bin} = 0.04$. For the planet's eccentricity the models investigated values from 0 to 0.9 with a step size of 0.1 and for the semi-major axis of the planet the step size was $\Delta a_p = 0.025\,a_{bin}$ with a shifting range adjusted to the stability limits for the given eccentricity. The planets are initialized 180° apart in peri- and apocenter. The relation to the angle between planet and binary orbit was probed and the most unstable configuration of an argument of periastron difference of $\pi/2$ is therefore used in the models.

When comparing a one-planet test case in this setup with the work of Quarles

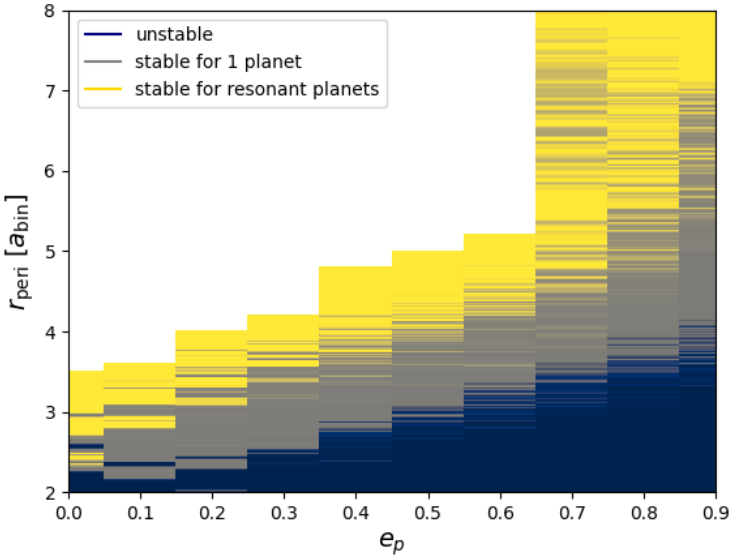

Figure 5.7: The orbit stability of single planets around Kepler-413-like binary stars (yellow and grey area) and for 1:1 resonant planets (yellow only) for a time integration of $10^5\,T_{\mathrm{bin}}$ depending on the planet's eccentricity and the orbits pericentre.

et al. (2018) the limits of stability agree well. For the two planet case the stability limit retracts outwards, but still there are close 1:1 resonant stable orbits around binaries. As a simple model the stability of the orbit follows a linear relation, such that the first stable pericentre can be fitted with $r_{\mathrm{peri}} = (3.365\,e_p + 2.386)\,a_{\mathrm{bin}}$. So in fact, many stable 1:1 resonant orbits exist around binary stars, even up to a few binary separations.

5.4 Further possible improvements

As the real world is complex, so can be numerical models. Many more effects, considerations and enhancements are possible, as the protoplanetary environment is an interplay of not just dynamical, hydrodynamical and thermal effects of gas but also of dust and electromagnetic interaction, chemistry and radiation on various energy levels, embedded in a star-forming structured cloud that is part of its local galactic surroundings, all of which will impose additional effects on various scales. And as the binary system by nature can occur for very different mass scales and

environments between binary asteroids and merging super-massive black holes, a seemingly infinite list of improvements could be considered. Here, we will describe ideas of improvements that have already been studied or that we started to investigate, including general circumbinary systems with multiple planets, the effect of stellar irradiation on the disc, 3–dimensional models, improving initial conditions closer to the convergent disc shape, using the advantages of different numerical methods by comparing to smoothed particle hydrodynamics, and including dust in the simulations.

5.4.1 Multiplanet systems

With the work by Orosz et al. (2019) a circumbinary multi-planet system in Kepler-47 has been observed. As we have already seen in Secs. 4.4 & 5.3 multiple planets can find stable orbits around a circumbinary disc. However, the case of multiple planets around binaries has not been given much attention in hydrodynamics simulations. For an n-body configuration, Chen et al. (2022) very recently investigated the stability of circumbinary multi-planet systems for a wide orbit parameter space. In light of the already existing models we presented in Penzlin et al. (2021) (see Sec. 4.3) it is simple to include more bodies to the model using the N-body module.

As an easy starting point the observation of Kepler-38b (Orosz et al. 2012) suggested that the planet is one of the heaviest close circumbinary planets with $M_\mathrm{p} \sim 0.3\,M_\mathrm{Jup}$ and will have an easy migration path. Preliminary findings for a Kepler-38-like system with an additional planet of the same, doubled or halved the mass show, that stable orbits for multiple planets are well possible and both planets can reach stable parking orbits. This is shown in the time evolution in Fig. 5.8. But trailing heavy planets can cause scattering of the inner lighter planet, that migrates slower and parks slightly further out.

A second, more interesting case is looking at Kepler-35, with a planet mass of only $\sim 0.12\,M_\mathrm{Jup}$ that will have much weaker gap-opening capabilities and migrate more slowly in the disc. The orbit evolution is shown in Fig. 5.9. In this case, if we have sequel migration of planets, they will get close in the inner disc, jump in and out of 1:1 resonances, swap orbits and are eventually all unstable. This might just be the case due to the small initial orbital separation between them and highly influenced by the masses of the planets that are in this case all similar to the observed planet sizes. But as a preliminary result there are two facts that should be further investigated. First the resonant behaviour we have previously

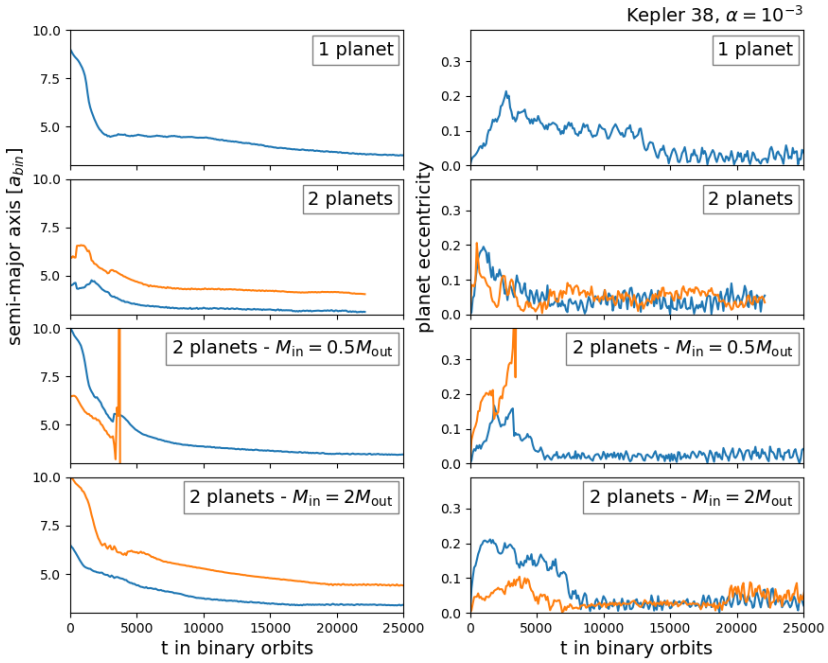

Figure 5.8: Time evolution of planets orbits inside the disc seen in 4.10 for the Kepler 38 like system. Semi-major axis are shown left and eccentricities right. The rows include the cases from top to bottom of 1 planet with $0.3\,M_{\rm Jup}$, two planets of this mass, a planet of half the mass further in and a second with the full mass, a planet with half the mass further out and a full mass planet closer to the binary.

only seen in the presence of eccentric discs occurs here for short phases in a fairly circular disc (compare Fig. 4.13) and secondly the question of what should be a planet configuration to reach a binary system of multiple planets if at least equal-mass planets lead to scattering. Further investigation should follow and complete the picture of how the Kepler-47 system could have formed.

5.4.2 Irradiation

For the models in Kley et al. (2019) and in Sec. 5.2 we have considered the viscous heating from the disc to be the main contributor to the temperature balance of the system. While this is a fair approximation for the highly dynamical close–in system it would not be true for the best physical model of a wide circumbinary disc, where

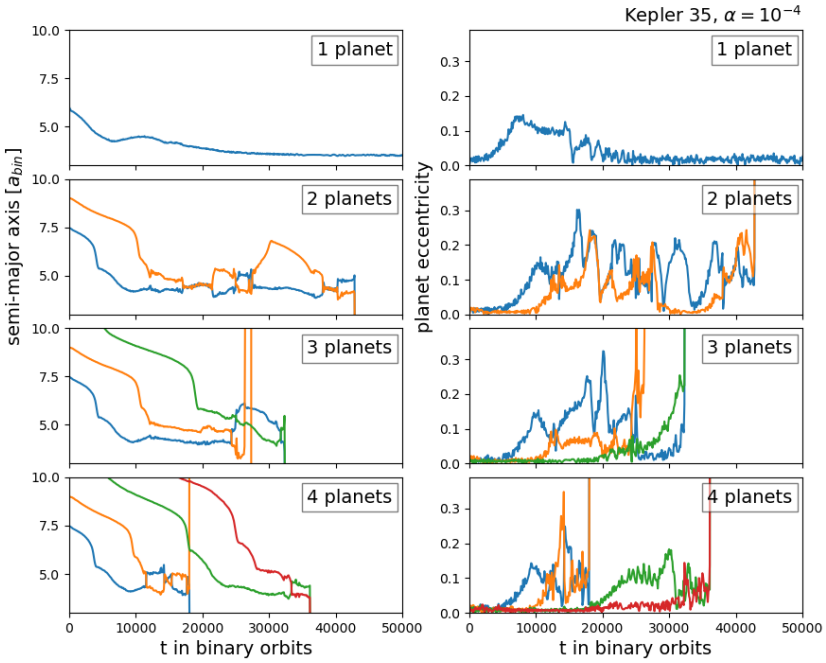

Figure 5.9: Time evolution of planets orbits inside the disc seen in 4.10 for the Kepler-35-like system. Semi-major axes are shown left and eccentricities right. The rows include the cases from top to bottom of one planet, two planets, three planets and four planets with 0.12 M_{Jup}.

the gas becomes thinner and less dynamic and the stellar irradiation becomes a very relevant term. We did not include the irradiation term (as described in Chiang & Goldreich 1997) in the models yet, as it would also require a dynamic motion of the two moving radiation sources in the best model scenario. For very wide systems like GG Tau A the scalable and easy locally isothermal model gives fair approximations of the known temperature structure. However, in future research the additional effect of this heating term are worth investigating.

5.4.3 3D-models

Pierens et al. (2020, 2021) presented models in 3 dimensions. The general structure of the circumbinary disc in 3D showed the growth in eccentricity seen in the 2D simulations, as well as spiral features, streamers and the overdensity at the apocenter. The drawback of performing hydrodynamical 3D simulations, however,

is the computational cost. The simulations by Pierens et al. (2020, 2021) only ran for several thousands of orbits and the evolution of the eccentricity did not appear to be complete after this already long and computationally costly time. Therefore to create a setup that allows running 3D simulations of converged disc shapes is still a task to be solved in the future. One possible way to tackle the problem would be to use the 2D final state of the disc as an initial condition, expanded to 3D via the hydrostatic equilibrium equation. However, even with such a shortcut the convergence of the 3D disc still needs to be checked by a significant time evolution.

5.4.4 Initial conditions

As just discussed, especially for 3D simulations, long simulation times are not feasible so far. One of the difficulties in creating a circumbinary disc model is the long time needed to reach the converged eccentric disc profile usually from axisymmetric conditions. To reduce computation time for the physical model state a better prescription of initial conditions would be helpful. For such a better guess on the initial shape, the disc shape maps in Sec. 5.1 can be useful but only combined with a sensible analytical description of the disc profile. One approach to derive an initial profile representing a disc comparable to the evolved circumbinary disc is shown in Fig. 5.10 on the left, compared to a simulation of a converged profile on the right. To construct this profile the focal point of all the orbits lays in the center of mass and the second focal point c given by the cavity shape, such that $c^2 = a_{\mathrm{cav}} - b_{\mathrm{cav}} = a(x,y)^2 - b(x,y)^2$. In combination with the equation for an ellipse $(x/a)^2 + (y/b)^2 = 1$, the equation can be solved for the semi–major and semi–minor axes $a(x,y)$ and $b(x,y)$ and thereby the eccentricity at every point in the disc. Now applying the inner cut-off radius in Eq. (3.6) to the semi-major axis instead of the radius produces an elliptic gap profile. Now the last correction is to add the traffic jam at the apocentre of the disc by rescaling the density with the inverse normalized elliptic Kepler velocity $\Sigma_{\mathrm{jammed}} = \Sigma_{\mathrm{elliptic}}[r(2/r - 1/a)]^{-1}$. While this approximation and analytical description is already good to compare observed disc profiles to the parameter maps in Sec. 5.1, it has to be further tested to evaluate the possible speed–up for numerical simulations gained from this prescription.

The issue of well-defined initial conditions is very relevant for circumbinary disc calculations and needs more investigation.

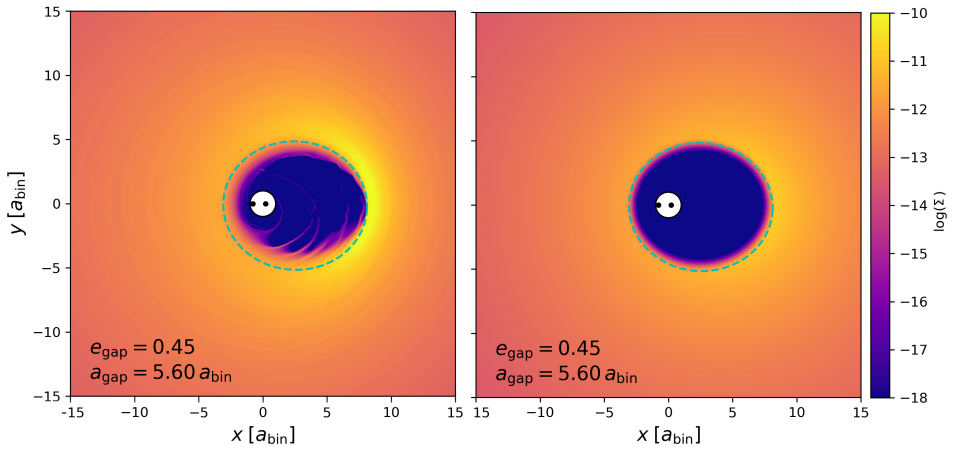

Figure 5.10: 2D surface density profile of a circumbinary disc simulation (left) compared to an artificial profile for the same cavity parameters (right).

5.4.5 Comparing to SPH

Recently many smoothed particle hydrodynamics (SPH) simulations have been applied to understand the structure of circumbinary discs for example Hirsh et al. (2020) or Ragusa et al. (2020). The SPH method of pressurized mass distribution associated with mass particles is quite different from the finite volume method in a fixed grid and presents advantages and drawbacks. While the disc will be highly resolved in this method, the low density gap region and especially the streams through this region are more difficult to resolve with the particle ansatz, as the assumed width of the particles increases at low densities. At the same time understanding accretion is much easier with this approach which we have used in the study summarized in Sec. 4.2. For all the differences that the numerical methods have, a comprehensive comparison study is needed and circumbinary disc pose an interesting test case here as they are rich in structure and features at differing density levels while not requiring too many assumptions of additional physics differently described for both methods. So far the results of SPH and finite volume methods appear qualitatively comparable.

5.4.6 Dust

One more aspect relevant for direct comparison between simulations and observations is the dynamic evolution of dust inside the gas disc. In the recent models by Pierens et al. (2021) dust has been included and they found dust mixing well with

the turbulent gas in the inner region of the disc, while the dust in the outer less eccentric parts of the disc settled back to the midplane. Additionally, the density peak of the inner disc presented a dust barrier such that the dust beyond the inner disc might be accumulated to levels allowing for streaming instabilities depending on the dust content and other disc parameters. One issue Pierens et al. (2021) as well as previous attempts to include dust in simulations (Calcino et al. 2019) face is to reach the time of a converged system with their models. However, including dust in long-term simulations is a very important step to compare simulations and observations with more certainty.

6 Summary

While the problem of circumbinary discs and planets is complex it provides us with additional constraints and challenges in the search for the explanation to the observations. This can help us understand more about the circumstellar environment and planet formation in general. In this work we have seen how we get from observing the circumbinary system, to understanding the dynamics that cause these observations. To reach this goal hydrodynamics simulations are a powerful tool to create realistic models of the physical universe, but only when we include the most relevant effects and carefully evolve to equilibrium states that are no longer affected by initial estimations.

The whole system for the circumbinary disc, stars and planets is interacting and exchanging angular momentum, while shaping each other's orbits and dynamics. For this exchange the viscosity of the disc is one critical property, as it can change not only the accretion on the binary, but also the shape of the disc and the capability of planets to open gaps that affect their migration. The observation of the GG Tau A circumbinary disc, as well as the observed circumbinary planets point to an α viscosity as low as $\alpha = 10^{-3} - 10^{-4}$. This is an independent hint on the level of turbulent viscosity present in PPDs.

Not just the viscosity but also the temperature and thereby pressure in the disc affects the disc dynamics. Varying cooling time scales can change the shape of the inner circumbinary disc, while variations in a locally isothermal temperature changes the shape and size of the cavity. Understanding the full range of temperature-induced disc structures, other properties like the binary separation and the viscosity can be constrained from models of observations.

Following the descriptions given in this thesis we utilise physical models and numerical methods to generate protoplanetary systems around binary objects that explain not just the structure but also the story of the circumbinary disc and planets we observe.

Acknowledgements

In memory of my "Doktorvater" Willy Kley. I know Willy wanted to see this thesis written (given the length, however, likely not to have to read it) so it is all for him. When I first met him I had failed to get any PhD position I had hoped for. He lured me with the vague promise that he might have some money for maybe 2 years and a project I had no idea about to Tübingen, to the Morgenstelle to be exact, and I honestly never regretted it. Somehow he got the idea that I would be a good PhD candidate and that was the best thing that could have happened to me. There are many good reasons to do science and computational astrophysics in particular, but his excitement for the subject still ranks pretty high on that list. No matter the issue, you could count on him having a question and an idea and usually an intriguing one that just makes you want to work through the next night and week to see what happens. I am grateful for all the time and tea (formerly known as coffee&tea) we shared talking about science, planets, the world, life and all the things that make them interesting. He gave us so many lessons not just on astrophysics but on life, that I will continue learning from him for years to come. He filled our institute with a warmth, that made it one of the most appealing places to me even in the winter break with the central heating gone. I could and should go on about his scientific accomplishments and shaping of the field of planet formation, but then I had to write a few extra theses. He was the brightest and warmest star in our midst, giving us energy and joy and, in the end, with his life creating countless more sparkling lights scattered all around the globe, remembering all the things he gave us in his too short time. However, there is just so much to say that, at least in this section of the dissertation, I definitely fail to put the meaning he has to us into words. If nothing else in this thesis, remember Willy Kley!

As part of the Computational Physics Tübingen (CPT), I have many people to thank for completing this work. Among those, Alexandros Ziampras needs to be mentioned for his literally tireless effort to not just read this whole ordeal in advance but for all the time invested in explaining things to me (and others) I should have know to begin with. Any chocolate will taste better shared with an office mate like him. Cursing binac and scratching our heads in front of the blackboard, those were just wonderful times. I feel honoured to work on projects with students like Prakruti Sudarshan and Stefan Adelbert. Little work and much gain is just what you want, while you try to get through your own paper revision at

the same time. I thank the office of Thomas Rometsch, Lucas Jordan and Tobias Moldenhauer for the always open door, countless scientific discussions and willingness to join a little break when I needed one, as well as Christoph Burger and Oliver Wandel for brightening any day with bit of dark humour and a contagious smile. I am especially grateful to my predecessor Daniel Thun, who left me with an extraordinarily well-working code that allowed me to just play with the physics with very little effort and I am glad to know that the research into binaries will be continued by my successor Hugo Audiffren. Everyone in CPT contributed to make our group feel like a slightly chaotic but caring family. In that especially our adored secretary Heike Fricke was one source of organization, supporting us with any annoying bureaucratic request I still do not have the faintest clue how to handle without her. But no computer, no lecture, and no project would run without Christoph Schäfer. As it is with admins they often only get noticed when a problem occurs, working silently and tirelessly in the background. And there were way too few problems to get him the recognition he would deserve. But he does not just quietly keep our machines running, but also the soul of our group alive. How much he has invested in the recent months to give everyone in our group a way forward and keep us together is inconceivable. And I am unbelievably lucky and glad to be part of the CPT group.
Also I want to thank both of my supervisors. Firstly, Kees Dullemond who endured possibly too many of my talks over the last three years, but always would still have a good question I had not thought about before. It was always good to know I could count on his support, if I needed it. Secondly Klaus Werner, though we only really talked in the last few months, I will forever be grateful for him being there to help.
Working in this field of research fills me with joy and I want to thank my project collaborators and fellow researchers for sharing it with me, Carolin Kimmig, Miriam Keppler, Gesa Bertrang, Paola Pinilla, Richard Nelson and countless others.
Last but not least, I thank my friends and family for supporting me, Thomas for being at my side and even coming to Tübingen, my father for finding all my missing "s", my brothers for letting me be the first for once and my muother, as well as all the people that shared a part of my way in sorrow and laughter over the years, helping me grow.

7 Publications

Penzlin et al. (2019)

Title: 1:1 orbital resonance of circumbinary planets
Authors: Anna B. T. Penzlin, Sareh Ataiee, Wilhelm Kley
Journal: Astronomy & Astrophyiscs, 630, L1
Status: published
DOI: 10.1051/0004-6361/201936478
Contribution: Discovering the 1:1 stable resonance, creating and running all hydrodynamics simulations, analysing the data and plotting all figures, writing the majority of all sections.

Keppler et al. (2020)

Title: Gap, shadows, spirals, and streamers: SPHERE observations of binary-disk interactions in GG Tauri A
Authors: M. Keppler, A. Penzlin, M. Benisty, R. van Boekel, T. Henning, R. G. van Holstein, W. Kley, A. Garufi, C. Ginski, W. Brandner, G. H.-M. Bertrang, A. Boccaletti, J. de Boer, M. Bonavita, S. Brown Sevilla, G. Chauvin, C. Dominik, M. Janson, M. Langlois, G. Lodato, A.-L. Maire, F. Ménard, E. Pantin, C. Pinte, 3, T. Stolker, J. Szulágyi, P. Thebault, M. Villenave3, A. Zurlo, P. Rabou, P. Feautrier, M. Feldt, F. Madec, F. Wildi
Journal: Astronomy & Astrophyiscs, 639, A62
Status: published
DOI: 10.1051/0004-6361/202038032
Contribution: Introducing the idea to prove that no larger binary separation is needed to explain the disc cavity, creating and executing all hydrodynamics models, providing 3D data for artificial observations, plotting the evolution of hydrodynamics models, writing Sec. 5 and App. B and part of Sec. 6, proof-reading and correcting all sections, discussing and advising on the dynamics of circumbinary discs.

Penzlin et al. (2021)

Title: Parking planets in circumbinary discs
Authors: Anna B. T. Penzlin, Wilhelm Kley, Richard P. Nelson
Journal: Astronomy & Astrophyiscs, 645, A68
Status: published
DOI: 10.1051/0004-6361/202039319
Contribution: Initialising the investigation with various disc parameters to alter migration and creating the parameter sets and setups, creating and running all hydrodynamics simulations, analysing the data and plotting all figures, writing the majority of all sections.

Penzlin et al. (accepted)

Title: Binary orbital evolution driven by a circumbinary disc
Authors: Anna B. T. Penzlin, Wilhelm Kley, Hugo Audiffren, Christoph M. Schäfer
Journal: Astronomy & Astrophyiscs
Status: accepted
DOI: -
Contribution: Creating and running the PLUTO hydrodynamics simulations, implementing models to dynamically evaluate torque and advected angular momentum, analysing the data and plotting Fig. 1, 3, 4, 7, 8, 10, 12, 16, 17, writing the majority of all sections, except for the Appendix.

A&A 630, L1 (2019)
https://doi.org/10.1051/0004-6361/201936478
© ESO 2019

Astronomy & Astrophysics

LETTER TO THE EDITOR

1:1 orbital resonance of circumbinary planets

Anna B. T. Penzlin, Sareh Ataiee, and Wilhelm Kley

Institut für Astronomie und Astrophysik, Universität Tübingen, Auf der Morgenstelle 10, 72076 Tübingen, Germany
e-mail: anna.penzlin@uni-tuebingen.de, sareh.ataiee@uni-tuebingen.de, wilhelm.kley@uni-tuebingen.de

Received 7 August 2019 / Accepted 22 August 2019

ABSTRACT

The recent detection of the third planet in Kepler-47 has shown that binary stars can host several planets in circumbinary orbits. To understand the evolution of these systems we have performed two-dimensional hydrodynamic simulations of the circumbinary disc with two embedded planets for several Kepler systems. In two cases, Kepler-47 and -413, the planets are captured in a 1:1 mean-motion resonance at the planet "parking position" near the inner edge of the disc. The orbits are fully aligned and have mean eccentricities of about 0.25 to 0.30; the planets are entangled in a horseshoe-type motion. Subsequent n-body simulations without the disc show that the configurations are stable. Our results point to the existence of a new class of stable resonant orbits around binary stars. It remains to be seen if such orbits exist in reality.

Key words. hydrodynamics – planet-disk interactions – binaries: general – planets and satellites: formation

1. Introduction

To date, about a dozen planets orbiting around binary star systems have been detected by the Kepler space mission. All of them are single-planet systems, except Kepler-47 whose third planet was recently detected (Orosz et al. 2019), demonstrating that circumbinary systems can host multiple planets. This raises the question about their formation, evolution, and stability.

Following previous approaches we assume that the planets formed further away from the central binary in more quiet disc regions and then migrated inwards where they remained, "parked" at the cavity edge. Using hydrodynamical disc simulations, we modelled the migration of multiple planets in six of the known Kepler circumbinary systems and discovered stable coorbital resonant configurations in Kepler-47 and -413.

Thus far, 1:1 resonances have not yet been observed in exoplanet systems, but only for minor solar system objects. Well known are the population of Trojans of Jupiter and Saturn, and the moons Janus and Epimetheus that orbit Saturn, which have similar mass and are on mutual horseshoe orbits (Yoder et al. 1983). For the latter, Rodríguez et al. (2019) have recently presented a formation mechanism involving migration in a circumplanetary disc. Relating to exoplanets, the formation of 1:1 resonance objects can proceed for example in situ (Beaugé et al. 2007) or through a convergent migration process (Cresswell & Nelson 2006). In the first scenario the planets begin on tadpole orbits, in the second case they start out with a horseshoe motion that later turns into a tadpole as well (Cresswell & Nelson 2006).

However, continued migration of the resonant pair in a gas disc will lead to an increase in the libration amplitude, which can destabilise the system (Cresswell & Nelson 2009), in particular for more massive planets (Pierens & Raymond 2014). Stabilisation of a system can be achieved if the pair is in resonance with a third planet (Cresswell & Nelson 2009; Leleu et al. 2019a), whose presence may also assist in forming the 1:1 resonance in the first place, by providing additional perturbations. Around a binary star, planets reach a stable parking position near the disc's inner cavity, as determined by the binary and the disc parameters. In the case of a successful capture near this position one might expect long-term stability for such coorbital configurations as they do not migrate any further.

For the pure n-body case, the dynamics and stability of eccentric coplanar coorbitals around single stars has been studied for the equal planet mass case in Leleu et al. (2018). They show that for low mass planets around 10^{-5} of the stellar mass, stable horseshoe and tadpole orbits exist up to an orbital eccentricity of about 0.5. The stability of 1:1 resonances between low mass planets has been studied in the special case of an equal mass binary star on a circular orbit by Michalodimitrakis & Grigorelis (1989), who found stability only in the zero mass limit of the planets.

Here we present the disc-driven migration of two small and equal mass planets in the Kepler-47 and Kepler-413 systems. We show that in both cases stable 1:1 resonant configurations are possible. In Sect. 2 we describe our model set-up, in Sect. 3 we focus on the resulting 1:1 resonances, and in Sect. 4 we discuss out results.

2. Models

To model discs around binary stars, we performed viscous hydrodynamic simulations of thin discs in two dimensions (2D) using a modified version of the PLUTO-code (Mignone et al. 2007) that allows for computation on graphics processing units (Thun et al. 2017). We used a locally isothermal disc because the final equilibrium structure of circumbinary discs with full radiative cooling and viscous heating is similar to a locally isothermal model using the equilibrium temperature (see Kley et al. 2019). They find the disc aspect ratios, h, to be between 0.04 and 0.05, depending on the binary system and disc parameters. Here, we chose $h = 0.04$, for the viscosity parameter $\alpha = 0.001$, and a disc mass of 1% of the binary mass. The orbital parameter of the two modelled systems, Kepler-413 and -47, are listed in the upper block of Table 1.

Table 1. Parameters for Kepler-413 and -47, as used in the simulations.

	Kepler	413	47
Binary	M_A [$M_\odot$]	0.82	1.04
	M_B [$M_\odot$]	0.54	0.36
	$a_{\rm bin}$ [au]	0.10	0.08
	$e_{\rm bin}$	0.04	0.02
Cavity	$a_{\rm cav}$ [$a_{\rm bin}$]	5.18	5.24
	$e_{\rm cav}$	0.45	0.43
	$T_{\rm prec}$ [$T_{\rm bin}$]	2271	2573

Notes. Top: M_A and M_B denote the stellar masses of the binary, with semi-major axis, $a_{\rm bin}$, and eccentricity, $e_{\rm bin}$. Bottom: Mean equilibrium orbit parameters of the inner cavity of the disc without planets, as obtained by the hydrodynamical evolution. $T_{\rm prec}$ is the precession period, $a_{\rm cav}$ the cavity semi-major axis, and $e_{\rm cav}$ its eccentricity.

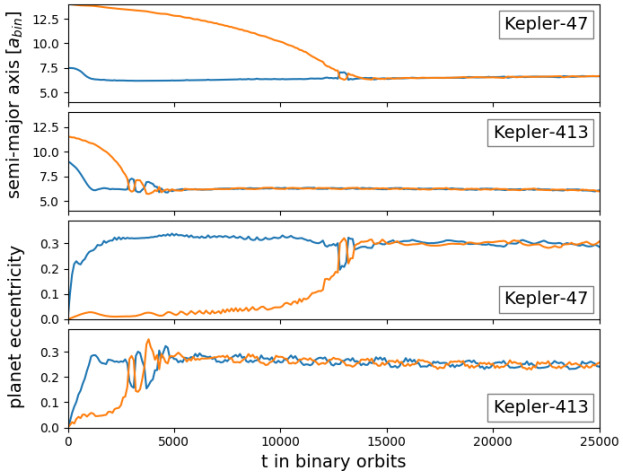

Fig. 1. Time evolution of the orbital elements of the inserted planets in the Kepler-413 and -47 systems while embedded in a disc, simulated for 20 000 $T_{\rm bin}$ prior to insertion.

The simulations presented here were performed using the same approach and method as described in Thun & Kley (2018) and Kley et al. (2019). We used cylindrical coordinates centred on the barycentre of the binary and a radially logarithmic grid with 684 × 584 cells, which stretches from 1 to 40 binary separations, $a_{\rm bin}$. This domain size and resolution has shown to be sufficient for this type of study (Thun & Kley 2018). For the n-body integrator we used a fouth-order Runge-Kutta scheme, which is of sufficient accuracy, given an average time-step size of $2 \times 10^{-3}\ T_{\rm bin}$.

First, we simulated the discs without planets to their convergent states, which are reached after about 20 000 binary orbits, $T_{\rm bin}$, and then embedded the planets. The simulations of the circumbinary discs converged to a disc with a large, eccentric, and precessing inner cavity. The mean orbital parameters of the cavities, calculated by fitting the inner disc edge (see Thun et al. 2017 for details), are given in the lower block of Table 1. The cavity size and eccentricity are determined by the binary eccentricity and mass ratio, and the disc height and viscosity. In agreement with Thun & Kley (2018), systems with low $e_{\rm bin}$ show very high cavity eccentricities. In our case we obtained $e_{\rm cav} \sim 0.45$ (see Table 1).

Then we added the planets into the disc at different initial locations on circular orbits, and let them migrate. The planets did not accrete mass. In the case of Kepler-47, we added three planets, initially at 7.5, 14, and 20 $a_{\rm bin}$. The two inner planets each have a mass of 25 $M_\oplus$, while the outer planet has 5 $M_\oplus$. The masses of the planets lie within the error bars of the newly discovered three-planet system in Kepler-47 (Orosz et al. 2019). As the additional outer planet has a much lower mass, and remains further out in the disc, it has little effect on dynamical evolution of the two inner planets, and is not discussed here any further. Even though in Kepler-413 only one planet is observed, we embedded two planets at 9 and 11.5 $a_{\rm bin}$ each with 0.21 $M_{\rm Jup}$ which is identical to the observed planet mass in Kepler-413 (Kostov et al. 2014).

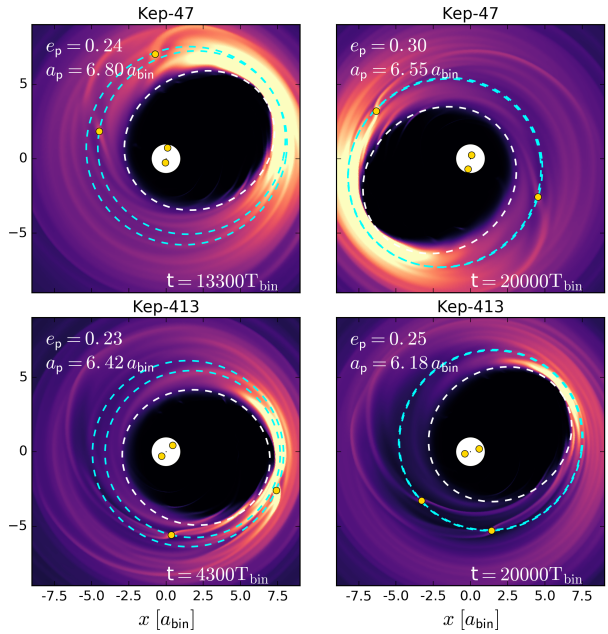

Fig. 2. Density distribution at the time right before the capture (*left*) and in the coorbital configuration (*right*) for Kepler-47 (*top*) and Kepler-413 (*bottom*). The white ellipse indicates the location of the cavity in the disc and the light blue ellipses show the orbits of the two planets, where the yellow dots mark their positions. The orbital parameters of the outer planet are quoted in the top left corner.

3. Forming a stable 1:1 resonance

In both cases the planets migrate toward the stable parking position near the inner cavity of the disc, which is first reached by the inner planet (blue curves in Fig. 1). Such low mass planets do not open a complete gap, hence their orbits align with the cavity and gain in eccentricity (Kley et al. 2019). The second planet, starting further out, takes more time to reach the cavity and acquire eccentricity. This process takes longer for Kepler-47, as lower mass planets migrate more slowly, and the outer planet is initialised further away.

As the parking position of planets around binaries is determined by the disc's cavity edge, the incoming second planet reaches the same orbit as the first. In our case this leads to capture in 1:1 orbital resonant configurations. As shown in Fig. 1, this happens after ∼5000 $T_{\rm bin}$ for Kepler-413 and ∼13 000 $T_{\rm bin}$ for Kepler-47. During the capture process the two planets show initially larger excursions in semi-major axis and eccentricity. During this process the planets do not collide with each other, as the minimum distance between them is $\sim 10^{-2}\ a_{\rm bin}$. The excursions are damped by the action of the disc, but the orbits remain eccentric. After the capture, we continued the hydrodynamical simulations for more than 10 000 $T_{\rm bin}$ and the final orbital configuration of the planets remained stable.

The shape of the orbits in relation to the disc's structure in this phase of the simulations is displayed in Fig. 2, where

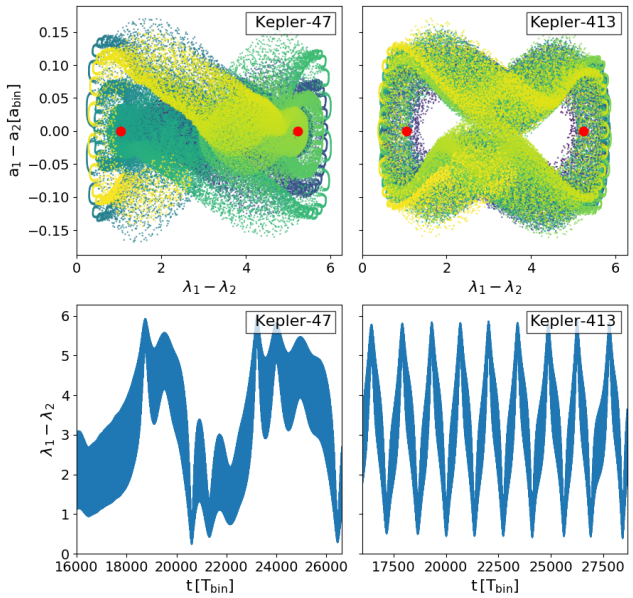

Fig. 3. Dynamical structure of the 1:1 resonances while the planets are still embedded in the disc, on the left Kepler-413 and on the right Kepler-47. *Top*: semi-major axis difference of the planets vs. the difference in mean longitude. The colour changes linearly from blue to yellow over the time span displayed in the *lower panels*. The red dots indicate the location of the Lagrange points L4 and L5 in the case of circular motion. *Bottom*: angular distance between the planets vs. time.

snapshots of the configurations are plotted at around the capture time (left panels) and in equilibrium at 20 000 T_{bin} after planet insertion (right panels). The orbits lie near the disc's inner edge, are more circular than the cavity, but still have an eccentricity of ∼0.25−0.30. They begin to align just before capture, and their precession rate and that of the cavity match exactly as soon as the planets arrive in their stable parking positions. In the subsequent evolution, the orbits remain fully aligned with a maximum libration angle of 6°. For Kepler-413 the precession rate of the cavity is lowered to 1900 T_{bin} after introducing the planets. In Kepler-47, whose planets are less massive than those of Kepler-413, the cavity almost maintains its previous precession rate of 2600 T_{bin}. The presence of these small planets does not significantly change the cavity size and eccentricity for either system.

The orbital dynamics of the two planets engaged in the 1:1 resonance while still embedded in the disc is displayed in Fig. 3. It shows that the difference in mean longitude between the two planets never drops below 20°. So they never have a close encounter and do not collide, but are rather engulfed in a periodic motion of a 1:1 resonance. In both cases the planets move on horseshoe orbits around the Lagrange points L4 and L5. In the case of Kepler-413 the motion is quite regular with a libration period of about 1330 T_{bin}. In the case of Kepler-47 the motion is more irregular and a planet moves multiple times around one Lagrange point before switching over to the other. We suspect that the reason for this irregular behaviour is the lower mass of the planets and stronger perturbed disc compared to Kepler-413. In such a condition, the disc perturbation can give higher random acceleration to the planets and send them back and forth to the horseshoe and Lagrange points.

To check the long-term stability of these orbits in the absence of the disc, we extracted the final positions and velocities of the planets and stars, and used them as the initial condition for a pure n-body simulation containing the two stars with the planets ($n = 4$). In Fig. 4, we show the evolution of semi-major axis and eccentricity over a time span 22 000 T_{bin}. In both systems, the orbits are stable and the planets remain in the 1:1 resonance. The orbits retain their previous eccentricity (with disc) and change periodically their positions upon close approach, where the planet in the inner position switches to the outer and vice versa, as is typical for horseshoe orbits.

In the pure n-body case, the orbits are much more regular than in the case with the disc, and in both systems the planets are on regular, smooth horseshoe orbits (see Fig. 5). Without the disc, the radial excursions of the planets are similar to the case with the disc present. The libration period is 1920 T_{bin} for Kepler-47 and 1055 T_{bin} for Kepler-413. With the disc present, these periods are longer, for example by 300 T_{bin} in the case of Kepler-413, because interaction with the disc influences the orbital properties of the embedded planets. During one libration period in the n-body simulation, the planets approach each other only up to a mean longitude difference between the planets of about 25°, ensuring stability (see Fig. 5).

Without the disc, the aligned planetary orbits precess around the binary at a slower rate than with a disc present. This is expected as the precession of the planets in the disc was aligned with the inner cavity. In the n-body simulation we find precession periods of 4245 T_{bin} for Kepler-47 and 2275 T_{bin} for Kepler-413. These periods correspond to that of a single planet with the mean orbital elements of the planet pair.

4. Discussion and conclusion

Using a migration scenario for two planets in a circumbinary disc we have shown that low eccentricity binary systems like Kepler-47 and -413 are able to host two small, equal-mass planets in a stable coorbital resonance where the planets are on horseshoe-type orbits with an average eccentricity of about 0.25 to 0.30. The orbits are aligned and precess slowly around the binary.

These properties are different from the coorbital resonances observed to date. In the Saturnian system, Janus and Epimetheus are on nearly circular orbits and in the case of Trojans, very small objects are in resonance with a much larger planet whose orbit is nearly circular. However, for Trojans the small asteroid can be on an eccentric and inclined orbit that changes the resonant structure (Namouni et al. 1999). In our case, the resonant planet pair orbits a binary star on quite eccentric orbits.

Having found possible resonant states for only two cases of the Kepler sample, it is presently not known for which orbital parameters of a binary star system stable coorbital configurations can exist. Our investigated systems both have very low e_{bin}, 0.02 and 0.04, which appears to be an important factor for the stability of such systems. Using a comparable set-up for Kepler-35 (e_{bin} = 0.14), we did not find any coorbital resonant orbits, but one of the planets was ejected after an interaction between the two planets. In the case of the highly eccentric binary Kepler-34 with e_{bin} = 0.52, both planets were ejected after a close encounter.

In addition to our equal planet mass studies, we ran a model with a different planet-planet mass ratio for the Kepler-47 case. In this simulation, the mass of the inner planet was about 20% greater than the outer one with otherwise identical initial conditions. The system evolved again into a stable coorbital configuration. However, in this case the planets ended up in a tadpole type orbit around each other with a mean eccentricity of about 0.28. Further exploration of the parameter space using different binary eccentricities and planet masses will be the topic of future work.

The disc surrounding appears to be essential for the trapping mechanism of the planets. We also tested the Kepler-47 system with a less viscous disc $\alpha = 10^{-4}$. In such a low viscosity disc, the

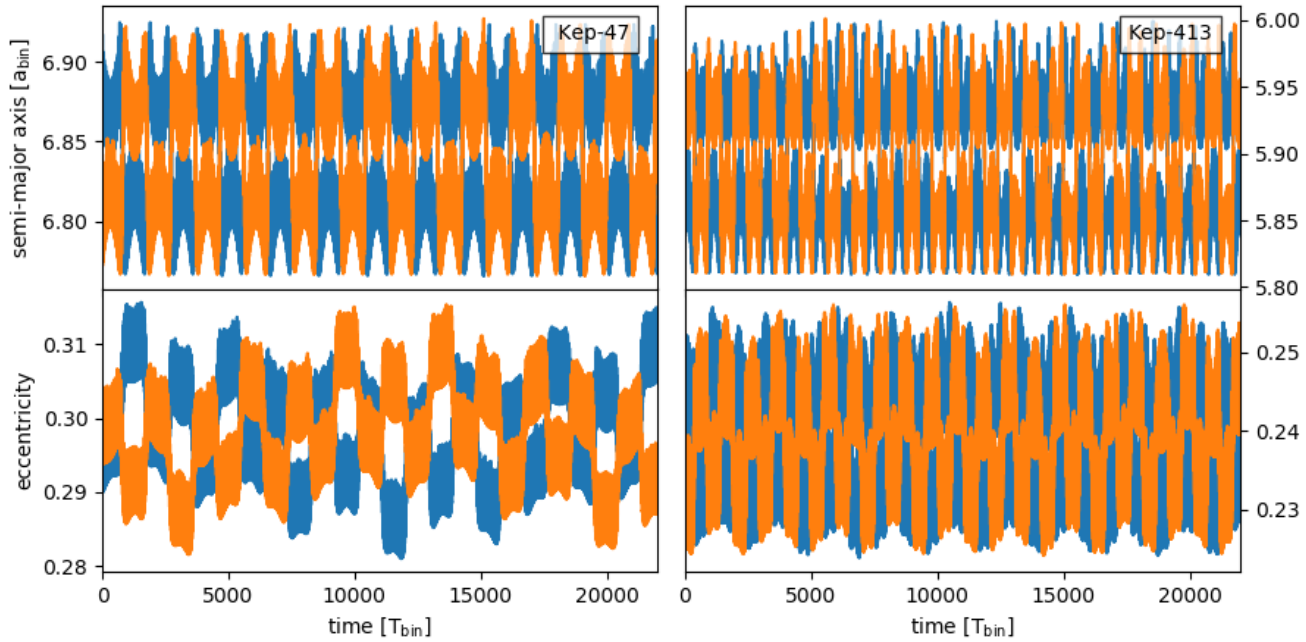

Fig. 4. Evolution of semi-major axes and eccentricities of the two planets orbiting Kepler-413 and -47 for the pure n-body case without disc.

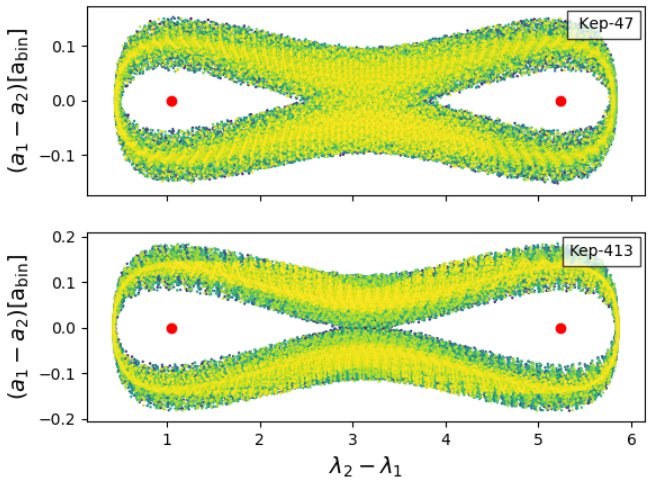

Fig. 5. Difference in mean longitude of the two planets for the pure n-body case without a disc. The colour changes linearly with time over 1600 years or 57 900 T_{bin} for Kepler-413 and 78 500 T_{bin} for Kepler-47.

planets are able to open a gap, which leads to joint inward migration where the outer planet pushes the inner planet inward, while exciting the eccentricity of the inner planet. As a result the inner planet gets ejected as soon as the outer planet migrates closer than two binary separations to the inner planet. In the case of massive planets (masses $\geq \frac{1}{3} M_{Jup}$) both planets reach stable orbits at different semi-major axes. Therefore, massive planets and inviscid environments may inhibit formation of coorbital resonances.

Compared to the observations, our planets are located further away from the stars, which is the consequence of their being trapped at the parking position away from the cavity edge. The more massive the planets are, the closer they migrate towards the edge of the cavity. Lower disc viscosities and aspect ratios also bring the cavity edge closer to the stars[1]. However, in such cases, the planets are more vulnerable to the gap-opening which, as explained, can prevent them from getting into 1:1 resonance. Hence, we do not expect the coorbitals to form sufficiently close to the stars such that the stars' perturbation can affect them. To analyse the general stability of these coorbitals closer to the stars and to check whether they are similar to single planet orbits will require extensive future parameter studies, for example thorough n-body simulations.

After showing that stable coorbital resonances with moderate orbital eccentricities around binary stars are a natural outcome of a convergent migration process, it will be worthwhile to search for such systems in the Kepler data. A recent study suggests that the single star TOI-178 is orbited by a coorbital planet pair, and an additional planet (Leleu et al. 2019b).

[1] These results will be published in a future study.

Acknowledgements. We thank Zsolt Sandor for fruitful discussions. Anna Penzlin was funded by grant KL 650/26-1 of the German Research Foundation (DFG). The authors acknowledge support from the High Performance and Cloud Computing Group at the Zentrum für Datenverarbeitung of the University of Tübingen, the state of Baden-Württemberg through bwHPC, and the German Research Foundation (DFG) through grant no INST 37/935-1 FUGG. All plots in this paper were made with the Python library matplotlib (Hunter 2007).

References

Beaugé, C., Sándor, Z., Érdi, B., & Süli, Á. 2007, A&A, 463, 359
Cresswell, P., & Nelson, R. P. 2006, A&A, 450, 833
Cresswell, P., & Nelson, R. P. 2009, A&A, 493, 1141
Hunter, J. D. 2007, Comput. Sci. Eng., 9, 90
Kley, W., Thun, D., & Penzlin, A. B. T. 2019, A&A, 627, A91
Kostov, V. B., McCullough, P. R., Carter, J. A., et al. 2014, ApJ, 784, 14
Leleu, A., Robutel, P., & Correia, A. C. M. 2018, Celest. Mech. Dyn. Astron., 130, 24
Leleu, A., Coleman, G., & Ataiee, S. 2019a, ArXiv e-prints [arXiv:1901.07640]
Leleu, A., Lillo-Box, J., Sestovic, M., et al. 2019b, A&A, 624, A46
Michalodimitrakis, M., & Grigorelis, F. 1989, JApA, 10, 347
Mignone, A., Bodo, G., Massaglia, S., et al. 2007, ApJS, 170, 228
Namouni, F., Christou, A. A., & Murray, C. D. 1999, Phys. Rev. Lett., 83, 2506
Orosz, J. A., Welsh, W. F., Haghighipour, N., et al. 2019, AJ, 157, 174
Pierens, A., & Raymond, S. N. 2014, MNRAS, 442, 2296
Rodríguez, A., Correa-Otto, J. A., & Michtchenko, T. A. 2019, MNRAS, 487, 1973
Thun, D., & Kley, W. 2018, A&A, 616, A47
Thun, D., Kley, W., & Picogna, G. 2017, A&A, 604, A102
Yoder, C. F., Colombo, G., Synnott, S. P., & Yoder, K. A. 1983, Icarus, 53, 431

A&A 639, A62 (2020)
https://doi.org/10.1051/0004-6361/202038032
© M. Keppler et al. 2020

Astronomy & Astrophysics

Gap, shadows, spirals, and streamers: SPHERE observations of binary-disk interactions in GG Tauri A⋆

M. Keppler[1], A. Penzlin[2], M. Benisty[3,4], R. van Boekel[1], T. Henning[1], R. G. van Holstein[5,6], W. Kley[2], A. Garufi[7], C. Ginski[8,5], W. Brandner[1], G. H.-M. Bertrang[1], A. Boccaletti[9], J. de Boer[5], M. Bonavita[10,11], S. Brown Sevilla[1], G. Chauvin[3,4], C. Dominik[8], M. Janson[12], M. Langlois[13,14], G. Lodato[15], A.-L. Maire[16,1], F. Ménard[3], E. Pantin[17], C. Pinte[18,3], T. Stolker[19], J. Szulágyi[20], P. Thebault[21], M. Villenave[3], A. Zurlo[22,23,14], P. Rabou[3], P. Feautrier[3], M. Feldt[1], F. Madec[14], and F. Wildi[24]

(Affiliations can be found after the references)

Received 26 March 2020 / Accepted 15 May 2020

ABSTRACT

Context. A large portion of stars is found to be part of binary or higher-order multiple systems. The ubiquity of planets found around single stars raises the question of whether and how planets in binary systems form. Protoplanetary disks are the birthplaces of planets, and characterizing them is crucial in order to understand the planet formation process.
Aims. Our goal is to characterize the morphology of the GG Tau A disk, one of the largest and most massive circumbinary disks. We also aim to trace evidence for binary-disk interactions.
Methods. We obtained observations in polarized scattered light of GG Tau A using the SPHERE/IRDIS instrument in the *H*-band filter. We analyzed the observed disk morphology and substructures. We ran 2D hydrodynamical models to simulate the evolution of the circumbinary ring over the lifetime of the disk.
Results. The disk and also the cavity and the inner region are highly structured, with several shadowed regions, spiral structures, and streamer-like filaments. Some of these are detected here for the first time. The streamer-like filaments appear to connect the outer ring with the northern arc. Their azimuthal spacing suggests that they may be generated through periodic perturbations by the binary, which tear off material from the inner edge of the outer disk once during each orbit. By comparing observations to hydrodynamical simulations, we find that the main features, in particular, the gap size, but also the spiral and streamer filaments, can be qualitatively explained by the gravitational interactions of a binary with a semimajor axis of ∼35 au on an orbit coplanar with the circumbinary ring.

Key words. stars: individual: GG Tau A – protoplanetary disks – methods: observational – methods: numerical – techniques: high angular resolution – techniques: polarimetric

1. Introduction

Almost half of all main-sequence solar-type stars are found in binary or higher-order multiple systems (e.g., Raghavan et al. 2010; Duchêne & Kraus 2013), and it is thought that the fraction of multiple systems is even higher among pre-main sequence stars (e.g., Duchêne 1999; Kraus et al. 2011). More than 4000 detections of extrasolar planets around single stars to date show that the assembly of planetary bodies is a common byproduct of star formation. The high abundance of multiple stars on the one hand and planetary companions on the other hand thus raises the question about the possible formation pathways and prevalence of planets in multiple systems.

While our understanding of the building-up of planets within protoplanetary disks around single stars has significantly advanced in the past years, less is known about the conditions of planet formation in multiple systems (e.g., Thebault & Haghighipour 2015). In contrast to the single-star case, the evolution of material in the circumbinary and individual circumstellar disks in multiple systems will (depending on the binary parameters such as mass ratio, orbital separation, and eccentricity) be dominated by the gravitational perturbation of the central binary. As a consequence, the binary-disk interaction has severe implications for the planet formation process. Tidal interactions exerted by the binary are expected to truncate the individual circumstellar disks, reducing their masses, outer radii, and viscous timescales (e.g., Papaloizou & Pringle 1977; Artymowicz & Lubow 1994; Rosotti & Clarke 2018). In addition, the tidal torques will truncate the circumbinary disk from the inner edge by opening a large inner cavity. Despite the resulting separation of circumbinary and circumstellar material, gas streams through the gap may form, supplying the circumstellar disks with material from the outer circumbinary disk (e.g., Artymowicz & Lubow 1996; Muñoz et al. 2020). While observational trends infer binary interaction to be indeed destructive for disks in many cases (e.g., Bouwman et al. 2006; Duchêne 2010; Harris et al. 2012; Cox et al. 2017; Akeson et al. 2019; Manara et al. 2019), potentially impeding the formation of planets, several massive disks around binary systems are known and have been observed at high angular resolution (e.g., UY Aur, HD142527, HD 34700 A; Hioki et al. 2007; Tang et al. 2014; Avenhaus et al. 2017; Monnier et al. 2019).

Despite the potential complications for planet formation induced by the gravitational perturbations from the binary, more

⋆ Based on observations performed with VLT/SPHERE under program ID 198.C-0209(N).

Open Access article, published by EDP Sciences, under the terms of the Creative Commons Attribution License (http://creativecommons.org/licenses/by/4.0), which permits unrestricted use, distribution, and reproduction in any medium, provided the original work is properly cited.
Open Access funding provided by Max Planck Society.

than 100 planets in binary systems have already been discovered (e.g., Martin 2018; Bonavita & Desidera 2020)[1]. Most of these planets are found to orbit only one of the binary stars (i.e., "S-type", i.e., circumstellar planets). The reason for this certainly is that the radial velocity and transit photometry methods, which represent the most successful planet detection methods in terms of numbers, are strongly biased toward planets on short orbital periods. Nevertheless, about 20 planets have been discovered on orbits surrounding both binary components (i.e., "P-type", i.e., circumbinary planets) (e.g., Doyle et al. 2011; Orosz et al. 2019). The statistical analysis of the first direct-imaging survey dedicated to finding planets orbiting two stars suggests that the distributions of planets and brown dwarfs are indistinguishable between single and binary stars within the error bars (Bonavita et al. 2016; Asensio-Torres et al. 2018). This implies that planet formation in multiple systems, and in particular, in circumbinary disks indeed occurs.

Most of the circumbinary planets were detected with the Kepler space telescope on close ($\lesssim$1 au) orbits around eclipsing binary systems. Interestingly, they seem to orbit their host systems close to the stability limit, implying that migration processes and planet-disk interactions may have played a crucial role during their early evolution (e.g., Kley & Haghighipour 2014). It is therefore clear that the observation and characterization of circumbinary disks provide the unique opportunity of testing the conditions and setup for possible planet formation in multiple systems.

One of these cases is GG Tau. Located at a distance of 150 pc (see Sect. 2; Gaia Collaboration 2016, 2018), GG Tau is a young (~1–4 Myr; White et al. 1999; Hartigan & Kenyon 2003; Kraus & Hillenbrand 2009) hierarchical quintuple system composed of two main components, GG Tau Aa/b and GG Tau Ba/b, at a projected separation of about ~10″ (~1500 au) (Leinert et al. 1991, 1993). The northern and more massive binary, GG Tau Aa/b (projected separation ~0.25″, corresponding to ~38 au) is surrounded by a bright and well-studied circumbinary disk. Recent interferometric observations suggest that the secondary component, GG Tau Ab, is a binary itself (GG Tau Ab1/2) at a projected separation of about 31.7 mas (~4.8 au) (Di Folco et al. 2014).

The circumbinary disk around GG Tau A is observed as a large and massive disk with a cleared cavity. While the gaseous disk extends out to more than ~850 au and reveals a reduced amount of gas in the inner region (e.g., Guilloteau et al. 1999; Dutrey et al. 2014; Phuong et al. 2020a), the population of large dust grains observed at (sub-)millimeter wavelengths is confined within a narrow ring surrounding a deeply depleted dust cavity, spanning a full width of ~60–80 au centered at a radial distance of about 250 au with respect to the system barycenter (e.g., Andrews et al. 2014; Dutrey et al. 2014; Tang et al. 2016). Scattered-light observations in the optical, near- and thermal infrared regime infer that the inner edge of the outer disk of the small-grain population is located at about ~190–200 au (e.g., Krist et al. 2002; Duchêne et al. 2004; Itoh et al. 2014; Yang et al. 2017). Such a radial concentration of dust is indicative of particles being trapped within a pressure maximum at the edge of the cavity, as expected for binary-disk interactions (e.g., de Juan Ovelar et al. 2013; Cazzoletti et al. 2017).

To what extent the tidal interactions of GG Tau Aa/b are responsible for the observed gap size has remained controversial, however. Because the radial location of the gas pressure maximum depends on the binary semimajor axis and eccentricity (e.g., Artymowicz & Lubow 1994), the knowledge of the binary orbit is required in order to compare the observed gap size with theoretical predictions. Based on almost two decades of orbital monitoring, a best-fit orbit with a semimajor axis of 36 au and an eccentricity of 0.28 has been established (Köhler 2011). However, this orbital solution assumes that the orbit is coplanar with the circumbinary ring; when this assumption is relaxed, the orbital solution is less well constrained and allows for larger orbit sizes. Several theoretical studies have concluded that in order to explain the observed gap size of ~190 au, the binary orbit should have a semimajor axis of about ~ 65 au, that is, about one-third of the gap size. To still remain consistent with the astrometric constraints, such a large binary orbit would have to be misaligned with respect to the circumbinary disk (e.g., Beust & Dutrey 2005; Cazzoletti et al. 2017; Aly et al. 2018). It is clear that the respective geometry and orientation of binary orbit and circumstellar and circumbinary disk will have a severe effect on the potential of planet formation. Therefore, a detailed knowledge of these parameters is required.

We present new high-resolution (~0.04″) near-infrared polarimetric observations of the GG Tau A system obtained with the SPHERE instrument. Our observations reveal the circumbinary environment at unprecedented detail. We confirm previously known disk substructures and reveal new features within the circumbinary disk. We compare our observations to hydrodynamical simulations in order to investigate whether the observed structures can be explained by binary-disk interactions. Our paper is structured as follows: first, we revise the stellar parameters of GG Tau A in Sect. 2, followed by the presentation of our observations in Sects. 3 and 4. Section 5 presents our modeling efforts, which are discussed in context with the observations in Sect. 6.

2. Stellar properties

Although several authors have studied the stellar properties of GG Tau A (e.g., White et al. 1999; Hartigan & Kenyon 2003; Kraus & Hillenbrand 2009), the discovery of the binarity of GG Tau Ab by Di Folco et al. (2014) needs to be taken into account. In this work, we re-calculated the stellar masses and ages following this notion and the newly known distance d to the system. A negative parallax has been reported for GG Tau A (Gaia Collaboration 2018), probably because of its binarity (see also Luhman 2018), with an absolute value of 6.65 mas. GG Tau B, lying about 10″ farther south than GG Tau A, has a positive parallax of 6.66 mas. Because the two components are known to be bound, we used a parallax of 6.66 mas (150 pc) as a proxy for the distance of GG Tau A. We note, however, that the parallax measured for GG Tau B is likely affected by its own binarity as well, such that the distance of the system remains somewhat uncertain.

We assumed spectral types of M0, M2, and M3 for GG Tau Aa, Ab1, and Ab2 and an extinction of 0.3 mag for Aa and 0.45 mag for Ab1/2, as determined by Hartigan & Kenyon (2003) and Di Folco et al. (2014). The corresponding stellar effective temperatures were obtained using the temperature scale of Rajpurohit et al. (2013) calibrated by their NTT spectra. We further assumed stellar luminosities derived by Hartigan & Kenyon (2003), rescaled to 150 pc, considering that their luminosity measured for Ab represents the sum of the luminosities of Ab1 and Ab2 with a respective luminosity ratio of ~2:1 (see Di Folco et al. 2014; Brauer et al. 2019). We derived stellar masses and ages by comparing the locations of the GG Tau A

[1] see also http://www.univie.ac.at/adg/schwarz/multiple.html (Schwarz et al. 2016).

Table 1. Properties of the GG Tau A system assumed in this study.

Stellar parameters	Aa	Ab1	Ab2	Ref.
Spectral type	M0	M2	M3	a,b
L [$L_\odot$]	0.44	0.153	0.077	a,b,c
Teff [K]	3900	3400	3200	d
Mass [$M_\odot$]	0.65	0.30	0.20	e
Age [Myr]	2.8	2.8	3.1	e
Disk properties				
Inclination		37 ± 1°		f
Position angle		277 ± 1°		f

References. (a) Hartigan & Kenyon (2003), (b) Di Folco et al. (2014), (c) Brauer et al. (2019), (d) Rajpurohit et al. (2013), (e) this work, (f) Guilloteau et al. (1999).

components on a Hertzsprung-Russell diagram with those predicted by a set of five pre-main-sequence tracks (Siess, PARSEC, MIST, Baraffe, Dartmouth; Siess et al. 2000; Bressan et al. 2012; Dotter 2016; Choi et al. 2016; Baraffe et al. 2015; Dotter et al. 2008). This yielded the following possible ranges for stellar masses and ages: 0.6–0.7 $M_\odot$ and 2.4–3.1 Myr for Aa, 0.3–0.5 $M_\odot$ and 2.2–5.6 Myr for Ab1, and 0.2–0.4 $M_\odot$ and 2.7–10.0 Myr for Ab2. We adopted the median of these values as our final stellar masses and ages: 0.65 $M_\odot$ and 2.8 Myr for Aa, 0.3 $M_\odot$ and 2.8 Myr for Ab1, and 0.2 $M_\odot$ and 3.1 Myr for Ab2.

Our inferred ages are well within the range of ages derived in previous studies (~1–4 Myr; White et al. 1999; Hartigan & Kenyon 2003; Kraus & Hillenbrand 2009). Stars in multiple systems are generally assumed to form simultaneously and thus to be coeval. While Aa and Ab1 appear to be coeval according to our analysis, the age derived for Ab2 appears slightly older. However, increasing the luminosity of Ab2 by only 7% reconciles the ages of all three stars. This has almost no effect on the derived mass of Ab2 because the evolutionary tracks run almost vertically in the Hertzsprung-Russell diagram at these young ages.

While the median values of our inferred stellar masses add up to 1.15 $M_\odot$, which is slightly lower than the dynamical mass of the system derived through the CO observations of 1.37 ± 0.08 $M_\odot$ (Guilloteau et al. 1999, scaled to 150 pc), the range of possible stellar masses constrained by our models does not exclude a total mass of 1.37 $M_\odot$. We note, however, that the determination of spectral types, effective temperatures, and luminosities, as well as the evolutionary models (e.g., by not taking the effect of magnetic fields into account; Simon et al. 2019; Asensio-Torres et al. 2019) is hampered by some uncertainty, which might explain any discrepancy between our inferred values and those derived from the CO observations. Furthermore, our inferred total stellar mass might be underestimated if any of the components has an additional as yet undiscovered close-in stellar companion.

The circumbinary disk is observed at an inclination of 37° and at a position angle of 277° (Guilloteau et al. 1999). The system parameters are summarized in Table 1.

3. Observations and data reduction

GG Tau A was observed with SPHERE (Beuzit et al. 2019) as part of the guaranteed-time observations (GTO) during the night of 2016 November 18. The IRDIS instrument (Dohlen et al. 2008) was used in the dual-beam polarimetric imaging (DPI) mode (Langlois et al. 2014; de Boer et al. 2020; van Holstein et al. 2020), applying the H-band filter (1.625 μm; pixel scale 12.25 mas px^{-1}), and the telescope operated in field-tracking mode. One polarimetric cycle consisted of tuning the half-wave plate position at four different angles (0°, 45°, 22.5°, and 67.5°, respectively). At each of these positions, we took 15 frames with an exposure time of 4 s each. A total of 11 polarimetric cycles was carried out, resulting in a total integration time on the science target of about 44 min. No coronagraph was used during the observations, inducing a slight saturation at the location of both Aa and Ab. Weather conditions were relatively stable during the observations (seeing at 500 nm ~ 0.6″–0.9″, coherence time ~3 ms, and wind speed ~10 m s^{-1}). We measured a point spread function (PSF) full width at half-maximum (FWHM) of about 43 mas by fitting a Moffat pattern to the unsaturated images obtained with a neutral density filter.

The data were reduced using the IRDAP pipeline[2] (van Holstein et al. 2020). In short, after basic steps of data reduction (dark subtraction, flat fielding, bad-pixel correction, and centering), the pipeline obtains the clean Stokes Q and U frames using the double-difference method. The data are then corrected for instrumental polarization and cross-talk effects by applying a detailed Mueller matrix model that takes the complete optical path of the light beam into account. After correcting for instrumental effects, the pipeline determines, and if desired, also subtracts, any remaining stellar polarization. This is measured by quantifying the flux in the Q and U images from regions without polarized disk emission. From the final Q and U images, a linear polarized intensity (PI) image is then obtained, following PI = $\sqrt{Q^2 + U^2}$. This final image is corrected for true north (Maire et al. 2016). For details regarding the pipeline, we refer to van Holstein et al. (2020). Finally, the images were recentered on the expected location of the center of mass, assuming a mass ratio between GG Tau Aa and GG Tau Ab1/2 of 0.77 (see Sect. 2).

4. Results

The final PI image is shown in Fig. 1. In our image, the binarity of GG Tau Ab1/2 is not resolved, therefore we refer to this component in the following as Ab. The image shows bright emission close to Aa and Ab, followed by a gap that is surrounded by the bright circumbinary ring. The circumbinary ring is highly structured, with several shadowed regions, as well as several fine filament structures connecting the northern side of the ring with the close environment of the binary, and spiral structures in the southern disk region. Figure 2 presents a schematic overview of the detected features in the outer disk region. The following sections are dedicated to a detailed characterization of the different disk regions and categories of substructures.

4.1. Inner region

Our final image, after correction for the instrumental polarization effects, reveals a residual unresolved polarized intensity signal at the locations of both Aa and Ab. We measure a linear polarization degree and angle of 0.33% and 37.1° at the location of Aa, and 1.12% and 8.7° at the location of Ab. A non-negligible amount of residual polarization can be interpreted as signal from unresolved circumstellar material such as a disk observed at nonzero inclination (e.g., van Holstein et al. 2020; Keppler et al. 2018; Garufi et al. 2020). The circumstellar

[2] https://irdap.readthedocs.io

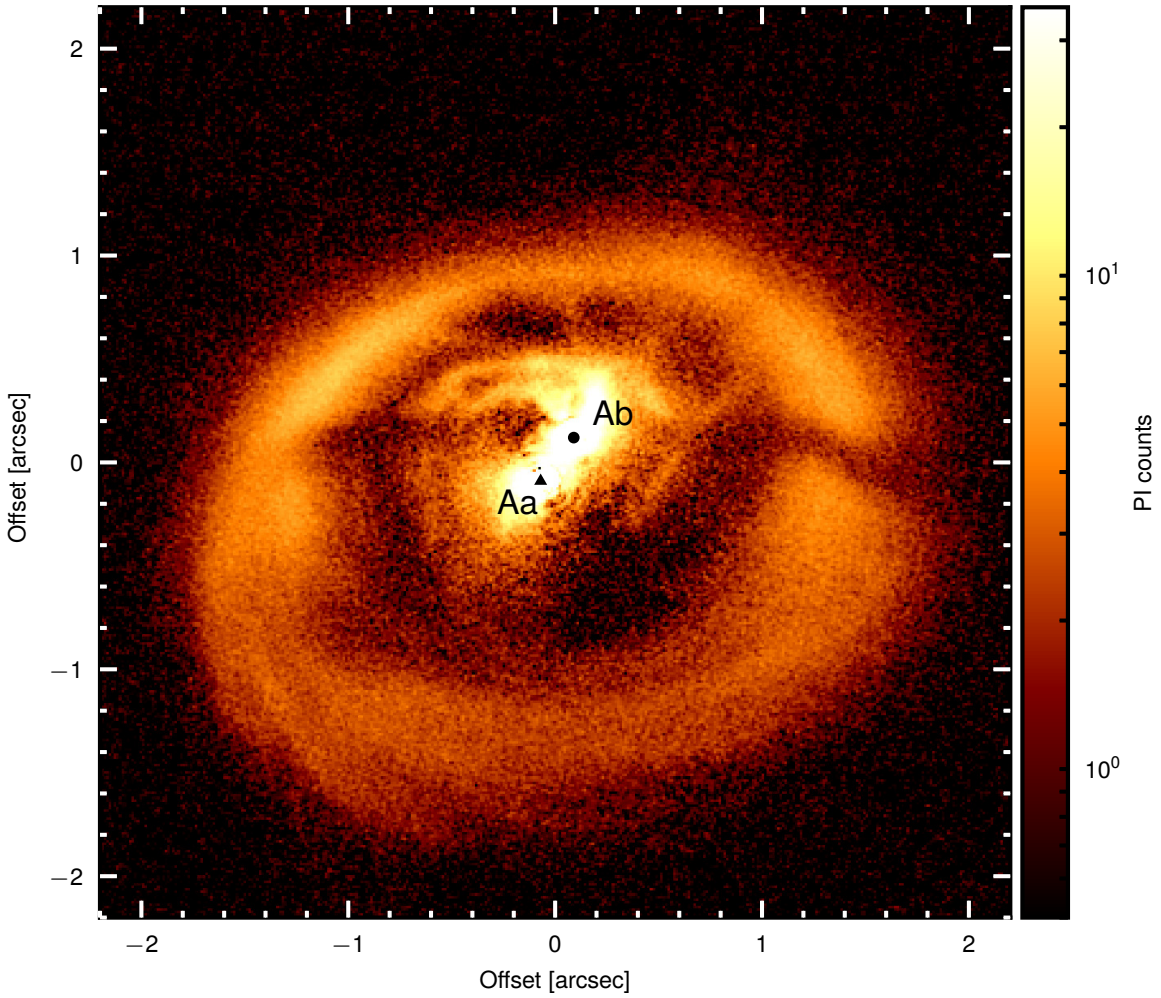

Fig. 1. SPHERE polarized intensity (PI) image of GG Tau A. The image is centered on the expected location of the system's center of mass. The locations of GG Tau Aa and Ab are marked by a black triangle and circle, respectively. North is up and east is to the left.

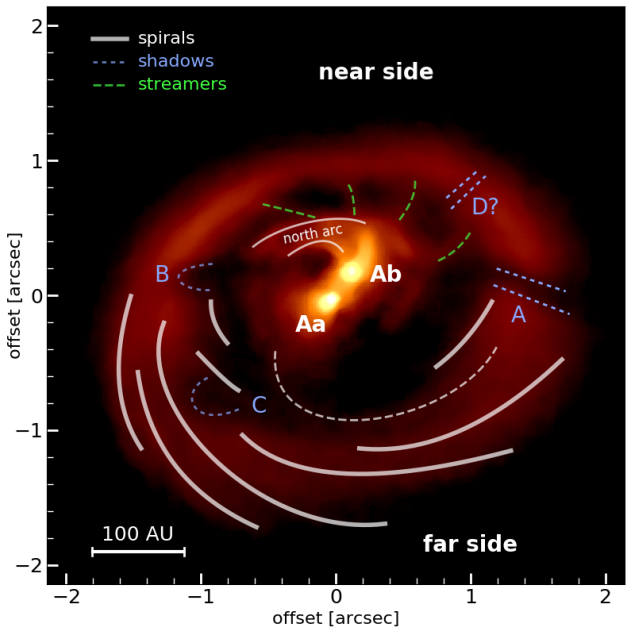

Fig. 2. Schematic overview of the features in the outer circumbinary ring detected in our SPHERE PI image. The image is centered on the location of GG Tau Aa and was smoothed for illustration purposes.

material around both components is confirmed by the measurement of non-negligible extinction ($A_V = 0.3$ mag and 0.45 mag toward Aa and Ab, respectively; Hartigan & Kenyon 2003), as well as accretion signatures from hydrogen-recombination lines and 10 μm silicate features found at the location of both components (White et al. 1999; Hartigan & Kenyon 2003; Skemer et al. 2011). While we cannot make a statement about the inclinations of the disks from our measurements (except for excluding the case where the disks would be seen face-on and are circular symmetric: in this case, the polarized signal would cancel out), the measured angles of linear polarization indicate that the disks are oriented at position angles of ~127° and ~99° (i.e., perpendicular to the direction of linear polarization), respectively. We note that close to the stars, the radiation field is dominated by their individual illumination, and the contribution to the measured residual PI from the respective other star can be neglected (see Appendix A). Observations at higher angular resolution and/or detailed modeling are required to better constrain the orientation of the circumstellar disks.

Any unresolved circumstellar material may create a halo of polarization signal around the star. Because this unresolved polarized signal can affect the analysis of the immediate circumstellar environments, we subtracted these polarized signals (i.e., the total intensity halo multiplied by the degree of polarization) individually for Aa and Ab. While subtracting the

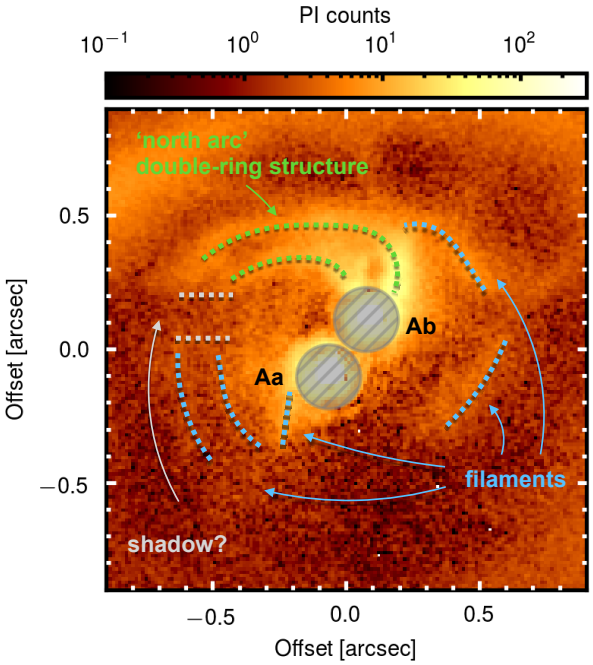

Fig. 3. Zoom on the inner region after subtraction of the stellar polarization on Aa. The dotted lines highlight the detected features: the "north arc", revealing a double-arc structure (green), several filaments (light blue) and a possible shadow lane (gray dashed). See Sect. 4.1 for details. The immediate stellar environments (<120 mas) are masked out. North is up and east is to the left.

polarization signal of Aa slightly increases the contrast of the fine structures in the immediate stellar environment, subtracting the polarization signal of Ab instead blurs these structures. This can be explained by the fact that the measured polarization degree of Ab is somewhat higher than that of Aa. Therefore, subtracting the polarization signal of Ab adds an artificial polarization halo around Aa, which weakens the fine structures in its environment. Subtracting the (less strongly) polarized signal of Aa, however, does not noticeably affect the environment of Ab. Figure 3 shows the resulting image after subtraction of the polarization signal of Aa with annotations of the detected features. The immediate stellar environments that are affected by the diffraction pattern are masked out. In all the images, the inner region appears highly structured, as highlighted in Fig. 3 by the dotted lines. Most prominently, the "north arc", an extended structure to the northeast of Ab observed in previous scattered light images (e.g., Krist et al. 2002, 2005; Itoh et al. 2014; Yang et al. 2017), is clearly detected and appears in our SPHERE image to be composed of a double-arc structure at projected separations of ∼0.38″ and ∼0.48″. This double-arc structure may extend along the entire eastern side to the south, interrupted by a dark lane extending from Ab toward the east (see the dotted gray lines in Fig. 3). This dark lane seems to be connected to the shadow observed in the outer disk at a similar position angle (see Sect. 4.4). We furthermore detect two additional filament structures northwest and southwest of Ab. It is unclear, however, whether they are related to the double-arc system on the eastern side. Finally, another filament is detected immediately southeast of Aa, pointing toward the south.

Figure 4 (left panel) shows the angles of linear polarization overplotted on the inner disk region. The polarization angles θ were calculated according to $\theta = 0.5 \times \arctan(U/Q)$, within bins of 3 pixels. Within the entire inner region, the polarization vectors appear to be generally aligned in azimuthal direction, as expected for light that is scattered off dust particles illuminated by a central source. Deviations from azimuthal polarization, as in the southwest from Aa, for example, may be due to the complex illumination pattern by the binary, or they might indicate multiple scattering events (e.g., Canovas et al. 2015). We note that the disk substructures we detected and highlight in Fig. 3 cannot be explained by a potential interference of polarization vectors in the presence of two illumination sources, which might in principle lead to cancelling PI out if the polarization vectors included an angle of 90° (see Appendix A). This illustrates that small grains scatter light from the central illumination sources within a large region around the binary.

4.2. Outer disk geometry

As in previous observations, the outer circumbinary disk appears as a large elliptical ring. The polarization angles in the center panel of Fig. 4 (here calculated within bins of 6 pixels) show that also in the outer disk, the detected signal is overall well polarized in the azimuthal direction. Only emission within two shadowed regions (shadows A and B, see Sect. 4.4) appears to be less consistently aligned, owing to the lower signal-to-noise ratio. We note that while the circumbinary ring appears bright in (sub-)millimeter continuum observations (e.g., Guilloteau et al. 1999; Dutrey et al. 2014; Tang et al. 2016; Phuong et al. 2020a), the region inside the ring reveals little to no signal at these wavelengths, except for an unresolved source at the location of Aa. This is illustrated by an overlay of the SPHERE image with the contours of the ALMA dust continuum at 0.9 mm (Phuong et al. 2020a) in Fig. 4 (right). This may imply that dust grains are mostly of small size inside the cavity, consistent with large grains being trapped in the outer circumbinary ring, while small grains, well coupled to the gas, can still enter the cavity (e.g., Pinilla et al. 2012; de Juan Ovelar et al. 2013; Cazzoletti et al. 2017). The comparison of the SPHERE and ALMA images also shows an obvious shift of the ring roughly along the disk minor axis, which is due to a projection effect related to the fact that the ALMA dust continuum traces the disk midplane, while the near-infrared SPHERE observations image the scattering surface of the disk. This is explained in detail in the following.

Figure 5 shows the radial deprojected profiles of the linear polarized intensity averaged along the major and minor axes, as well as averaged over the complete range of azimuthal angles. The polarized intensity along the major axis peaks around 200 au. Although the derivation of the profiles takes the projection by the disk inclination into account, the profiles along the near (north) and far (south) side of the minor axis appear very different: while the profile along the near side is quite peaked and peaks farther in than the major axis (∼175 au), the profile of the far side is much broader and peaks at a much larger distance (∼250 au). The different peak locations along the minor axis reflect a shifted geometric center of the ring because the ring is not geometrically flat, but has a non-negligible thickness. Similarly, the different profile shapes (broad versus peaked) are also connected to the geometrical thickness because the inclination of the disk allows us to see the inner rim of the southern (far) side, while for the north (front) side, the inner wall is hidden and only the upper surface is visible (e.g., Silber et al. 2000; Krist et al. 2005).

To quantify the outer ring geometry, we extracted radial profiles within azimuthal bins of 20° width. For each azimuthal bin, we determined the location of maximum brightness by fitting a polynomial function to the radial profile and then fitting an ellipse to the radial peak locations at all position angle bins.

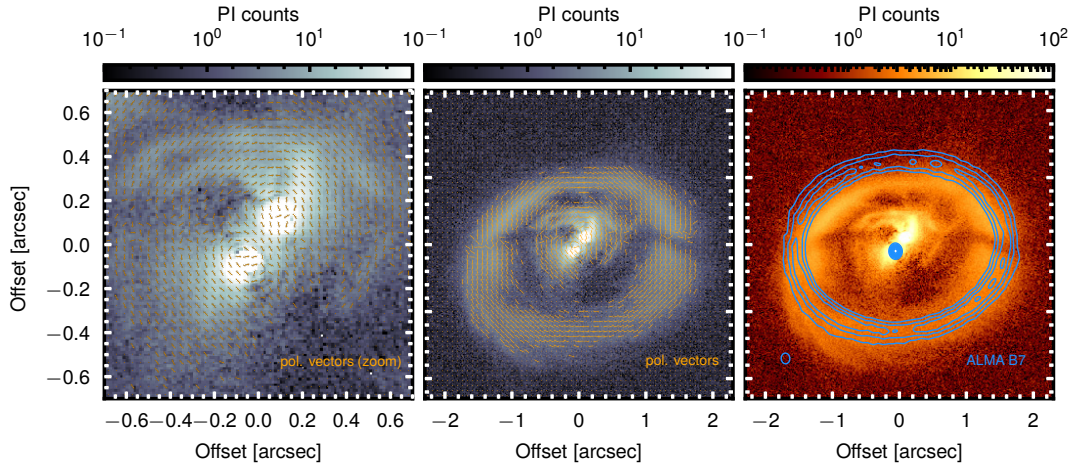

Fig. 4. *Left and center*: SPHERE PI image with lines indicating the angle of linear polarization overplotted, showing two different fields of view (0.7″ × 0.7″, 2.3″ × 2.3″). The lines have an arbitrary length. For the computation of the polarization angles, we ignored bins at which the binned polarized intensity values ≤1.9. *Right*: polarized intensity image with ALMA Band 7 (0.9 mm) continuum contours overplotted (blue). The ALMA observations were published in Phuong et al. (2020a). The ALMA image was registered such that the inner continuum emission, attributed to a circumstellar disk around Aa, coincides with the NIR position of Aa. Contours are shown at 20, 30,.., 80, 90% of the peak intensity. The beam size is indicated in the lower left corner.

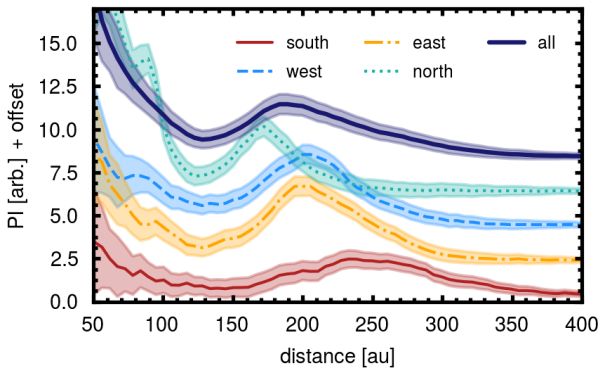

Fig. 5. Radial disk profiles, taking into account the disk inclination of 37°. The profiles are drawn along the major (east, west) and minor (north, south) axes within an azimuthal cone of ±20° around the corresponding axes, as well as averaged over all azimuths. The radial bin size is 3 pixels.

We find that the ring can be fit with an ellipse of eccentricity 0.64, a semimajor axis of 216 au, and a position angle of 288°. The geometric center of the ellipse is offset by 32 au toward the south from the assumed center of mass. These results compare well with the values found in previous scattered-light studies at similar wavelengths (e.g., McCabe et al. 2002). If the disk were geometrically flat and intrinsically circular, an eccentricity of 0.64 would imply an inclination of 39.7°. This value is slightly higher than the inclination of 37° ± 1° derived from (sub-)millimeter continuum observations (Guilloteau et al. 1999; Andrews et al. 2014) because the geometric thickness of the disk affects the scattered-light observations (e.g., Guilloteau et al. 1999; McCabe et al. 2002; Krist et al. 2002). The measured offset Δs of the geometric center of the ellipse from the assumed system barycenter can be used to constrain the scattering surface height $H_{\tau=1}$ along the ellipse according to $H_{\tau=1}(r) = \Delta s(r)/\sin(i)$ (e.g., de Boer et al. 2016). Our measured offset Δs of 32 au therefore corresponds to a scattering height of ~53 au at the inner edge of the ring (~200 au). Because the scattering surface height typically traces layers at about 2–3 times the pressure scale height H_p, this would imply an aspect ratio of $H_p/R \sim 0.09$–0.13, which compares well with constraints from other disks (e.g., Villenave et al. 2019). We stress that this should only be considered as a rough estimate because azimuthal variations of the surface brightness, due to the azimuthal dependence of phase function and polarization degree, as well as the abundance of disk substructures such as shadows and spirals, may complicate a precise determination of the isophotes to which our ellipse was fit.

Finally, a precise knowledge of the vertical thickness of the ring is required in order to determine the disk eccentricity from the scattered-light data. However, optically thin millimeter observations indicate that the intrinsic eccentricity of the ring is rather low because the continuum, which traces the emission from the disk midplane and whose shape is therefore less biased by geometrical effects, can be well fit by an intrinsically circular model ring at the given angular resolution (beam major axes of 0.45″and 0.67″; Piétu et al. 2011; Andrews et al. 2014).

4.3. Streamers

We detect four filament-like structures connecting the inner edge of the outer disk and the outer edge of the northern arc, as indicated in green in Fig. 2. Some of these structures have previously been described as "bridges" by Itoh et al. (2014) and Yang et al. (2017).

In order to measure the position angles of these structures, we deprojected the image, assuming $i = 37°$ and PA = 277°. The connecting points of the filaments at the inner edge of the outer disk are found at approximately PA ~ 296°, 331°, 0°, and 36° (from west to east). The filaments are not aligned with the radius vector pointing toward the center of mass, but are tilted by increasing angles from west to east of ~13° to 26° with respect to the radial direction. The measured PAs imply that the azimuthal spacing of the filaments is about 29°, 35° , and 36°. When we adopt an arbitrary uncertainty on the PA measurement of 5°, this translates into a mean spacing of 33.3 ± 2.9°. When we assume that the outer disk is in Keplerian rotation around a center of mass with 1.15 $M_\odot$, the azimuthal spacing of the filaments may imply that the filaments are launched by periodic perturbations occurring at the inner edge of the disk (180 ± 20 au) every 208 ± 29 years.

The binary best-fit semimajor axis of 36.4 au constrained by Köhler (2011) (scaled here to 150 pc) translates into an orbital

period of about 205 yr, assuming a central binary mass of 1.15 $M_\odot$. The azimuthal spacing of the filaments would therefore be compatible with being triggered by a periodic perturbation occurring once every binary orbit, when the secondary passes at apocenter and comes closest to the disk edge. Interestingly, when we assume that the binary orbit is coplanar with the disk, the binary has just passed apastron (McCabe et al. 2002).

We interpret the filaments as accretion streams. Accretion streams close to the north arc have previously been suggested by continuum observations at 1.1 mm (Piétu et al. 2011), as well as by the CO $J = 6$–5 emission line, which show deviation from Keplerian rotation that may be compatible with infall motion (Dutrey et al. 2014). Furthermore, the ^{12}CO gas distribution within the cavity shows a highly inhomogeneous structure consisting of several fragments (Dutrey et al. 2014). One of these CO fragments coincides with the location of the northern arc. As noted by Yang et al. (2017), the entire northern arc may thus itself be part of a large accretion stream.

4.4. Shadows

We detect three shadowed regions, known from previous scattered-light observations (e.g., Silber et al. 2000; Itoh et al. 2014; Yang et al. 2017), at PA ∼275°, ∼86°, and ∼132°, and labeled A, B, and C in Fig. 2. In addition, we detect a tentative fourth shadow, labeled "D", at a PA of about 320° and possibly related to a less prominent gap detected at a similar location (PA ∼ 310°) by Krist et al. (2005).

The most prominent shadow is a dark lane close to the western major axis of the disk (shadow "A"). To measure the shadow location, we deprojected the disk assuming an inclination of 37°, transformed the image into polar coordinates, and traced the azimuthal profile of the shadow in different radial bins (see Fig. 6). We then fit a Gaussian profile with negative amplitude to these profiles. At the inner and outer edge of the ring (∼175 au and ∼245 au), we find the shadow center to be located at *PA* of 274.8° and 266.7°, respectively. The tilt of the shadow is therefore about 8°. We furthermore measured the contrast of the surface brightness in polarized intensity within the shadow lane with respect to the disk just north of it, resulting in a contrast of about 2.6.

Using the Subaru datasets taken in 2001 January and 2011 September, Itoh et al. (2014) measured an anticlockwise rotation of the shadow of 5.9° and 4.9° between both epochs for the inner and outer disk edges, respectively. If the movement were linear in time, we would expect a further displacement by ∼2.5–3° between 2011 and our SPHERE dataset taken in 2016 November. In order to verify the movement, we repeated our procedure of determining the shadow location on the total intensity frame of the 2011 Subaru dataset. We measure a shadow PA of 274.4° and 268.1° at the inner and outer edge of the disk as defined above. Compared to the values we measured on our SPHERE dataset above (274.8° and 266.7°), we therefore cannot confirm a linear movement of the shadow between 2011 and 2016. The shadow positions instead appear to be stable.

It has been suspected that this western shadow may be cast by circumstellar material (e.g., Itoh et al. 2014), such as by an inclined disk around one of the binary components, as in the case of HD 142527 (Marino et al. 2015). Shadow "B" (and the dark lane to the east of Ab detected in the inner region, see Sect. 4.1) may be just the east side of this same shadow (see also Brauer et al. 2019). We can estimate the expected brightness contrast of the shadow lane with respect to the adjacent nonshadowed

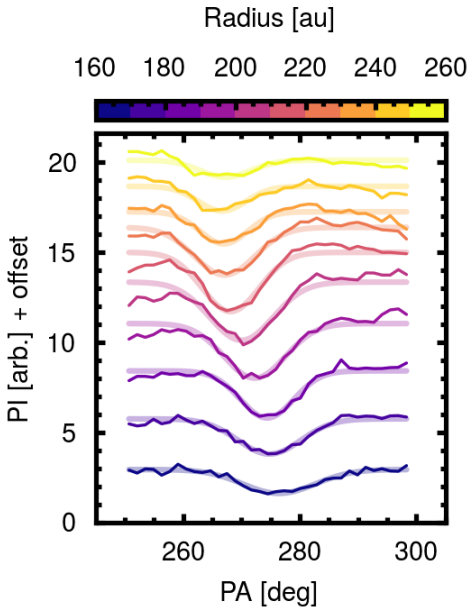

Fig. 6. Azimuthal profiles of the western shadow at different (deprojected) radial bins between 160 and 260 au. The smooth, shadowed lines correspond to the best-fit Gaussian profiles, respectively.

disk region under the hypothesis that one or two of the illumination sources are blocked by an optically thick inclined disk. A disk region that does not lie in any shadow is illuminated by all three stars, and it will therefore receive a total flux of $F_{\rm tot} = (1/4\pi) \times (L_{\rm Aa}/d^2_{\rm Aa} + L_{\rm Ab1}/d^2_{\rm Ab1} + L_{\rm Ab2}/d^2_{\rm Ab2})$, where d_x is the distance of component x to the shadowed disk region. When one of the stellar components is surrounded by an inclined optically thick disk, this will cast a shadow on the outer disk, which will therefore only be illuminated by the two remaining sources. Using the stellar luminosities as defined in Table 1, and estimating a distance of Aa and Ab to shadow "A" of ∼181 au and ∼156, respectively (as measured on the deprojected image), we would expect a contrast of ∼2.4 for a disk around Aa, a contrast of ∼1.7 for a disk around Ab (i.e., a circumbinary disk around Ab1/2), and a contrast of ∼1.4 and ∼1.2 for a disk around Ab1 and Ab2, respectively. The measured contrast of 2.6 from our SPHERE data would therefore favor the shadow to be cast by an inclined disk around Aa or Ab, rather than around Ab1 or Ab2.

Min et al. (2017) have developed an analytical description with which the orientation of an inner shadow-casting disk can be derived from measuring the orientation of the shadows cast on the outer disk. We repeated the same procedure for GG Tau A, assuming that the shadow is cast by a disk around either Aa or Ab. For this purpose, we measured the position angle of the line connecting the two shadows of about 90°, and the vertical (projected) offset of this line of 21.2 au and −9.7 au from Aa and Ab, respectively. Inserting these values into Eqs. (7) and (10) of Min et al. (2017), we obtain a disk position angle of about 90° for the shadow-casting disk for both cases. Assuming an outer disk aspect ratio of 0.1–0.15, and assuming that the scattering surface is found at about 2–3 times the pressure scale height, we furthermore find an inclination of ∼72°–81° if the disk were found around Aa, and an inclination of ∼96°–100° if it were found around Ab. Considering the outer disk inclination of 37°, the misalignment of a disk around Aa and Ab would then be ∼35°–44° and ∼59°–63°, respectively.

Recently, Brauer et al. (2019) have investigated the effect of circumstellar disks around the binary components on the

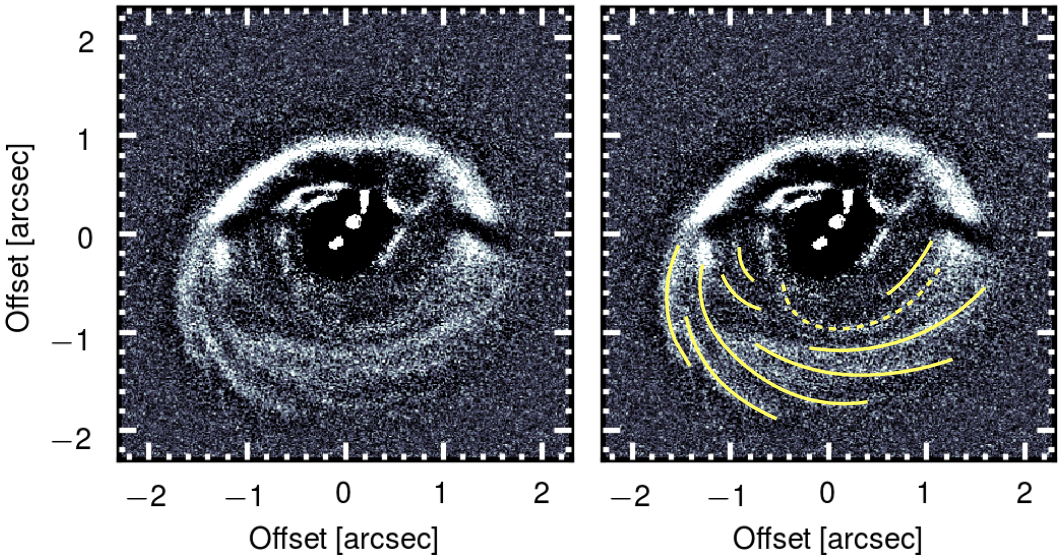

Fig. 7. High-pass filtered PI image of GG Tau A (*left*) with highlighted spiral structures (*right*). The dashed line highlights the possible connection of the outer disk to Aa.

brightness distribution within the circumbinary ring using radiative transfer modeling. In one of their setups, they simulated an inclined circumstellar disk around Ab2 (while keeping a coplanar disk around Aa). In this case, their simulations were able to reproduce a sharp shadowed lane at the location of shadow "A", as well as a symmetric eastern shadow (corresponding to shadow "B"), although they found it to be shallower in brightness contrast than in the observations. We suggest here that an inclined disk around Ab (i.e., a circumbinary disk around both Ab1 and Ab2) or around Aa would be more compatible with the measured contrast.

4.5. Spirals

We detect multiple spiral structures in the southern part of the disk. For an improved identification, we processed the image by a high-pass filter, that is, we convolved the image with a Gaussian filter ($\sigma = 9$ px) and subtracted it from the original image. The spiral structures are clearly seen in this image (Fig. 7). Interestingly, one spiral arm is tentatively found to cross the gap, and if confirmed, connects the southwestern circumbinary ring to the immediate circumstellar environment of Aa (see the dashed yellow line in Fig. 7, right). Thin filaments in the southeast disk have previously been suggested from the observations by Krist et al. (2005), who interpreted these structures as possible signs of binary-disk interactions. Furthermore, Tang et al. (2016) and Phuong et al. (2020b) found at an angular resolution of ~0.3–0.4″, that the radial distribution of CO brightness in the outer disk exhibits several spiral structures.

5. Modeling

We performed hydrodynamical simulations in order to model the system and its evolution. The main goal was to verify whether the binary might be qualitatively responsible for the observed gap size and features within the circumbinary ring.

5.1. Hydrodynamical model setup

We carried out hydrodynamical simulations of the gas disk using the GPU version of PLUTO (Mignone et al. 2007) by Thun & Kley (2018). The simulations were 2D and isothermal. We used a polar radially logarithmic grid ranging from one binary semimajor axis ($a_{\rm bin}$, 35 au) to 40 $a_{\rm bin}$ (1400 au) with 684 cells in radial and 584 cells in azimuthal direction. Because the separation of Ab1 and Ab2 (~5 au; Di Folco et al. 2014) is smaller than the inner edge of the circumbinary ring (~200 au), we considered Ab1 and Ab2 together as a single component, Ab, and the entire system was treated as a binary. The binary components Aa and Ab were assumed to have masses of 0.75 $M_\odot$ and 0.67 $M_\odot$, implying a mass ratio of 0.89, similar to the mass ratio of 0.77 derived in Sect. 2. As shown in Thun & Kley (2018), minor changes in the mass ratio of the binary affect the disk dynamics only very slightly. The binary orbit was set to have a semimajor axis of 35 au and an initial eccentricity of 0.28, consistent with the observations (Köhler 2011). Furthermore, the binary orbit was assumed to be coplanar with the circumbinary disk plane. We ran two different models that differed only in the adopted radial temperature profile. In the first model, we considered a temperature profile constrained by the ^{13}CO molecule (Guilloteau et al. 1999), tracing the disk surface temperature, and in the second model, we applied a temperature profile constrained by the dust continuum (Dutrey et al. 2014), tracing the midplane temperature,

$$T_{\rm surface} = 20\,K \cdot \frac{300\,\mathrm{au}}{R} \tag{1}$$

$$T_{\rm midplane} = 13.8\,K \cdot \frac{200\,\mathrm{au}}{R.} \tag{2}$$

By considering these two different temperature profiles, which are sensitive to the warm disk surface and to the cool midplane, respectively, we covered the two limiting cases. The aspect ratio $h = H/R$ of the disk was determined by the sound speed $c_{\rm s}$ and Keplerian orbital frequency $\Omega_{\rm k}$, and therefore results from the assumed temperature profile as follows:

$$h = \frac{c_{\rm s}}{\Omega_{\rm k} R} = \sqrt{\frac{k_{\rm B}}{G M_{\rm bin} \mu m_{\rm p}}} \cdot \sqrt{TR}, \tag{3}$$

with $M_{\rm bin}$ the binary mass, $\mu = 2.3$ the mean molecular weight, $m_{\rm P}$ the proton mass, and R the radial distance from the system

barycenter in the disk plane. With our chosen temperature profile, we obtain a constant aspect ratio corresponding to the following values:

$$h_{\rm surface} \approx 0.15 \quad (4)$$

$$h_{\rm midplane} \approx 0.11. \quad (5)$$

The initial surface density follows a power law $\propto R^{-1.5}$ normalized in such a way that the total disk mass amounts to 10% of the binary mass ($0.14\,M_\odot$). As the inner $3\,a_{\rm bin}$ of the disk are unstable, the initial density profile inside of $2.5\,a_{\rm bin}$ exponentially decays to e^{-1} of the smooth profile within $0.1\,a_{\rm bin}$. The boundary conditions of the simulations were defined as in Thun & Kley (2018). We simulated the gas content of the disk assuming an α viscosity with a constant Shakura-Sunyaev parameter of 10^{-3} throughout the disk.

The computational time needed to reach the actual disk structure from the initial power-law profile can be long (Kley et al. 2019). To ensure a feasible time step for the grid code, we did not include the stars themselves in the simulation domain, but the inner grid boundary was set to a radius of $1\,a_{\rm bin}$ (35 au) and we added the binary as n-bodies inside the domain to create the potential, using a gravitational softening parameter of 0.6 (see Kley et al. 2019). As discussed in Kley et al. (2019), such an inner boundary does not change the dynamics of the circumbinary disk or gap width. The outer disk edge is an open boundary that assumes a continuation of the power-law disk. We note that the simulations do not take GG Tau B into account, which is observed at a projected separation of about 1400 au from GG Tau A. Because this outer companion may accrete from and/or truncate the outer parts of the disk (see, e.g., Beust & Dutrey 2006), it is therefore possible that the density in the outer parts of the disk is overestimated in the simulation. We ran both models for 28 000 binary orbits (≈ 4.9 Myr).

5.2. Postprocessing of hydrodynamical simulations

To investigate the appearance of our simulated disks in scattered light, we generated images in polarized intensity using the radiative transfer code RADMC-3D (Dullemond et al. 2012). We included a radiation field from two stellar components with luminosities of $0.44\,L_\odot$ and $0.20\,L_\odot$ and temperatures of 3900 and 3400 K, respectively. In order to generate a 3D view from the simulated disk, we expanded the 2D surface density distribution resulting from the hydrodynamical simulations along the vertical axis, assuming a Gaussian density distribution with constant aspect ratios of 0.15 and 0.11, consistent with the assumed temperature laws in the simulations (see Sect. 5.1). We assumed the dust to be well mixed with the gas. This is a valid assumption because at $1.67\,\mu$m, the scattered light is dominated by micron-sized dust grains, which are well coupled to the gas. We thus assumed the dust density distribution to be identical to that of the gas, scaled by a factor of 0.01, which corresponds to a typically assumed dust-to-gas ratio of 1–100 in protoplanetary disks.

We assumed the dust number density n as a function of grain size a to follow a power law of the form $n(a) \propto a^{-3.5}$. The grains were considered to be distributed between sizes of 0.005 and $0.5\,\mu$m, as assumed in the modeling efforts by Brauer et al. (2019). We assumed that 5% of the total dust mass is contained within this population of small grains, corresponding to a fraction of 5×10^{-4} of the total disk gas mass. Our dust mixture was composed of 70% astronomical silicates (Draine 2003) and 30% amorphous carbon grains (Zubko et al. 1996). We computed the Stokes Q and U frames at $1.67\,\mu$m, taking the observed inclination and position angle of the disk into account. The simulations were run using 10^8 photon packages in order to obtain images with high signal-to-noise ratios (S/Ns). Finally, we convolved our images with a Gaussian kernel with an FWHM of 43 mas.

5.3. Modeling results and comparison to observations

Both models ran for 28 000 binary orbits (≈ 4.9 Myr), during which the system reached a converging configuration of a stable sized, eccentric, precessing cavity around the binary and a stable circumbinary disk after about 10 000 binary orbits (≈ 1.7 Myr). In the simulations, mass is constantly accreted onto the stars through accretion streams. Therefore the disk looses a fraction of about 5.2×10^{-6} of its mass per binary orbit (or 3.0×10^{-8} per year). As a result, the initial disk mass of $0.14\,M_\odot$ has decreased at the end of the simulation to 86% of its initial value ($0.12\,M_\odot$). This is in excellent agreement with the disk mass constraints from observations ($\sim 0.12\,M_\odot$, Guilloteau et al. 1999). We did not take the accretion onto the stars into account as it is not resolved in the domain.

The final gas density distributions for both simulations are displayed in Fig. 8 (left and center left columns). They show evidence of large cleared inner regions. The gap in the gas is found to have a semimajor axis (defined as the location where the gas density has decreased to 10% of its peak value) of $4.77\,a_{\rm bin}$ (167 au) and an eccentricity of 0.34 in the case of the midplane temperature ($h = 0.11$), and a semimajor axis of $3.85\,a_{\rm bin}$ (135 au) and an eccentricity of 0.25 in the case of the (higher) surface temperature ($h = 0.15$).

The surface density shows an azimuthal asymmetry, with the density peaking in direction of the disk apocenter. The reason is that the gas velocity is slowest at these locations, leading to an enhancement of material in these regions. Figure 8 (left column) shows that the circumbinary ring is structured by numerous tightly wound fine spirals. Furthermore, the logarithmic color stretch for the surface density (Fig. 8, center left column) reveals the structure of material flow through the cavity. Spiral streams occur in the simulation, periodically driven by the circumbinary rotation, accelerating the close-by infalling material. Our simulations show regularly stripped-off material streams from the outer disk, similar to the observations, while the exact morphology and orientation of the filaments is not reproduced. These differences may be related to the fact that we do not know the exact initial conditions of the system, with some parameters such as its mass related to some uncertainty. Another possible caveat in the simulations is the fact that we did not simulate the direct circumstellar material, but the simulation domain was cut inside of about 35 au. The presence of material in that region (such as the "northern arc") may affect the flow dynamics and dust morphology within the cavity. Furthermore, it may affect the morphology of the material flow that Ab itself is a binary.

The postprocessed polarized intensity images are shown in the center right column of Fig. 8. The intensity also shows clear azimuthal variations here. Because the disk is optically thick in the near-infrared regime, the azimuthal dependence of the large-scale surface brightness is not sensitive to the surface density, but to the dust phase function and polarization degree. As expected, the near side is significantly brighter than the far side. The simulated polarized intensity images also show substructures within the circumbinary ring. While the contrast of the spirals in the circumbinary ring appears faint, they become very well visible when the images are treated with a high-pass filter, similarly to the observations (Fig. 8, right column). We note, however, that the simulated view of the disk in scattered light may be biased by our simplified treatment of the vertical structure of the disk.

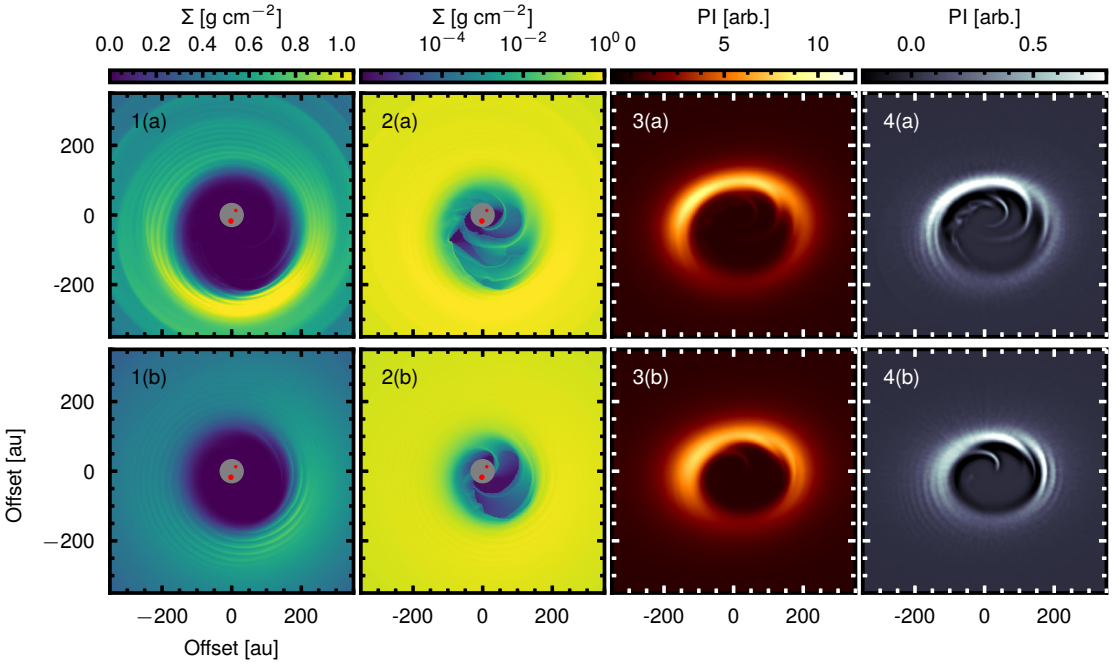

Fig. 8. Surface density output of our simulations in linear (*left column*; 1(*a*) and (*b*)) and logarithmic (*center left column*; 2(*a*) and (*b*)) color stretch. The *center right column* (3(*a*) and (*b*)) shows the simulated polarized intensity images evaluated at 1.67 μm. This image was calculated after inclining and orienting the disk as in the observations. The *right column* (4(*a*) and (*b*)) shows the polarized intensity image of the center right column, processed with a high-pass filter. In each column, the panel in the first row (*a*) corresponds to the model with $h = 0.11$, the panel in the second row (*b*) to $h = 0.15$.

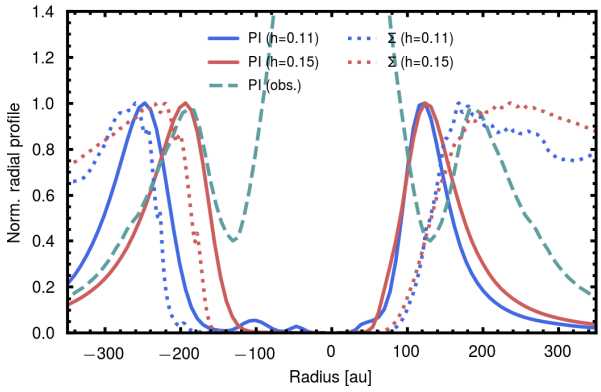

Fig. 9. Radial profiles along the disk major axes (within a cone of ±30°) of the two models drawn from the gas surface densities (dotted) and the deprojected, simulated polarized intenisty images (solid lines). As a comparison, the radial profile of the observed, deprojected disk averaged over all azimuths is plotted (dashed).

Figure 9 shows the radial profiles of the simulated gas surface densities (dotted blue and red lines) along the disk major axes. We find a disk semimajor axis (defined as the distance where the profile peaks) of about 215–230 au. Assuming that the large dust particles traced by millimeter observations are being trapped at the location of maximum gas density, these findings are well comparable with the observations: using the optically thin continuum emission between 1.3 and 7.3 mm, Andrews et al. (2014) observed the continuum to peak at about 250 au. Figure 9 also shows the radial profiles of the simulated deprojected polarized intensity images along the disk major axes (solid blue and red lines). In each of the cases, the polarized intensity profile peaks slightly ahead of the gas density. This can be explained by the fact that the peak of the scattered light profile traces the location of the inner wall of the ring, where illumination is strongest, and not directly the dust density distribution. The semimajor axes of the disk in the polarized intensity images are measured to be 180 au and 160 au, respectively. This is slightly shorter than the location of the peak of the mean (i.e., averaged over all azimuths) deprojected radial profile of the observed PI image (~190 au). One reason might be that the slope of the inner edge of the gas disk may in reality be somewhat sharper than in the simulations, which might be connected to the exact value of the binary eccentricity (e.g., Miranda et al. 2017), or to other disk properties such as the assumed temperature profile, density, distribution, and viscosity. Furthermore, the rim location inferred from the scattered light observations may be overestimated because of possible shadowing from one (or several) circumstellar disks around the three individual components (Brauer et al. 2019).

Finally, the simulated gap cleared by the binary becomes eccentric, with mean eccentricity values of ~0.2–0.3. As noted in Sect. 4.2, it is difficult to extract reliable information about the disk eccentricity from the scattered-light observations, but the (sub-)millimeter observations indicate that the eccentricity of the disk is probably rather low (Guilloteau et al. 1999; Andrews et al. 2014). This might indicate a lower disk viscosity than assumed in our simulations, as discussed in Sect. 6.3.

6. Discussion

6.1. Accretion streams within the circumbinary gap

We interpret the filaments detected in our observations that we described in Sect. 4.3 as accretion streams. According to theoretical models, circumbinary accretion is thought to proceed onto the stars from the outer circumbinary disk through accretion streams, which are repeatedly torn off at the inner edge of the disk near the apocenter of the binary orbit. This is consistent with what is seen in our simulations. Such a phase-dependent pulsed accretion process has been seen in numerous theoretical

studies (e.g., Günther & Kley 2002; Dunhill et al. 2015; Duffell et al. 2019). Time-variable spectroscopic signatures of accretion activity (e.g., through hydrogen recombination lines) correlated with the binary orbital phase have been observed in some tight (spectroscopic) binary systems (e.g., Mathieu et al. 1997; Kóspál et al. 2018). While the detection of pulsed accretion is usually restricted to very tight systems (because of the restricted time base), the detection of periodic streamers in GG Tau A, if confirmed, would be the first indication of such processes in a wider system.

The hypothesis that the filaments in GG Tau A indeed trace accretion streams fits the overall picture well. With large grains being trapped in the outer circumbinary disk, the detected streamers refill the immediate environment of Ab predominantly with gas and small grains, which is compatible with the strong silicate feature observed at the location of GG Tau Ab (Skemer et al. 2011). The formation of large, massive circumstellar disk(s) around Ab1/2, however, may be inhibited by its binary nature despite continuous replenishment of material, which could explain the nondetection of millimeter flux at the location of Ab (Dutrey et al. 2014).

6.2. Spiral structures as imprints of binary-disk interaction

Our SPHERE observations show several spiral structures in the southern disk region. Our simulations show that this is an expected outcome of binary-disk interactions and is also consistent with other modeling efforts, which do show that the generation of spiral density waves is a common result of binary-disk interaction, in particular, for cases where the binary orbit has nonzero eccentricity (e.g., Miranda et al. 2017; Price et al. 2018). Observations of circumbinary disks have brought observational evidence of such spiral structures in these systems (e.g., Avenhaus et al. 2017; Monnier et al. 2019). In addition, large accretion streams, such as the tentative connection from the southern disk to the primary, Aa, are also expected from simulations (e.g., Mösta et al. 2019). In this respect, the detected spiral features agree well with our expectations from simulations of circumbinary disks, where the binary orbit has moderate eccentricity. We note that in addition to this, the external binary-disk interactions with GG Tau B (projected separation of ∼1500 au) might also be able to trigger spiral waves in the GG Tau A disk (e.g., Dong et al. 2016). This scenario may be addressed by future work.

However, theoretical models have shown that in addition to binary-disk interactions, several different processes can also drive the generation of spirals in disks, such as a low-mass companion on an orbit inside or outside of the disk (e.g., Dong et al. 2015a), gravitational instability (e.g., Dong et al. 2015b; Dipierro et al. 2015; Nelson & Marzari 2016; Meru et al. 2017), or a combination of both (e.g., Pohl et al. 2015), as well as temperature fluctuations as a result of shadowing by a warped or misaligned inner disk (e.g., Montesinos et al. 2016). In order to discern between the companion and gravitational instability scenario, observations at comparably high resolution of the dust continuum, probing the midplane of the disk, are required (e.g., Rosotti et al. 2020). However, we regard the last scenario as rather unlikely because in this case, the spiral arms would be expected to diverge from a location close to where the scattered-light shadows are located. In contrast, several spiral arms seem to rather originate from a point located on the outer ring at a PA of ∼120°. Interestingly, at this PA (but slightly outward of the near-infrared peak emission, at radial distances of ∼215–270 au), an asymmetric structure within the CO distribution has been found, showing evidence of a significantly increased temperature (Dutrey et al. 2014; Tang et al. 2016). This so-called "hot spot" was interpreted as an area with locally enhanced density and temperature, heated by a possible embedded planet at the formation stage (Phuong et al. 2020b). While we still consider binary-disk interaction as the most obvious driving force for the spirals observed in the scattered light, a possible connection or interference with this hypothetical forming body needs to be investigated with complementary observations.

6.3. Gap size as a result of binary-disk interactions

Our simulations show that a binary with a semimajor axis of 35 au is able to create a gap in a coplanar disk with a size that is comparable to our observations. Our inferred gap sizes (4.8 $a_{\rm bin}$ and 3.9 $a_{\rm bin}$ for the two temperature regimes) agree with previous studies of other systems, in which cavity sizes ranging from three to six binary separations were found (e.g., Thun & Kley 2018).

We note that our gap estimates are significantly larger than those derived by previous studies of the GG Tau A circumbinary ring. As an example, considering the best-fit astrometric solution of the binary under the assumption that the orbit is coplanar with the outer disk ($a_{\rm bin}$ ∼ 36 au), Beust & Dutrey (2005) predicted a gap size of 2–3.3 $a_{\rm bin}$, which they noted to be obviously incompatible with the observations. This apparent discrepancy between observed and simulated gap sizes was confirmed by the hydrodynamical simulations of Cazzoletti et al. (2017), who tested the binary-disk coplanar case considering different disk temperature profiles and a range of values for the viscosity. The authors found the simulated gas distribution to peak at radial distances smaller than ∼160 au, which contrasts with the observed millimeter continuum peak at about 250 au. As a possible solution of this discrepancy, Beust & Dutrey (2005) proposed to drop the assumption that the binary orbit was coplanar with the disk. In this case, the most plausible orbit has a semimajor axis of ∼65 au, an eccentricity of 0.44, and a disk-orbit misalignment of about 25° (Köhler 2011). This latter scenario, a binary on a wide, disk-misaligned orbit was tested with hydrodynamical simulations by Aly et al. (2018). The authors found that they were indeed able to reproduce the observed gap size, assuming a binary separation of ∼60 au and a binary-disk misalignment of ∼30°.

The differences between these earlier estimates and our own gap values are probably mainly due to a difference in timescales. While our simulations were run for 28 000 orbits, previous studies such as those of Nelson & Marzari (2016), Cazzoletti et al. (2017) and Aly et al. (2018) stopped their simulations after about 1000–2000 orbits or fewer, and they therefore studied earlier stages of the disk evolution to define the gap size and eccentricity. Because the disk evolution starts from an azimuthally symmetric density distribution, our simulations show that the disk crosses meta-stable symmetric states between 1100 and 1700 orbits. This is illustrated in Fig. B.1, which shows the evolution of the gap semimajor axis and gap eccentricity over the first 20 000 orbits. However, this meta-stable state is an artifact of the setup and does not correspond to the convergent behavior of a circumbinary disk because the binary will excite the disk to eccentric motion. The disk will eventually evolve to a larger, more eccentric, stable gap, as the full evolution in Fig. 10 shows. Although this evolution is slow, it converges well within the lifetime of the disk. Therefore the simulations of Cazzoletti et al. (2017) and our simulations agree well with each other during the earlier stages, but our longer simulation time shows that the gap will widen with progressing evolution. We accordingly conclude

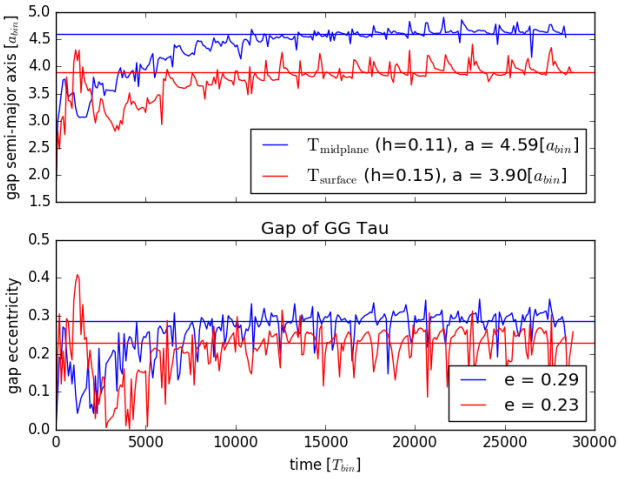

Fig. 10. Size and eccentricity evolution of the cavity around GG Tau A created by the PLUTO simulations for the midplane temperature and surface temperature of the disk. $a_{\rm bin}$ is 35 au and the initial disk mass is 0.1 binary masses.

that the observed gap size can be explained by the long-term action (10 000 orbits) of a binary with a separation of 35 au that is coplanar with the disk.

We note that our choice for the viscous α-parameter of 10^{-3} does not affect our conclusion. As the disk starts at more than 10 au with rather low density, a low level of turbulence driven by the magnetorotational instability seems to be a reasonable assumption, and we consider our value a realistic choice. However, the relatively high mass of the disk may lead to an even lower viscosity. We therefore compared our results with a simulation using an even lower α parameter of 10^{-4}. Our test run shows that lowering α affects the gap size only slightly, reducing it by less than 10%. The fact that in this case, a lower α viscosity slightly shrinks the gap size, is related to the relatively high binary eccentricity of GG Tau A ($\epsilon \sim 0.3$). For eccentricities $\gtrsim$0.15, the eccentricity of the disk is directly affected by the binary eccentricity. Because the transfer of angular momentum is weaker, lowering α decreases the apocenter distance of the disk, while the pericenter distance remains constant, thus lowering the gap eccentricity and resulting in a slightly smaller net gap size (Penzlin et al., in prep.). Similarly, Cazzoletti et al. (2017) observed no strong dependence of the location of the gas density peak on the assumed value of α. However, a lower α value would result in a significantly less eccentric gap. Therefore a low viscosity may even be consistent with the fact that the disk does not appear very eccentric in the continuum observations.

In summary, our simulations suggest that a tight, ~35 au binary orbit that is coplanar with the outer disk is sufficient to create a gap in the disk of the observed size. However, we note that some misalignement within the system cannot be excluded, in particular, in view of the shadows on the outer disk, which may imply the presence of misaligned circumstellar material. Final conclusion on the orbital parameters of the binary and the respective disk-orbit orientation requires further astrometric monitoring as the current orbital coverage is still sketchy (Maire et al., in prep.).

7. Summary and conclusions

We have observed the circumbinary environment of GG Tau A in polarized light with SPHERE/IRDIS in H-band at unprecedented angular resolution. We analyzed the disk morphology and compared our observations to hydrodynamical simulations. The following section summarizes our findings.

The inner region appears to be highly structured. Our image suggests that the previously reported northern arc is composed of a double-arc structure. We furthermore detect various filament-like structures in the immediate circumbinary environment. Small dust grains scattering off light from the binary appear to be distributed in a large area around the binary. We clearly detect previously suggested filament-like structures connecting the outer ring with the northern arc. The azimuthal spacing of the streamers may be consistent with a periodic perturbation by the binary, tearing off material from the inner edge of the outer disk once during each orbit. We confirm detection of three shadowed regions cast on the outer disk, as well as a tentative fourth shadow, suggesting the presence of an inclined circumstellar disk around Aa or Ab. We do not confirm a linear movement of the western shadow lane since 2011 that was suggested by previous observations.

We ran hydrodynamical simulations including the binary on an eccentric and disk coplanar orbit with a semimajor axis of 35 au. The simulations ran for 28 000 orbits, which covers the estimated age of the system. The final disk configuration shows evidence of spiral structures in the outer ring as well as within the cavity, similar to the observations. The resulting disk size is in qualitative agreement with the observations, which implies that a coplanar binary orbit ~35 au in size may be sufficient to explain the size of the ring. Astrometric follow-up observations are required to provide a final conclusion on the size and orientation of the binary orbit.

Acknowledgements. We thank the referee, Ruobing Dong, for providing constructive comments which helped improve the manuscript. We thank A. Müller, P. Pinilla, D. Price and J. Sanchez for fruitful discussions, as well as Y. Itoh for kindly sharing the previous Subaru data with us. M.K. warmly thanks Th. Müller for help with the visualization of the data. T.H. acknowledges support from the European Research Council under the Horizon 2020 Framework Program via the ERC Advanced Grant Origins 83 24 28. M.Be., F.Me. and M.V. acknowledge funding from ANR of France under contract number ANR-16-CE31-0013 (Planet Forming Disks). C.P. acknowledges funding from the Australian Research Council via FT170100040 and DP180104235. G.L. has received funding from the European Union's Horizon 2020 research and innovation programme under the Marie Skłodowska-Curie grant agreement No 823823 (RISE DUSTBUSTERS project). A.Z. acknowledges support from the FONDECYT Iniciación en investigación project number 11190837. SPHERE is an instrument designed and built by a consortium consisting of IPAG (Grenoble, France), MPIA (Heidelberg, Germany), LAM (Marseille, France), LESIA (Paris, France), Laboratoire Lagrange (Nice, France), INAF - Osservatorio di Padova (Italy), Observatoire de Genève (Switzerland), ETH Zurich (Switzerland), NOVA (Netherlands), ONERA (France), and ASTRON (The Netherlands) in collaboration with ESO. SPHERE was funded by ESO, with additional contributions from CNRS (France), MPIA (Germany), INAF (Italy), FINES (Switzerland), and NOVA (The Netherlands). SPHERE also received funding from the European Commission Sixth and Seventh Framework Programmes as part of the Optical Infrared Coordination Network for Astronomy (OPTICON) under grant number RII3-Ct2004-001566 for FP6 (2004–2008), grant number 226604 for FP7 (2009–2012), and grant number 312430 for FP7 (2013–2016).

References

Akeson, R. L., Jensen, E. L. N., Carpenter, J., et al. 2019, ApJ, 872, 158
Aly, H., Lodato, G., & Cazzoletti, P. 2018, MNRAS, 480, 4738
Andrews, S. M., Chandler, C. J., Isella, A., et al. 2014, ApJ, 787, 148
Artymowicz, P., & Lubow, S. H. 1994, ApJ, 421, 651
Artymowicz, P., & Lubow, S. H. 1996, ApJ, 467, L77
Asensio-Torres, R., Janson, M., Bonavita, M., et al. 2018, A&A, 619, A43
Asensio-Torres, R., Currie, T., Janson, M., et al. 2019, A&A, 622, A42
Avenhaus, H., Quanz, S. P., Schmid, H. M., et al. 2017, AJ, 154, 33
Baraffe, I., Homeier, D., Allard, F., & Chabrier, G. 2015, A&A, 577, A42
Beust, H., & Dutrey, A. 2005, A&A, 439, 585
Beust, H., & Dutrey, A. 2006, A&A, 446, 137
Beuzit, J. L., Vigan, A., Mouillet, D., et al. 2019, A&A, 631, A155

Bonavita, M., & Desidera, S. 2020, Galaxies, 8, 16
Bonavita, M., Desidera, S., Thalmann, C., et al. 2016, A&A, 593, A38
Bouwman, J., Lawson, W. A., Dominik, C., et al. 2006, ApJ, 653, L57
Brauer, R., Pantin, E., Di Folco, E., et al. 2019, A&A, 628, A88
Bressan, A., Marigo, P., Girardi, L., et al. 2012, MNRAS, 427, 127
Canovas, H., Ménard, F., de Boer, J., et al. 2015, A&A, 582, L7
Cazzoletti, P., Ricci, L., Birnstiel, T., & Lodato, G. 2017, A&A, 599, A102
Choi, J., Dotter, A., Conroy, C., et al. 2016, ApJ, 823, 102
Cox, E. G., Harris, R. J., Looney, L. W., et al. 2017, ApJ, 851, 83
de Juan Ovelar, M., Min, M., Dominik, C., et al. 2013, A&A, 560, A111
de Boer, J., Salter, G., Benisty, M., et al. 2016, A&A, 595, A114
de Boer, J., Langlois, M., van Holstein, R. G., et al. 2020, A&A, 633, A63
Di Folco, E., Dutrey, A., Le Bouquin, J.-B., et al. 2014, A&A, 565, L2
Dipierro, G., Pinilla, P., Lodato, G., & Testi, L. 2015, MNRAS, 451, 974
Dohlen, K., Langlois, M., Saisse, M., et al. 2008, Proc. SPIE, 7014, 70143L
Dong, R., Zhu, Z., Rafikov, R. R., & Stone, J. M. 2015a, ApJ, 809, L5
Dong, R., Hall, C., Rice, K., & Chiang, E. 2015b, ApJ, 812, L32
Dong, R., Zhu, Z., Fung, J., et al. 2016, ApJ, 816, L12
Dotter, A. 2016, ApJS, 222, 8
Dotter, A., Chaboyer, B., Jevremović, D., et al. 2008, ApJS, 178, 89
Doyle, L. R., Carter, J. A., Fabrycky, D. C., et al. 2011, Science, 333, 1602
Draine, B. T. 2003, ApJ, 598, 1026
Duchêne, G. 1999, A&A, 341, 547
Duchêne, G. 2010, ApJ, 709, L114
Duchêne, G., & Kraus, A. 2013, ARA&A, 51, 269
Duchêne, G., McCabe, C., Ghez, A. M., & Macintosh, B. A. 2004, ApJ, 606, 969
Duffell, P. C., D'Orazio, D., Derdzinski, A., et al. 2019, ArXiv e-prints [arXiv:1911.05506]
Dullemond, C. P., Juhasz, A., Pohl, A., et al. 2012, Astrophysics Source Code Library [record ascl:1202.015]
Dunhill, A. C., Cuadra, J., & Dougados, C. 2015, MNRAS, 448, 3545
Dutrey, A., di Folco, E., Guilloteau, S., et al. 2014, Nature, 514, 600
Gaia Collaboration (Prusti, T., et al.) 2016, A&A, 595, A1
Gaia Collaboration (Brown, A. G. A., et al.) 2018, A&A, 616, A1
Garufi, A., Avenhaus, H., Pérez, S., et al. 2020, A&A, 633, A82
Guilloteau, S., Dutrey, A., & Simon, M. 1999, A&A, 348, 570
Günther, R., & Kley, W. 2002, A&A, 387, 550
Harris, R. J., Andrews, S. M., Wilner, D. J., & Kraus, A. L. 2012, ApJ, 751, 115
Hartigan, P., & Kenyon, S. J. 2003, ApJ, 583, 334
Hioki, T., Itoh, Y., Oasa, Y., et al. 2007, AJ, 134, 880
Itoh, Y., Oasa, Y., Kudo, T., et al. 2014, Res. Astron. Astrophys., 14, 1438
Keppler, M., Benisty, M., Müller, A., et al. 2018, A&A, 617, A44
Kley, W., & Haghighipour, N. 2014, A&A, 564, A72
Kley, W., Thun, D., & Penzlin, A. B. T. 2019, A&A, 627, A91
Köhler, R. 2011, A&A, 530, A126
Kóspál, Á., Ábrahám, P., Zsidi, G., et al. 2018, ApJ, 862, 44
Kraus, A. L., & Hillenbrand, L. A. 2009, ApJ, 704, 531
Kraus, A. L., Ireland, M. J., Martinache, F., & Hillenbrand, L. A. 2011, ApJ, 731, 8
Krist, J. E., Stapelfeldt, K. R., & Watson, A. M. 2002, ApJ, 570, 785
Krist, J. E., Stapelfeldt, K. R., Golimowski, D. A., et al. 2005, AJ, 130, 2778
Langlois, M., Dohlen, K., Vigan, A., et al. 2014, Proc. SPIE, 9147, 91471R
Leinert, C., Haas, M., Mundt, R., Richichi, A., & Zinnecker, H. 1991, A&A, 250, 407
Leinert, C., Zinnecker, H., Weitzel, N., et al. 1993, A&A, 278, 129
Luhman, K. L. 2018, AJ, 156, 271
Maire, A. L., Bonnefoy, M., Ginski, C., et al. 2016, A&A, 587, A56
Manara, C. F., Tazzari, M., Long, F., et al. 2019, A&A, 628, A95
Marino, S., Perez, S., & Casassus, S. 2015, ApJ, 798, L44
Martin, D. V. 2018, Handbook of Exoplanets (Berlin: Springer), 156
Mathieu, R. D., Stassun, K., Basri, G., et al. 1997, AJ, 113, 1841
McCabe, C., Duchêne, G., & Ghez, A. M. 2002, ApJ, 575, 974
Meru, F., Juhász, A., Ilee, J. D., et al. 2017, ApJ, 839, L24
Mignone, A., Bodo, G., Massaglia, S., et al. 2007, ApJS, 170, 228
Min, M., Stolker, T., Dominik, C., & Benisty, M. 2017, A&A, 604, L10
Miranda, R., Muñoz, D. J., & Lai, D. 2017, MNRAS, 466, 1170
Monnier, J. D., Harries, T. J., Bae, J., et al. 2019, ApJ, 872, 122
Montesinos, M., Perez, S., Casassus, S., et al. 2016, ApJ, 823, L8
Mösta, P., Taam, R. E., & Duffell, P. C. 2019, ApJ, 875, L21
Muñoz, D. J., Lai, D., Kratter, K., & Miranda, R. 2020, ApJ, 889, 114
Nelson, A. F., & Marzari, F. 2016, ApJ, 827, 93
Orosz, J. A., Welsh, W. F., Haghighipour, N., et al. 2019, AJ, 157, 174
Papaloizou, J., & Pringle, J. E. 1977, MNRAS, 181, 441
Phuong, N. T., Dutrey, A., Diep, P. N., et al. 2020a, A&A, 635, A12
Phuong, N. T., Dutrey, A., Di Folco, E., et al. 2020b, A&A, 635, L9
Piétu, V., Gueth, F., Hily-Blant, P., Schuster, K.-F., & Pety, J. 2011, A&A, 528, A81
Pinilla, P., Benisty, M., & Birnstiel, T. 2012, A&A, 545, A81
Pohl, A., Pinilla, P., Benisty, M., et al. 2015, MNRAS, 453, 1768
Price, D. J., Cuello, N., Pinte, C., et al. 2018, MNRAS, 477, 1270
Raghavan, D., McAlister, H. A., Henry, T. J., et al. 2010, ApJS, 190, 1
Rajpurohit, A. S., Reylé, C., Allard, F., et al. 2013, A&A, 556, A15
Rosotti, G. P., & Clarke, C. J. 2018, MNRAS, 473, 5630
Rosotti, G. P., Benisty, M., Juhász, A., et al. 2020, MNRAS, 491, 1335
Schwarz, R., Funk, B., Zechner, R., & Bazsó, Á. 2016, MNRAS, 460, 3598
Siess, L., Dufour, E., & Forestini, M. 2000, A&A, 358, 593
Silber, J., Gledhill, T., Duchêne, G., & Ménard, F. 2000, ApJ, 536, L89
Simon, M., Guilloteau, S., Beck, T. L., et al. 2019, ApJ, 884, 42
Skemer, A. J., Close, L. M., Greene, T. P., et al. 2011, ApJ, 740, 43
Tang, Y.-W., Dutrey, A., Guilloteau, S., et al. 2014, ApJ, 793, 10
Tang, Y.-w., Dutrey, A., Guilloteau, S., et al. 2016, ApJ, 820, 19
Thebault, P., & Haghighipour, N. 2015, Planet Formation in Binaries (Berlin: Springer), 30
Thun, D., & Kley, W. 2018, A&A, 616, A47
van Holstein, R. G., Girard, J. H., de Boer, J., et al. 2020, A&A, 633, A64
Villenave, M., Benisty, M., Dent, W. R. F., et al. 2019, A&A, 624, A7
White, R. J., Ghez, A. M., Reid, I. N., & Schultz, G. 1999, ApJ, 520, 811
Yang, Y., Hashimoto, J., Hayashi, S. S., et al. 2017, AJ, 153, 7
Zubko, V. G., Mennella, V., Colangeli, L., & Bussoletti, E. 1996, MNRAS, 282, 1321

[1] Max Planck Institute for Astronomy, Königstuhl 17, 69117 Heidelberg, Germany
e-mail: keppler@mpia.de
[2] Institut für Astronomie und Astrophysik, Universität Tübingen, Auf der Morgenstelle 10, 72076 Tübingen, Germany
[3] Univ. Grenoble Alpes, CNRS, IPAG, 38000 Grenoble, France
[4] Unidad Mixta Internacional Franco-Chilena de Astronomía (CNRS, UMI 3386), Departamento de Astronomía, Universidad de Chile, Camino El Observatorio 1515, Las Condes, Santiago, Chile
[5] Leiden Observatory, Leiden University, PO Box 9513, 2300 RA Leiden, The Netherlands
[6] European Southern Observatory, Alonso de Córdova 3107, Casilla 19001, Vitacura, Santiago, Chile
[7] INAF, Osservatorio Astrofisico di Arcetri, Largo Enrico Fermi 5, 50125 Firenze, Italy
[8] Anton Pannekoek Institute for Astronomy, Science Park 904, 1098 XH Amsterdam, the Netherlands
[9] LESIA, CNRS, Observatoire de Paris, Université Paris Diderot, UPMC, 5 place J. Janssen, 92190 Meudon, France
[10] SUPA, Institute for Astronomy, University of Edinburgh, Blackford Hill, Edinburgh EH9 3HJ, UK
[11] Centre for Exoplanet Science, University of Edinburgh, Edinburgh EH9 3HJ, UK
[12] Department of Astronomy, Stockholm University, AlbaNova University Center, 106 91 Stockholm, Sweden
[13] CRAL, UMR 5574, CNRS, Université de Lyon, Ecole Normale Supérieure de Lyon, 46 allée d'Italie, 69364 Lyon Cedex 07, France
[14] Aix Marseille Univ., CNRS, CNES, LAM, Marseille, France
[15] Dipartimento di Fisica, Università degli Studi di Milano, Via Giovanni Celoria 16, 20133 Milano, Italy
[16] STAR Institute, Université de Liège, Allée du Six Août 19c, 4000 Liège, Belgium
[17] AIM, CEA, CNRS, Université Paris-Saclay, Université Paris Diderot, Sorbonne Paris Cité, Gif-sur-Yvette, France
[18] School of Physics and Astronomy, Monash University, Clayton, VIC 3168, Australia
[19] Institute for Particle Physics and Astrophysics, ETH Zurich, Wolfgang-Pauli-Strasse 27, 8093 Zurich, Switzerland
[20] Institute for Theoretical Astrophysics and Cosmology, Institute for Computational Science, University of Zürich, Winterthurerstrasse 190, 8057 Zürich, Switzerland
[21] LESIA-Observatoire de Paris, UPMC Univ. Paris 06, Univ. Paris-Diderot, France
[22] Nùcleo de Astronomía, Facultad de Ingeniería y Ciencias, Universidad Diego Portales, Av. Ejercito 441, Santiago, Chile
[23] Escuela de Ingeniería Industrial, Facultad de Ingeniería y Ciencias, Universidad Diego Portales, Av. Ejercito 441, Santiago, Chile
[24] Geneva Observatory, University of Geneva, Chemin des Mailettes 51, 1290 Versoix, Switzerland

Appendix A: Polarized intensity pattern in the presence of two illumination sources

In order to investigate how the presence of two illumination sources affects the morphology of PI, we generated a toy model of the GG Tau A disk. We considered two illumination sources at a respective separation of 38 au, and with luminosities ($L_a = 0.44\,L_\odot$, $L_b = 0.23\,L_\odot$) such as is found for GG Tau Aa and Ab. We assumed that the luminosity ratios of Aa and Ab are representative for their H-band flux ratios, which is consistent with the observations by Di Folco et al. (2014), who reported an H-band flux ratio of ∼2.1. For each point in the disk plane, we computed the received stellar illumination $F_{tot} = F_a + F_b \propto L_a/d_a^2 + L_b/d_b^2$, where d_a and d_b is the distance to Aa and Ab, respectively. This received stellar flux is proportional to the intensity of scattered linearly polarized light, assuming a homogeneous surface density and degree of linear polarization throughout the disk. We also assumed a flat-disk geometry for simplicity.

Figure A.1 (left) shows the distribution of F_{tot} for a face-on view of the disk. The dotted circles trace contours at which the contribution from the respective other star to F_{tot} is 5, 10 and 20%, that is, where $F_a/F_{tot} = (0.05, 0.1, 0.2)$ (green) and $F_b/F_{tot} = (0.05, 0.1, 0.2)$ (red). The 5% contours are found as close as ∼9 au (∼5 au) to the location of Aa (Ab). Because the PSF FWHM of our SPHERE observations is about 40 mas (i.e., 6 au at 150 pc, thus corresponding to a PSF radius of ∼3 au) the contribution of scattered polarized light from the respective other star to the unresolved polarized signal measured at the locations of GG Tau Aa and Ab is thus expected to be negligible.

We furthermore investigated whether any of our detected disk substructures might be related to the respective orientation of the polarization vectors in the presence of two illumination sources, rather than to a variation in disk surface density or scale height. If, for example, the polarization vectors at a certain point in the disk due to light scattered from Aa and Ab enclosed an angle of about 90°, the polarized signal could cancel out, leading to a locally depressed PI. Because the orientation of the linear polarization vectors is expected to be orthogonal to the radius vectors connecting a certain point in the disk with the respective illumination sources, it is possible to map the angles enclosed by the two polarization vectors throughout the disk. This map is shown in Fig. A.1 (right). A region with a respective polarization angle difference of 90° indeed lies close to the stars. Farther away, however, from $\sim a_{bin}$ on, polarization vectors tend to be aligned with respect to each other. This is consistent with our observations, where the polarization vectors are clearly azimuthally orientated throughout the outer disk. While we cannot exclude that some spatial PI variation close to the binary is caused by the superposition of the polarization vectors, we conclude that this effect cannot be responsible for the generation of any of the disk substructures we detected that are illustrated in Fig. 3.

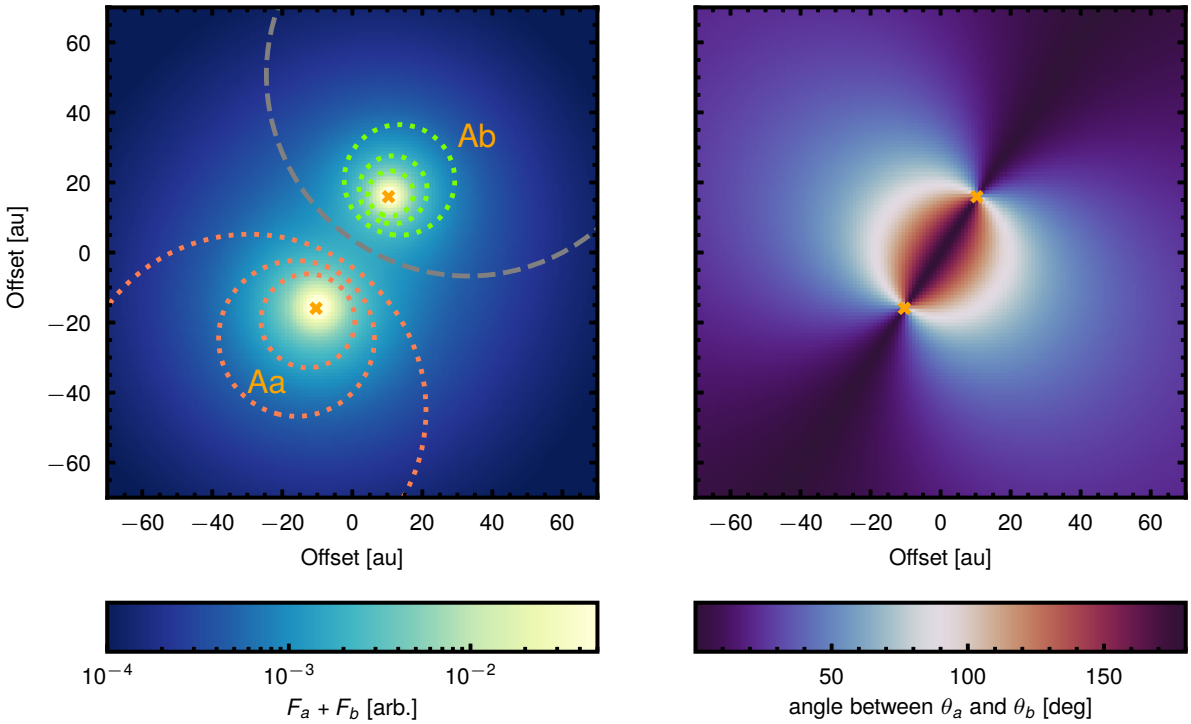

Fig. A.1. Toy model of the inner disk region of GG Tau A including two illuminating sources. The *left panel* shows the radiation field generated by the two stars. For each star, the dotted contours mark the regions where the contribution from the other star to the total flux is 5, 10, and 20% (in red, the contribution from GG Tau Ab in the immediate surrounding of GG Tau Aa; in green, vice versa). The grey dashed line traces the contour where F_a equals F_b. The *right panel* maps the angles between the linear polarization vectors resulting from scattering of light from Aa and Ab. In regions in which this angle becomes close to 90°, PI could theoretically cancel out.

Appendix B: Early meta-stable simulation phase

Cazzoletti et al. (2017) found a smaller inner cavity after a simulation of about 1000 binary orbits. We can confirm this finding for the early simulation, as shown in Fig. B.1. However, we find that this feature is created by the symmetric initial condition of the gas distribution. After clearing the inner disk from gas in unstable orbits during the first few hundred orbits, the disk reaches a meta-stable configuration. This symmetric configuration will be disturbed by the higher modes of the binary potential and transform into the stable eccentric cavity that is reached after about 10 000 binary orbits. The same behavior occurs for less viscous systems a few hundred orbits earlier.

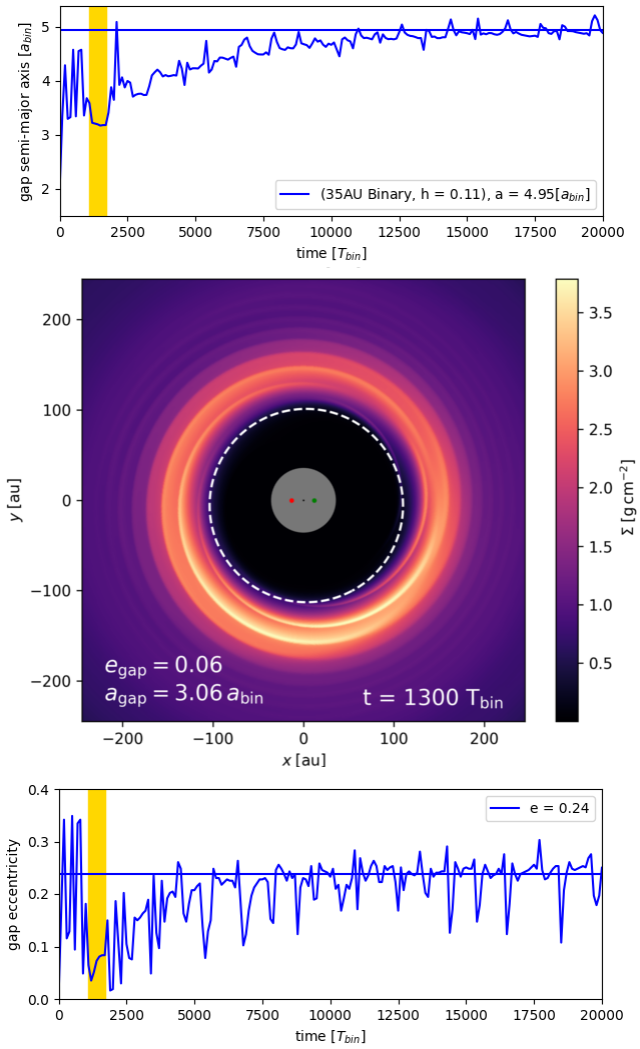

Fig. B.1. Gap size (*top*) and eccentricity (*bottom*) evolution of the cavity around GG Tau A created by our PLUTO simulation for the midplane temperature of the disk. The disk encounters a meta stable symmetric state (highlighted in yellow) with reduced gap size and eccentricity for about 600 orbits. The 2D surface density plot after 1300 orbits is shown in the *middle*.

A&A 645, A68 (2021)
https://doi.org/10.1051/0004-6361/202039319
© ESO 2021

Astronomy & Astrophysics

Parking planets in circumbinary discs

Anna B. T. Penzlin[1], Wilhelm Kley[1], and Richard P. Nelson[2]

[1] Institut für Astronomie und Astrophysik, Universität Tübingen, Auf der Morgenstelle 10 72076, Germany
e-mail: anna.penzlin@uni-tuebingen.de
[2] Astronomy Unit, School of Physics and Astronomy, Queen Mary University of London, London E1 4NS, UK

Received 1 September 2020 / Accepted 5 December 2020

ABSTRACT

The *Kepler* space mission has discovered about a dozen planets orbiting around binary stars systems. Most of these circumbinary planets lie near their instability boundaries, at about three to five binary separations. Past attempts to match these final locations through an inward migration process were only shown to be successful for the Kepler-16 system. Here, we study ten circumbinary systems and attempt to match the final parking locations and orbital parameters of the planets with a disc-driven migration scenario. We performed 2D locally isothermal hydrodynamical simulations of circumbinary discs with embedded planets and followed their migration evolution using different values for the disc viscosity and aspect ratio. We found that for the six systems with intermediate binary eccentricities ($0.1 \leq e_{\rm bin} \leq 0.21$), the final planetary orbits matched the observations closely for a single set of disc parameters, specifically, a disc viscosity of $\alpha = 10^{-4}$ and an aspect ratio of $H/r \sim 0.04$. For these systems the planet masses are large enough to open at least a partial gap in their discs as they approach the binary, forcing the discs to become circularised and allowing for further migration towards the binary – ultimately leading to a good agreement with the observed planetary orbital parameters. For systems with very small or large binary eccentricities, the match was not as good as the very eccentric discs and the large inner cavities in these cases prevented close-in planet migration. In test simulations with higher than observed planet masses, a better agreement was found for those systems. The good agreement for six out of the ten modelled systems, where the relative difference between observed and simulated final planet orbit is ≤10% strongly supports the idea that planet migration in the disc brought the planets to their present locations.

Key words. planets and satellites: dynamical evolution and stability – binaries: general – planet-disk interactions

1. Introduction

The first circumbinary planet (CBP) discovered by the *Kepler* space mission was Kepler-16b (Doyle et al. 2011). Since then, about a dozen more circumbinary p-type planets have been discovered (see overview in Martin 2019 and Table 1). In 2012, multiple CBPs around Kepler-47 were detected (Orosz et al. 2012b, 2019). Some time later, the Planet Hunters project discovered a planet in the quadruple star system PH1b, also named Kepler-64b (Schwamb et al. 2013). The most recent discovery is TOI-1338b by the TESS mission (Kostov et al. 2020).

All of the above systems, and most of the discovered innermost CBPs, share a set of comparable properties in their orbits. Firstly, they are in good alignment with the binary's orbital plane, hinting at their formation in a protoplanetary disc that was aligned with the binary. Secondly, the planetary orbits (the semi-major axes) are all near 3.5 binary separations, which is close to the instability limit (Dvorak 1986). Additionally, the eccentricities of the planetary orbits are small. All of this points to a common formation mechanism for most observed CBPs in aligned, coplanar discs.

Concerning the general stability of circumbinary discs it has been suggested that in addition to the coplanar situation, the perpendicular case is also a stable binary-disc configuration (Martin & Lubow 2017; Lubow & Martin 2018; Cuello & Giuppone 2019). However, no planets have been observed in perpendicular orbits yet due to observational constraints.

The in situ formation of planets at such close orbits around binaries is an unlikely scenario. Tidal forces close to the binary cause perturbations in the inner disc that inhibit planetesimal and dust accretion (Paardekooper et al. 2012; Silsbee & Rafikov 2015; Meschiari 2012), while the turbulence induced by hydrodynamical parametric instabilities can dramatically reduce pebble accretion efficiencies (Pierens et al. 2020). A more likely formation scenario is based on planet formation in the outer disc and subsequent disc-driven migration to the observed close orbits (Pierens & Nelson 2008; Bromley & Kenyon 2015). However, this scenario does not in itself explain the particular stopping positions of most CBPs.

Several studies have already been dedicated to the investigation of planetary migration in circumbinary discs (Pierens & Nelson 2008, 2013; Kley & Haghighipour 2014, 2015; Kley et al. 2019). Due to gravitational torques, the binary clears out an inner cavity and, hence, planet migration is halted at the inner edge of the disc at a location close to the binary, but the findings does not yet match the observations in most cases studied. Numerical simulations have shown that the shape of the inner disc and, hence, the final orbital parameters of the given planet depend on disc parameters such as viscosity and scale height, and the mass ratio and eccentricity of the binary (Mutter et al. 2017; Thun & Kley 2018).

Two recent studies by Mutter et al. (2017) and Kley et al. (2019) were able to reproduce the observed CBP orbits for Kepler-16b and Kepler-38b. In the current work, we plan to find a common formation scenario for most observed CBPs using a sample of ten planets, as described in Table 1.

To limit the parameter space, we consider discs characterised by properties that are in agreement with the low α-viscosity that

Table 1. Observed circumbinary parameters.

Kepler	38	35	453	64	34	47	16	413	1661	TOI-1338
$M_{\rm bin}$ $[M_{\rm sun}]$	1.20	1.70	1.14	1.77	2.07	1.32	0.89	1.36	1.10	1.34
$q_{\rm bin}$	0.26	0.91	0.21	0.28	0.97	0.35	0.29	0.66	0.31	0.28
$e_{\rm bin}$	0.10	0.14	0.05	0.21	0.52	0.02	0.16	0.04	0.11	0.16
$m_{\rm p}$ $[m_{\rm jup}]$	0.38	0.12	0.05	0.1	0.22	0.05	0.33	0.21	0.05	0.10
$a_{\rm p}$ $[a_{\rm bin}]$	3.16	3.43	4.26	3.64	4.76	3.53	3.14	3.55	3.39	3.49
$e_{\rm p}$	0.03	0.04	0.04	0.05	0.18	0.03	0.006	0.12	0.06	0.09
$m_{\rm p}/M_{\rm bin}$ $[\times 10^{-5}]$	30	7.1	4.3	5.4	10	3.7	35	15	4.6	6.8

Notes. $M_{\rm bin}$, $q_{\rm bin}$ and $e_{\rm bin}$ are the total mass, the mass ratio (M_2/M_1) and the eccentricity of the binary star, $m_{\rm p}$, $a_{\rm p}$, $e_{\rm p}$ are the mass, semi-major axis and eccentricity of the planet on its orbit.

References. Orosz et al. (2012a), Welsh et al. (2012), Welsh et al. (2015), Schwamb et al. (2013), Orosz et al. (2019), Doyle et al. (2011), Kostov et al. (2014), Kostov et al. (2020), Socia et al. (2020).

was observed in the D-sharp survey (Dullemond et al. 2018) and scale heights comparable to the results of Kley et al. (2019). There, we also showed that the geometry of the disc, specifically the eccentricity of the inner cavity, can be influenced by an embedded planet. Gap-opening planets typically circularise the disc, while lighter planets or discs with higher viscosity exhibit eccentric holes. We will explore the effect of a wider disc parameter range on the disc architecture in a future study.

To study the parking of planets, we performed numerical hydrodynamical simulations of circumbinary discs using three different parameter sets for the disc physics in order to find a likely combination of viscosity and scale height that results in disc shapes that allow for suitable stopping locations of the planets. Hence, this study extends the work of Pierens & Nelson (2013), where the authors looked at a subset of three systems. The binary and planet parameters used in our simulations are those given by the observations, as presented in Table 1.

In Sect. 2, the adopted model assumptions and initial conditions are defined. Section 3 shows the results of the simulations, where we discuss the influence of viscosity on the planet migration in general and show the effects of different sets of disc parameters on the final orbits of the observed Kepler planets. We discuss the difficulties related to reaching the final orbit and the limitations of our model and we summarise our findings in Sect. 4.

2. Simulations

We used the Pluto Code (Mignone et al. 2007) in the GPU version by Daniel Thun (Thun et al. 2017) to simulate 2D hydrodynamic disc models. We chose a cylindrical grid stretching from 1 to 40 $a_{\rm bin}$ with 684 logarithmically spaced radial grid cells and 584 azimuthal cells. The general design of the simulation follows the setup of Thun & Kley (2018). We modelled nine of the known Kepler binary planet systems, in addition to TOI-1338, for which we used the observed binary and planet properties, as displayed in Table 1.

For the surface density profile, we use $\Sigma \propto R^{-3/2}$ with a disc mass of $M_{\rm d} = 0.01\,M_{\rm bin}$. To speed up the equilibration process for the disc, we initialised the surface density with an inner cavity reaching to about 2.5 $a_{\rm bin}$. Inside of this region, the disc is expected to be cleared due to the action of the binary.

All discs are evolved initially for >25 000 binary orbits, $T_{\rm bin}$, without a planet being present, depending on the specific system setup. A typical time scale for a locally isothermal protoplanetary disc around a binary to reach a convergent quasi-equilibrium state is a few 10 000 $T_{\rm bin}$. Hence, in this work, we use locally isothermal models as they converge faster than a viscously heated radiative disc, which can require up to 200 000 $T_{\rm bin}$, but they eventually reach comparable final states with a pressure profile that is consistent with an unflared inner disc with a constant aspect ratio between 0.05 and 0.03, depending on the system; see Kley et al. (2019) for details. During this initialisation phase the binary is not influenced by the disc. As the final planetary orbits depend on disc properties, we simulated discs for the observed systems in Table 1 for different values of h and α. The viscously heated, radiative models in Kley et al. (2019) result in an unflared inner disc. Therefore, we chose a constant aspect ratio of $h = H/R$. Based on our previous experience (Thun & Kley 2018; Kley et al. 2019), we chose the following three combinations: $h = 0.04, \alpha = 10^{-3}$; $h = 0.04, \alpha = 10^{-4}$; and $h = 0.03, \alpha = 10^{-4}$. It was only for Kepler-38 that we additionally used $h = 0.05$.

After the disc reached a convergent behaviour, we added a planet with an observed mass (see Table 1) in the outer disc that is a few $a_{\rm bin}$ beyond the maximum of the surface density in the disc. In cases where only a upper planet-mass limit was observed, as with Kepler-38, we used the observed upper limit. This might overestimate the actual mass of a planet, but it is still in agreement with the observations. Across the whole sample, the planet masses range from 0.05 $M_{\rm jup}$ to 0.38 $M_{\rm jup}$. The disc exerts gravitational forces on the planet, which will then start migrating through the disc. The disc forces acting on the central binary star are also switched on at this point, but during the time span of the simulations, the binary elements do not change substantially.

3. Results

In this section, we present the results of our numerical studies of the systems quoted in Table 1. We first present the results for different viscosities on the specific system Kepler-35 and then we go on to concentrate on the complete set of systems. An overview of the disc shapes that resulted in planetary evolutions that matched best with the observations is given below in Sect. 3.2.

3.1. Influence of viscosity

To analyse in greater detail the impact of viscosity on the inner cavity, we present the results on the Kepler-35 system in more detail, starting with the disc structure without a planet and then the impact of the planet. The binary system Kepler-35 has a mass ratio that is close to unity, $q_{\rm bin} = 0.91$, and a relatively

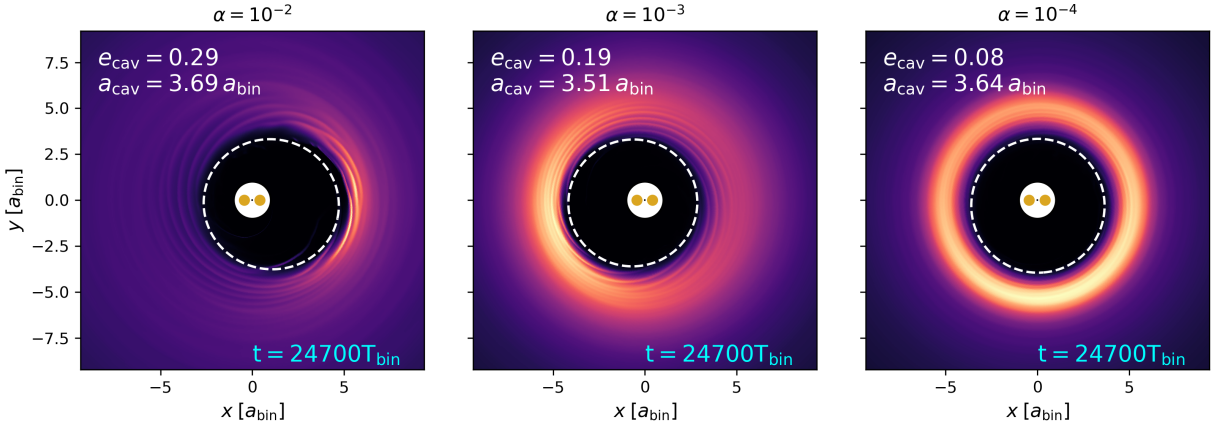

Fig. 1. Surface density for discs around a Kepler-35 like binary for different α-values and an aspect ratio of 0.04. The dashed white line denotes a fitted ellipse (Thun & Kley 2018) which marks the edge of the inner cavity with the parameters displayed in the top left corner.

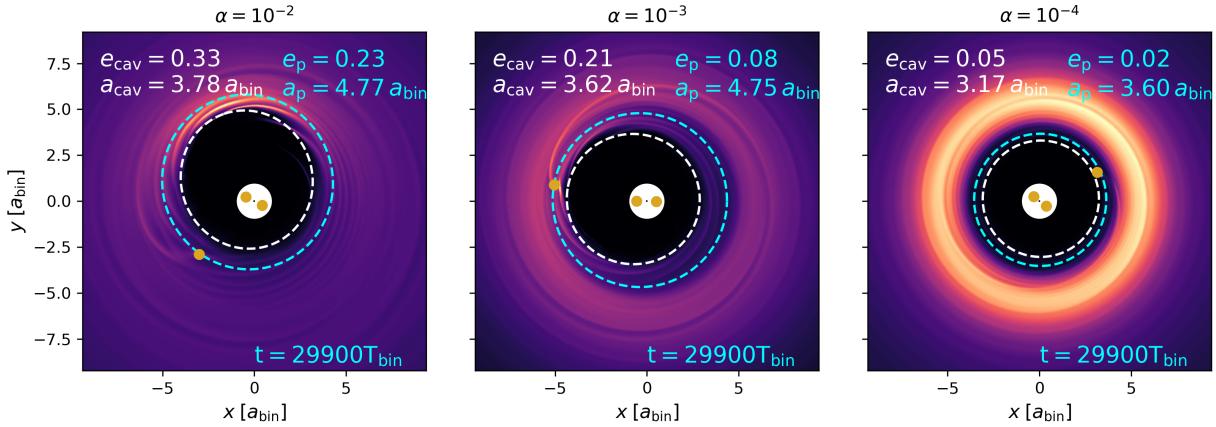

Fig. 2. Discs for a Kepler-35 like system with different α-values with a planet embedded for 29 900 binary orbits. The dashed white line marks the edge of the inner cavity with the parameters displayed in the top right corner. The light blue line marks the orbits of the planet with the parameter displayed in the top left corner.

small eccentricity of $e_{\rm bin} = 0.14$, which puts the system on the lower branch of the bifurcation diagram in the precession period versus cavity size graph (Thun & Kley 2018). In Fig. 1, equilibrium discs with different α-values are displayed for a given scale height $h = 0.04$ to show how much the viscosity influences the disc and cavity structure. The cavity parameters are calculated as described in Thun et al. (2017), meaning that they correspond to the parameters of an ellipse fitted to the location where the azimuthally averaged density is 10% of the maximum density. The cavity and planet orbital parameters are calculated using Jacobi coordinates for the planet-binary system. The disc eccentricity decreases with decreasing viscosity, while the sharpness of the density maximum increases. As all observed planets reside in orbits with relatively low eccentricity, low eccentric cavities will be favourable for their formation, however the presence of the planet will also change the geometry of the disc, as discussed in Mutter et al. (2017) and Kley et al. (2019). Planets with orbits near the inner edge of the disc can circularise the cavity and disc. But high disc eccentricities, as they occur for binaries on circular and high eccentric orbits (Thun & Kley 2018), can hinder a planet from reaching this orbit. Therefore, lower viscosities leading to less eccentric discs are favourable in explaining planet migration into the observed orbits.

A planet with the observed mass of Kepler-35 ($0.12\,m_{\rm jup}$) is embedded in the disc at an initial distance of $6\,a_{\rm bin}$ on a circular orbit and allowed to migrate in the disc. Initially, the embedded planet follows the eccentric gas flow in the disc which makes its orbit eccentric. Planets that do not open a gap in the disc remain embedded and are pushed back by the overdensity at the cavity (see Fig. 1) to a parking position on an eccentric orbit within the disc. This case is shown in the left panel of Fig. 2, where the high disc viscosity does not allow for a planetary gap to be cleared.

However, if planet and disc parameters are such that the planet can open a gap (high planet mass and low disc viscosity and temperature as discussed in Crida et al. 2006), the disc goes on to be circularised and it can pass through the cavity overdensity to a more circular orbit inside of the cavity, as shown in Mutter et al. (2017) and Kley et al. (2019). Kepler-35b and all other observed planets have masses much lower than a Jupiter mass which puts constraints on the disc parameters that are linked to gap opening, such as the viscosity and aspect ratio.

In Fig. 2, the final position and orbit of the planet in these discs is displayed. The gradual deepening of the planetary gap is evident between $\alpha = 10^{-2}$ to $\alpha = 10^{-3}$. Even though the gap in the middle panel is only partially open, it has already begun leading to a reduction in the orbital eccentricity of the cavity and planet. However, in both cases the planet is still too firmly embedded in the disc and influenced by its dynamics, such that the orbit of the planet and the cavity are fully aligned and precess at the same rate, as was also observed in Kley et al. (2019)

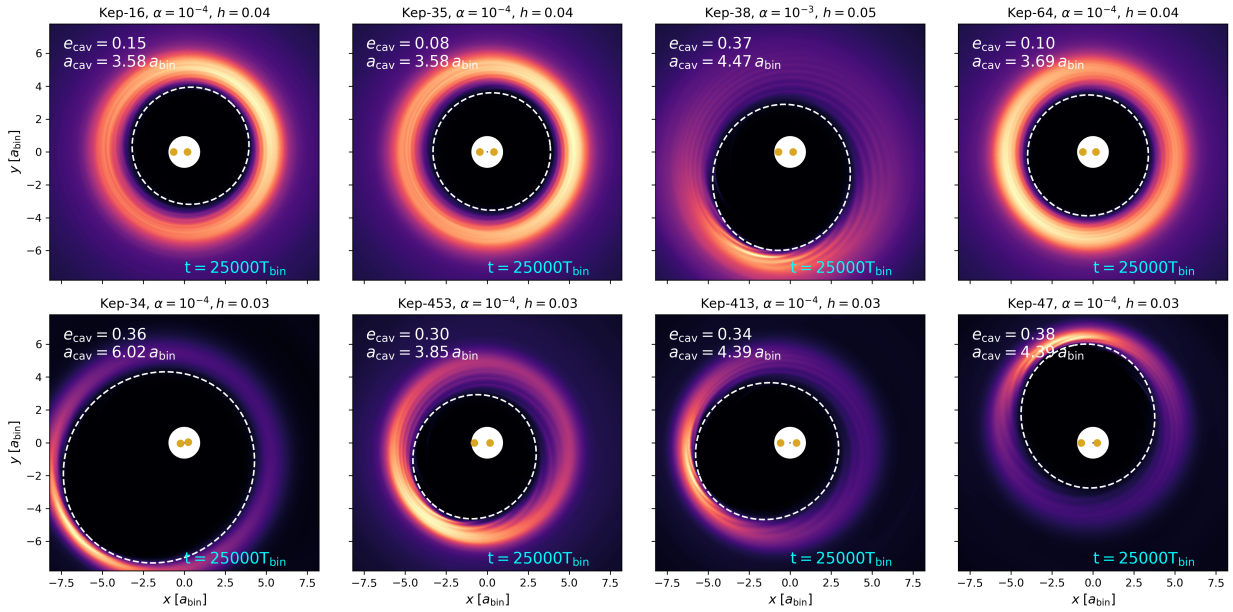

Fig. 3. Surface density of eight modelled Kepler circumbinary systems, listed in Table 1, before the planet was embedded. The chosen h and α correspond to those models that eventually could reproduce the observed final planetary orbits best. The white dashed ellipse marks the inner cavity edge with the parameters shown in the top left.

and Penzlin et al. (2019). For an even lower viscosity of $\alpha = 10^{-4}$ (right panel), the planet opens a deeper gap that directly erases the disc-driven planet dynamics and allows the planet to reach a stable orbit inside the cavity. Therefore, a low disc viscosity tends to have a positive effect on disc structure and planet migration because this favours final planet orbits with low eccentricity, as observed in many systems. Colder and less viscous discs have, on average, a less eccentric cavity. This aids the passage of the planet through the inner cavity.

3.2. Kepler systems

After having demonstrated the main impact of the viscosity on the disc structure and outcome of the planet orbit for Kepler-35, we now present the results for the other systems. Instead of presenting results on the general impact of disc and binary parameters on the cavity dynamics, here we focus solely on that parameter set for which the simulations most successfully reproduced the observed planetary orbits and which is reasonable for a protoplanetary disc. We defer our analysis of a broader parameter range to a future work.

In Fig. 3, we display the disc structure for models that could most successfully reproduce the planetary orbits. The discs are shown at a time before the planet was embedded. As suggested by the results for Kepler-35, discs with low viscosity and also small aspect ratios are favourable in producing the observed orbits, as this combination of disc parameters ensures that the planet opens a gap in its orbit, which results in a more circular disc cavity that allows the planet to migrate closer to the binary. In the top row, we give examples where the final planet orbits matched the observed locations well, while in the lower panel, we show where the agreement was not as good. Indeed, the main difference between the 'successful' top row and the 'unsuccessful' bottom row is the cavity's eccentricity. While the discs in the top row are typically more circular even without any planet, the bottom row discs are noticeably eccentric even for low α-values, due to the low (Kepler-47, Kepler-413, and Kepler-453) or high (Kepler-34) binary eccentricities.

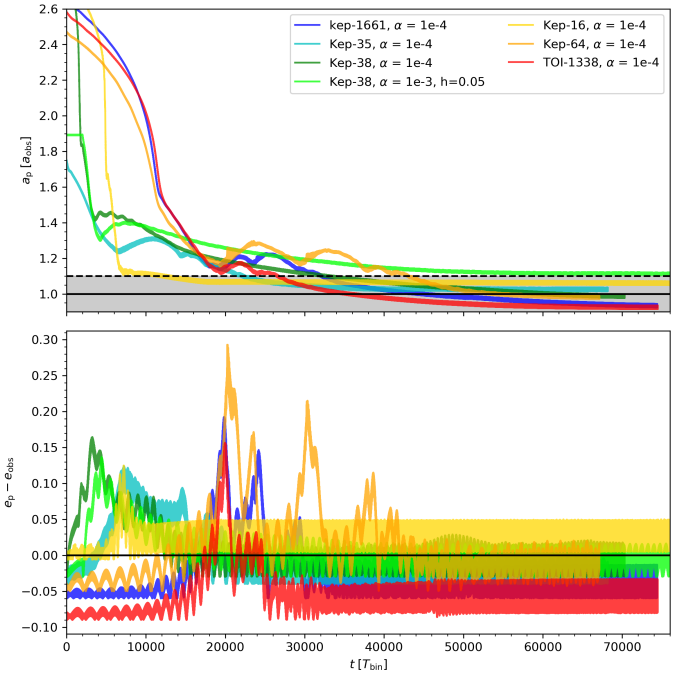

Fig. 4. Migration history for all planets that get close to the observed orbit. The semi-major axis and eccentricity are scaled with the observed a_{obs} and e_{obs}, see Table 1. The grey area marks the success criterion, where the final parking position of the planet deviates by no more than 10% from the observed value, that is, $\Delta a_p/a_{p,obs} \leq 10\%$. For the discs, we chose $\alpha = 10^{-4}$ and $h = 0.04$, plus one additional model for Kepler-38 using the stated values.

After the discs reached a quasi-equilibrium structure, the planets with the observed masses were embedded in the disc at a distance $\geq 6a_{bin}$. Their subsequent migration histories are illustrated in Fig. 4 for those six cases where the match between simulated and observed location was closest. The systems with an intermediate value of e_{bin} show good convergence to the

Table 2. Check-table indicating if a simulation for a given viscous α-value, aspect ratio, h, and planet mass reached the observed orbit.

Kepler-System	$\alpha = 10^{-3}$, $h = 0.04$	$\alpha = 10^{-4}$, $h = 0.04$	$\alpha = 10^{-4}$, $h = 0.03$	$\alpha = 10^{-4}$, $h = 0.04$, $2\,m_p$	$\alpha = 10^{-4}$, $h = 0.04$, $10\,m_p$	obs. a_p, e_p
47	6.6 a_{bin}, 0.23	6.6 a_{bin}, 0.23	5.0 a_{bin}, 0.18	5.0 a_{bin}, 0.18	✓	3.53 a_{bin}, 0.03
413	6.0 a_{bin}, 0.21	5.7 a_{bin}, 0.18	4.8 a_{bin}, 0.15	5 a_{bin}, 0.15	< 3.1 a_{bin}, 0.025	3.55 a_{bin}, 0.12
453	eject	eject	4.8 a_{bin}, 0.12	5.2 a_{bin}, 0.15	< 3.1 a_{bin}, 0.025	4.26 a_{bin}, 0.036
38	3.8 a_{bin}, 0.02	✓				3.16 a_{bin}, 0.03
1661		✓				3.39 a_{bin}, 0.06
35	4.7 a_{bin}, 0.1	✓				3.43 a_{bin}, 0.04
TOI-1338	4.2 a_{bin}, 0.08	(✓), 0.05				3.49 a_{bin}, 0.09
16	4.1 a_{bin}, 0.04	✓				3.14 a_{bin}, 0.006
64	4.8 a_{bin}, 0.08	✓	✓			3.64 a_{bin}, 0.05
34	> 9 a_{bin}, 0.15	7.8 a_{bin}, 0.18	6.4 a_{bin}, 0.17	< 4.5 a_{bin}, < 0.05	4.5 a_{bin}, 0.025	4.76 a_{bin}, 0.18

Notes. The systems are ordered from lowest e_{bin} to highest. Every cell contains the semi-major axis and eccentricity of the final planet orbit of the stated simulation. If not stated (Cols. 2–4), the planet mass corresponds to the observed mass in Table 1. For boxes with a "✓", the planet's final location lies within 0.1 a_{bin} of the observed position. In Cols. 5 and 6 the planet mass in the simulations have been increased by a factor of two and ten, respectively. For comparison, the inferred parameters from the Kepler data are on the right. Blank fields were not simulated.

observed orbits for an α-value of 10^{-4} and an aspect ratio of 0.04 to 0.03. We find here that a low viscosity of $\alpha = 10^{-4}$ is needed for the discs to allow the migration into the observed orbits. For Kepler-38b, we performed an additional run with a higher aspect ratio, $h = 0.05$, because Kepler-38b is the most massive planet of the sample and, as shown in Fig. 4, it reaches just the success-limit with $\alpha = 10^{-3}$, $h = 0.05$ and is expected to cross the dashed line after $120\,000 T_{bin}$. With this slightly higher pressure the density maximum of the disc is reduced leading to a reduce positive torque of the disc onto the planet, allowing it to park closer to the binary than with lower temperatures. Another important factor for this single planet is its high mass. As shown in Table 2, all other planet orbits stay further out for $\alpha = 10^{-3}$, $h = 0.04$ than Kepler-38b. Thereby, Kepler-16, -35, -38, -64, TOI-1338, and also the recently discovered Kepler-1661b (Socia et al. 2020), can be simulated with a single parameter set of $\alpha \sim 10^{-4}$, $h = 0.04$ to produce a final orbit with an accuracy of 0.1 $a_{p,obs}$, as shown in Fig. 4. As can also be seen in Fig. 4, the initial migration in the outer disc is typically very fast because the planets are fully embedded in the disc and have not yet opened any gap. The systems Kepler-1661, -64, and TOI-1338b have a comparable migration rate as their planet-to-binary-mass ratios are very similar. When they reach the high density ring at around 5 a_{bin} or 1.5 a_{obs}, the migration is slowed down. They are influenced by the high density inner disc region and the binary and subsequently experience some variations in their semi-major axis and eccentricity evolutions. The first migration reversal occurs when they are getting close to a semi-major axis of about 4 a_{bin}.

The two systems Kepler-16 and -38 show initially a very fast inward migration. As they have a higher planet-binary mass ratio than the other planets, they would – in the embedded type-I migration phase – exhibit faster inward migration (Kley & Nelson 2012). Additionally, being in the Saturn mass range they are subject to rapid type-III migration (Masset & Papaloizou 2003). In the later evolutionary phase, they begin to circularise the disc and can migrate inwards smoothly. This is especially evident in the unique model of Kepler-38 with high viscosity where the disc eccentricity drops from $e_{cav} \approx 0.37$ without a planet to $e_{cav} \approx 0.09$ with an embedded planet.

Eventually all of them reach an orbit close to the inner cavity edge and stop their inward migration there because the migration torques vanish due to the changing disc structure. The cavity acts in the same way as a classic planet trap where a positive density gradient can stop a planet (Masset et al. 2006). This can be seen in the top row of Fig. 5, where we display the final surface density distribution for the previously shown discs, now with embedded planets, after their migration has stopped. Displayed are the orbital elements of the disc cavity and the planet, in the top left and right corners, respectively. As discussed above, the 'successful' evolutions have a final disc structure with small eccentricity, reduced by the presence of the planet. The planets typically reach a final destination with nearly circular orbits at a distance of approximately 3.4 to 3.6 a_{bin}, as shown in top row of Fig. 5

As already shown in Thun & Kley (2018), binaries with very low and high eccentricities form highly eccentric inner cavities, as shown in Fig. 3 (bottom row). The planet has to overcome the density bulk at the cavity. This is more difficult for more eccentric cavities that have a higher peak density and, therefore, for the high and low e_{bin} systems Kepler-34, -413, -435, and -47. Figure 5 shows the best models of these system with 'non-successful' evolutions in the bottom row. In the top row, the planets reach a final position close to the observed one, whereas in the bottom row, the planets stall further out. In comparing the top systems the lower systems, the discs clearly show a different structure, namely, one in which the planets around the high and low eccentric binaries are more embedded in the disc and remain at larger distances from the binary, also exhibiting a more eccentric orbit. In Fig. 5, the blue and white ellipses in the bottom row show the same orientation, which indicates that the disc-driven planet orbit has become fully aligned with the eccentric cavity. This is shown for Kepler-413 in Fig. 6, the final pericentres of planet and disc orbits are aligned and the ellipses precess at the same rate, as also seen in Kley & Haghighipour (2015), Kley et al. (2019) and Penzlin et al. (2019). There are no clear signs of dynamical interaction (e.g. an oscillation of $\Delta\omega$) visible. However, the determination of the elements of the disc is quite noisy. All the final orbits are aligned with the disc either embedded within the disc or located at the inner cavity edge.

The orbital evolution of the embedded planets in these "unsuccessful" systems (shown in Fig. 7) starts with the same fast initial migration as in the previous cases, but then the inward migration is stalled by the disc too far out. Kepler-34, being the most eccentric binary with an eccentricity of 0.52, produces an

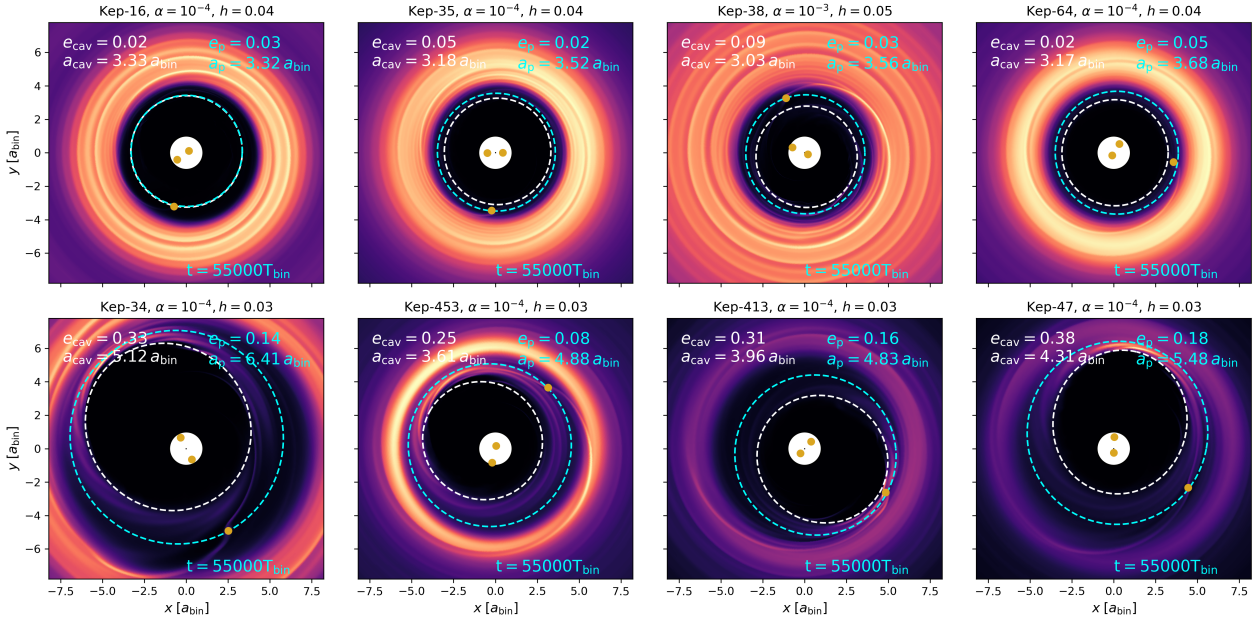

Fig. 5. Discs and planets of eight of the considered Kepler systems listed in Table 1 and shown in Fig. 3, here shown with the embedded planets. The quoted times are measured after insertion of the planets. The chosen aspect ratio, h, and viscosity, α, correspond to those models that most successfully could reproduce the observed planet orbits (see Table 2 below). The white dashed line marks the inner cavity edge and the light blue line the planet orbit. *Top row*: planets that correspond to our success criteria of reaching the observed orbit by $\pm 0.1 a_{\rm obs}$, while *lower row*: systems that did not reach the observed orbit, due to their eccentric discs.

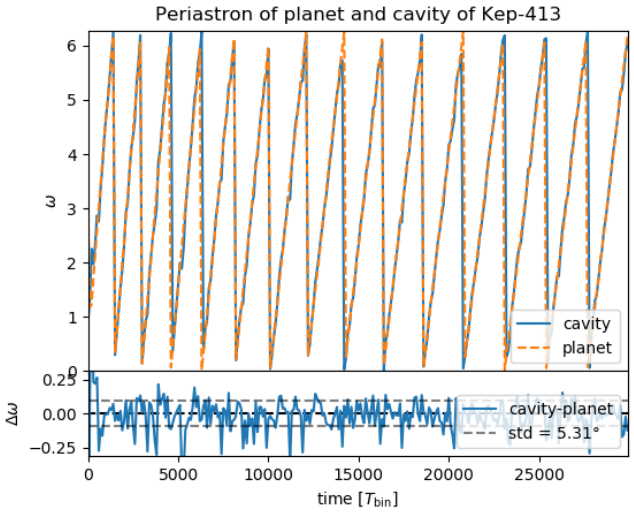

Fig. 6. Argument of pericentre of the elliptic cavity and planet orbit for Kepler-413. The standard deviation of $\Delta\omega = |\omega_{\rm p} - \omega_{\rm cav}|$ is 5.31 degree.

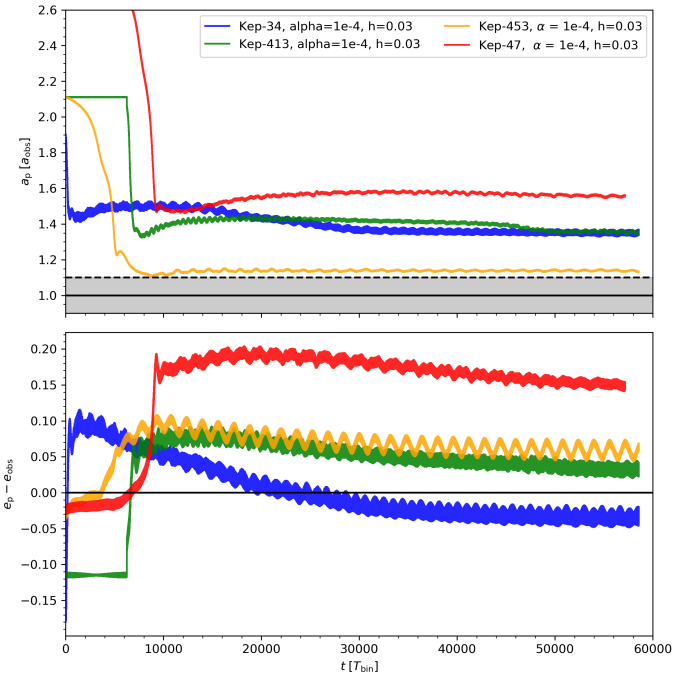

Fig. 7. Migration history for all planets that do not get close enough to the observed orbit. Semi-major axis and eccentricity are scaled with the observed $a_{\rm obs}$ and $e_{\rm obs}$. The grey area marks the success criterion.

eccentric disc with a large cavity and subsequently a planet on a large orbit.

Kepler-453b has the furthest observed orbit of all CBPs (normalised to the binary separation) around low eccentric binaries and it almost reaches the required orbit. In this case, the planet-to-binary-mass ratio is very small, such that the planet is not able to alter the disc structure considerably with the given disc parameters. Kepler-453b has a four times smaller planet-to-binary-mass ratio than Kepler-413b, which is observed to be $0.75\,a_{\rm bin}$ further in. This hints, in a qualitative sense, at the importance of the planet mass for reaching orbits closer to the binary since the dimensions of these systems are comparable. We explore the effect of mass in detail in the next section using models that only shift the planet masses. However, in these simulations, both are stopped by the disc rather than reach an orbit inside the inner cavity. The planets' distant final location for systems with nearly circular binaries and low disc viscosity is not necessarily caused by low planet masses because Kepler-413b has a relatively high mass, with $0.21\,m_{\rm jup}$.

In order to test the hypothesis that the ability of the planet to open a gap is crucial for its detachment from the disc and to reach the observed low eccentric orbits, we ran additional simulations for the low and high $e_{\rm bin}$ systems with planets of two and ten times the observed best-fit mass. Due to the transit observation method, the uncertainty of the observed masses is high and the confidence interval reaches masses of around a factor of two of the best-fit model. For the ten-times heavier model, we chose to vastly overestimate the mass of the planet for the sake of the theoretical exploration and no longer work within the constraints of the observation. We compare this to all the other models in the study in the following subsection.

3.3. Model results and best-fit parameter set

All simulation results are summarised in Table 2, where we make note whether a simulation has successfully reproduced the observational parameter of a given planet. The systems are sorted by the eccentricity of the host binary. With the exception of the heaviest planet, Kepler-38b, the $\alpha = 10^{-3}$ environment is not sufficient to explain the observations. Just by reducing the viscosity to $\alpha = 10^{-4}$, we find that for six out of the ten systems, the final semi-major axis deviates by no more than 10% from the observed value; for more, see the grey shaded region in Fig. 4.

To understand the reasons for the unsuccessful simulations, we have to analyse the differences in the systems. The first three binary systems have $e_{\rm bin} \leq 0.05$. The next six systems have $0.10 \leq e_{\rm bin} \leq 0.21$, while the last system has $e_{\rm bin} = 0.52$. The results can be split into these three regimes.

For the nearly circular binaries, it is difficult to match the observations. However, by reducing the disc scale height and the viscosity to $\alpha = 10^{-4}$ and $h = 0.03$, the planets are able to all migrate further inwards as they are more easily able to clear more of their orbit. In these systems, the effect of a two-fold planet mass increase is comparable to the impact of lowering the disc aspect ratio by 0.01. With the ten-fold mass increase, a planet of $0.5\,m_{\rm jup}$ in the Kepler-47 system can migrate to the observed position. The other heavy planets with a ten-fold mass increase will migrate towards a less eccentric and closer-in position than the observed location and may potentially reach unstable orbits.

The second regime of intermediate eccentric binaries can easily be simulated with the set of $\alpha = 10^{-4}$ and $h = 0.04$. This is a good indication that the conditions in the disc should be comparable to this parameter set. In our previous study (Kley et al. 2019), we showed that in a viscously heated disc, the inner disc scale height is unflared and close to $h = 0.04$. Recent studies, observationally in the D-sharp survey (Dullemond et al. 2018) and theoretically (Flock et al. 2020) suggest that viscosities are $\alpha \leq 10^{-3}$, and therefore our choice of a low viscosity is reasonable. The well-matched final planet orbits can be taken as an additional indicator for low viscosities in protoplanetary discs.

The single observation with very high binary eccentricity Kepler-34 is hard to reproduce. With an increase in planet mass, the correct semi-major axis of the planet could be reached, however the eccentricity is lowered to values below the observed one and it is already too low in a system with a reduced scale height.

4. Discussion and summary

In this work, we perform 2D hydrodynamical simulations of circumbinary discs with embedded planets to explain the orbits of the observed sample of circumbinary planets. One simplification of the model is to use a locally isothermal disc. In a previous work (Kley et al. 2019), we explored viscously heated, radiatively cooled discs. The results showed a plateauing aspect ratio at $0.03 < h < 0.05$ for the inner $15\,a_{\rm bin}$. According to those results, we chose a constant aspect ratio in this range, as this produced a reasonable and well-defined test disc.

In contrast to previous studies, where the planets typically were parked at overly large distances from the binary, our simulations show that we can explain the planetary orbits in systems which have a binary eccentricity between 0.05 to 0.3 by applying a simple locally isothermal model with a parameter set of a viscous $\alpha = 10^{-4}$, and a scale height of $H/r = 0.04$. Variations in the binary mass ratio do not change the results in any significant way (as also found in Thun & Kley 2018). For these systems with intermediate binary eccentricity, planet-to-binary-star-mass ratios between 4.6×10^{-5} (Kepler-1661) and 30×10^{-5} (Kepler-38) are sufficient to carve out planetary gaps, move independently of the disc, and settle to closer orbits. Additionally, the small viscosity circularises the disc even when there is no planet, which allows for tighter orbits as well. Using this parameter set ($\alpha = 10^{-4}, h = 0.04$), we can reproduce the observed orbits of 6 of 10 Kepler circumbinary planets with hydrodynamical simulations and obtain a much closer agreement to the observations for the other four systems than in previous studies.

It is useful to compare our findings to the standard gap opening criteria derived for planets emdedded in discs around single stars. The mass of a planet required to open a gap can be estimated by a thermal and a viscous criterion. The thermal criterion requires the Hill radius to exceed the local pressure scale height, while the viscous criterion requires the gravitational torque to exceed the viscous one. In terms of the aspect ratio, the visocity α and the mass ratio, $q_{\rm p} = m_{\rm p}/M_{\rm bin}$, they read (Bryden et al. 1999):

$$q_{\rm p,th} > 3h^3 \quad \text{and} \quad q_{\rm p,visc} > 40\alpha h^2\,. \tag{1}$$

Up to factors of order unity, these values agree with other criteria (Crida et al. 2006; Ziampras et al. 2020).

For $\alpha = 10^{-4}$ and $h = 0.04$, we find $q_{\rm p,th} \approx 2 \times 10^{-4}$ and $q_{\rm p,visc} \approx 6.4 \times 10^{-6}$. While the viscous criterion is matched by all systems, the thermal one is only fulfilled clearly for Kepler-38b and marginally by Kepler-16b and Kepler-413b. This explains why a larger viscosity ($\alpha = 10^{-3}$) is still sufficient for the Kepler-38 system.

There have been a number of recent studies of the opening and structure of gaps attributed to the activity of planets around single stars (Crida et al. 2006; Duffell & MacFadyen 2013; Fung et al. 2014; Duffell & Dong 2015; Kanagawa et al. 2015, 2016). Given that circumbinary discs and planets become eccentric, planet-induced gap structures are likely to be different in this scenario. Undertaking a detailed study of this goes beyond the scope of this paper, but it would make an interesting topic for future work.

The systems that could not be matched that well were those with very small and large binary eccentricities. For both of these extreme cases, the inner cavity of the disc is most eccentric and the planets were not able to to 'free' themselves from the dynamical forcing of the disc given their masses are at most $0.2\,M_{\rm jup}$. This might be due to the fact that for these eccentric discs higher planet masses are required to clear a gap. This is supported by simulations with artificially increased planet masses, where we observed orbital parameters in closer agreement with the observations. The close, eccentric orbit around the highly eccentric binary (Kepler-34) is still difficult to explain by this simple approach of planet migration within a disc because the presence

of the disc damped the planet eccentricity below the observed value. The study of possible further (tidal) interactions following the dissipation of the disc, however, exceeds the scope of this work.

Even though the thermal mass is nearly reached by the planet for the low $e_{\rm bin}$ Kepler-413 system, the final planet orbit is not in very good agreement with the observed one, which is probably due to the high disc eccentricity. In the other small $e_{\rm bin}$ system Kepler-453, the planet has a very low mass and a relatively large orbit. So for this planet, it appears that the migration was halted by the disc earlier than for the comparable heavier planet in the low eccentricity binary (as in the case of Kepler-413b). Kepler-47 is the only observed multi-planet circumbinary system which may influence the migration.

The upper mass of close-in circumbinary planets in the observations is limited to $\sim 0.4\,M_{\rm jup}$. When we simulated the more massive planets, we observed that heavy planets migrate further in, so they might reach unstable orbits and suffer ejections, which is in agreement with Pierens & Nelson (2008).

The binary parameters may also change over time. However, to make a comparison with the existing systems, we kept them fixed in the initial disc simulation. As the binaries are close, $10\,000\,T_{\rm bin}$ is less than 2000 yr. For the planetary evolution simulations, the binary orbit is also effected by the forces from the disc but changes in the binary parameters over this time frame are negligible, amounting to about 1% in $60\,000\,T_{\rm bin}$. The shrinkage of the binary orbit on longer time scales could be accounted for by starting the system at larger separations than observed today, but that would not be possible via direct hydrodynamical simulations and would lead to the same result eventually.

The reason why some of the systems are characterised by final orbits that remain too eccentric and too far out may also be the result of missing physics in the models. In our models, we neglected radiative transport vertically and within the disc's plane and this could potentially reduce the disc eccentricity. We modelled the discs with 2D simulations but by moving to 3D, it might be possible to obtain better agreement for the systems because disc eccentricities and cavity sizes are different in 3D versus 2D. For example, in their 3D simulations, Pierens & Nelson (2018) found that the planet in the (difficult-to-match) system Kepler-413 indeed moved closer to the binary.

Possibly, multiple planets are present in some of the systems that are even slightly inclined, such that we see only one of the planets. In Penzlin et al. (2019), we showed that a secondary planet does not change the orbit of the first one significantly, hence, we did not include multi-planet simulations here.

It may also be possible to reduce the binary eccentricity through tidal interaction with the planet after the disc has been dispersed. Thereby, the low eccentric binaries may have been more eccentric during the planet formation phase and only lost the eccentricity after the planets reached stable orbits and were thus undisturbed by the outer disc (Zoppetti et al. 2019).

After all, the fact that all planets in systems where the circumbinary discs have an intermediate eccentricity could be matched well shows that the migration scenario of explaining short-period circumbinary planets is very likely to be valid. It is only those systems with highly eccentric discs and large cavities that point towards missing physics or 3D effects to explain their properties.

Acknowledgements. A.P. was funded by grant KL 650/26 of the German Research Foundation (DFG). R.N. acknowledges support from STFC through the Consolidated Grants ST/M001202/1 and ST/P000592/1 and from the Leverhulme Trust through grant RPG-2018-418. The authors acknowledge support by the High Performance and Cloud Computing Group at the Zentrum für Datenverarbeitung of the University of Tübingen, the state of Baden-Württemberg through bwHPC and the German Research Foundation (DFG) through grant no INST 37/935-1 FUGG. The plots in this paper were prepared using the Python library matplotlib (Hunter 2007).

References

Bromley, B. C., & Kenyon, S. J. 2015, ApJ, 806, 98
Bryden, G., Chen, X., Lin, D. N. C., Nelson, R. P., & Papaloizou, J. C. B. 1999, ApJ, 514, 344
Crida, A., Morbidelli, A., & Masset, F. 2006, Icarus, 181, 587
Cuello, N., & Giuppone, C. A. 2019, A&A, 628, A119
Doyle, L. R., Carter, J. A., Fabrycky, D. C., et al. 2011, Science, 333, 1602
Duffell, P. C., & Dong, R. 2015, ApJ, 802, 42
Duffell, P. C., & MacFadyen, A. I. 2013, ApJ, 769, 41
Dullemond, C. P., Birnstiel, T., Huang, J., et al. 2018, ApJ, 869, L46
Dvorak, R. 1986, A&A, 167, 379
Flock, M., Turner, N. J., Nelson, R. P., et al. 2020, ApJ, 897, 155
Fung, J., Shi, J.-M., & Chiang, E. 2014, ApJ, 782, 88
Hunter, J. D. 2007, Comput. Sci. Eng., 9, 90
Kanagawa, K. D., Muto, T., Tanaka, H., et al. 2015, ApJ, 806, L15
Kanagawa, K. D., Muto, T., Tanaka, H., et al. 2016, PASJ, 68, 43
Kley, W., & Haghighipour, N. 2014, A&A, 564, A72
Kley, W., & Haghighipour, N. 2015, A&A, 581, A20
Kley, W., & Nelson, R. P. 2012, ARA&A, 50, 211
Kley, W., Thun, D., & Penzlin, A. B. T. 2019, A&A, 627, A91
Kostov, V. B., McCullough, P. R., Carter, J. A., et al. 2014, ApJ, 784, 14
Kostov, V. B., Orosz, J. A., Feinstein, A. D., et al. 2020, AJ, 159, 253
Lubow, S. H., & Martin, R. G. 2018, MNRAS, 473, 3733
Martin, D. V. 2019, MNRAS, 488, 3482
Martin, R. G., & Lubow, S. H. 2017, ApJ, 835, L28
Masset, F. S., & Papaloizou, J. C. B. 2003, ApJ, 588, 494
Masset, F. S., Morbidelli, A., Crida, A., & Ferreira, J. 2006, ApJ, 642, 478
Meschiari, S. 2012, ApJ, 761, L7
Mignone, A., Bodo, G., Massaglia, S., et al. 2007, ApJS, 170, 228
Mutter, M. M., Pierens, A., & Nelson, R. P. 2017, MNRAS, 469, 4504
Orosz, J. A., Welsh, W. F., Carter, J. A., et al. 2012a, ApJ, 758, 87
Orosz, J. A., Welsh, W. F., Carter, J. A., et al. 2012b, Science, 337, 1511
Orosz, J. A., Welsh, W. F., Haghighipour, N., et al. 2019, AJ, 157, 174
Paardekooper, S.-J., Leinhardt, Z. M., Thébault, P., & Baruteau, C. 2012, ApJ, 754, L16
Penzlin, A. B. T., Ataiee, S., & Kley, W. 2019, A&A, 630, L1
Pierens, A., & Nelson, R. P. 2008, A&A, 483, 633
Pierens, A., & Nelson, R. P. 2013, A&A, 556, A134
Pierens, A., & Nelson, R. P. 2018, MNRAS, 477, 2547
Pierens, A., McNally, C. P., & Nelson, R. P. 2020, MNRAS, 496, 2849
Schwamb, M. E., Orosz, J. A., Carter, J. A., et al. 2013, ApJ, 768, 127
Silsbee, K., & Rafikov, R. R. 2015, ApJ, 808, 58
Socia, Q. J., Welsh, W. F., Orosz, J. A., et al. 2020, AJ, 159, 94
Thun, D., & Kley, W. 2018, A&A, 616, A47
Thun, D., Kley, W., & Picogna, G. 2017, A&A, 604, A102
Welsh, W. F., Orosz, J. A., Carter, J. A., et al. 2012, Nature, 481, 475
Welsh, W. F., Orosz, J. A., Short, D. R., et al. 2015, ApJ, 809, 26
Ziampras, A., Ataiee, S., Kley, W., Dullemond, C. P., & Baruteau, C. 2020, A&A, 633, A29
Zoppetti, F. A., Beaugé, C., Leiva, A. M., & Folonier, H. 2019, A&A, 627, A109

Astronomy & Astrophysics manuscript no. cb_revise
February 11, 2022
©ESO 2022

Binary orbital evolution driven by a circumbinary disc

Anna B. T. Penzlin, Wilhelm Kley*, Hugo Audiffren and Christoph M. Schäfer

Institut für Astronomie und Astrophysik, Universität Tübingen, Auf der Morgenstelle 10, D-72076, Germany
e-mail: anna.penzlin@uni-tuebingen.de

ABSTRACT

The question whether the interaction of a circumbinary disc with the central binary system leads to shrinking or expansion of the binary orbit has attracted considerable interest as it impacts the evolution of binary black holes and stellar binary stars in their formation phase. We performed two-dimensional hydrodynamical simulations of circumbinary discs for a large parameter set of disc viscosities and thicknesses and two different binary mass ratios for binaries on circular orbits. For those we measured carefully the net angular momentum and mass transfer between disc and binary system, and evaluate the normalised specific angular momentum accretion, j_s. This is compared to the theoretical, critical specific angular momentum change $j_{s,crit}$ that separates contracting from expanding cases which depends on the the binary's mass ratio and the relative accretion onto the two stars. Using finite and infinite disc models we show that the inferred binary evolution is very similar for both setups and confirm that j_s can be measured accurately with cylindrical simulations that do not include the central binary. However, to obtain the relative accretion onto the stars for non-equal mass binaries, simulations that cover the whole domain including the binary are required. We find that for thick discs with aspect ratio $h = 0.1$ the binaries expand for all viscosities, while discs with $h = 0.05$ lead to an expansion only for larger viscosities with α exceeding ~ 0.005. Overall, the regime of binary expansion extends to a much wider parameter space than previously anticipated, but for thin, low viscosity discs the orbits shrink.

Key words. Hydrodynamics – Binaries: general – Accretion, accretion discs – Protoplanetary discs

1. Introduction

Circumbinary (CB) discs orbiting two gravitating objects exist over a wide range of spatial scales, starting from spectroscopic binary stars, then to large binary systems like GG Tau, and finally all the way to galactic discs around binary black holes. The binary star and the disc resemble a coupled system that exchanges mass and angular momentum between its components leading possibly to a secular evolution of the binary's orbit, i.e. changes in its semi-major axis and eccentricity. Due its gravitational action the binary transfers angular momentum to the disc. As a consequence the disc recedes from the binary opening a central cavity, while the binary reacts with a shrinkage of its orbit accompanied by an increase in its eccentricity (Artymowicz et al. 1991). In the context of black holes such a disc induced orbital evolution was already suggested by Begelman et al. (1980) to overcome the so called 'final parsec problem' (Milosavljević & Merritt 2003), i.e. the necessary contraction of the orbit such that gravitational wave emission can set in. In the context of binary star formation a CB-disc will be formed that determines the binary orbital evolution similarly.

Given the binary's gravitational torque acting on the CB-disc and its own angular momentum loss, it was always assumed that the binary can only react with a shrinkage of the orbit. This point of view was questioned by Miranda et al. (2017) who argued that for certain binary parameter the mass accretion and, hence, accreted angular momentum onto the central binary can counterbalance and even overcome the disc torques leading to an expansion of the orbit. This has led to an increased activity to study the still controversial issue of binary orbit evolution in more detail using various numerical approaches.

In their simulations Miranda et al. (2017) used a grid-code operating in cylindrical coordinates, where the binary stars orbited inside of the computational domain, and their evolution was calculated by monitoring mass and angular momentum balance of the surrounding disc. Concerns about the impact of the grid's inner radius on the outcome were resolved by simulations that covered the whole domain including the stars. Using a moving mesh code, Muñoz et al. (2019) presented simulations that covered the whole domain and clearly demonstrated that the orbits of binary stars can indeed expand due to the action of a CB-disc, a result which was confirmed by Moody et al. (2019) using a Cartesian grid. The topic of binary evolution was treated subsequently by different groups (e.g. Muñoz et al. 2020; Duffell et al. 2020; Tiede et al. 2020; Heath & Nixon 2020; Zrake et al. 2021) using different numerical approaches.

The first works (Miranda et al. 2017; Muñoz et al. 2019; Moody et al. 2019) focused primarily on equal mass binaries surrounded by discs with high viscosity ($\alpha = 0.1$) and larger thickness ($H/r = 0.1$) because those reach a quasi-stationary state earlier, and are easier to simulate. Taking into account the disc's backreaction on the binary Muñoz et al. (2019) shows that initially circular binaries remain circular during the evolution. Later, Muñoz et al. (2020) performed a larger parameter survey where they varied the viscous α parameter from 0.01 to 0.1 and the binary star mass ratio M_2/M_1 from 0.1 to 1.0. They found that bina-

* passed away

ries with larger mass ratio ($M_2/M_1 > 0.3$) expand independently of the used α-value.

The quoted studies agree that for an equal mass binary system inside a thick disc with $H/r \sim 0.1$ and a large viscosity, the added angular momentum of the disc is sufficient to allow for an expanding binary orbit. However, Tiede et al. (2020) applying a constant kinematic viscosity , varied the disc thickness and found that for thinner discs with $H/r \lesssim 5\%$ the trend reverses and the binary orbit shrinks again. According to Tiede et al. (2020) the reason for the change of this behaviour lies in the fact that in thinner discs the cavity is deeper and more material remains near the cavity walls exerting a negative torque on the binary.

In general, disc parameters such as scale height and viscosity influence shape and size of the eccentric inner disc cavity (Thun et al. 2017; Thun & Kley 2018; Hirsh et al. 2020; Penzlin et al. 2021), which in turn impacts the transfer of angular momentum between disc and binary. It is still an open question how the binary's orbit will evolve for ranges of physical disc parameter towards low viscosity and disc heights. In this paper we present our results of a wider parameter study. In particular, we are interested in thin discs resembling a protoplanetary environment.

Using two binary mass ratios we compute the evolution of a CB-disc varying the viscosity and aspect ratio independently and calculate the binary's orbital evolution. We will present models using an α-type disc viscosity, as well as constant viscosity models. Our study is restricted to circular binaries to reduced the changing orbit parameters to the semi-major axis and make long model runs for low viscosities feasible.

We confirm the statement made by Miranda et al. (2017) that for circular binaries their change in semi-major axis can be accurately obtained from simulations using a cylindrical grid that surrounds the binary, if all the relevant fluxes across the boundaries are measured, and for a known mass accretion ratio between the stars. Using infinite as well as finite disc profiles we show that the inferred binary evolution is very similar for both setups (see also Muñoz et al. 2020). We expand the parameter range to thinner as well as less viscous discs, relevant for protoplanetary scenarios, and determine the transition between expanding and shrinking binary orbits. To validate our results, we use two grid codes utilising different numerical algorithms, `RH2D` (Kley 1989, 1999) and `PLUTO` (Mignone et al. 2007; Thun et al. 2017). To estimate directly the mass accretion onto the individual stars, we used `RH2D` on a Cartesian grid and additionally Smoothed Particle Hydrodynamics (SPH) simulations (Schäfer et al. 2016) (see Appendix B).

In Section 2 we discuss the angular momentum evolution of disc and binary from a theoretical standpoint, and define a critical specific angular momentum accretion rate that separates inspirals from expansions. We present our physical and numerical setup for the two simulation codes in Section 3 and display in Section 4 the results of the simulations for one standard model. Section 5 gives an overview of the results for our parameter sets in viscosity, scale height and binary mass ratio. Finally, we discuss and summarise our findings in Sections 6.

2. Angular momentum evolution of disc and binary

Before presenting our numerical results we briefly discuss the orbital evolution of the central binary from a theoretical standpoint. Similar considerations were presented for example by Muñoz et al. (2019) and Dittmann & Ryan (2021). For a binary with total mass M_b, semi-major axis a and eccentricity e the orbital angular momentum is given by

$$J_\mathrm{b} = \mu_\mathrm{b} \left[G M_\mathrm{b} a (1-e^2) \right]^{1/2} , \tag{1}$$

where

$$\mu_\mathrm{b} = \frac{M_1 M_2}{M_1 + M_2} = \frac{q}{(1+q)^2} M_\mathrm{b} \tag{2}$$

is the reduced mass and $q = M_2/M_1$ is the mass ratio of the binary star with $M_2 \leq M_1$. The time evolution of the angular momentum involves changes of the four quantities $M_\mathrm{b}(t), q(t), a(t)$ and $e(t)$, which requires in turn knowledge about four parameters: the change in total mass, orbital angular momentum, momentum, and a knowledge about how the accreted mass and momentum is distributed amongst the two stars. These distributions can be calculated in simulations that include the binaries and flows onto the binaries in the domain with high resolution, as done for example in Muñoz et al. (2020) for thick discs. For long runs with low viscosity and thin discs a domain including the binary is currently not feasible.

In this work we will from now on assume $e = 0$. By restricting our study to circular binaries with maximum angular momentum for given masses, any addition of angular momentum will not raise the eccentricity, but rather lead to an expansion of the orbit that remains circular. This is supported by simulations of Muñoz et al. (2019) who find only very small increase of binary eccentricity in their simulations. Hence, we do not consider any change of the binary eccentricity and set $\dot{e} = 0$. Taking the time derivative of eq. (1) for circular binaries yields

$$\frac{\dot{J}_\mathrm{b}}{J_\mathrm{b}} = \frac{\dot{q}}{q}\frac{1-q}{1+q} + \frac{3}{2}\frac{\dot{M}_\mathrm{b}}{M_\mathrm{b}} + \frac{1}{2}\frac{\dot{a}}{a} , \tag{3}$$

where the change in mass ratio, $\dot{q}/q$ in terms of the mass changes of the individual stars is given by

$$\frac{\dot{q}}{q} = \frac{\dot{M}_2}{M_2} - \frac{\dot{M}_1}{M_1} . \tag{4}$$

The change in binary mass is directly given by the mass accretion rate from the disc, i.e. the material that is advected from the disc onto the stars, $\dot{M}_\mathrm{b} = \dot{M}_\mathrm{adv}$, but for the change in angular momentum there are two contributions, first the accreted angular momentum from disc, $\dot{J}_\mathrm{adv}$, which accompanies the mass flux, and secondly the gravitational torque exerted by the disc on the binary, $\dot{J}_\mathrm{grav}$. In principle, there could also be a viscous angular momentum flux across the inner boundary (positive or negative) but this turned out to be very small in our simulations and is neglected here.

The angular momentum change of the binary can either go into the orbit and/or the spins of the individual stars. Here, we assume that the latter contribution is overall small, as shown in Muñoz et al. (2019), and consider only the change of the binary's orbit.

In our typical longterm simulations the stars are not within the computational domain, hence in order to account for the a priori unknown distribution of mass amongst the

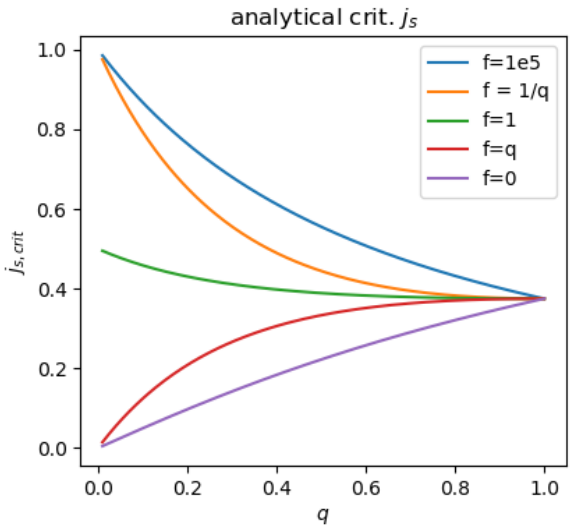

Fig. 1: Critical angular momentum transfer to the binary as a function of the binary mass ratio for different values of the accretion factor, see eq. (9). If the binary receives angular momentum at a rate larger than $j_{\rm s,crit}$ then its orbit expands. Displayed are 5 different values for the factor f that enclose all cases between the two limiting cases of $f = 0$ (accretion only on the primary) and $f \to \infty$ (accretion only on the secondary).

two stars, we introduce the factor f. It denotes the mass distribution between the individual stars and is defined by

$$\dot{M}_2 = f\dot{M}_1\,, \tag{5}$$

i.e. the secondary receives f times as much mass as the primary. Then we find with eq. (4)

$$\frac{\dot{q}}{q} = \frac{1+q}{1+f}\left(\frac{f}{q}-1\right)\frac{\dot{M}_{\rm adv}}{M_{\rm b}}\,. \tag{6}$$

To rewrite eq. (3) in terms of the change in semi-major axis as we use $\dot{J}_{\rm b} = \dot{J}_{\rm adv} + \dot{J}_{\rm grav}$, and define the (normalised) *specific angular momentum transfer*, $j_{\rm s}$, to the binary as

$$\frac{\dot{J}_{\rm b}}{\dot{M}_{\rm adv}}\frac{M_{\rm b}}{J_{\rm b}} = \frac{\dot{J}_{\rm b}}{\dot{M}_{\rm adv}}\frac{1}{\sqrt{GM_{\rm b}a}}\frac{(q+1)^2}{q} \equiv j_{\rm s}\frac{(q+1)^2}{q}\,. \tag{7}$$

The change in semi-major axis of the binary can then be written as

$$\frac{\dot{a}}{a} = \frac{\dot{M}_{\rm adv}}{M_{\rm b}}\left[2\,j_{\rm s}\frac{(q+1)^2}{q} - 3 - 2\frac{1-q}{1+f}\left(\frac{f}{q}-1\right)\right]. \tag{8}$$

This equation is equivalent to eq. (9) in Muñoz et al. (2020), where their angular momentum accretion eigenvalue is given by $l_0 = j_s a^2\Omega_{\rm b}$ and their 'preferential accretion ratio' is $\eta \equiv \dot{M}_2/M_{\rm b} = f/(1+f)$. A similar expression was given by Dittmann & Ryan (2021). To find the critical $j_{\rm s}$, at which the orbit changes from contracting to expanding, we set $\dot{a} = 0$ and obtain

$$j_{\rm s,crit} = \frac{2+q}{2(1+q)^2} - \frac{1-q}{(1+f)(1+q)}\,. \tag{9}$$

If the specific angular momentum transfer is larger than $j_{\rm s,crit}$ the binary orbit will expand, while it will contract for $j_{\rm s}$ smaller than the critical value. For equal mass binaries with $q = 1$, only the first term remains and equals $3/8$, identical to the value found by Miranda et al. (2017), and used later by Tiede et al. (2020). In Fig. 1 the critical values of the angular momentum transfer, $j_{\rm s,crit}$, are shown as a function of the mass ratio, q, for selected sample values for the mass accretion ratio, f, between the stars. All values of $j_{\rm s,crit}$ are between 0 and 1, for any value of q or f. As discussed above, for $q \to 1$ all curves converge to $j_{\rm s,crit} = 3/8$. In the case that both stars accrete the same mass, $f = 1$, the critical $j_{\rm s,crit}$ lies always above $3/8$. It becomes maximal if the secondary star would accrete all mass, $f \to \infty$.

In the following we present the results of our hydrodynamical simulations to analyse for which binary and disc parameter the specific angular momentum accretion is larger than $j_{\rm s,crit}$ and thereby sufficient to lead to an expanding binary orbit.

3. Modelling

In this section we describe first our physical setup, then the numerical methods and boundary conditions and finally the measuring procedure of the mass and angular momentum balance.

3.1. Physical setup

In our study we restrict ourselves to infinitesimally thin two-dimensional (2D) discs that orbit a central binary. The plane of the disc and the binary are coplanar. The system is modelled using polar coordinates with the origin at the centre of mass (COM) of the binary star. For the simulations we keep the binary's orbit fixed and the disc is not self-gravitating. To allow for a scale free setup, we adopt a locally isothermal equation of state, with respect to the binary's COM. The disc is not flared but has a constant disc aspect ratio $h = H/r$, where H is the pressure scale height of the disc at distance r. For the viscosity we assume the classic alpha-ansatz and write for the kinematic viscosity coefficient $\nu = \alpha c_{\rm s} H$, where $c_{\rm s}$ is the isothermal sound speed of the gas.

For the initial setup of our problem we follow Muñoz et al. (2020) and use a finite extent of the initial density distribution, which has the shape of a circular gas torus around the binary. For this purpose we define the two radii $r_{\rm in}$ and $r_{\rm out}$, as well as the two functions

$$g_{\rm in}(r) = \frac{1}{1+\exp\left[-(r-r_{\rm in})/(0.1\,r_{\rm in})\right]} \tag{10}$$

and

$$g_{\rm out}(r) = \frac{1}{1+\exp\left[r-r_{\rm out}\right]}\,. \tag{11}$$

The initial density is then given by

$$\Sigma_0(r) = \Sigma_{\rm base}(r) \times \left[1 - \frac{0.7}{\sqrt{r}}\right] \times g_{\rm in}(r) \times g_{\rm out}(r)\,. \tag{12}$$

Here, $\Sigma_{\rm base}(r)$ denotes a basic power law profile for the density for which we use $\Sigma_{\rm base}(r) \propto r^{-1/2}$ throughout. The constants are chosen such that shapes similar to Muñoz et al. (2020) can be constructed. These cut-off functions create

q	α	h	$r_{\rm in}$	$r_{\rm out}$
0.5	0.1	0.1	2.5	6.0

Table 1: Summary of the physical parameters for the standard model. The values are: the binary star mass ratio $q = \mathrm{M}_2/\mathrm{M}_1$, the disc viscosity α, aspect ratio h, and the disc's initial radial extent $r_{\rm in}, r_{\rm out}$ (see eqs. 10 and 11).

a smooth transition to a low density beyond $r_{\rm in}$ and $r_{\rm out}$. Varying these can be useful start from conditions closer to the convergent state. An example of such an initial Σ-profile is displayed below in Fig. 2 for our standard model.

To have a well defined test case we define a *standard model* which has the following parameter: For the binary we chose $q = M_2/M_1 = 0.5$, and for the disc $\alpha = 0.1$ and $h = H/r = 0.1$ (like Muñoz et al. 2019). Here, the large viscosity and disc thickness allow for a fast evolution of the disc, and disc matter will be accreted rapidly onto the binary and spread outwards.

The parameter of the standard model and for the initial surface density are summarised in Table 1. In a detailed parameter study we will study the effect of varying the viscosity α, and aspect ratio h for two values of the binary mass ratio q.

3.2. Numerics

For the main part of this paper we performed numerical simulations over very long time scales in order to cover discs with alpha-viscosities down to 10^{-3}. To allow for a reasonable computational time the binary stars are not included in the domain. In the Appendix B.1 we present an example of a completely covered inner domain for the standard model to the derive the accretion ratio f.

We use two grid-based codes operating on a cylindrical grid stretching from $r_{\rm min} = a$ to $r_{\rm max} = 40a$ with 684 logarithmically spaced radial grid cells and 584 azimuthal cells. Following our previous study (Thun & Kley 2018) the value $r_{\rm min} = a$ captures the essential dynamics for discs with a significant inner cavity, and we used this value for our parameter study. We will show in section 4.3 how the choice of $r_{\rm min}$ possibly affects our measured accretion of mass, angular momentum and $j_{\rm s}$. Concerning the outer radius, it has to be chosen large enough such that it does not impact the disc's evolution for large and eccentric cavities. Here, we found $r_{\rm max} = 40a$ sufficient. The simulations are carried out in dimensionless units where the unit of length is the binary separation a, the gravitational constant $G = 1$, the binary mass $M = 1$ and the binary orbital angular velocity $\Omega_{\rm b} = 1$.

An important ingredient of grid-based simulations is the necessity of a density floor to prevent negative densities and pressures. For the standard case with its high aspect ratio and large viscosity the inner region close to the stars will never be very empty such that a floor density of $\approx 10^{-6}$ of the initial maximum density is sufficient. However, for the parameter studies with very small h and α the cavities around the binary become very deep and much lower floor values $\approx 10^{-10} - 10^{-8}$ are required, in order to follow the very small mass and angular momentum accretion onto the binary.

In order to validate our results we first calculated the standard model using two grid codes with different numerics, `RH2D` (Kley 1989) and `PLUTO` (Mignone et al. 2007). We describe the details of the codes and comparison runs in the appendix A.

3.3. Boundary conditions

The cylindrical grid simulations conserve global angular momentum, at least within the active domain. In our models the inner boundary (at $r_{\rm min}$) is open to angular momentum and mass flow towards the star. We use an inner radial boundary condition of $\partial\Sigma/\partial r = 0$ for the density, $\partial\Omega/\partial r = 0$ for the azimuthal velocity, and a diode-type radial infall with $v_{r,\rm ghost} = \min(v_{r,\rm min}, 0)$. The zero gradient condition for the angular velocity implies a vanishing torque at the inner boundary, at least for circular flows, and ensures that the disc is not artificially torqued from inside. We tested other conditions for $\Omega(r_{\rm min})$, such as zero gradients of the angular momentum, but found no differences in the disc's evolution. At the outer boundary we use reflecting conditions where the radial velocity is set to zero at the outer boundary, $v_{r,\rm max} = 0$. For the azimuthal velocity we assume the circular Keplerian velocity around the binary's COM. While the outer boundary is closed to mass flow angular momentum is nevertheless transmitted through $r_{\rm max}$ through viscous torques which is monitored during the evolution. Additional models resembling an 'infinite' disc setup are presented in Subsection 5.4.

3.4. Measuring the angular momentum and mass balance

To calculated the orbital evolution of the binary, we need to monitor the mass and angular momentum accretion from the disc, Even though these are losses with respect to the disc, we consider here the gain with respect to the binary star and take them as positive quantities, denoting them as $\dot{M}_{\rm adv}$ and $\dot{J}_{\rm adv}$. The subscript 'adv' denotes advection (transport) of the quantities across the inner radius of the disc. For the mass flux this transport is solely advective and given by

$$\dot{M}_{\rm adv} = \oint \Sigma r\,|v_r|\,d\phi\Big|_{r=r_{\rm min}}\,, \tag{13}$$

where v_r is the radial velocity of the gas, which can only be negative (or zero) for the used boundary condition, i.e. $v_r(r_{\rm min}) \le 0$. For the angular momentum accretion the advective transport across the inner boundary reads

$$\dot{J}_{\rm adv} = \oint \Sigma r\,|v_r|\,r v_\phi\,d\phi\Big|_{r=r_{\rm min}}\,. \tag{14}$$

We evaluated the angular momentum and mass flow rate through the inner boundary, typically at $r_{\rm min} = a$. As a consistency test we also measured the flow at different inner radii in the same model ($r = [1.25, 1.5, 2]\,a$). For the equilibrium state we find the same values, as expected. However, for even smaller inner evaluation radii the circum-secondary disc can interfere with the calculated advection, depending on the mass ratio. More details on smaller $r_{\rm min}$ models are shown below in Sect. 4.3. The second change of the binary angular momentum is due the disc's gravitational torque

$$\dot{J}_{\rm grav} = \sum_{k=1}^{2} GM_k \int_{\rm disc} \Sigma(r,\phi)\frac{\mathbf{r}_k \times (\mathbf{r} - \mathbf{r}_k)}{|\mathbf{r} - \mathbf{r}_k|^3} r d\phi dr\,. \tag{15}$$

While the advective transport is always positive this last contribution can take both signs.

While the quantities $\dot{M}_{\rm adv}$ and $\dot{J}_{\rm adv}+\dot{J}_{\rm grav}$ are sufficient to evaluate the orbital evolution for circular binaries, it is very useful to have a simple alternative measuring instrument. This is accomplished by simply monitoring the total disc mass, $M_{\rm disc}$, and angular momentum $J_{\rm disc}$ within the computational domain. As the outer boundary at $r_{\rm max}$ is closed $-\dot{M}_{\rm disc} = \dot{M}_{\rm adv}$. For the angular momentum there is an additional viscous loss channel through the outer boundary given by

$$\dot{J}_{\rm visc} = \int_0^{2\pi} \left(\Sigma\nu r^2 T_{r\phi} d\phi\right)\Big|_{r=r_{\rm max}} \tag{16}$$

with the viscous stress tensor

$$T_{r\phi} = r\frac{\partial\Omega}{\partial r} + \frac{1}{r}\frac{\partial v_r}{\partial\phi}\,. \tag{17}$$

Written as such, the sign of $\dot{J}_{\rm visc}$ denotes either gains (>0) or losses from the disc (<0). Thus the angular momentum can be compared using: $-\dot{J}_{\rm disc}=\dot{J}_{\rm adv}+\dot{J}_{\rm grav}+\dot{J}_{\rm visc}$. This monitoring of the global disc properties throughout the simulations allows for a very useful consistency check on overall mass and angular momentum conservation of the numerics.

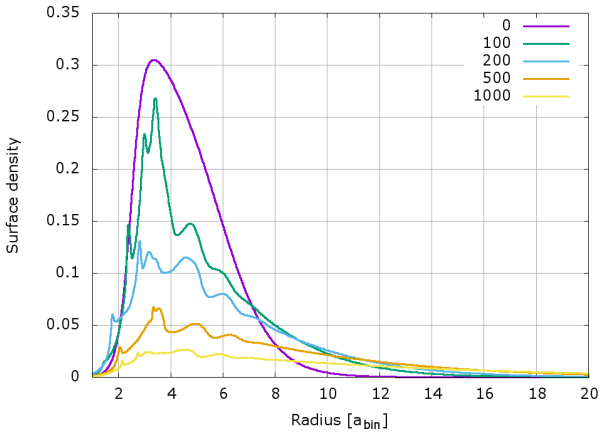

Fig. 2: Azimuthally averaged surface density for the standard model ($q=0.5, h=0.1, \alpha=0.1$) at five different times, quoted in binary orbits.

4. The standard model

In this section we present our results for the standard model which has the parameter stated in Table 1. First, a general overview of the main disc physics will be given, followed by a discussion on the choice of the inner radius of the domain, $r_{\rm min}$, and then the expected binary evolution.

4.1. Disc structure

Most of the results quoted in this subsection are obtained with the RH2D code, unless otherwise stated. Given the inner and outer radii, $r_{\rm in}=2.5$ and $r_{\rm out}=6$ for the standard model, an initial density setup similar to Muñoz et al. (2020) was generated as shown in Fig. 2. The density has its maximum near $r=3.5a$ and drops smoothly inwards and outwards. The initial and subsequent evolution of the azimuthally averaged surface density, displayed at five different snapshots in Fig. 2, shows a radial spreading of this initial ring-like density, while the maximum of $\Sigma(r)$ remains always close to the initial one. The evolution is very fast for this setup, already at $t=200\,T_{\rm bin}$ the density maximum has dropped by about a factor of three, and the disc has lost about 20% of its initial mass through the inner boundary. To give an impression of the dynamical features of the disc flow in the vicinity of the binary we present in Fig. 3 the 2D density distribution after a simulated time of $500\,T_{\rm bin}$.

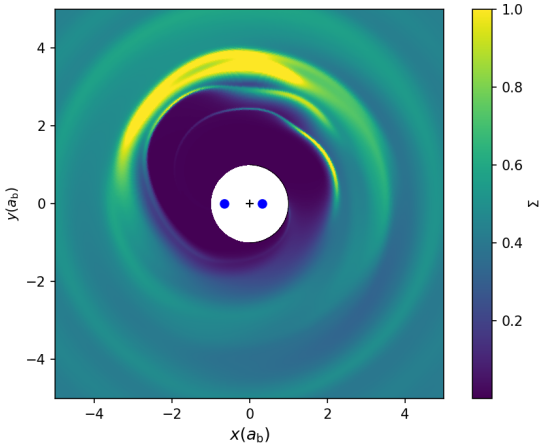

Fig. 3: The 2D surface density distribution at $500\,T_{\rm bin}$ for the standard setup. The black cross marks the binary's barycenter and the region within $r=1\,a_{\rm bin}$ is not part of the computational domain.

To have an indicator of the size and distortion of the inner cavity as the simulations evolves, we fit approximate ellipses to its shape using the procedure described in Thun et al. (2017). The result for the semi-major axis $a_{\rm cav}$ and eccentricity $e_{\rm cav}$ of the cavity is displayed in Fig. 4 for the two different codes used in our main study. After a brief initial growth phase, lasting for about 200-300 binary orbits, the cavity size reaches a maximum radial extent of $a_{\rm cav}\sim 2.25a$ and a moderate eccentricity of $e_{\rm cav}\sim 0.18$. The shape of the cavity is (for these disc parameter) only an approximate ellipse, such that the automatic fitting routine (see Thun et al. 2017) may be misguided by local density maxima peaks as seen in Fig. 3. As a consequence the values vary a lot as indicated by the grey shaded points. This issue is significantly reduced for simulations with smaller viscosities as the density inside the spirals is reduced and the peak density is clearly located at the apocentre of the inner disc, see also Penzlin et al. (2021). The results for the two grid-codes agree reasonably well. Differences can be due the fact that in RH2D results are computed automatically 'on the fly' while the simulations are running, whereas for PLUTO they are obtained in a post-processing step from different snapshots, here once every $T_{\rm bin}$. In the following we will display smoothed results, here averaged over $10\,T_{\rm bin}$.

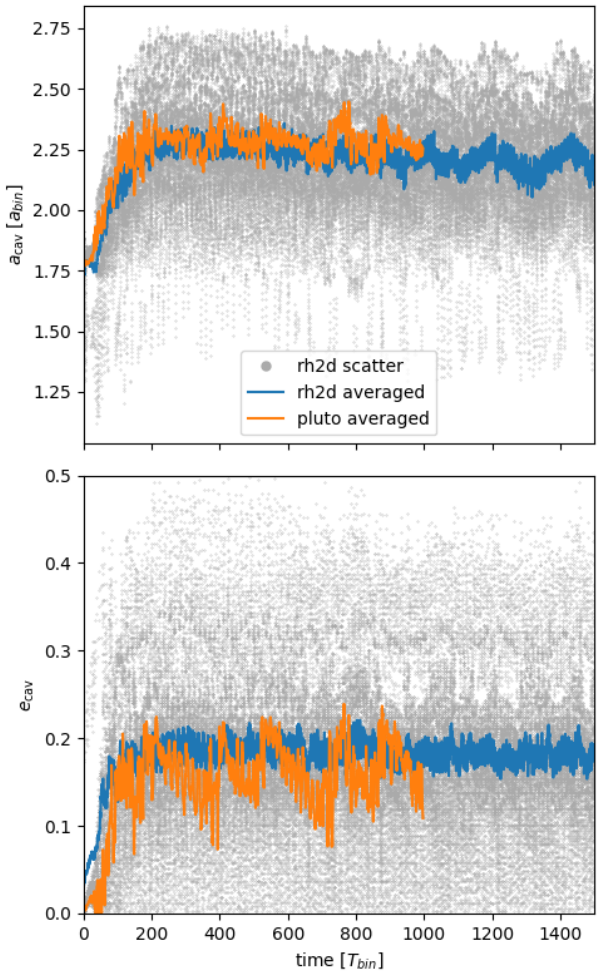

Fig. 4: Approximated cavity size and eccentricity for the standard model. The curves denoted 'averaged' denote the sliding averages over 10 orbits for 3 different codes used. The grey dots show the instantaneously estimated values.

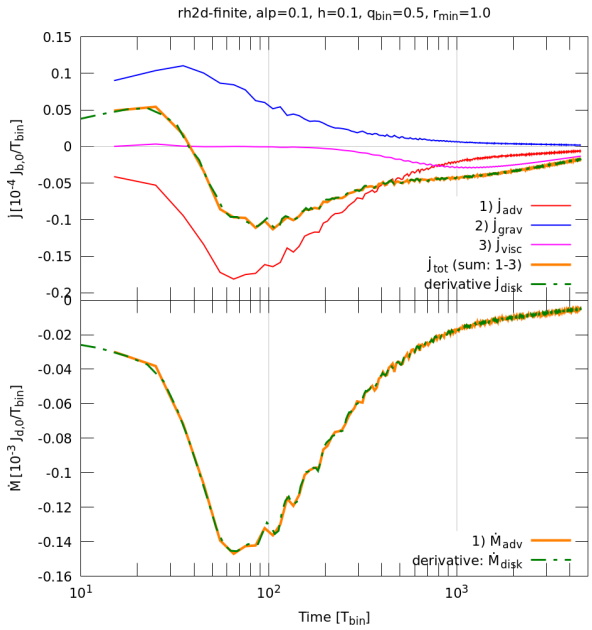

Fig. 5: Loss/gain channels of mass and angular momentum (AM) of the disc. The curves denote: 1) $\dot{J}_{\rm adv}$ (through $r_{\rm min}$), 2) $\dot{J}_{\rm grav}$ (torque by binary), and 3) $\dot{J}_{\rm visc}$ (through $r_{\rm max}$). The dashed curves labelled 'derivative' denote the time derivative of the disc's total mass/AM. The sum of 1-3 (green curve) matches exactly the calculated changes.

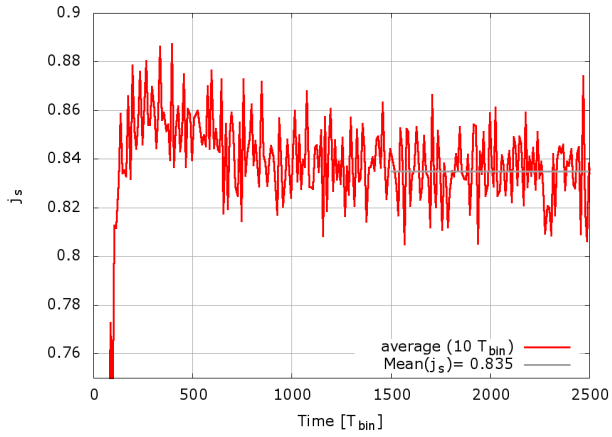

Fig. 6: Specific angular momentum transfer, $j_{\rm s}$, onto the binary for the standard model. The curve represents a sliding average over 10 orbits, and the grey line shows the average over the last 1000 orbits.

4.2. Mass and angular momentum balance

During the computation we monitor the global mass and angular momentum (AM), and the fluxes across the outer and inner boundary as well. To obtain an idea of the importance of the individual contributions, we display the individual loss/gain channels in Fig. 5, labelled by 1) to 3). In addition, we display the sum of all 3 contributions and show that it matches exactly the rate of change in mass and AM as calculated from the time evolution of the global disc values, denoted by 'derivative' in the plot. This shows that our measurements are fully consistent and that we can accurately track all loss/gain channels of mass and AM. As seen in Fig. 5 the torques from the binary create a positive input of AM to the disc (blue curve) while the loss through the inner boundary represents a loss term (red curve). The sum (in green) shows that during a short initial phase ($\approx 40\,T_{\rm bin}$) the disc gains more angular momentum from the binary than it loses. After that the losses overwhelm and the disc loses angular momentum to the binary. The loss of angular momentum through the outer boundary (purple curve) is negligible for the first $1000\,T_{\rm bin}$. However, it begins to be the main loss channel after about $2300\,T_{\rm bin}$ when the disc has spread so much that $|\dot{J}_{\rm visc}| > |\dot{J}_{\rm adv}|$.

The results on the mass and AM fluxes displayed in Fig. 5 are then used to calculate the specific angular momentum transfer, $j_{\rm s}$, to the binary according to eq. (7). The outcome is displayed in Fig. 6, where we plot $j_{\rm s}$ as a function of time for the standard model. Initially, $j_{\rm s}$ rises steeply until is reaches a maximum at $t \approx 300\,T_{\rm bin}$, after that it drops slowly to reach an equilibrium value after about $1000\,T_{\rm bin}$ of about $j_{\rm s} = 0.84$. This equilibrium of $j_{\rm s}$ is obtained despite the fact that the overall disc density, mass and AM

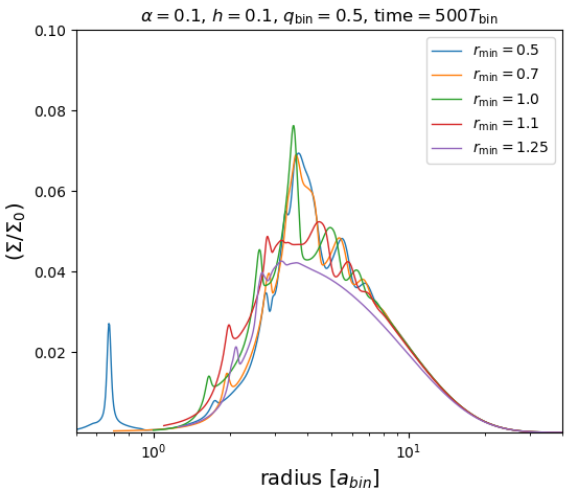

Fig. 7: Azimuthally averaged density for five different inner grid radii $r_{\rm min}$ after 500 binary orbits, for simulations using the PLUTO code.

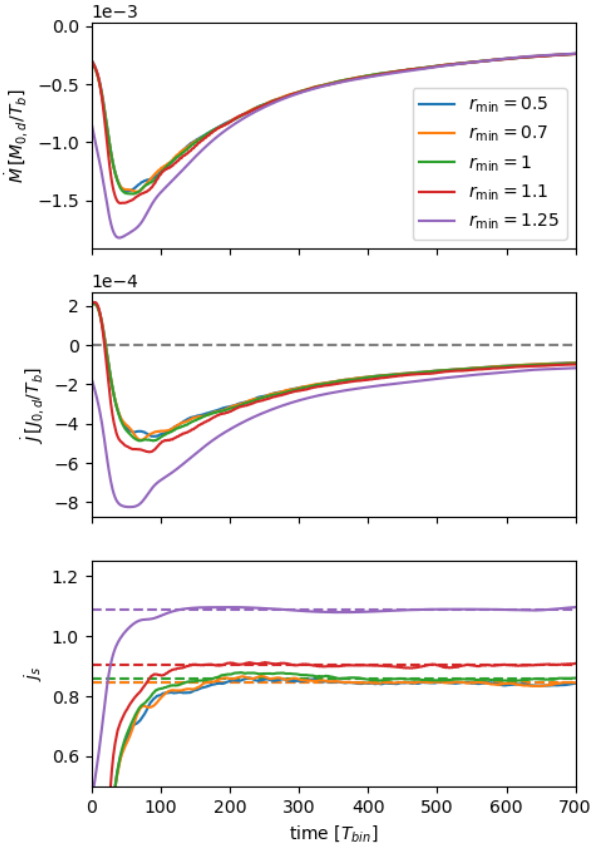

Fig. 8: Evolution of mass and angular momentum gain/loss rates of the disc, and $j_{\rm s}$ for different inner disc radii, using the PLUTO code. The dashed lines in the bottom panel indicate the obtained average values between $200-700\,T_{\rm bin}$.

are still evolving in time, and formally not a steady state has been reached. The reason lies in the fact that the inner disc region has reached dynamical equilibrium as Fig. 4 already indicated. The angular momentum flux $j_{\rm s}$ represents a eigenvalue of the disc as shown already by Miranda et al. (2017) and Muñoz et al. (2019).

Using the measured $j_{\rm s} = 0.84$ and the quoted critical values in Fig. 1, we can argue that this will lead to an expansion of the binary's orbit for a mass ratio $q = 0.5$ and the chosen disc parameter because $j_{\rm s} = 0.84 > j_{\rm s,crit}$ for all possible accretion ratios f. This statement about the orbital evolution of a circular binary is possible even though we do not include the binary explicitly in the computational domain, because all the mass and angular momentum that crosses the inner boundary has to be accreted by the binary. A necessary requirement is the establishment of a quasi-stationary state at least in the inner regions of the disc which can be checked for example by monitoring properties such as $a_{\rm cav}$, $e_{\rm cav}$, and of course $j_{\rm s}$ directly. The value of $r_{\rm min}$ must be chosen small enough to include the relevant disc dynamics and the diode inner boundary condition does not impact the results. In the next section we show that the measured value of $j_{\rm s}$ does not depend on the exact location of the inner boundary once $r_{\rm min} \lesssim a_{\rm bin}$.

4.3. Varying the inner radius of the grid

The determination of the angular momentum flux $j_{\rm s}$ depends on the details of the disc structure around the binary. Knowing from previous studies (Thun et al. 2017) this can depend on the location of the inner grid radius, $r_{\rm min}$. In order to validate our results and check for the numerical impact of this choice we performed additional computations using different values $r_{\rm min} = 1.25$, 1.1, 1.0, 0.7 and 0.5. For this study we adapted the number of radial grid cells such that we always had the same spatial resolution in the overlapping region. In Fig. 7 we display the azimuthally averaged surface density at 500 binary orbits for the standard model for the different $r_{\rm min}$, now for the whole spatial domain. In the outer disc region, beyond roughly $4\,a$ the density distributions are very similar for all $r_{\rm min} \leq 1.0\,a$. They all reach similar maximum densities, however, the two models with larger $r_{\rm min}$ (1.1, 1.25) have substantially smaller peak values, and are much smoother. This means that in spirals in the disc are reduced that cause perturbations in the density profile. The $r_{\rm min} = 1.25$ model displays not more spirals, and is therefore dynamically very different. For the model with the smallest $r_{\rm min} = 0.5$ there is a pronounced maximum in the density distribution at the location of the secondary star because material is collecting in its potential minimum. Concerning the overall size and shape of the cavity, i.e. its eccentricity and semi-major axis, we also find good agreement for the smaller $r_{\rm min}$, and deviations for the two larger values.

A similar result is obtained for the important mass and AM balance of the disc. In the top panels of Fig. 8 we display the time evolution of the disc's mass and AM loss/gain rates. For the models with $r_{\rm min} \lesssim 1$ they are identical during the whole evolution, however for larger inner boundaries the accretion rates increases non-physically. For the specific angular momentum accretion $j_{\rm s}$ onto the binary, displayed in bottom panel of Fig. 8, the results are very close as well for the three models with the smaller $r_{\rm min}$. Hence, for sufficiently small $r_{\rm min}$ the evolution is indeed solely given by the physical parameter of the system. Thereby, we conclude that $r_{\rm min} = 1.0$ is sufficient even for the highest values of viscosity and aspect ratio where the inner region around the

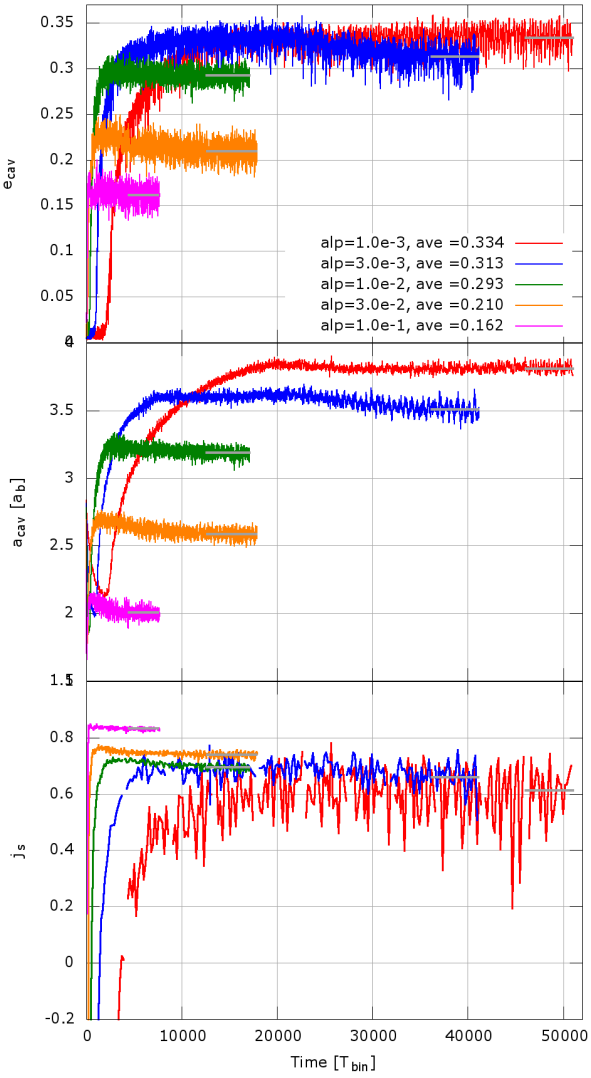

Fig. 9: The shape and size of the cavity around the binary (with $q = 0.5$) and the specific angular momentum j_s transferred, as a function of time for models with different viscosity, and an aspect ratio $h = 0.1$. The top two panels show sliding time averages over $10\,T_{\rm bin}$, in the bottom panel it was $200\,T_{\rm bin}$ for the two lowest α models, over $100\,T_{\rm bin}$ for $\alpha = 0.01$, and over 50 $T_{\rm bin}$ for $\alpha = 0.03$ and 0.1. The grey lines indicate the averaging interval for the final quoted equilibrium values. Simulations were performed with the RH2D-code.

two stars is not entirely empty. Hence, we adopt this value for our subsequent models and the parameter study as it represents a good compromise between physical accuracy and computational speed.

5. Parameter studies

After having analysed the physics of the standard model we investigated in more detail the dependence on the disc physics and ran models for different viscosities and aspect ratios. Additionally, we varied the mass ratio of the binary.

5.1. Varying α for the standard model

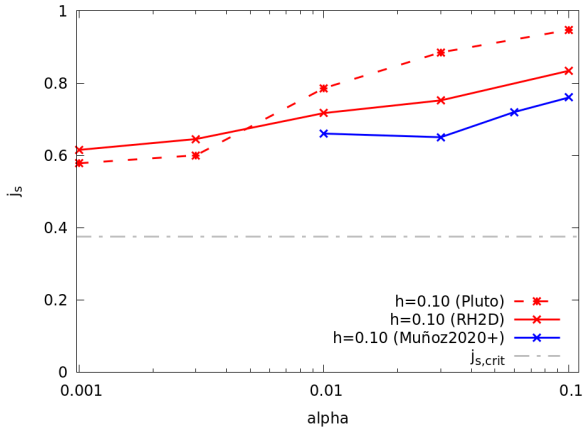

Fig. 10: The specific angular momentum j_s transferred to the binary (with $q = 0.5$) as a function of the viscosity with an aspect ratio of $h = 0.1$. The red data points and lines refer to the models in this work using two different codes, and the blue points and line refer to the results of Muñoz et al. (2020).

To study the impact of viscosity we present here models using a different α-parameter with values of [0.1,0.03,0.01,0.003,0.001], while keeping $H/r = 0.1$ and $q = 0.5$. This allows a direct comparison to Muñoz et al. (2020) who performed a similar study using four different α values. For lower viscosities the expected cavity size will become larger because the viscous torques are reduced (Artymowicz & Lubow 1994; Miranda & Lai 2015). To account for this, we changed the initial profile and moved the ring further out by choosing $r_{\rm in} = 4\,a$ and $r_{\rm out} = 10\,a$ in eqs. ((10) and (11). We have checked that identical equilibria, concerning the dynamics of the inner disc region (i.e. $a_{\rm cav}, e_{\rm cav}$ and j_s), are obtained independent of the choice of the initial density distribution.

To give an impression of the evolution towards equilibrium we show in Fig. 9 the time evolution of the cavity size, its eccentricity and j_s as a function of time for the 5 different α-values. Again, we obtain $a_{\rm cav}$ and $e_{\rm cav}$ using the fitting procedure described in Thun et al. (2017). As expected, the models with the lower viscosities take much longer to reach equilibrium as this is given by the viscous timescale. The time needed for the $\alpha = 10^{-3}$ model to fully evolve is $> 30\,000\,T_{\rm bin}$. The $\alpha = 0.1$ model is used most often in the literature, because the equilibration time is by far the shortest. For this case the cavity size is smallest ($a_{\rm cav} = 2.0$) with a mean eccentricity of 0.16. Lowering the viscosity, $a_{\rm cav}$ and $e_{\rm cav}$ increase monotonically and reach a maximum size and eccentricity for the model with the smallest $\alpha = 0.001$.

The corresponding evolution of the normalised angular momentum accretion onto the binary is displayed in the bottom panel of Fig. 9. To obtain the final j_s value we average over the length marked in grey and obtain the quoted values. The averaging time increases for smaller viscosities due to larger noise in the data. During the initial cavity filling phase j_s is negative because the gravitational torques overwhelm the inflow of angular momentum $|\dot{J}_{\rm grav}| > |\dot{J}_{\rm adv}|$

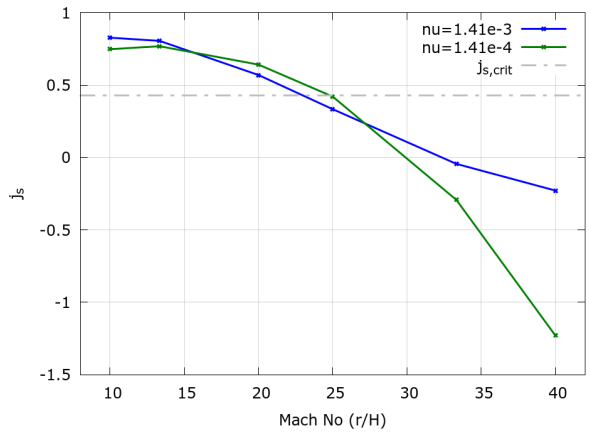

Fig. 11: The specific angular momentum j_s transferred to the binary as a function of the disc's Mach number for models with two different values of the kinematic viscosity, for a mass ratio $q = 0.5$. The dashed dotted line refers to a critical $j_{s,crit} = 0.43$.

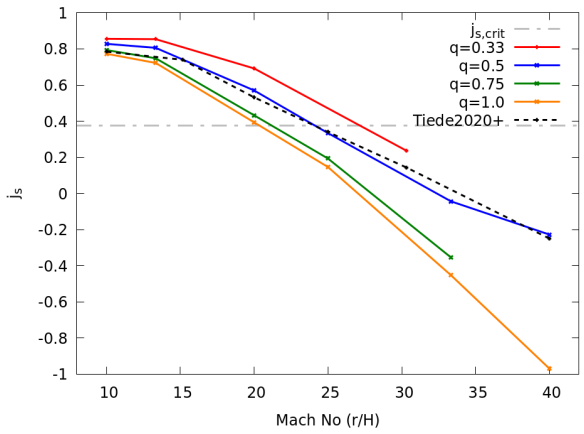

Fig. 12: The specific angular momentum j_s transferred to the binary as a function of the disc's Mach number. Presented are models using a constant kinematic viscosity, $\nu = \sqrt{2} \times 10^{-3}$, for different values of the binary mass ratio. The dashed dotted line refers to the critical $j_{s,crit} = 3/8$ for the case $q = 1$.

as seen for example in Muñoz et al. (2020) and Tiede et al. (2020). Again, the approach to equilibrium proceeds on the same (long) viscous timescales, and the final values show a monotonic drop with viscosity.

In Figure 10 we display the obtained j_s as a function of viscosity for the two different codes we used (`RH2D` and `PLUTO`). Both series show very similar behaviour, an increase of the angular momentum transfer to the binary with increasing viscosity. Overplotted are results extracted from Muñoz et al. (2020) which are for this study slightly lower than ours. The deviations in j_s could be caused by numerical differences like time steps or different grid structures as Muñoz et al. (2020) uses mesh refined grids but also be the result of the occurring uncertainty in the measurement of j_s. However, all models agree in the fundamental finding that thick discs with $h = 0.1$ lead to expanding orbits, even for viscosities as low as $\alpha = 10^{-3}$.

5.2. Models with constant viscosity

To allow for an individual and independent variation of viscosity and disc scale height, we ran a series of models using a constant kinematic viscosity ν and varied disc thickness and mass ratio. We studied two different values of ν, first we took the same value as Tiede et al. (2020) $\nu = \sqrt{2} \times 10^{-3}\,[a^2\,\Omega_{bin}]$, which allows a direct comparison to their work, and then a ten times lower value. The chosen ν refer to α values of 0.1 and 0.01 at a distance of $r = a$ for $H/r = 0.1$. In Fig. 11 j_s is displayed as a function of the disc's Mach number ($= r/H$) for a binary with our standard mass ratio $q = 0.5$, for the two different viscosities. For both viscosity values we find that j_s drops with Mach number and turns negative for Mach numbers between 30 and 33. This implies that in thin discs the binary orbit will expand where the turning point lies around a Mach number of 23-25, given by the point at which the curves cross the grey dashed-dotted line denotes a $j_{s,crit} = 0.43$, calculated for a mass accretion ratio of $f = 1.6$. See appendix B.1 for a discussion about the mass accretion ratio.

In addition to their study we varied now the mass ratio (ranging from $q = 0.33$ to $q = 1.0$), and display our results in Fig. 12. We find the trend that smaller mass ratios q lead to an increase in j_s, while the general behaviour of decreasing j_s with increasing Mach number is not impacted significantly by changing q. To determine the transition point between expansion and shrinkage for the values of $q \neq 1$ requires knowledge of the mass accretion factor f. For a rough estimate we added the dashed dotted line, which refers to $j_{s,crit} = 3/8$ for $q = 1$. The true values for the other q will be only slightly larger as argued in appendix B.1. For equal mass binaries we find an orbit expansion for thicker discs with Mach number smaller than ~ 20. To compare to earlier results, we overplot the results of Tiede et al. (2020) obtained for $q = 1$ (black dashed line). While the general trend is similar the absolute values differ, possibly due to the different numerical methods applied. Our simulations are 2D on a cylindrical grid not containing the binary while theirs are 2D Cartesian.

5.3. Parameter space of H/r and α

Here, we extended our parameter study to standard α-disc models models using five different values $\alpha = [0.1, 0.03, 0.01, 0.003, 0.001]$ and 3 different aspect ratios $H/r = [0.1, 0.05, 0.04]$, both for mass ratios of $q = 0.5$ and $q = 1$. As explained in Sect. 5.1 we run all the models long enough to reach a quasi-stationary equilibrium state with constant a_{cav}, e_{cav} and j_s.

In Fig. 13 the results for $q = 1$ are displayed obtained with two different codes, `PLUTO` and `RH2D`. The results obtained with `RH2D` are shown by the crosses and solid lines while the `PLUTO` results feature the asterisks and the dashed lines. The grey dashed-dotted line denotes the critical $j_{s,crit} = 0.375$ for $q = 1$. As already shown in Sect. 5.2 above, for a thick disc with $h = 0.1$ expanding binary orbits are possible for all values of the viscosity (at least down to $\alpha = 0.001$). This is due to the fact that in thick discs the high pressure leads to a continuous refill of the inner cav-

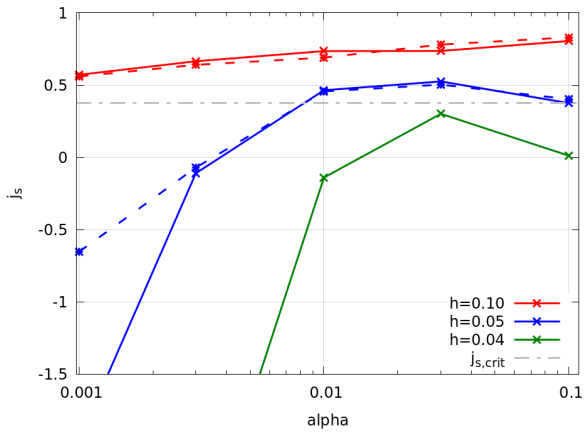

Fig. 13: The specific angular momentum j_s transferred to the binary as a function of the disc's viscosity, for a mass ratio, $q = 1.0$ and different aspect ratios. For $q = 1$ the critical rate is given by $j_{s,crit}$=3/8. Results for two different codes, RH2D (crosses, solid lines) and PLUTO (asterisks, dashed lines), are displayed.

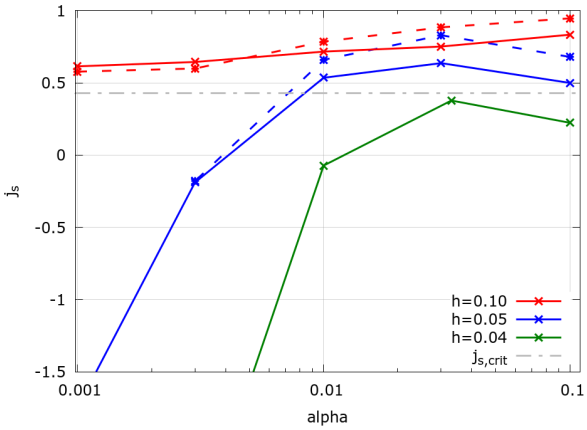

Fig. 14: The specific angular momentum j_s transferred to the binary as a function of the disc's viscosity, for a mass ratio, $q = 0.5$ and different aspect ratios, using the same notation as in Fig. 13. For the critical rate we assumed here $q = 0.5$ and $f = 1.6$, and obtain $j_{s,crit}$=0.43.

ity at a high rate carrying a significant amount of angular momentum with it. For thinner discs the pressure effect is reduced as well as the viscosity, which scales with h^2, and the resulting j_s-values become smaller, such that the possibility of expanding orbits will be reduced. The smallest aspect ratio, $h = 0.04$, results only in shrinking binary orbits, similar to what has been discussed already in section 5.2 above for the case of constant viscosities. For $h = 0.05$ only for a small window of viscosities between $\alpha = 0.01$ and 0.1 an expanding orbit is possible. We find a maximum in j_s for $\alpha \approx 0.03$ and a steep decrease of j_s towards smaller viscosities.

In systems with a mass ratio of $q = 0.5$, as shown in Fig. 14, the same trends apply. The denoted $j_{s,crit}$ corresponds to an accretion ratio $f = 1.6$, as motivated by our accretion studies presented in section B.1. The overall shape

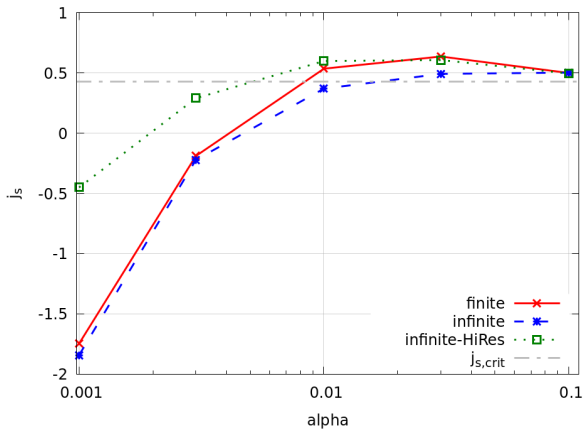

Fig. 15: Comparison of the normalised angular momentum accretion, j_s, for model with $q = 0.5$ and $H/R = 0.05$ for torus-like (finite) and infinite disc models using the standard (684x584) vs. higher (968x824) grid resolutions.

of the curves is very similar to the $q = 1$ case. For large viscosities $\alpha \geq 0.01$ the values for j_s lie above the $q = 1$ case, but as $j_{s,crit}$ is also increased, the possible parameter range in which orbit expansion is possible remains the same as in the case of equal mass binaries.

For our two model sequences, $q = 1.0$ and 0.5, shown in Figs. 13 and 14, we performed for the thicker discs with $h = 0.1$ and 0.05 comparison simulations with our two grid codes (RH2D, PLUTO). In general the agreement between the two codes is very good. Both show an identical behaviour upon changing the disc viscosity and scale height, even though the absolute values show some differences. Only for the lowest viscosity, $\alpha = 10^{-3}$, the differences become more pronounced but these models suffer more from numerical effects such as density floor, or diffusion.

In the analysis for very low viscosities the uncertainties in the measured and averaged j_s increase, and a much longer time evolution of several $\geq 10\,000\,T_{bin}$ is needed to reach a stable state of the disc. Additionally, the finite density floor begins to affect the results due to the very low density in the cavity. Even given these challenges in the simulations, the general picture emerges that low viscosities and small aspect ratios lead to shrinking binary orbits as the cavities become very deep and the advected angular momentum decreases.

5.4. Infinite disc models

The models discussed so far suffer from the problem that no genuine global stationary state is reached. To investigate a different physical setup and check for possible shortcomings of this approach we ran additional models using an 'infinite' disc setup, where we covered the full viscosity range for the $q = 0.5, H/R = 0.05$ model in different numerical resolutions. To model an infinite disc, r_{out} in eq. (11) is set to very large values, implying that $g_{out} \rightarrow 1$. At the same time we apply damping boundary conditions such that the density at $r_{max} = 40$ is always damped towards the initial state (de Val-Borro et al. 2006), while the velocities are kept at their original values. This setup will allow a quasi-stationary equilibrium state to be reached and is

hence comparable to the infinite disc models of Muñoz et al. (2020). Due to the outflow condition at the inner boundary, at $r_{min} = a$, there is a mass flow through the disc and the (time averaged) mass accretion will be radially constant, see also Kley & Haghighipour (2014). It is crucial to set a very low density floor in the models, because the small viscosity simulations can reach very low densities inside the cavity. Here, we used floor values as low as 10^{-10} of the initial $\Sigma(r = 1)$.

The resulting j_s is shown in Fig. 15 where we display results for the finite torus models from above (red data termed 'finite') and new simulations using the 'infinite' disc setup at two different grid resolutions, the standard 684x584 (blue-dashed) and a higher resolution 968x824 case (green-dotted). To save computational time, the higher resolution models are not started from $t = 0$ but are continued from the standard resolution runs at a time when those reached approximately their equilibrium state. All simulations in Fig. 15 follow the same overall trends but differ in the actual values of j_s. Concerning j_s, we find an increase for the higher resolution runs for the lower viscosities, however it is not sufficient to lead to an expansion of the binary because the values lie consistently below $j_{s,crit}$. We confirm the finding of Muñoz et al. (2020), that the outer boundary will not significantly change the inner angular momentum transport relevant for the binary. Additional tests for $H/R = 0.05, \alpha = 0.003$ with even higher resolution show no further changes in j_s, and we believe the shrinking of the binary to be real for very low viscosities.

For our locally isothermal infinite disc models in quasi-equilibrium for which the density at the outer boundary is fixed, the mass accretion rate should scale linearly with the viscosity, due to the classic relation $\dot{M} = 3\pi\nu\Sigma$. In the top panel of Fig. 16 we plot the mass accretion rate onto the binary (measured at r_{min}) as a function of α for models with $q = 0.5$ and $h = 0.05$ at two numerical resolutions, using the line style of Fig. 15. Apart from the smallest α-values the expected linear relation (grey line) is well satisfied, but the agreement with the linear relation improves with higher grid resolution. The bottom panel of Fig. 16 shows the absolute value of the two contributions to $\dot{J}_b$, the gravitational part ($\dot{J}_{grav}$, green and blue lines) and the advective part ($\dot{J}_{adv}$, in grey). The gravitational term removes angular momentum from the binary, while the advection term adds angular momentum to it. The two advective terms, $\dot{J}_{adv}$ and $\dot{M}_{adv}$, follow the same slope such that the advective $j_{s,adv} = \dot{J}_{adv}/\dot{M}$ is almost constant at a value of 1.25 ± 0.04, upon varying the viscosity. It has a lowest value of ~ 1.21 for $\alpha = 0.003$ and increases to ~ 1.27 for $\alpha = 0.1$, and is ~ 1.23 for the smallest $\alpha = 0.001$. At the same time the gravitational contribution $\dot{J}_{grav}$ flattens towards smaller viscosities and equals the advective part for $\alpha \sim 0.002$, making the total j_s negative, as seen in Fig. 15.

In order to understand the observed behaviour better we show in Fig. 17 the two-dimensional surface density distribution for the 'infinite' disc models for the different viscosities. The computed cavity edges are marked by the white, dashed ellipses, computed with the method described in Thun et al. (2017). Clearly seen are the eccentric inner cavities, which are more pronounced in these thinner discs ($h = 5\%$) compared to the standard model (with $h = 10\%$) even at a logarithmic scale. The cavity's size and eccentricity are both smallest for the highest viscosity

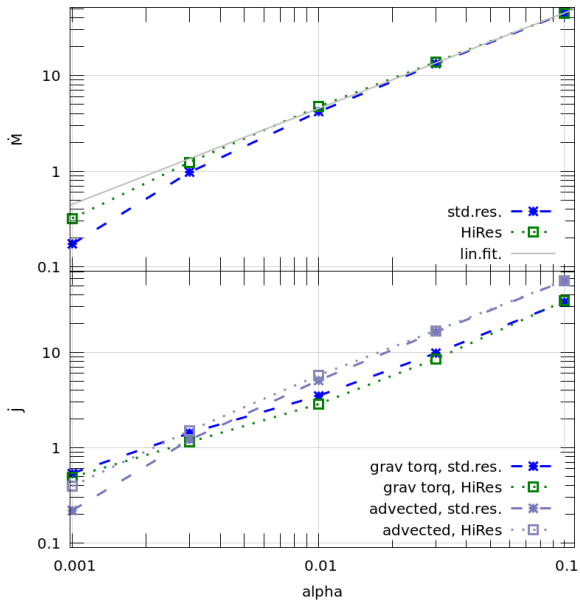

Fig. 16: Top: The mass accretion rate onto the binary as a function of viscosity for infinite disc models with $q = 0.5$ and $h = 0.05$. The grey line indicates a linear slope. Bottom: The corresponding absolute value of gravitational (blue and green lines) and advective (grey lines) angular momentum transfer, $\dot{J}_{grav}$ and $\dot{J}_{adv}$ respectively. Shown are the results for the standard (asterisks, dashed lines) and higher resolution (squares, dotted).

case ($\alpha = 10^{-1}$) and increase upon lowering α. Maximum values for a_{cav} and e_{cav} are reached for intermediate α and they drop again for even smaller viscosities. Using the logarithmic colour scale the streamers and infalling gas inside the cavity are visible. The strength of streamers weakens with reduced viscosity, coinciding with the generally declining trend in the advective angular momentum contribution seen in Fig. 16. As expected the cavity becomes wider and deeper upon lowering the viscosity. When the viscosity becomes very low, however, this trend is slowed and even reverses. At the same time with reduced accretion the mass in the streamers declines and torque from inside the cavity reduces proportionally. However, the always eccentric disc causes the gravitational contribution in Fig. 16 to change its slope around $\alpha = 0.01$, aided by the slight contraction of the disc, resulting in shrinking binary orbits for the lowest viscosities.

6. Discussion and conclusion

We presented 2D hydrodynamical simulations of discs around a circular binary where disc and binary are coplanar. We monitored the mass and angular momentum balance of the disc in order to calculate the binary's orbital evolution. Our prime interest was to evaluate shrinkage or expansion of the binary by determining the sign of the semi-major axis evolution, for different mass ratios of the binary and various disc parameter. Based on the assumption that the binary's orbit remains circular under this accretion process we showed that its change in semi-major axis due to the mass and angular momentum transfer between circumbinary disc and binary is directly proportional to the mass

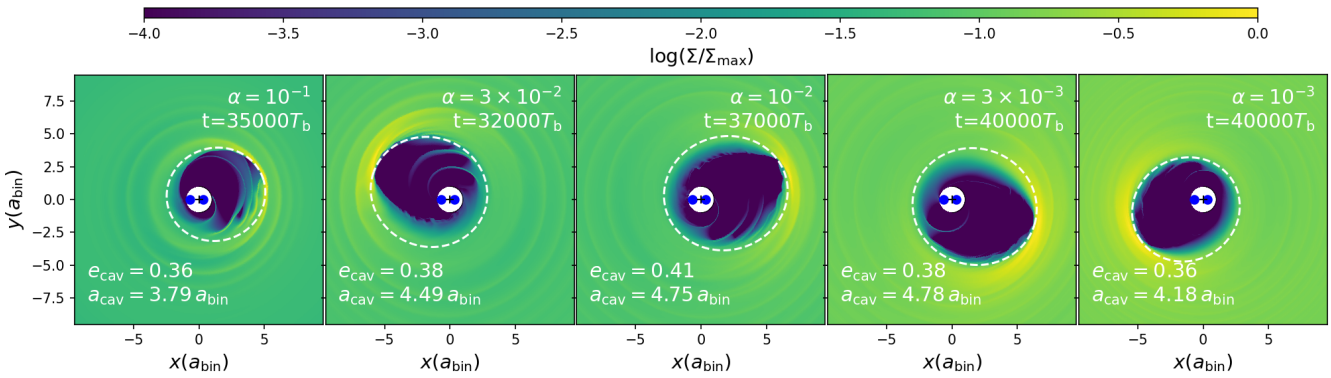

Fig. 17: Snapshots of the surface density for infinite disc models with $q = 0.5$ and $H/R = 0.05$ for different viscosities, ranging from $\alpha = 0.1$ (left) to $\alpha = 0.001$ (right). Shown is the inner region of the disc for the higher resolution models in their final state at the times indicated. The white dashed lines indicate the ellipses fitted to the cavity with the parameters quoted. The blue dots mark the position of the stars.

accretion rate times a function that depends on the stellar mass ratio q, the specific angular momentum transfer j_s, and the relative mass accretion onto the binary f, see eq. (8).

In agreement with the studies of Miranda et al. (2017) our simulations show that the specific angular momentum transfer rate j_s serves as an eigenvalue of the problem that can be calculated using a cylindrical grid with an inner hole which has a radius of $r_{in} \sim a_{bin}$, i.e. the grid does not contain the central binary system. Additionally, we confirm results of Muñoz et al. (2020) that in order to obtain a quasi-equilibrium for j_s it is sufficient to model a torus like configuration with limited radial extent, because it is sufficient to bring the inner disc regions into equilibrium and not the whole disc. This finding is supported by additional simulations using an infinite disc setup that allows for a global stationary state with resulted in j_s-values very similar to the torus models.

While for q=1 the critical value is given by $j_{s,crit} = 3/8$, for all $q \neq 1$ knowledge of f is required to find the exact threshold $0 < j_{s,crit} < 1$. In the work of Muñoz et al. (2020) the mass accretion ratio of systems with $q = 0.5$ averages $f \approx 1.5$, which is consistent with the trend in Dittmann & Ryan (2021). In order to compare, we performed supplemental simulations covering the whole domain in the appendix using Cartesian grids and the SPH method. We found that for a mass ratio of $q = 0.5$ the mass accretion ratio lies somewhere between 1.3 and 1.8, i.e. the secondary star accretes more mass from the disc than the primary. As these studies are very time consuming and depend on numerical treatments such as potential smoothing, sink radii and others, we will leave a more detailed analyses to future studies for the full range of parameters.

Using an average value $f = 1.6$ we showed for two mass ratios ($q = 1$ and 0.5) that binaries expand for sufficiently high viscosity, $\alpha \geq 0.01$, and disc aspect ratios, $h \geq 0.05$. For thinner and less viscous discs the binaries tend to shrink. Thick discs with $h = 0.1$ result in expansion for all viscosities, while discs with $h = 0.05$ show expansion for α larger than ~ 0.005. Independent of the mass ratio we find that thin and low viscosity disc cause the binary orbit to shrink, only thick and highly viscous discs can lead to expanding binary orbits.

For our simulations we assumed a coplanar configuration where the disc and binary lie the same plane. This is motivated by the observed coplanar distribution of detected circumbinary planets and the fact that the inner disc will align towards the binary plane over time, see e.g. Pierens & Nelson (2018). Additionally, we restricted ourselves to a 2D treatment and neglected the vertical disc structure. Only this simplification allowed us to perform the simulations over viscous timescales. The aligned 3D SPH-model in Hirsh et al. (2020) produce comparable cavity structures and sizes as 2D models, and therefore we expect that the restriction to a 2D-setup can produce realistic results.

In our models we kept the binary stars on a fixed orbit. Muñoz et al. (2019) carefully evaluated the binary migration rate $\dot{a}/a$ in a dynamic model and find to be on the order of 2 time the mass accretion rate for the $\alpha = h = 0.1$ case. For even smaller viscosities it will migration will be considerably slower, accordingly. We tested $\dot{a}/a$ in the disc structure caused by the gravitational term $\dot{J}_{grav}$ and found no deviations with or without "live" binaries in the simulations for various viscosities. We did not include the momentum transfer onto the binary stars in this study, as it is not computationally feasible to create models with very lower viscosity including the motion of the binaries directly, due to the very long convergence time needed.

In Eq. (8) we omitted the eccentricity term as we only looked at circular binaries. Considering also the change in eccentricity would lead to a second variable to solve for and the resulting equation would not be solvable with just angular momentum conservation. The additional property to look for is the momentum change of the binary induced by the mass accretion which can only be computed if the stars are contained within the computational domain, which is not feasible for the current models. As circular binaries represent that configuration with maximum angular momentum for a given semi-major axis we might expect as a consequence that positive angular momentum transfer will always keep the orbit circular. Models with live binaries show indeed that the induced eccentricity remains indeed very small for initially circular orbits (see for example Muñoz et al. 2019; Heath & Nixon 2020).

By using the simple prescription of a locally isothermal environment, the model is simple but scalable. This

allows for general parameter studies for diverse astronomical discs. In case a specific system is examined, a radiative model that includes viscous heating and possibly irradiation can be more physical. In Kley et al. (2019) we tested viscously heated and radiatively cooled circumbinary discs using the parameters of the Kepler-38 and Kepler-16 systems and found that the locally isothermal assumption with a flat aspect ratio between 4% and 5% for the inner disc provides a good approximation to the more realistic case.

In the models with low viscosities the accretion of mass and angular momentum becomes very small due to the large cavity size and long viscous evolution time scales. This also implies that the occurring temporal variations in the accretion rate result in larger fluctuations of the measured j_s. Therefore, to obtain the mean j_s we have to calculate a rolling average over larger time interval, up to $100\,T_{\rm bin}$, or 1000 outputs if obtained from individual snapshot. Still j_s for $\alpha = 10^{-3}$ varies over ± 0.2. Nevertheless, our result that for low viscosity thin discs the binary orbits shrink seems to be robust as the decline of j_s is much larger than these fluctuations. Since for small values of viscosity and H/r numerical effects may affect the results we ran additional simulations using higher grid resolutions and in addition an infinite disc setup. The results, presented in 5.4, show that j_s increases for higher resolution but not enough to change our conclusion.

We do consider the binary as point like gravitational sources. However, the planet hosting Kepler binary systems are close binaries that in addition to the disc's impact are influenced by tidal interactions between the stars. In a theoretical study of Kepler 47b (Graham et al. 2020), the binary stars have roughly a semi-major axis change of 0.5% over 10^9 years. This would be a much slower change than the effect we see from the disc. Therefore we can safely assume that the disc is dominant in changing the semi-major axis even for such kinds of close binaries.

Overall, the regime of binary expansion extends to a much wider parameter space than previously anticipated which will have consequences with respect to the orbital evolution of binary black holes prior to merger or the evolution of stellar binaries in their formation phase. These results for very low disc thicknesses and viscosities are somewhat preliminary as our numerical resolution may not have been high enough to cover these cases properly. Additional simulations using higher numerical resolution suggest that j_s increases, which could imply that the range of binary expansion will be somewhat larger, not changing our conclusion of shrinking binaries for low α and small H/r.

Future simulations need to address more realistic physical conditions where radiative effects are included. The geometry needs to be extended to full 3D to verify the thin disc approach as recent simulations of massive embedded planet in discs point towards a discrepancy between 2D and 3D simulations with respect to the eccentricity of the outer disc (Li et al. 2021).

Acknowledgements. During the course of the revision of this paper, our colleague Willy Kley passed away unexpectedly. We want to express our sincere gratitude to him, who was not only our mentor, but also a dear and supportive friend. Thank you, Willy! Anna Penzlin and Hugo Audiffren were both funded by grant 285676328 from the German Research Foundation (DFG). The authors acknowledge support by the High Performance and Cloud Computing Group at the Zentrum für Datenverarbeitung of the University of Tübingen, the state of Baden-Württemberg through bwHPC and the German Research Foundation (DFG) through grant no INST 37/935-1 FUGG. Some of the plots in this paper were prepared using the Python library matplotlib (Hunter 2007).

References

Artymowicz, P., Clarke, C. J., Lubow, S. H., & Pringle, J. E. 1991, ApJ, 370, L35
Artymowicz, P. & Lubow, S. H. 1994, ApJ, 421, 651
Begelman, M. C., Blandford, R. D., & Rees, M. J. 1980, Nature, 287, 307
de Val-Borro, M., Edgar, R. G., Artymowicz, P., et al. 2006, MNRAS, 370, 529
Dittmann, A. J. & Ryan, G. 2021, ApJ, 921, 71
Duffell, P. C., D'Orazio, D., Derdzinski, A., et al. 2020, ApJ, 901, 25
Flebbe, O., Muenzel, S., Herold, H., Riffert, H., & Ruder, H. 1994, ApJ, 431, 754
Graham, D. E., Fleming, D. P., & Barnes, R. 2020, arXiv e-prints, arXiv:2011.10430
Heath, R. M. & Nixon, C. J. 2020, A&A, 641, A64
Hirsh, K., Price, D. J., Gonzalez, J.-F., Ubeira-Gabellini, M. G., & Ragusa, E. 2020, MNRAS, 498, 2936
Hunter, J. D. 2007, Computing In Science & Engineering, 9, 90
Kley, W. 1989, A&A, 208, 98
Kley, W. 1999, MNRAS, 303, 696
Kley, W. & Haghighipour, N. 2014, A&A, 564, A72
Kley, W., Thun, D., & Penzlin, A. B. T. 2019, A&A, 627, A91
Li, Y.-P., Chen, Y.-X., Lin, D. N. C., & Zhang, X. 2021, ApJ, 906, 52
Mignone, A., Bodo, G., Massaglia, S., et al. 2007, ApJS, 170, 228
Milosavljević, M. & Merritt, D. 2003, in American Institute of Physics Conference Series, Vol. 686, The Astrophysics of Gravitational Wave Sources, ed. J. M. Centrella, 201–210
Miranda, R. & Lai, D. 2015, MNRAS, 452, 2396
Miranda, R., Muñoz, D. J., & Lai, D. 2017, MNRAS, 466, 1170
Monaghan, J. 1989, Journal of Computational Physics, 82, 1
Moody, M. S. L., Shi, J.-M., & Stone, J. M. 2019, ApJ, 875, 66
Muñoz, D. J., Lai, D., Kratter, K., & Miranda, R. 2020, ApJ, 889, 114
Muñoz, D. J., Miranda, R., & Lai, D. 2019, ApJ, 871, 84
Penzlin, A. B. T., Kley, W., & Nelson, R. P. 2021, A&A, 645, A68
Pierens, A. & Nelson, R. P. 2018, MNRAS, 477, 2547
Schäfer, C., Riecker, S., Maindl, T. I., et al. 2016, A&A, 590, A19
Schäfer, C., Speith, R., Hipp, M., & Kley, W. 2004, A&A, 418, 325
Schäfer, C. M., Wandel, O. J., Burger, C., et al. 2020, Astronomy and Computing, 33, 100410
Thun, D. & Kley, W. 2018, A&A, 616, A47
Thun, D., Kley, W., & Picogna, G. 2017, A&A, 604, A102
Tiede, C., Zrake, J., MacFadyen, A., & Haiman, Z. 2020, ApJ, 900, 43
Zrake, J., Tiede, C., MacFadyen, A., & Haiman, Z. 2021, ApJ, 909, L13

Appendix A: Code comparison

In order to validate complex hydrodynamical simulations it is very helpful, if not mandatory, to perform simulations using completely different numerical approaches on the same physical problem. Even though in this paper we have compared the two grid codes for a wider parameter range it is usually prohibited to do this for all different choices of parameter. Hence, we have chosen our standard model and performed simulations for three different codes: The finite volume codes `PLUTO` and `RH2D`, and a SPH code. 2007Mignone, The first code used is a full GPU version of the hydrodynamical part of the `PLUTO`-code (Mignone et al. 2007) as described in Thun et al. (2017). It is a Riemann-solver based finite volume code, where we used the van Leer limiter for the reconstruction and a second order time-stepping. As an alternative grid code we used `RH2D` which is a classic second-order upwind code working on a staggered

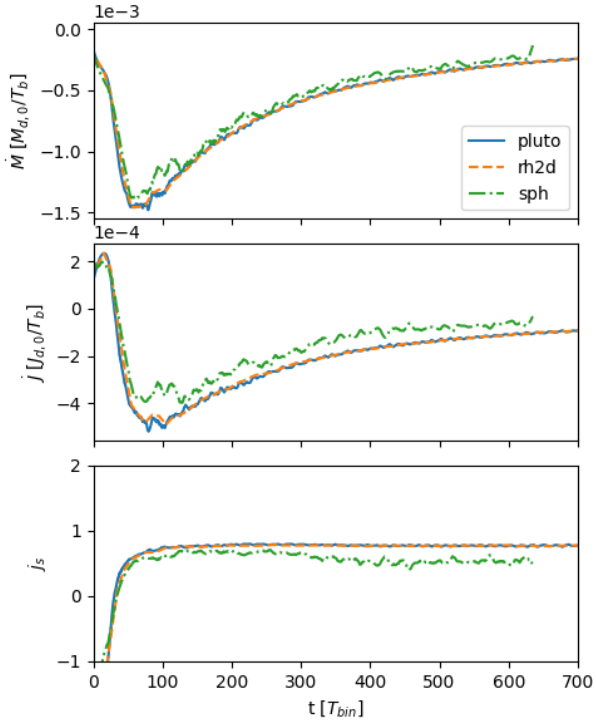

Fig. A.1: The mass accretion, angular momentum change of the disc and resulting j_s over time for our two grid codes `PLUTO` (blue, solid), `RH2D` (orange, dashed), and the SPH code `miluphcuda` (green, dash-dotted).

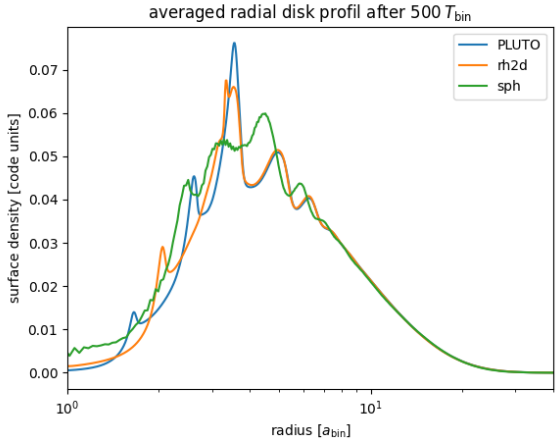

Fig. A.2: The azimuthally averaged surface density profile at 500 binary orbits of our two grid codes `PLUTO` (blue) and `RH2D` (orange), and the SPH code `miluphcuda` (green).

grid (Kley 1989, 1999), using again the van Leer limiter for the slopes.

For the SPH simulations we used the GPU code `miluphcuda` (Schäfer et al. 2016, 2020). In the standard model, we chose the same inner and outer boundary radius of the computational domain as the grid simulations, $1a$ to $40a$. Particles that cross the inner or outer boundary during the simulation are taken out of the computation. All particles have the same mass and are distributed in the beginning to represent the initial density profile. The initial smoothing lengths of the particles are chosen to ensure an overall constant number of interactions and to match the density profile. We apply variable smoothing and integrate the smoothing length using the standard approach (in 2D)

$$\frac{\mathrm{d}h_{\mathrm{SPH}}}{\mathrm{d}t} = -\frac{h_{\mathrm{SPH}}}{2}\nabla \cdot \mathbf{v}, \tag{A.1}$$

where h_{SPH} is the smoothing length and $\mathbf{v}$ the velocity. The code solves the Navier-Stokes equations following the scheme by Flebbe et al. (1994), where the kinematic viscosity is given by the α model (see above). Additionally, an artificial bulk viscosity is applied following Schäfer et al. (2004) and the XSPH algorithm for additional smoothing of the particle velocities is used (Monaghan 1989). The standard setup includes initially 500 000 particles.

All three simulations start from the same initial setup and are run for at least $600\,T_{\mathrm{bin}}$. In Fig. A.1 we show the time evolution for mass accretion and angular momentum change of the disc, and the specific angular momentum transfer j_s. The results for the `RH2D` code are identical to those displayed in Fig. 5 above. The two grid based codes show an excellent agreement for all three variables throughout the whole evolution. The SPH code has a slightly lower mass and angular momentum transfer resulting in a lower j_s but it lies still well above $j_{s,\mathrm{crit}}$. This difference is possibly caused by the different treatment of the viscosity in SPH. In the very low density region in the inner parts of the disc near the central binary there are fewer particles leading possibly to an inaccurate estimate of the viscosity. In Fig. A.2 we compare the azimuthally averaged radial density profile after $500\,T_{\mathrm{bin}}$. The results of all codes are almost perfectly aligned, except for highly dynamic spiral features in the density profile in the central regions. At the inner boundary the SPH code has slightly higher density, but the position of the density maximum, the onset of the spiral features, and the density of in the outer disc match well between all models. In particular, it is worth noting that the viscous outward spreading of the initial torus is identical for all 3 codes, indicating identical viscosity. We conclude that (at least for the standard model) the physical behaviour and conclusion about the binary evolution is robust.

Appendix B: Estimating the accretion ratio

Here, we present briefly our initial studies in estimating the accretion factor f. For this purpose we use two different approaches. First the grid-code `RH2D`, now in a Cartesian setup, and secondly the particle based SPH-code `miluphcuda`.

Appendix B.1: Cartesian grid simulation

To calculate the orbital evolution of the binary an estimate of the accretion factor, f, i.e. the mass accretion ratio onto the two stars is required. As this is not possible for a cylindrical grid which has an inner hole at r_{min}, we ran in addition Cartesian simulations using the two grid codes. Here, we cover the a domain of $[-20:20, -20:20]$ for the standard model with a Cartesian grid using different number of grid cells, ranging from 1200×1200 up to 4800×4800. In deviation from the standard model we use here a constant (dimensionless) viscosity of $\nu = 1.41 \cdot 10^{-3}$, to avoid prob-

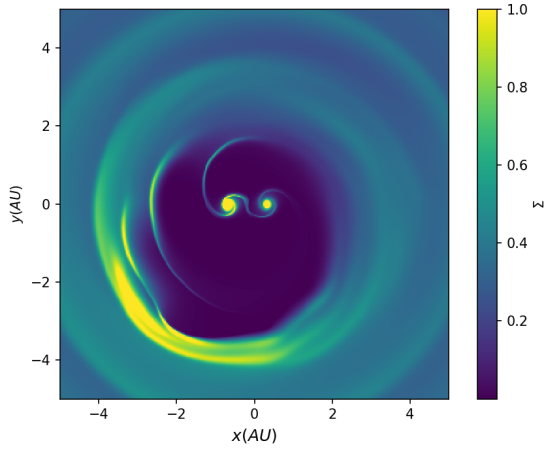

Fig. B.1: Density structure in the central region for the RH2D model with 3400 × 3400 cells with the parameters of the standard model after 500 binary periods.

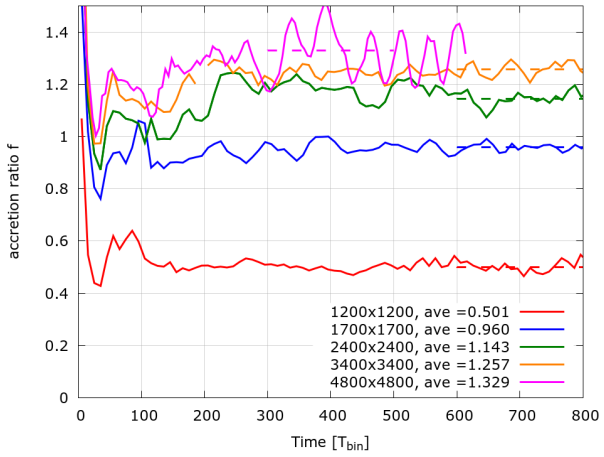

Fig. B.2: The stellar mass accretion ratio, $f = \dot{M}_2/\dot{M}_1$, onto the two stars, for Cartesian simulations with different grid resolutions. Shown is the time evolution with the corresponding averages, taken over the time interval indicated by the dashed lines.

lems in defining suitable disc thicknesses in the vicinity of the two stars. The initial density distribution is identical to the standard model, using $r_{\rm in} = 2.5$ and $r_{\rm out} = 6$. For the stellar potentials we use a Plummer-type smoothing with $r_{\rm sm1} = 0.15\,M_1$ and $r_{\rm sm2} = 0.15\,M_2$ for the two stars. For the sink radii we use $2/3\ r_{\rm sm}$ for the two stars. Inside the sink radii of the two stars mass is taken out at with a half-emptying time of $\tau_{1/2} \sim 7\,T_{\rm bin}$.

The 2D density distribution of such a Cartesian simulation is displayed in Fig. B.1 for the standard model after a simulated time of $500\,T_{\rm bin}$. Despite the accretion of mass the circumstellar discs are still visible around both stars, implying that the relatively short $\tau_{1/2}$ is not effective enough to get rid of the circumstellar discs entirely. From such simulations we can obtain the mass accretion rates on the two stars and the important accretion ratio, f. We did not monitor in these simulations the angular momentum transfer to the stars, and leave this to future studies.

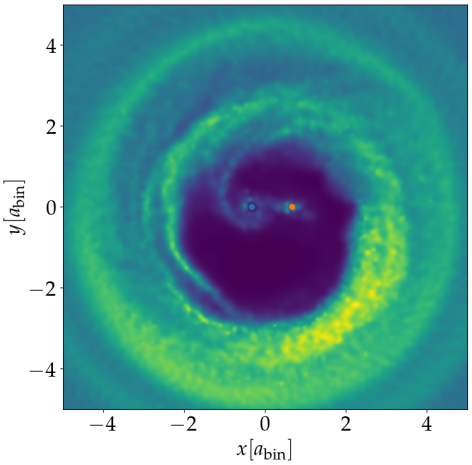

Fig. B.3: Density structure in the central region for the SPH model with the parameters of the standard model using 5×10^5 particles after 500 binary periods. For the colour scaling see Fig. B.1.

The measured accretion ratio for $q = 0.5$ onto the stars is displayed in Fig. B.2 for different grid resolutions. The models settle to an equilibrium at about 250 to $300\,T_{\rm bin}$ after which the accretion ratios remain approximately constant. Increasing the grid resolution increases the accretion factor, and the results converge for the standard model against a value $f_{\rm lim} \approx 1.37$. As a test for the accretion procedure, we performed the same simulation for a model with two equal mass stars ($q = 1, \alpha = 0.1$, and $h = 0.1$) and found a mass accretion ratio $f = 1$, meaning equal accretion onto both stars, as expected.

Appendix B.2: SPH-Miluphcuda

For the SPH simulations conducted in this project we define individual accretion radii around the stars, which are scaled with the corresponding mass. Whenever a particle crosses the accretion radius of a star, we monitor its mass, velocity and accretion time and remove it from the simulation. However, we chose the accretion radii small enough to prevent overlapping, i.e. $r_{\rm acc1} = 0.1\,M_1$ and $r_{\rm acc2} = 0.1\,M_2$.

The 2D density distribution of the model after a time $t = 500\,T_{\rm bin}$ is shown in Fig. B.3. The overall structure is very comparable to the results of the cylindrical and Cartesian grid models with similar cavity size. The density distribution was calculated by interpolating the particles to a cylindrical grid such that the same analysis tools could be used as for the grid codes. The SPH accretion ratio is plotted in Fig. B.4, and the mean value $f_{\rm SPH,mean} \approx 1.86$ is computed over the last 200 orbits.

In our parameter study we used an average $f = 1.6$ for the relative mass accretion rates in calculating the critical $j_{\rm s,crit}$, assuming that a similar value will be taken for other values of α and h. This value is in good agreement with the recent study by Dittmann & Ryan (2021) who performed a more detailed analyses of mass and angular momentum accretion using different numerical recipes, and with Muñoz et al. (2020) who used the moving mesh code AREPO, and found a slightly higher accretion ratio of ~ 1.7 after about

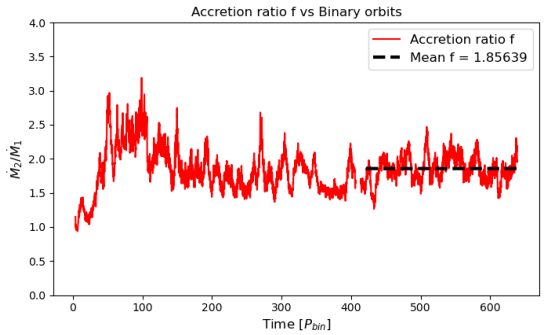

Fig. B.4: Accretion ratio evolution for the SPH model shown in Fig. B.3.

400 orbits for similar disc and binary parameter (see their Fig. 9).

List of Symbols and Abbreviations

Symbols

a	semi-major axis
$\mathbf{A}$	matrix in the Riemann solution
a_{bin}	common binary semi-major axis
a_{cav}	cavity semi-major axis
a_{p}	planet semi-major axis
α	viscous Shakura-Sunyeav parameter
b	semi-minor axis
b_{cav}	cavity semi-minor axis
β	normalized cooling time scale in local Kepler orbits
$c_{\mathrm{s,iso}}$	isothermal sound speed
c_{s}	sound speed
C	Courant number
e	specific energy
e_{bin}	binary eccentricity
e_{cav}	eccentricity of the inner cavity
e_{p}	eccentricity of the planet orbit
E	eccentric anomaly
f_{cav}	initial inner cut–off function
F_{grav}	gravitational force
$\mathbf{F}$	flux between cells
G	gravitational constant
γ	adiabatic index
h	disc aspect ratio
h_{ini}	initial disc aspect ratio
h_{mid}	aspect ratio derived from the midplane temperature
h_{surf}	aspect ratio derived from the surface temperature
H	pressure scale height
j_s	normalized specific angular momentum
$j_{\mathrm{s,crit}}$	critical normalized specific angular momentum
$\dot{J}_{\mathrm{adv}}$	advected angular momentum transfer
$\dot{J}_{\mathrm{disc}}$	angular momentum change to the disc
κ	opacity
$\vec{L}$	angular momentum
M	mean anomaly

m	mass
M_1	mass of the primary component
M_2	mass of the secondary component
$M_{\rm bin}$	binary mass
$M_{\rm Jup}$	Jupiter masses
$M_\odot$	solar masses
$\dot{M}$	mass accretion
$\dot{M}_{\rm adv}$	advected mass transfer
μ	dynamic viscosity
$\mu_{\rm bin}$	reduced mass of the binary
$\mu_{\rm gas}$	mean molecular weight of gas
ν	kinetic viscosity
N	number (of cells)
r	radius
r_a	radius for evaluation
R	radial grid
$R_{\rm hill}$	hill radius
$\mathfrak{R}$	ideal gas constant
$\Omega_{\rm K}$	Kepler angular velocity
$\Omega_{\rm p}$	angular velocity of a planet
p	exponent of the surface density
P	pressure
ϕ	azimuthal angle
q	exponent of the temperature profile
$q_{\rm bin}$	binary mass ratio
$q_{\rm p}$	mass ratio between planet and the central object
$Q_{\rm rad-}$	radiative cooling term
$Q_{\rm visc+}$	viscous heating
ρ	density
$\rho_{\rm mid}$	density at the midplane
Σ	surface density
S	source and sink terms of heating
$\Sigma_{\rm ini}$	initial surface density
σ	Stefan-Boltzmann constant
t	time
Δt	time step
T	temperature

T_0	temperature at a reference radius
$T_{\rm bin}$	binary orbit time
$T_{\rm prec}$	precession time
Θ	disc torque
τ	optical depth
$\boldsymbol{\tau}$	viscous stress tensor
$\tau_{\rm eff}$	effective optical depth
$\tau_{\rm grav}$	gravitational torque
$\mathbf{U}$	vector of density, velocity and pressure
$\vec{v}$	velocity vector
v_ϕ	azimuthal velocity
v_r	radial velocity
$v_{\rm K}$	azimuthal Kepler velocity
x, y	Cartesian coordinates
Δx	cell width
z	polar coordinate or height above the midplane

Abbreviations

2D, 3D	two dimensional, three dimensional
ALMA	Atacama Large Millimeter/submillimeter Array
au	astronomical units
CPU	central processing unit
CBD	circumbinary disc
CBP	circumbinary planets
e.g.	exempli gratia (for example)
Eq.	equation
GPU	graphics processing unit
i.e.	id est (that is)
Kep	Kepler (object observed in the Kepler Mission)
PPD	protoplanetary disc
SED	spectral energy distribution
SPH	smoothed particle hydrodynamics
SPHERE	Spectro-Polarimetric High-contrast Exoplanet REsearch instrument
TESS	Transiting Exoplanet Survey Satellite
VLT	Very Large Telescope array
yr	years

Bibliography

Andrews, S. M., Huang, J., Pérez, L. M., et al. 2018, ApJ, 869, L41

Armitage, P. J. 2019, Saas-Fee Advanced Course, 45, 1

Armitage, P. J. 2020, Astrophysics of Planet Formation, 2nd edn. (Cambridge University Press)

Artymowicz, P. & Lubow, S. H. 1994, ApJ, 421, 651

Balbus, S. A. & Hawley, J. F. 1991, ApJ, 376, 214

Benítez-Llambay, P. & Masset, F. S. 2016, The Astrophysical Journal Supplement Series, 223, 11

Bergin, E. A. & Tafalla, M. 2007, ARA&A, 45, 339

Beuzit, J. L., Vigan, A., Mouillet, D., et al. 2019, A&A, 631, A155

Calahan, J. K., Bergin, E. A., Zhang, K., et al. 2021, ApJS, 257, 17

Calcino, J., Price, D. J., Pinte, C., et al. 2019, MNRAS, 490, 2579

Cassan, A., Kubas, D., Beaulieu, J. P., et al. 2012, Nature, 481, 167

Cazzoletti, P., Ricci, L., Birnstiel, T., & Lodato, G. 2017, A&A, 599, A102

Chen, C., Franchini, A., Lubow, S. H., & Martin, R. G. 2019, MNRAS, 490, 5634

Chen, C., Lubow, S. H., & Martin, R. G. 2020, MNRAS, 494, 4645

Chen, C., Lubow, S. H., & Martin, R. G. 2022, MNRAS, 510, 351

Chiang, E. I. & Goldreich, P. 1997, ApJ, 490, 368

Cresswell, P. & Nelson, R. P. 2009, A&A, 493, 1141

Crida, A., Morbidelli, A., & Masset, F. 2006, Icarus, 181, 587

Dodson-Robinson, S. E., Evans, Neal J., I., Ramos, A., Yu, M., & Willacy, K. 2018, ApJ, 868, L37

Doyle, L. R., Carter, J. A., Fabrycky, D. C., et al. 2011, Science, 333, 1602

Duchêne, G. & Kraus, A. 2013, ARA&A, 51, 269

Dullemond, C. P., Birnstiel, T., Huang, J., et al. 2018, ApJ, 869, L46

Dullemond, C. P., Juhasz, A., Pohl, A., et al. 2012, RADMC-3D: A multi-purpose radiative transfer tool

Dürmann, C. & Kley, W. 2015, A&A, 574, A52

Dutrey, A., di Folco, E., Guilloteau, S., et al. 2014, Nature, 514, 600

Dvorak, R. 1986, A&A, 167, 379

Fontanive, C. & Bardalez Gagliuffi, D. 2021, Frontiers in Astronomy and Space Sciences, 8, 16

Frank, J., King, A., & Raine, D. J. 2002, Accretion Power in Astrophysics: Third Edition

Gammie, C. F. 2001, ApJ, 553, 174

Goldreich, P. & Tremaine, S. 1979, ApJ, 233, 857

Gressel, O., Turner, N. J., Nelson, R. P., & McNally, C. P. 2015, ApJ, 801, 84

Guilloteau, S., Dutrey, A., & Simon, M. 1999, A&A, 348, 570

Haffert, S. Y., Bohn, A. J., de Boer, J., et al. 2019, Nature Astronomy, 3, 749

Hirsh, K., Price, D. J., Gonzalez, J.-F., Ubeira-Gabellini, M. G., & Ragusa, E. 2020, MNRAS, 498, 2936

Holman, M. J. & Wiegert, P. A. 1999, AJ, 117, 621

Hubeny, I. 1990, ApJ, 351, 632

Hunziker, S., Schmid, H. M., Ma, J., et al. 2021, A&A, 648, A110

Johansen, A. & Youdin, A. 2007, ApJ, 662, 627

Keppler, M., Benisty, M., Müller, A., et al. 2018, A&A, 617, A44

Keppler, M., Penzlin, A., Benisty, M., et al. 2020, A&A, 639, A62

Keppler, M., Teague, R., Bae, J., et al. 2019, A&A, 625, A118

Klahr, H. H. & Bodenheimer, P. 2003, ApJ, 582, 869

Kley, W. 2019, Saas-Fee Advanced Course, 45, 151

Kley, W., Thun, D., & Penzlin, A. B. T. 2019, A&A, 627, A91

Köhler, R. 2011, A&A, 530, A126

Kostov, V. B., McCullough, P. R., Carter, J. A., et al. 2014, ApJ, 784, 14

Kostov, V. B., Orosz, J. A., Feinstein, A. D., et al. 2020, AJ, 159, 253

Kostov, V. B., Powell, B. P., Orosz, J. A., et al. 2021, AJ, 162, 234

Kounkel, M., Covey, K. R., Stassun, K. G., et al. 2021, arXiv e-prints, arXiv:2107.10860

Larson, R. B. 2003, Reports on Progress in Physics, 66, 1651

Leleu, A., Lillo-Box, J., Sestovic, M., et al. 2019, A&A, 624, A46

Li, G., Holman, M. J., & Tao, M. 2016, ApJ, 831, 96

Lin, D. N. C. & Papaloizou, J. 1985, in Protostars and Planets II, 981–1072

Lin, D. N. C. & Papaloizou, J. 1986, ApJ, 309, 846

Lynden-Bell, D. & Pringle, J. E. 1974, mnras, 168, 603

Lyra, W. & Umurhan, O. M. 2019, PASP, 131, 072001

Martin, D. V. 2018, in Handbook of Exoplanets, ed. H. J. Deeg & J. A. Belmonte, 156

Masset, F. S. & Papaloizou, J. C. B. 2003, ApJ, 588, 494

Mayor, M. & Queloz, D. 1995, Nature, 378, 355

Meschiari, S. 2012, ApJ, 761, L7

Mignone, A., Bodo, G., Massaglia, S., et al. 2007, ApJS, 170, 228

Miranda, R., Muñoz, D. J., & Lai, D. 2017, MNRAS, 466, 1170

Miranda, R. & Rafikov, R. R. 2020, ApJ, 892, 65

Molyarova, T., Akimkin, V., Semenov, D., et al. 2017, ApJ, 849, 130

Moody, M. S. L., Shi, J.-M., & Stone, J. M. 2019, ApJ, 875, 66

Muñoz, D. J., Lai, D., Kratter, K., & Miranda, R. 2020, ApJ, 889, 114

Muñoz, D. J., Miranda, R., & Lai, D. 2019, ApJ, 871, 84

Müller, T. W. A. & Kley, W. 2012, A&A, 539, A18

Nelson, R. P., Gressel, O., & Umurhan, O. M. 2013, MNRAS, 435, 2610

Öberg, K. I. & Bergin, E. A. 2021, Phys. Rep., 893, 1

Öberg, K. I., Guzmán, V. V., Walsh, C., et al. 2021, ApJS, 257, 1

Orosz, J. A., Welsh, W. F., Carter, J. A., et al. 2012, ApJ, 758, 87

Orosz, J. A., Welsh, W. F., Haghighipour, N., et al. 2019, AJ, 157, 174

Paardekooper, S. J., Baruteau, C., Crida, A., & Kley, W. 2010, MNRAS, 401, 1950

Paardekooper, S.-J., Leinhardt, Z. M., Thébault, P., & Baruteau, C. 2012, ApJ, 754, L16

Papaloizou, J. C. B., Nelson, R. P., Kley, W., Masset, F. S., & Artymowicz, P. 2007, in Protostars and Planets V, ed. B. Reipurth, D. Jewitt, & K. Keil, 655

Penzlin, A. B. T., Ataiee, S., & Kley, W. 2019, A&A, 630, L1

Penzlin, A. B. T., Kley, W., & Nelson, R. P. 2021, A&A, 645, A68

Pierens, A., McNally, C. P., & Nelson, R. P. 2020, MNRAS, 496, 2849

Pierens, A. & Nelson, R. P. 2013, A&A, 556, A134

Pierens, A., Nelson, R. P., & McNally, C. P. 2021, MNRAS, 508, 4806

Pinte, C., Dent, W. R. F., Ménard, F., et al. 2016, ApJ, 816, 25

Popova, E. A. & Shevchenko, I. I. 2016, Astronomy Letters, 42, 474

Pringle, J. E. 1981, ARA&A, 19, 137

Quarles, B., Satyal, S., Kostov, V., Kaib, N., & Haghighipour, N. 2018, ApJ, 856, 150

Raghavan, D., McAlister, H. A., Henry, T. J., et al. 2010, ApJS, 190, 1

Ragusa, E., Alexander, R., Calcino, J., Hirsh, K., & Price, D. J. 2020, MNRAS, 499, 3362

Rein, H. & Liu, S. F. 2012, A&A, 537, A128

Rein, H. & Spiegel, D. S. 2015, MNRAS, 446, 1424

Rein, H., Tamayo, D., & Brown, G. 2019, MNRAS, 489, 4632

Ricker, G. R., Winn, J. N., Vanderspek, R., et al. 2015, Journal of Astronomical Telescopes, Instruments, and Systems, 1, 014003

Schwamb, M. E., Orosz, J. A., Carter, J. A., et al. 2013, ApJ, 768, 127

Shakura, N. I. & Sunyaev, R. A. 1973, A&A, 24, 337

Silsbee, K. & Rafikov, R. R. 2015, ApJ, 808, 58

Socia, Q. J., Welsh, W. F., Orosz, J. A., et al. 2020, AJ, 159, 94

Strom, K. M., Strom, S. E., Edwards, S., Cabrit, S., & Skrutskie, M. F. 1989, AJ, 97, 1451

Tazaki, R. 2021, MNRAS, 504, 2811

Thun, D. & Kley, W. 2018, A&A, 616, A47

Thun, D., Kley, W., & Picogna, G. 2017, A&A, 604, A102

Thun, D. G. 2019, PhD thesis, University of Tübingen, Germany

Tiede, C., Zrake, J., MacFadyen, A., & Haiman, Z. 2020, ApJ, 900, 43

Tiede, C., Zrake, J., MacFadyen, A., & Haiman, Z. 2021, arXiv e-prints, arXiv:2111.04721

Toro, E. 2009, Riemann Solvers and Numerical Methods for Fluid Dynamics: A Practical Introduction

van Holstein, R. G., Girard, J. H., de Boer, J., et al. 2020, A&A, 633, A64

Weidenschilling, S. J. 1977, Ap&SS, 51, 153

Welsh, W. F., Orosz, J. A., Carter, J. A., et al. 2012, Nature, 481, 475

Welsh, W. F., Orosz, J. A., Short, D. R., et al. 2015, ApJ, 809, 26

Youdin, A. N. & Goodman, J. 2005, ApJ, 620, 459